# 17

# Modeling Water Storage Dynamics in Large Floodplains and Wetlands



Model grid

Drainage direction and river basins with discharge stations

Lakes and wetlands

Surface elevation

Landcover
Hydrogeology
Soil texture
Soil water capacity
Climate data

## Linda Adam

Frankfurt a. M. 2017

# Frankfurt Hydrology Paper

Frankfurt Hydrology Papers:

01  **A Digital Global Map of Irrigated Areas - An Update for Asia**

02  **Global-Scale Modeling of Nitrogen Balances at the Soil Surface**

03  **Global-Scale Estimation of Diffuse Groundwater Recharge**

04  **A Digital Global Map of Artificially Drained Agricultural Areas**

05  **Irrigation in Africa, Europe and Latin America -
Update of the Digital Global Map of Irrigation Areas to Version 4**

06  **Global data set of monthly growing areas of 26 irrigated crops**

07  **The Global Crop Water Model (GCWM):
Documentation and first results for irrigated crops**

08  **Towards mapping the extent of irrigation in the last century:
time series of irrigated area per country**

09  **Global estimation of monthly irrigated and rainfed crop areas
on a 5 arc-minute grid**

10  **Entwicklung der transdisziplinären Methode
„Akteursbasierte Modellierung" und ihre Anwendung
im Problemfeld der mobilen, organischen Fremdstoffe**

11  **Expert-based Bayesian Network modeling for environmental
management**

12  **Anthropogenic river flow alterations and their impacts on freshwater
ecosystems in China**

13  **Design, implementation and evaluation of a participatory strategy
development – A regional case study in the problem field of renewable
electricity generation**

14  **Global-scale modelling and quantification of indicators for assessing
transboundary aquifers. A contribution to the GEF Transboundary
Waters Assessment Programme (TWAP)**

15  **Evaluating alternative water sources and their use for small-holder
agriculture from a systemic perspective. A focus on water reuse and
rainwater harvesting in Namibia**

16  **Evaluation, modification and application of a global hydrological model**

17  **Modeling Water Storage Dynamics in Large Floodplains and Wetlands**

# Modeling Water Storage Dynamics in Large Floodplains and Wetlands

Dissertation

zur Erlangung des Doktorgrades

der Naturwissenschaften

vorgelegt im Fachbereich Geowissenschaften/ Geographie

der Johann Wolfgang Goethe-Universität

in Frankfurt am Main

von

Linda Adam

aus Leipzig

Frankfurt am Main 2017

(D 30)

# Modeling Water Storage Dynamics in Large Floodplains and Wetlands



Model grid

Drainage direction and river basins with discharge stations

Lakes and wetlands

Surface elevation

Landcover
Hydrogeology
Soil texture
Soil water capacity
Climate data
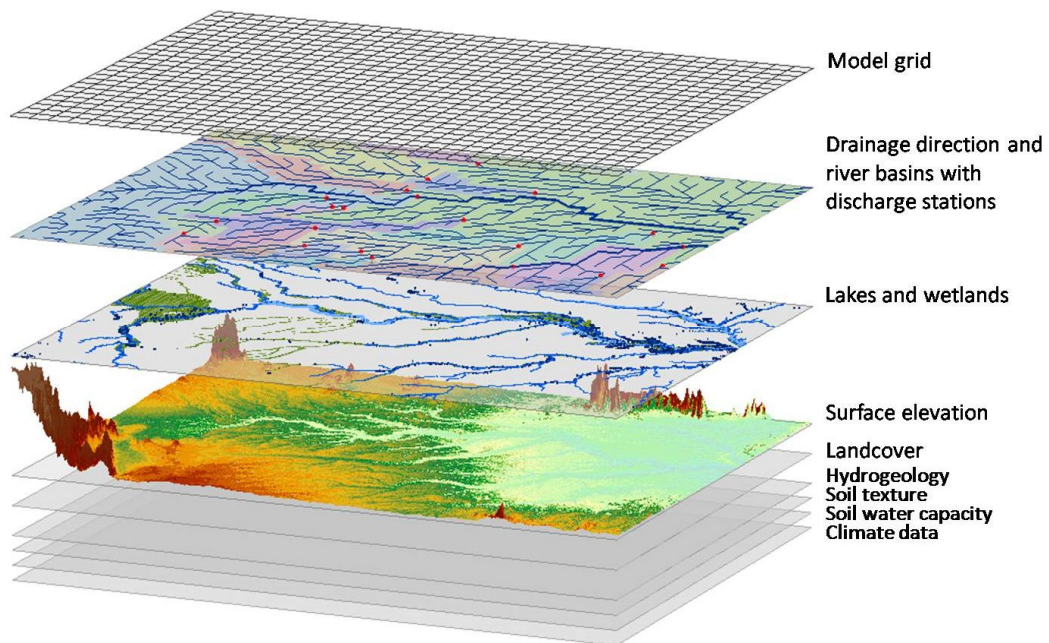
## Linda Adam

Frankfurt a. M. 2017

A dissertation submitted for the degree of doctor philosophiae, Dr. phil. nat.,

Department of Geosciences/ Geography of the University Frankfurt am Main

## Erklärung

Hiermit versichere ich, dass ich die vorliegende Dissertation selbständig und ohne uner-
laubte Hilfe angefertigt und andere als die in der Dissertation angegebenen Hilfsmittel
nicht benutzt habe. Alle Stellen, die wörtlich oder sinngemäß aus veröffentlichten oder
unveröffentlichten Schriften entnommen sind, habe ich als solche kenntlich gemacht.
Kein Teil dieser Arbeit ist in einem anderen Promotions- oder Habilitationsverfahren
verwendet worden.

Im Rahmen dieser Dissertation sind folgende Publikationen entstanden:

Adam, L., Döll, P., Prigent, C. and Papa, F.: Global-scale analysis of satellite-derived
time series of naturally inundated areas as a basis for floodplain modeling, Advances in
Geosciences, 2010.

# Danksagung

# Table of contents

# List of Abbreviations

| | |
|---|---|
| ACE | Altimeter Corrected Elevations |
| ADCP | Acoustic Doppler Current Profiler |
| ArcGIS | Geographical Information System (ESRI product) |
| ASTER | Advanced Spaceborne Thermal Emission and Reflection Radiometer |
| CDF | Cumulative Distribution Function |
| CRU | Climate Research Unit |
| DEM | Digital Elevation Model |
| DLR | Deutsches Zentrum für Luft- und Raumfahrt e.V. |
| ESRI | Environmental Systems Research Institute (software producer of Geo Information Systems (GIS)) |
| ETM | Enhanced Thematic Mapper |
| GDBD | Global Drainage Basin Database |
| GHM | Global Hydrological Model |
| GLWD | Global Lakes and Wetland Database |
| GRACE | Gravity Recovery And Climate Experiment |
| GRanD | Global database of reservoirs and Dams |
| GRDC | Global Runoff Data Centre |
| GPCC | Global Precipitation Climatology Center |
| HydroSHEDS | Hydrological data and maps based on SHuttle Elevation Derivatives at multiple Scales |
| JERS-1 | Japanese Earth Resources Satellite-1 |
| NASA | National Aeronautics and Space Administration |
| R | Free software environment for statistical computing and graphics |
| SAR | Synthetic Aperture Radar |
| SRTM | Shuttle Radar Topography Mission |
| SWE | Surface Water Extent |
| TWS | Total Water Storage |
| WaterGAP | Water Global Assessment and Prognosis |
| WGHM | WaterGAP Global Hydrology Model |

# List of Figures

# List of Tables

## Zusammenfassung

# Modellierung der Wasserspeicherdynamik in großen Überschwemmungs- und Feuchtgebieten

**Motivation**

Obwohl Überschwemmungs- und Feuchtgebiete schätzungsweise nur etwa 4% bis 6% der eisfreien Landoberfläche der Erde ausmachen (Mitsch und Gosselink 2000, Prigent et al. 2007), spielen sie eine wichtige Rolle in biochemischen und hydrologischen Kreisläufen.

Aufgrund des Mangels an konsistenten Daten und Techniken bleibt die Identifizierung und Charakterisierung von Feuchtgebieten weltweit weiterhin eine schwierige Herausforderung. Durch unterschiedlichste Fortschritte die räumlichen und zeitlichen Veränderungen von Oberflächengewässern mittels Fernerkundung zu bestimmen – wie Veränderungen der terrestrischen Wasserspeicherung (Tapley et al. 2004; Chen et al. 2010), die Höhe des Wasserspiegels und der Wassertiefe (Alsdorf et al. 2000, 2007; Durand et al. 2008, 2010), und die Ausdehnung von Oberflächengewässern (Prigent et al. 2007; Papa et al. 2010) – ändert sich diese Situation zunehmend. Variationen in Oberflächengewässern, wie sie von Satelliten beobachtet werden, sind in großräumigen hydrologischen Modellen nicht ausreichend repräsentiert. Diese Modelle stellen jedoch die einzige Möglichkeit dar, Süßwasserströme in großen Flusseinzugsgebieten für lange historische Zeitreihen zu berechnen und Vorhersagen zu simulieren.

Globale hydrologische Modelle (GHMs) sind in der Erdsystemwissenschaft aus vielen Gründen wichtig. Einige von ihnen repräsentieren die Wechselwirkung zwischen Land und Atmosphäre, wie die Auswirkungen von Bodenfeuchte und Evapotranspiration auf das Klima, und den Einfluss von kontinentalem Süßwasser auf den Ozean. GHMs sind auch äußerst wertvoll für die menschliche Gesellschaft. Flüsse, Seen und Feuchtgebiete bieten Wasser für die Industrie, die Landwirtschaft, die Stromerzeugung und den Hausgebrauch. Die zukünftige Bevölkerungszunahme in Bezug auf die veränderte Wasserverfügbarkeit durch Flächennutzung und Klimawandel kann die terrestrischen Wasserressourcen stark belasten. GHMs (oder auch Landoberflächenmodelle) kombinieren in der Regel Klimadaten mit physiographischen Daten (einschließlich Boden und Vegetation), um Zeitreihen von Süßwasserströmen (insbesondere Oberflächenabfluss und Durchfluss) und der Süßwasserspeicherung zu berechnen.

Eine verbesserte Quantifizierung, nicht nur der kontinentalen Süßwasserströme sondern auch der Süßwasserspeicherung in den verschiedenen Speicherkompartimenten, ermöglicht ein besseres Verständnis des globalen Wasserkreislaufs und des gesamten Erdsystems. Sie ermöglicht eine bessere Beurteilung der Süßwasserressourcen und deren

Auswirkungen auf den globalen Wandel. Kontinentale Wasserspeichervariationen sind abhängig von den Merkmalen der einzelnen Speicherkompartimente (z.B. Bodenbeschaffenheit und Wurzeltiefe bei der Bodenwasserspeicherung oder die Präsenz von Oberflächengewässern bei der Oberflächenwasserspeicherung) und werden durch Klimafaktoren, insbesondere durch Niederschlag, stark beeinflusst (Döll et al. 2012).

In den letzten Jahren haben Bemühungen in der hydrologischen Modellierung zu Verbesserungen bei der Simulation von Feuchtgebieten und der Integration von Überflutungsgebieten in globale hydrologische Modelle geführt. Überschwemmungsgebiete spielen eine wichtige Rolle im terrestrischen Wasserkreislauf und haben eine tiefgreifende Bedeutung für die Artenvielfalt (Evans et al. 2010; Schneider et al. 2011b), Methanemissionen (Ringeval et al. 2014; Petrescu et al. 2010), Kohlenstofflagerung (Richey et al. 2002; Decharme et al. 2008), Grundwasserneubildung (Wolski et al. 2006) und den Zeitpunkt von Hochwasserwellen (Richey et al. 1989; Vörösmarty and Moore 1991; Coe et al. 2008).

Die vorhandenen hydrologischen Modelle variieren stark in ihrer Modellkomplexität und bieten Potenzial für weitere Entwicklungen (Kapitel 2).

## Hintergrund und Zielsetzung

Diese Doktorarbeit ist im Rahmen des Forschungsprojektes REGHYDRO (kombinierte Hydrologische Modellierung und Regionale geodätische Schätzung von Wasserspeichervariationen in großen Flusseinzugsgebieten mittels GRACE-Daten) entstanden, welches Teil des Schwerpunktprogramms der Deutschen Forschungsgemeinschaft "Massentransporte und Massenverteilungen im System Erde" (DFG - SPP 1257) war. Das Projekt war ein Kooperationsprojekt von Geodäten, Hydrologen und Mathematikern, mit dem Ziel die gegenseitigen Vorteile der Gravitationsfeldanalyse und der hydrologischen Modellierung zu nutzen.

Die Ozeanzirkulation, die konvektive Strömung im Erdmantel, die Veränderung des Meeresspiegels, das Schmelzen von kontinentalen Eisschilden, der Durchfluss und die Veränderung des Grundwasserspiegels und der Bodenfeuchtigkeit erzeugen den Transport und die Umverteilung von Massen über die Grenzen zwischen Atmosphäre, Eis, Land und Ozean. Veränderungen in der Massenverteilung im Erdsystem verursachen Schwankungen im Erdschwerefeld. Solche Änderungen beeinflussen wiederum die Umlaufbahnen von Satelliten und können durch Satellitenschwerkraftmissionen wie GRACE (Gravity Recovery and Climate Experiment) unter Verwendung innovativer und hochpräziser Sensorsysteme (http://www.csr.utexas.edu/grace) gemessen werden.

Ein Ziel des REGHYDRO-Projekts war die Verbesserung der globalen hydrologischen Modellierung von Wasserspeichervariationen (und Wasserströmen) in den verschiedenen Speicherkompartimenten (Schnee und Eis, Vegetation, Boden, Grundwasser, Ober-

flächenwasser einschließlich Überschwemmungsgebieten) unter Verwendung von Informationen über die Schwankung des Gravitationsfeldes von GRACE. Im Rahmen des Projektes wurde das globale hydrologische Modell WaterGAP durch die Berücksichtigung von Grundwasserentnahmen (Döll et al. 2012) sowie die Integration von großen Überflutungsgebieten erweitert und verbessert.

Das übergeordnete Ziel dieser Doktorarbeit ist es, einen Algorithmus zur Modellierung von großen zeitlich und räumlich dynamischen Überflutungsgebieten innerhalb des globalen hydrologischen Modells WaterGAP zu entwickeln, welcher die Simulation von Wasserströmen und Wasserspeichervariationen in verschiedenen Speicherkompartimenten verbessert.

Um das Gesamtziel zu erreichen, werden mehrere untergeordnete Ziele definiert. Diese beinhalten zum einen die Aufbereitung von Modelleingangsdaten und Validierungsdaten und zum anderen generelle Anforderungen an den Überflutungsalgorithmus. Zu Letzterem zählt vor allem die globale Anwendbarkeit, d.h. die Simulation dynamischer Überflutungsflächen sollte in allen großen Flusseinzugsgebieten – mit unterschiedlichsten klimatischen Verhältnissen, hydrologischen Regimen, Vegetationsbedeckung und natürlichen saisonalen Schwankungen – akzeptable Ergebnisse liefern. Das neue Modell, WaterGAP mit Überflutungsalgorithmus (WaterGAP 2.2b_fpl), sollte auf dem neuesten Stand der Forschung sein. Dies bedarf einer ausführlichen Analyse der Modelleigenschaften bereits bestehender großskaliger hydrologischer und gekoppelter Landoberflächen-Routing Modelle, welche die Modellierung großflächiger Überflutungsgebiete beinhalten. WaterGAP 2.2b_fpl sollte in der Lage sein, das Wasser nicht nur flussabwärtsgerichtet zu leiten, sondern auch Rückstaueffekte zu modellieren.

Unter Berücksichtigung des oben dargestellten Gesamtbildes sowie der Anforderungen aus dem Projekt REGHYDRO werden folgende Forschungsfragen definiert, die innerhalb der einzelnen Kapitel dieser Dissertation bearbeitet und beantwortet werden:

1) Führt die Implementierung dynamischer Überflutungsgebiete in WaterGAP zu einer Verbesserung der Modellgüte hinsichtlich des Durchflusses, der Ausdehnung von Oberflächengewässern und/oder der Variationen im Gesamtwasserspeicher? Wenn ja, in welchen spezifischen geografischen Gebieten sind die Verbesserungen am deutlichsten?

2) Wie wirkt sich die rückwärtsgerichtete Strömung (Rückstaueffekte) auf den modellierten Durchfluss, die Ausdehnung von Oberflächengewässern und die Wasserspeichervariationen aus? Wie verändert sich die räumliche Verteilung der großen Überschwemmungsgebiete und der Variationen im Gesamtwasserspeicher im Einzugsgebiet des Amazonas bei der Modellierung von Rückstaueffekten?

3) Was ist der Beitrag der Wasserspeicherung in Überschwemmungs- und Feuchtgebieten zu Variationen im Gesamtwasserspeicher und Variationen im Durchfluss?

4) Was sind die einzugsgebietsspezifischen Ursachen der beobachteten Unterschiede zwischen den Variationen im Gesamtwasserspeicher abgeleitet von GRACE und Variationen simuliert mit dem WaterGAP Global Hydrological Model (WGHM)?

**Methoden**

Um einen Algortihmus zur Modellierung dynamischer Überflutungen zu entwickeln, ist es zunächst wichtig, die modellinternen Prozesse von WaterGAP näher zu untersuchen, um herauszufinden, von welchen Größen die Wasserspeichervariation in den Überschwemmungs- und Feuchtgebieten abhängig ist und in wie weit diese, sowie die Ausdehnung von Oberflächengewässern plausibel wiedergegeben werden (Kapitel 3). Dazu werden in Kapitel 3 die Korrelation zwischen Durchfluss und der Ausdehnung von Oberflächengewässern, sowie der Einfluss auf die maximale Wassertiefe in den Überschwemmungs- und Feuchtgebieten auf die Speichervariationen in verschiedenen Kompartimenten und im Gesamtwasserspeicher untersucht. Außerdem wurde, wie in Kapitel 3 vorgestellt, als Grundlage für die Validierung der modellierten Überschwemmungsdynamik ein Datensatz von Zeitreihen natürlich überschwemmter Gebiete (NIA, naturally inundated areas) generiert. Der Datensatz NIA basiert auf einer Zeitreihe (1993-2004) monatlicher, von Beobachtungen mehrerer Satelliten abgeleiteter, Überschwemmungsgebiete (Prigent et al. 2007, Papa et al. 2010), von denen künstlich hervorgerufenen Überschwemmungsflächen – hauptsächlich bewässerte Reisanbauflächen (MIRCA2000, Portmann et al. 2010) – subtrahiert wurden.

Die Methoden des Ansatzes zur Modellierung zeitlich und räumlich dynamischer Überflutungsgebiete umfassen im Wesentlichen fünf Punkte:

1) die Initialisierung der Überflutung,
2) die Interaktion zwischen Fluss und Überflutungsgebiet,
3) die Schätzung der Ausdehnung der überfluteten Fläche und der Wassertiefe im Überflutungsgebiet,
4) der Wassertransport zwischen den Gitterzellen und
5) die Fließgeschwindigkeiten im Fluss und Überflutungsgebiet.

Die Methodik zu den einzelnen Punkten wird in den folgenden Absätzen kurz zusammengefasst.

Die Initialisierung der Überflutung wird durch den bordvollen Durchfluss bestimmt. In WaterGAP ist der bordvolle Durchfluss eine zeitlich konstante Eingangsgröße für jede 0,5° Gitterzelle, berechnet mit einem statistischen Ansatz zur Hochwasseranalyse (Par

tial Duration Series; Verzano 2009, Schneider et al. 2011a). Eine im Rahmen dieser Doktorarbeit durchgeführte Analyse hat ergeben, dass die Frequenz, an denen der bordvolle Durchfluss – der Grenzwert zur Überflutungsinitiierung – überschritten wird, in vielen Gebieten zu gering ist (Amazonas, Ob; Kapitel 4.3.1), weshalb ein Parameter zur Reduzierung dieser Eingangsgröße eingeführt wurde.

Wird der bordvolle Durchfluss überschritten, fließt überschüssiges Wasser in das angrenzende Überflutungsgebiet. Sinkt der Durchfluss im Fluss wieder, fließt Wasser aus dem Überflutungsgebiet zurück in den Fluss. Die Menge Wasser, die vom Fluss in das Überflutungsgebiet oder umgekehrt fließt, wird mit Hilfe einer Exponentialfunktion in Abhängigkeit vom aktuellen Durchfluss und dessen Differenz zum bordvollen Durchfluss berechnet (Kapitel 4.3.2).

Eine kumulative Verteilungsfunktion relativer Geländehöhen – eine hypsographische Kurve – wird verwendet, um das Höhenprofil des Überflutungsgebietes zu beschreiben, wobei angenommen wird, dass sich eine Überflutung ausgehend von den niedrigsten Gebieten in einer Gitterzelle entwickelt. So lassen sich mit dem Wasservolumen im Überflutungsgebiet die Wassertiefe und die entsprechende dynamische Ausdehnung bestimmen. Die hypsographische Kurve für jede Gitterzelle basiert auf hochaufgelösten (3 Bogensekunden) digitalen Geländemodellen, deren Daten als Eingangsgrößen für WaterGAP aufbereitet wurden. So beinhaltet jede Halbgradgitterzelle in WaterGAP 100 Untergitter mit entsprechenden Geländehöhen. Um eine globale Abdeckung zu ermöglichen, wurden zwei digitale Geländemodelle (DEM – digital elevation model) kombiniert: HydroSHEDS (Hydrological data and maps based on Shuttle Elevation Derivatives at multiple Scales, Lehner et al. 2008b) und ACE (Altimeter Corrected Elevations, Smith 2009). Diese DEMs können Fehler aufweisen (Löcher, Artefakte) und spiegeln – beeinflusst durch Bebauung oder Bewuchs – nicht immer die Höhe des Erdbodens wieder. Die auf SRTM (Shuttle Radar Topography Mission) Daten basierenden HydroSHEDs Daten wurden in dem zu weiten Teilen dicht bewaldeten Einzugsgebiet des Amazonas um eine angenommene durchschnittliche Vegetationshöhe von 17 m korrigiert (Kapitel 4.4.1).

Der Wassertransport zwischen den einzelnen Gitterzellen ist in WaterGAP durch eine globale Durchflussrichtungskarte (global Drainage Direction Map DDM30, Döll und Lehner 2002) vorgegeben. In WaterGAP 2.2b_fpl kann das Wasser nicht nur im Fluss, sondern auch im Überflutungsgebiet weitergeleitet werden. Durch die Implementierung der DEM-Daten in WaterGAP 2.2b_fpl, ist es erstmals möglich, Wassergradienten zwischen Gitterzellen zu berechnen. Der Nutzer hat die Wahl zwischen einem ausschließlich stromabwärts gerichteten Wassertransport (kinematik) und einem Wassertransport, welcher, im Falle eines negativen Wassergradienten, anteilig Wasser stromaufwärts gerichtet transportiert und somit Wasserrückstaueffekte simuliert (backwater) (Kapitel 4.5).

Im Überflutungsgebiet wird eine höhere Rauigkeit angenommen, so dass die Fließgeschwindigkeit hier langsamer ist als im Fluss (Kapitel 4.6).

Schließlich werden die Modellergebnisse eingehend analysiert, mit geeigneten Beobachtungsdaten validiert und Unsicherheiten identifiziert.

**Ergebnisse und Diskussion**

Im Folgenden wird die Beantwortung der Forschungsfragen zusammengefasst.

*Führt die Implementierung dynamischer Überflutungsgebiete in WaterGAP zu einer Verbesserung der Modellgüte hinsichtlich des Durchflusses, der Ausdehnung von Oberflächengewässern und/oder der Variationen im Gesamtwasserspeicher? Wenn ja, in welchen spezifischen geografischen Gebieten sind die Verbesserungen am deutlichsten?*

Auf globaler Ebene hat sich die Modellgüte von WaterGAP aufgrund der Implementierung des Algorithmus zur Modellierung dynamischer Überflutungen deutlich verbessert. Die Verbesserungen umfassen alle analysierten Modellausgabegrößen: Durchfluss (auch die Fließgeschwindigkeit im Fluss), Wasserspeichervariationen und Oberflächengewässerausdehnung. Die Modellverbesserung ist im Amazonasbecken am größten, welches mehr als jedes andere Einzugsgebiet durch seine ausgedehnten Überschwemmungs- und Feuchtgebiete gekennzeichnet ist. Diese nehmen etwa 20% der Einzugsgebietsfläche ein (Melack und Forsberg 2001) und beeinflussen maßgeblich die Speicherung und Weiterleitung von Hochwasserwellen (Richey et al. 1989).

Im Vergleich zur früheren WaterGAP-Modellversion 2.2b (WG22b) stimmt der modellierte Durchfluss in der WaterGAP-Modellversion, die den Überflutungsalgorithmus enthält (WG22b_fpl) besser mit beobachteten Durchflüssen überein, insbesondere hinsichtlich der saisonalen Variation und des zeitlichen Verlaufs von geringen und hohen Durchflüssen. Durch das Vorhandensein von Überflutungsgebieten, werden Durchflussspitzen und Hochwasserwellen im Fluss abgeschwächt und tägliche Schwankungen im Durchfluss minimiert (Kapitel 5.4.2).

Die Implementierung des Überflutungsalgorithmus in WaterGAP führte zu einer besseren Simulation der Variation im Gesamtwasserspeicher (TWS (total water storage)-Variation) für die Mehrheit der acht im Detail untersuchten Flusseinzugsgebiete (Amazonas, Paraná, Mississippi, Ob, Lena, Ganges, Nil, Niger). TWS-Variationen steigen in den meisten Regionen der Erde aufgrund höherer Wasserspeichervariation in Überschwemmungs- und Feuchtgebieten. Die größeren TWS-Variationen passen besser zu den von GRACE abgeleiteten TWS-Variationen. Im Vergleich zu GRACE ist die Mo-

dellverbesserung am deutlichsten in den Einzugsgebieten des Amazonas und Mississippi. Im Amazonasbecken ist die Modellgüte, auch was den Zeitpunkt und die Lage der maximalen saisonalen TWS-Variation betrifft, gestiegen. Im Vergleich zu GRACE werden die saisonalen und zwischenjährlichen Amplituden des Gesamtwasserspeichers jedoch noch global unterschätzt, und die Modellgüte für arktische Einzugsgebiete (Ob und Lena) bleibt auch bei der Anwendung des Überflutungsalgorithmus in WaterGAP relativ gering oder verringert sich sogar (Ob). Eine Ursache dafür könnten Unsicherheiten in der Modellierung von Schnee und Schneeschmelze in WaterGAP sein.

Die Modellverbesserung von WG22b_fpl zum ehemaligen WG22b ist besonders deutlich hinsichtlich der Simulation der Ausdehnung von Oberflächengewässern (SWE (surface water extent)), welche sich in jeglicher Hinsicht – Lage des Überflutungsgebietes, Zeitpunkt der maximalen Ausdehnung, saisonale Schwankungen und durchschnittliche Ausdehnung – und in allen acht analysierten großen Flusseinzugsgebieten verbessert hat. Im Amazonasbecken stieg die Korrelation von modellierten und beobachteten (von Satellitenbeobachtungen abgeleiteten natürlichen Überschwemmungsgebiete NIA) monatlichen SWE im Zeitraum 1993 bis 2004 von $R^2 = 0,59$ für WG22b auf $R^2 = 0,83$ für WG22b_fpl. Obwohl die saisonale Variation von SWE durch die Implementierung des Überflutungsalgorithmus in WaterGAP gestiegen ist, ist sie im Vergleich zu den satellitengestützten Beobachtungen im Amazonasbecken immer noch zu gering.

*Wie wirkt sich die rückwärtsgerichtete Strömung (Rückstaueffekte) auf den modellierten Durchfluss, die Ausdehnung von Oberflächengewässern und die Wasserspeichervariationen aus? Wie verändert sich die räumliche Verteilung der großen Überschwemmungsgebiete und der Variationen im Gesamtwasserspeicher im Einzugsgebiet des Amazonas bei der Modellierung von Rückstaueffekten?*

Die Modellierung von Wasserrückstaueffekten innerhalb von WaterGAP 2.2b_fpl (WG22b_fpl b; b für Rückstau, engl. backwater) führt zu einer signifikanten Verbesserung der Modellergebnisse für das Einzugsgebiet des Amazonas. Für andere Einzugsgebiete variiert die Auswirkung der Simulation von Wasserrückstaueffekten: verbesserte Modellgüte für einige Modellausgabegrößen, Verschlechterung für andere und in vielen Fällen ohne signifikante Veränderung der Modellgüte.

Wasserrückstaueffekte im Amazonasbecken verursachen eine Abschwächung und Verzögerung der Flutwelle, wodurch, im Vergleich zu WaterGAP 2.2b_fpl mit ausschließlich flussabwärts gerichteter Strömung (WG22b_fpl k; k für kinematisch), die Korrelation mit den zu beobachteten Durchflussdaten steigt.

Durch die Modellierung von Wasserrückstaueffekten stimmt der Zeitpunkt der maximalen Oberflächengewässerausdehnung (SWE) besser mit den Satellitenbeobachtungen überein. Die Verbesserung ist, mehr oder weniger stark, in allen analysierten Flussein-

zugsgebieten zu verzeichnen. In vielen Regionen der Welt (vor allem im Einzugsgebiet des Amazonas und des Paranás) verbesserten sich außerdem die räumlichen Muster saisonaler Schwankungen in der Ausdehnung von Oberflächengewässern. Im Fall des Amazonasbeckens sank die saisonale Variation der SWE insbesondere im flussabwärts-gelegenen Teil des Einzugsgebietes, was, im Vergleich zu WG22b_fpl k, zu einer besseren Übereinstimmung mit der räumlichen Verteilung der beobachteten natürlichen Überschwemmungsgebiete (NIA) führt. Die Verbesserung der Modellgüte durch die Modellierung von Wasserrückstaueffekten in Bezug auf die monatlichen Zeitreihen der SWE auf Einzugsgebiets- und Untereinzugsgebietsebene, kann auf die geringeren saisonalen Schwankungen zurückgeführt werden. Besonders bei Niedrigwasserständen (in der Trockenzeit) bleibt die Ausdehnung der Überschwemmungs- und Feuchtgebiete größer.

Eine der wichtigsten Erwartungen an die Modellierung von Wasserrückstaueffekten bestand darin, die räumliche Verteilung saisonaler Variationen im Gesamtwasserspeicher (TWS) im Amazonasbecken zu verbessern. Während GRACE die maximale saisonale TWS-Variation im zentralen Teil des Amazonasbeckens beobachtet, simuliert WaterGAP die höchsten saisonalen TWS-Variationen in der Nähe der Flussmündung (Kapitel 5.4.4). Die Erwartungen wurden erfüllt; verglichen mit GRACE erreicht WG22b_fpl b von allen WaterGAP-Modellvarianten die besten Modellgütewerte. Die Verbesserungen waren jedoch kleiner als ursprünglich erwartet. Die Einbeziehung von Wasserrückstaueffekten in WG22b_fpl erhöht die saisonale Variation des Gesamtwasserspeichers an den Mündungen der Amazonas-Nebenflüsse Tapajos und Madeira, aber der Einfluss auf saisonale TWS-Schwankungen im zentralen Amazonas (an den Mündungen des Purus und des Rio Negro in den Amazonas-Hauptstrom) ist klein. Es gibt mehrere mögliche Gründe für die Diskrepanzen zwischen den Ergebnissen von GRACE und WaterGAP: Unsicherheiten in den GRACE-Lösungen, Fehler durch die Filterung der Datenprodukte und unzureichende Modellierung hydrologischer Prozesse in WaterGAP sind nur einige davon. Eine große Unsicherheit in WaterGAP ist die Simulation absoluter Höhen des Wasserspiegels und somit der Wasserspiegelgradienten – die Grundlage für die Modellierung von Wasserrückstaueffekten. Ein Vergleich zwischen modellierten Wasserspiegelhöhen und beobachteten Wasserspiegelhöhen von Topex/Poseidon (Abschnitt 5.4.1) an 80 Altimetrie-Stationen in 6 großen Flusseinzugsgebieten zeigt, dass WG22b_fpl b gute Ergebnisse simuliert in Bezug auf saisonale und zwischenjährliche Variationen der Wasserspiegel. Jedoch überschätzt WaterGAP die absoluten Werte der beobachteten Wasserspiegelhöhen für die meisten der 80 Stationen. Die Differenz der modellierten und beobachteten mittleren Wasserspiegelhöhen ist in tiefer gelegenen Regionen kleiner, als in höher gelegenen Regionen. Dies deutet darauf hin, dass die Minimalhöhe der Gitterzellen (Höhe des Ausflusses des Wassers in die stromabwärts gelegene Gitterzelle), die als Eingangsgröße auf Grundlage der digitalen Geländemodelle ins Modell eingeht, nicht mit den beobachteten Höhenmessungen übereinstimmt.

*Was ist der Beitrag der Wasserspeicherung in Überschwemmungs- und Feuchtgebieten zu Variationen im Gesamtwasserspeicher und Variationen im Durchfluss?*

Der einflussreichste Faktor für die Variation des Durchflusses in WaterGAP ist der Oberflächenabfluss, der hauptsächlich durch den Niederschlag bedingt ist. Weitere Faktoren sind Wasserentnahmen, Grundwasserrückflüsse und bei WaterGAP 2.2b mit Überflutungsalgorithmus (WG22b_fpl) auch Rückflüsse vom Überflutungsgebiet in den Fluss. Der Anteil, in den jeder Faktor zu Variationen im Durchfluss beiträgt, unterscheidet sich stark von Region zu Region. In WG22b_fpl ist der Beitrag der Wasserspeicherung von Überschwemmungs- und Feuchtgebieten zu Variationen im Durchfluss in Gebieten mit großen und dauerhaften Überflutungen hoch; die Variation im Durchfluss nimmt mit der Anwesenheit von Überflutungsgebieten aufgrund der Abschwächung von Spitzendurchflüssen ab (siehe Kapitel 5.4.2).

In WG22b_fpl – sowohl mit ausschließlich stromabwärts gerichteter Fließrichtung, als auch mit teilweise stromaufwärts gerichteter Fließrichtung (Wasserrückstau) – ist die Speichervariation in Überschwemmungs- und Feuchtgebieten eine der vier Hauptbeitragenden für saisonale Variationen im Gesamtwasserspeicher (TWS); im Amazonasbecken sogar der wichtigste. In der Mehrzahl der Einzugsgebiete werden saisonale TWS-Variationen durch Schwankungen im Bodenwasserspeicher dominiert. In borealen und arktischen Flusseinzugsgebieten spielt der Schneewasserspeicher eine große Rolle.

*Was sind die einzugsgebietsspezifischen Ursachen der beobachteten Unterschiede zwischen den Variationen im Gesamtwasserspeicher abgeleitet von GRACE und Variationen simuliert von dem WaterGAP Global Hydrological Model (WGHM)?*

Der Vergleich auf globaler Skala zwischen monatlichen und saisonalen Variationen im Gesamtwasserspeicher (TWS) von WaterGAP 2.2b_fpl und GRACE zeigt im Allgemeinen ähnliche räumliche und zeitliche Muster. Für die meisten Regionen auf der Erde ist die Korrelation hoch. Dennoch sind im globalen Durchschnitt die saisonalen und zwischenjährlichen Amplituden im Gesamtwasserspeicher für WaterGAP kleiner als für GRACE. Hinsichtlich der monatlichen Zeitreihen der TWS-Variationen auf Einzugsgebietsebene ist die Modellgüte in tropischen Einzugsgebieten (Amazon, Paraná, Ganges, Niger) am größten und in arktischen und gemäßigten Einzugsgebieten (Ob, Lena, Mississippi) relativ niedrig (siehe Kapitel 5.4.4).

Die Diskrepanzen zwischen TWS-Variationen simuliert von WaterGAP und denen abgeleitet von GRACE können mehrere Ursachen haben.

Die drei Hauptfehlerquellen von GRACE beim Auflösen hydrologischer Signale sind Messfehler, Leakage-Fehler und Fehler im Atmosphärendruck (Seo und Wilson 2005). Die Signale von GRACE leiden unter Leakage-Fehlern (Signalverlaufen) von einer Region zur anderen, wodurch bei der Analyse von spezifischen Regionen wie Flussein-

zugsgebieten die Signale von umliegenden Gebieten beeinflusst werden. Der Atmosphärendruck ist eng mit der Gesamtmasse der Atmosphäre verknüpft. GRACE-Signale unterliegen Restsignalen und Aliasing-Effekten von Variationen anderer Massen, die während der GRACE-Datenverarbeitung entfernt wurden (hauptsächlich die Masse der Atmosphäre und des Ozeans; z.B. Seo et al. 2008). Fehler die vom Schwerefeld herrühren sind Mess- und Verarbeitungsfehler. Diese werden durch Anwendung einer Nachbearbeitungsfiltertechnik reduziert (Swenson und Wahr 2006). Dabei ist eine Filtertechnik erstrebenswert, die sowohl GRACE-Schwerkraftfeldfehler als auch Signalverluste an der Grenze der interessierenden Region minimiert (Werth et al. 2009).

Für einen direkten Vergleich zwischen aus GRACE abgeleiteten TWS-Variationen und modellierten TWS-Variationen müssen die Modellausgabegrößen genauso gefiltert werden wie die GRACE-Daten (Güntner et al. 2009). Diese Filterung wirkt sich jedoch signifikant auf die saisonalen Amplituden der Wasserspeichervariationen in Einzugsgebieten aus und könnte eine Ursache für die Unterschätzung der saisonalen TWS-Variation von WaterGAP im Vergleich zu GRACE sein. Die Analyse von Chen et al. (2007) zeigt, dass die gaußsche Glättung (Filterung) auch zu nicht zu vernachlässigenden Phasenverschiebungen führt, möglicherweise aufgrund asymmetrischer spektraler Leckage-Fehler aus umliegenden Bereichen.

Unterschiede zwischen modellierten und beobachteten Variationen im Gesamtwasserspeicher können auch von Defiziten in der Modellierung hydrologischer Prozesse in WaterGAP herrühren. In tropischen und gemäßigten Einzugsgebieten könnten dies Defizite in der Modellierung der Grundwasserdynamik sein. WaterGAP beinhaltet zwar ein Grundwasserspeicherkompartiment und berechnet Basisabfluss und Grundwasserneubildung, dennoch gibt es Verbesserungsbedarf in der Modellierung von der Wechselwirkung zwischen Grundwasser und Oberflächengewässern. Eine weitere, in vielen globalen hydrologischen Modellen erwähnte, Unsicherheit könnte in der Modellierung der Evapotranspiration liegen (Ramilien et al. 2005; Alkama et al. 2010). In borealen und arktischen Einzugsgebieten wird oft die Modellierung von Schnee und Schneeschmelze als mögliche Unsicherheit genannt (van Beek and Bierkens 2009; Yamazaki et al. 2011; Decharme et al. 2012; Müller Schmied et al. 2016). In diesen Gebieten ist hauptsächlich die Variation im Schneespeicher für die Variation im Gesamtwasserspeicher verantwortlich.

**Schlussbetrachtung und Ausblick**

Das Ziel dieser Dissertation – die Weiterentwicklung des globalen hydrologischen Modells WaterGAP zur Verbesserung der Simulation von Wasserströmen und Wasserspeichervariationen in verschiedenen Speicherkompartimenten – wurde erfolgreich umgesetzt.

Im Rahmen dieser Arbeit entwickelte ich einen neuen Ansatz zur Simulation zeitlich und räumlich dynamischer Überflutungsgebiete auf globaler Ebene. Dieser Ansatz führte zu einem neuen Algorithmus in WaterGAP, der basierend auf hochauflösenden digitalen Geländemodellen, erstmals die Berechnung der Ausdehnung von Oberflächengewässern und Wasserspiegelhöhen sowie die Simulation von Wasserrückstaueffekten ermöglicht.

Die neue Modellversion WaterGAP 2.2b_fpl wurde zur Modellierung von Durchfluss, Fließgeschwindigkeit in Flüssen, Wasserspeicher, Wasserhöhen und Oberflächengewässer auf globaler Ebene angewendet. Die Modellergebnisse wurden eingehend gegen Bodenmessungen und Fernerkundungsdaten validiert und zeigen im Allgemeinen eine gute Übereinstimmung mit den Beobachtungsdaten. Im Vergleich zur bisherigen Version WaterGAP 2.2b hat sich die Modellgüte deutlich verbessert; insbesondere im Einzugsgebiet des Amazonas. Allerdings sind, im Vergleich zu den Beobachtungen, die saisonalen Schwankungen der Ausdehnung von Oberflächengewässern und die Variationen im Gesamtwasserspeicher in vielen Regionen auf der Erde noch zu niedrig. Eine detaillierte Analyse der Modellergebnisse suggeriert, dass im Amazonasbecken die Einführung von Wasserrückstaueffekten wichtig war, um Wasserspeichervariationen und Oberflächengewässerausdehnung realistischer zu modellieren.

Zukünftige Bemühungen sollten sich auf die Simulation von Wasserspiegelhöhen konzentrieren, um eine bessere Modellierung der Fließrichtung des Wassers entsprechend des Wasserspiegelgradienten zu erzielen. Dies impliziert Verbesserungen in der Fehlerkorrektur der ins Modell eingehenden Daten auf der Grundlage digitaler Geländemodelle (DEMs) und in der Simulation der Geometrie des Flussbettes (Höhe und Breite des Flusses).

Um die Modellgüte in bestimmten Regionen weiter zu verbessern, empfehle ich die Anpassung der global konstanten Modellparameter auf Einzugsgebiets- oder Teileinzugsgebietsebene. Dies sind Modellparameter, die die Überflutungsinitiierung, die Wechselwirkung zwischen Fluss und Überflutungsgebiet, die Vegetationskorrektur der DEM-Daten und die Wasserrückstaumenge beeinflussen.

Zukünftig könnte außerdem eine Verbesserung der Interaktion zwischen Grund- und Oberflächenwasser angestrebt werden. Da WaterGAP 2.2b_fpl nun in der Lage ist, Wasserspiegelgradienten zu berechnen, könnte die Grundwasserneubildung als Funktion der Wasserspiegelhöhen und der Tiefe des Grundwasserstands modelliert werden. Dies würde ein gradientenbasiertes Grundwassermodell erfordern. Mit der Information über den Grundwasserspiegel könnte wiederum der diffuse Austausch zwischen Grundwasser und Landoberfläche simuliert werden, was eine direkte Versorgung von Überschwemmungs- und Feuchtgebieten über das Grundwasser sowie eine Nachverdampfung des Grundwassers ermöglichen würde.

# Abstract

Floodplains and other wetlands depend on seasonal river flooding and play an important role in the terrestrial water cycle. They influence evapotranspiration, water storage and river discharge dynamics, and they are the habitat of a large number of animals and plants. Thus, to assess the Earth's system and its changes, a robust understanding of the dynamics of floodplain wetlands including inundated areas, water storages, and water flows is required.

This PhD thesis aims at improving the modeling of large floodplains and wetlands within the global-scale hydrological model WaterGAP, in order to better estimate water flows and water storage variations in different storage compartments. Within the scope of this thesis, I have developed a new approach to simulate dynamic floodplain inundation on a global-scale. This approach introduces an algorithm into WaterGAP, which has a spatial resolution of 0.5 degree (longitude and latitude) globally. The new approach uses subgrid-scale topography, based on high-resolution digital elevation models, to describe the floodplain elevation profile within each grid cell by applying a hypsographic curve. The approach comprises the modeling of a two-way river-floodplain interaction, the separate downstream water transport within the river and the floodplain – both with temporally and spatially different variable flow velocities – and the floodplain-groundwater interactions. The WaterGAP version that includes the floodplain algorithm, WaterGAP 2.2b_fpl, estimates floodplain and river water storage, inundated area and water table elevation, and also simulates backwater effects.

WaterGAP 2.2b_fpl was applied to model river discharge, river flow velocity, water storages, water heights and surface water extent on a global-scale. Model results were comprehensively validated against ground observations and remote sensing data. Overall, the modeled and observed data are in agreement. In comparison to the former version WaterGAP 2.2b, the model performance has improved significantly. The improvements are most remarkable in the Amazon River basin. However, the seasonal variation of surface water extent and total water storage anomalies are still too low in many regions on the globe when compared to observations. A detailed analysis of the simulated results suggests that in the Amazon River basin the introduction of backwater effects is important for realistically simulating water storages and surface water extent. Future efforts should focus on the simulation of water levels in order to better model the flow routing according to water slope. To further improve the model performance in specific regions, I recommend that the globally constant model parameters that affect inundation initiation, river-floodplain interaction, DEM correction for vegetation, and backwater amount at basin or subbasin-scale be adjusted.

CHAPTER 1

# Introduction

## 1.1   Motivation and Background

This PhD work is part of the research Project REGHYDRO in the framework of the Priority Program of the German Research Foundation "Mass transport and mass distribution in system Earth" (DFG - SPP 1257), which involves cooperation between geodesists, hydrologists, and mathematicians to exploit the mutual benefits of gravity field analysis and hydrological modeling.

Ocean circulation, convective flow in the Earth's mantle, sea level changes, the melting of continental ice sheets, river discharge, and changes in groundwater levels and soil moisture generate transport and the redistribution of masses across the borders between atmosphere, ice, land and oceans. Changes in the distribution of masses in the Earth's system cause variations in the earth's gravity field. Such changes, in turn, affect the orbits of satellites and can be measured by satellite gravity missions like GRACE (Gravity Recovery and Climate Experiment), using innovative and highly precise sensor systems (http://www.csr.utexas.edu/grace/).

One goal of the REGHYDRO project (Combined Hydrological Modelling and Regional Geodetic Estimation of Water Storage Variations in Large River Basins Using GRACE Data) was the improvement of global-scale hydrological modelling of water storage variations (and flows) in the different storage compartments (snow and ice, canopy, soil, groundwater, surface water including floodplains) using information on the variation of the gravity field from GRACE.

"Improved quantification of not only continental freshwater flows but also freshwater storage in [the] different compartments [...] enables a better understanding of the global water cycle and the overall Earth system. It allows a better assessment of freshwater resources and how they are impacted by global change. [...] Continental water storage variations depend on characteristics of the storage compartments (e.g. soil texture and rooting depth in the case of soil water storage or the existence of surface water bodies in the case of surface water storage) and are strongly driven by climate, in particular precipitation. In global-scale assessments, natural freshwater flows and storages are modelled by global hydrological models or land surface models. These models generally combine climate data with physiographic data (including soil and vegetation) to compute time series of freshwater flows (in particular runoff and river discharge). Some of the [existing] models do not include all relevant storage compartments such as surface water bodies and groundwater" (Döll et al. 2012, p. 2).

Within the framework of the REGHYDRO project, the WaterGAP Global Hydrology Model (WGHM) was expanded to introduce the withdrawal of groundwater (Döll et al. 2012) and large floodplains and wetlands into the model. As will be described later in more detail, this PhD work is located in this context.

Although wetlands and floodplains are estimated to cover only about 4% to 6% of the Earth's ice-free land surface (Mitsch and Gosselink 2000; Prigent et al. 2007), they play a major role in biochemical and hydrological cycles. "Approximately 60% of the world wetlands are inundated only during some portion of the year, leading to large seasonal and interannual variability of their extents [and storage]" (Papa et al. 2007, p. 1).

Due to the lack of consistent data and techniques, identifying and characterizing wetlands globally continues to be a difficult challenge. Fortunately this situation is rapidly changing, with various progress in the estimation of spatial and temporal variations in surface water from space, such as changes in terrestrial water storage (Tapley et al. 2004; Chen et al. 2010), water surface elevation and water depth (Alsdorf et al. 2000, 2007; Durand et al. 2008, 2010), and water surface extent (Prigent et al. 2007; Papa et al. 2010). For instance, Papa et al. (2010) used a multisatellite technique to develop a monthly dataset of surface water extent for more than one decade (1993-2004) with a spatial resolution of 773 km² (see Chapter 3). Variations in surface water, as observed by satellites, are not adequately represented in large-scale hydrological models, which are the only feasible instrument for simulating freshwater flows in large river basins applicable for large historical time series and predictions (Yamazaki et al. 2011). Recent efforts in hydrological modelling have led to improvements in wetland simulation, and to the inclusion of floodplains in global hydrological models. However, model complexity varies strongly, holding potential for further developments (Chapter 2).

For reasons of clarity and the readability of this thesis, an overview of the current state of the research field (regarding the existing global and continental-scale hydrological models containing macro-scale floodplain modelling, as well as a short review of available input data) was omitted from the introduction, but is presented in Chapter 2.

## 1.2 Research Objectives

As mentioned above, this PhD work is part of the research project REGHYDRO, which has the purpose of improving the global-scale hydrological model WaterGAP by introducing the withdrawal of groundwater, and large floodplains and wetlands into the model.

The overall objective of this PhD work is to develop an algorithm to improve the modelling of large floodplains and wetlands within the global-scale hydrological model WaterGAP, for the better estimation of water flows and water storage variations in different storage compartments. In order to meet the overall objective, several subordinate objectives are defined:

1) Monthly time series of flood inundation extent and water heights are to be determined on a global-scale. Additional model input data, such as subgrid elevation data from suitable digital elevation models, is therefore required, and needs to be generated.

2) Improved estimations of water storage variations in large wetlands and floodplains have to be obtained.

3) Independent validation data has to be processed, or even generated, to validate model output.

4) The model algorithm should be applicable on a global-scale. To be more precise, the simulation of dynamic floodplain inundation should provide acceptable results for large river basins in all climatic environments, encompassing a wide variety hydrological regime, vegetation cover and natural seasonality.

5) The model algorithm should account for backwater effects in flow routing.

6) The new model version of the global hydrological model WaterGAP, which finally includes the algorithm for dynamic floodplain inundation, should be on the current stage of research. This requires a detailed analysis of the model properties of already existing macro-scale hydrological models, and coupled land surface and river routing models, which include the modeling of large floodplains.

7) Inaccuracies in model outputs have to be identified and properly evaluated in the analysis and interpretation of the results.

Taking into consideration the overall picture briefly depicted above, as well as the requirements within the framework of the REGHYDRO project, the following main research questions are specified:

1) Does the implementation of dynamic floodplain inundation in WaterGAP lead to improvements in model performance regarding river discharge, surface water extent, and/or total water storage variations? If so, which specific geographic areas are improved most?

2) What is the effect of backwater flows on modeled river discharge, surface water extent and water storage variations? How does the spatial distribution of large floodplains/wetlands and total water storage variations in the Amazon River basin change when modeling backwater effects?

3) What is the contribution of water storage in floodplains and wetlands to total water storage variation and variations in river discharge?

4) What are the river basin-specific causes of the observed discrepancies between variations in total water storage, such as variations derived by GRACE, and by the WaterGAP Global Hydrological Model (WGHM)?

3

## 1.3   Theses outline

In addition to the general introduction (Chapter 1), this thesis consists of six chapters.

As a background to approach the objectives mentioned above, the state of the art of knowledge in modelling large floodplains and wetlands is summarized in Chapter 2. The literature review describes the strengths and weaknesses of the existing hydrological models and the available input data, and identifies opportunities for new developments. The global hydrological model WaterGAP, for which the implementation of floodplain inundation modelling is the main goal of this thesis, is also described in Chapter 2.

Another requisite for this study, presented in Chapter 3, is the analysis of satellite-derived time series of naturally inundated areas, as well as the analysis of current model outputs of surface water storage variations from WaterGAP. Because the contents of Chapter 3 are mainly based on an already published paper, it forms a largely independent study with corresponding introductory, main and closing sections.

With reference to the objectives of this study (Section 1.2) and the scientific background (Chapter 2), the methods of this study are defined in Chapter 4. The methods not only involve modelling concepts of the dynamic floodplain inundation approach within WaterGAP and suitable ways of model parameterization, but also comprise methods of validation and assessment of model efficiency.

The results – model outputs – are described and analyzed in Chapter 5, including model validation.

Chapter 6 brings the results together into a comprehensive discussion of the limitations and potentials of the modelling concept. Chapter 6 also answers the research questions defined in Section 1.2.

Finally, Chapter 7 summarizes the main findings of this thesis and draws a conclusion, with the outlook for further research.

CHAPTER 2

## State of the Art

### 2.1 Global Hydrological Models containing macro-scale floodplain modeling – strengths, weaknesses, and challenges

Global Hydrological Models (GHMs) are important in Earth's System Science for many reasons. Some GHMs simulate the land-atmosphere interaction, for example, the impact on climate due to soil moisture and evapotranspiration, and the influence of continental freshwater on the ocean. GHMs are also extremely valuable for the human society. Rivers, lakes, and wetlands provide water for industry, agriculture, electricity generation and household use. The future increase in population – in relation to changes in climate and water availability from land-use – may greatly stress terrestrial water resources.

Based on their origin, GHMs can be categorized into different types. Land Surface models (LSMs) were developed in atmospheric science to simulate energy balance at soil, vegetation and atmosphere interfaces on finer time scales (often hours); they originally do not have a flow routing. Macro-scale Hydrological Models (MHMs) were developed in the field of global hydrology and water resources to simulate the hydrological cycle and water availability.

GHMs have been improving constantly, increasing both functionality and resolution. Many of the LSMs add routing, reservoirs, human water abstractions and inundation; thus, becoming more MHM-like. In a similar way, MHMs add energy balances or plant physiology, or are coupled with river routing models; thus, becoming more LSM-like. Sood and Smakhtin (2015), and Bierkens (2015) reviewed global modeling efforts, giving a genealogy of existing GHMs, their applications, recent efforts and directions.

Recent hydrological modeling efforts have led, among other efforts, to the inclusion of floodplain simulation in GHMs. Floodplains play an important role in the terrestrial water cycle and have profound significance for biodiversity (Evans et al. 2010; Schneider et al. 2011b), methane emissions (Petrescu et al. 2010; Ringeval et al. 2014), carbon storage (Richey et al. 2002; Decharme et al. 2008), groundwater recharge (Wolski et al. 2006), and flood wave timing (Richey et al. 1989; Vörösmarty and Moore 1991; Coe et al. 2008).

Table 2.1 lists GHMs that simulate floodplain inundation, including MHMs distinguished in real global hydrological models (ISBA-TRIP, WBM-WTM, PCR-GLOBWB) and large-scale hydrological models (MGB-IPH, THMB, LISFLOOD-FP), as well as coupled LSMs with river routing models (CaMa-Flood, JULES-G2G).

**Table 2.1** Non-exhaustive overview of the various large-scale models from different communities and their properties focused on floodplain algorithms (extended from Sood and Smakhtin (2015), and Bierkens (2015)).

| Features | ISBA-TRIP (Interactions Between Soil, Biosphere, and Atmosphere - Total Runoff Integrating Pathways) | WBM-WTM/ WBMplus (Water Balance Model-Water Transport Model) | CaMa-Flood (Catchment-based Macro-scale Floodplain) model (runoff used from Land Surface Model MATSIRO) | PCR-GLOBWB (PCRaster GLOBal Water Balance) model | MGB- IPH (Modelo de Grandes Bacias - Instituto de Pesquisas Hidráulicas) | THMB (Terrestrial Hydrology Model with Biogeochemistry) - formerly HYDRA | JULES-G2G (Joint UK Land Environment Simulator - Grid-to-Grid) | LISFLOOD/ LISFLOOD-FP |
|---|---|---|---|---|---|---|---|---|
| **References** | Decharme et al. (2008), Decharme et al. (2012), Pedinotti et al. (2012) | Beighley et al. (2009), Beighley et al. (2011) | Yamazaki et al. (2011), Yamazaki et al. (2012b) | van Beek and Bierkens (2009), Wada et al. (2014), Ringeval et al. (2014) | Paiva et al. (2011), Paiva et al. (2013) | Coe (2000), Coe et al. (2002), Coe et al. (2008) | Dadson et al. (2010) | Bates and De Roo (2000), Wilson et al. (2007), Trigg et al. (2009), Biancamaria et al. (2009), Neal et al. (2012) |
| **Type of model** | Global Hydrology Model | Global Hydrology Model | Large-scale coupled river routing and land surface model (runoff from MATSIRO) | Global Hydrology Model | Large-scale hydrological model | Large-scale Hydrological model | Large-scale coupled land surface and routing model | Large-scale hydrological model |
| **Spatial resolution and extent** | 1.0 degree, global extent | 0.5 degree, global extent; floodplain modeling presented only for the Amazon River basin on an irregular computational grid | 0.25 degree, global extent, river flow simulation in continental-scale rivers on unit catchment elements | 0.5 degree, global extent | Catchment units, different basins in South America | 5 minute, Amazon and Tocantis River basins | 0.5 degree, selected areas on the globe; mainly UK; floodplain modeling presented for the Niger inland delta | Raster-based discretisation, resolution depends on input DEM, selected areas on the globe |
| **Validation regarding floodplain inundation** | global: floodplain area; Niger basin: floodplain area | Amazon river basin: floodplain width | global: floodplain area; Amazon river basin: floodplain area, floodplain height | Amazon river basin: floodplain extent and depth | Amazon river basin: floodplain area, floodplain height | Amazon river basin: floodplain area, floodplain height | Niger inland delta (study area ~13°x10°): inundated area | Ob river basin (study area 1°x5°): water heights, Amazon river basin (study area 2°x1.5°): water heights, Niger inland delta: heights and extent |
| **Temporal** | daily (internal 20 | daily (internal routing | daily (internal routing | daily | daily | daily | monthly (internal 30- | daily (Internal time |

| Features | ISBA-TRIP | WBM-WTM/ WBMplus | CaMa-Flood | PCR-GLOBWB | MGB- IPH | THMB | JULES-G2G | LISFLOOD/ LISFLOOD-FP |
|---|---|---|---|---|---|---|---|---|
| **resolution** | minutes to 1 hour) | time step of 15min) | time step of 20-30min) | | | | 60min) | step seconds) |
| **Drainage network** | Hydro1k | Derived from ground slopes using SRTM DEM | HydroSHEDS + SRTM3 and Global Drainage Basin Database (GDBD) | DDM30 | SRTM + GTOPO | Amazon Basin river directions (Costa et al. 2002) | Hydro1k | ACE (Ob), SRTM (Amazon) |
| **Inland water bodies** | No | Yes, Reservoirs only (GRanD) | No (lakes and wetlands are treated as floodplains; MATSIRO includes reservoirs) | Yes, GLWD; static but lake area is a function of lake volume | No | Yes, GGHYDRO; static | Yes, global lake database GLDBv2; static | Yes; static but evaporation is a function of lake level |
| **Human water use** | No | Yes | No (MATSIRO: Yes) | Yes | No | Yes | Yes, irrigation only | Yes |
| **Vegetation** | 12 vegetation types (ECOCLIMAP database) | Fixed, climatology of phenology, irrigated area change; 3 vegetation types, forest, grassland, and shrubland | Simple crop growth model (MATSIRO) | Fixed, climatology of phenology, irrigated area change; 3 categories natural vegetation, rain-fed crops, and irrigated crops; further subdivided into tall and short vegetation. | Fixed, climatology of phenology, vegetation map of South America from Eva et al. (2004) | Fixed, climatology of phenology | Dynamic + phenology + plant physiology; Optional: dynamic vegetation using TRIFFID | LAI-observed, LAI Climatology |
| **Channel geometry (river width and depth) and bankfull/flood initiation conditions** | As a function of river discharge and a basin specific coefficient; bankfull height is calculated as a non-linear function of river width | As a function of drainage area (bankfull depth and width and floodplain width based on relationships presented in Gummadi 2008) | As a function of discharge (channel width and bank height determined as a function of maximum 30 day upstream runoff) | As a function of discharge (channel depth and width calculated using hydraulic relationships after (Allen et al. 1994)); bankfull discharge based on statistical relationship between climate indicators and observed bankfull discharge for 296 stations (Vörösmarty et al. 1998), extrapolat- | As a function of drainage area (channel width and bank height), coefficients determined using cross section profiles from 341 gauge stations located in the Brazilian Amazon | As a function of drainage area (river stage height and width); coefficients determined based on visual inspection of observed hydrographs in the Amazon River basin) | Not specified | Amazon: cross-sections and bankfull depth from sonar survey data; Ob: constant width and depth; Niger: as a function of discharge (using hydraulic relationships after Leopold and Maddock 1953 with coefficients from Hey and Thorne 1986) |

| Features | ISBA-TRIP | WBM-WTM/ WBMplus | CaMa-Flood | PCR-GLOBWB | MGB- IPH | THMB | JULES-G2G | LISFLOOD/ LISFLOOD-FP |
|---|---|---|---|---|---|---|---|---|
| | | | | ed over the world. | | | | |
| **River - flood-plain interac-tion** | The flood reservoir fills when the river height exceeds the critical river bankfull height, and vice versa; river-floodplain interaction as a function of river-floodplain water slope | When discharge exceeds the bankfull capacity of the chan-nel, a portion of it is routed along the floodplain; backflow to river if discharge is below bankfull capacity; river water level equals floodplain water level | That water spilling from the river chan-nel (flood initiation storage) is stored in the floodplain. river water level equals floodplain water level | The volume of water in excess of bankfull discharge floods the surrounding areas; no backflow to river necessary as flood-plains are treated as regular river stretch-es; river water level equals floodplain water level | No interaction (water level (and flooded area) is calculated regarding river bot-tom elevation which is the lowest surface elevation of the DEM within a catchment); river water level equals floodplain water level | The volume of river water in excess of river bankfull volume (flood initiation vol-ume) is added to the floodplain reservoir; backflow to the river if river water storage is below flood initia-tion storage | Overbank flows flood fractions of land cover types | When bankfull depth is exceeded, water is transferred from the channel to the over-lying floodplain grid. |
| **Surface elevations** | GTOPO30; 30 arc sec, global coverage | SRTM; 3 arc sec, near global coverage (±60°N) | SRTM30 + GTOPO30; 30 arc sec, global coverage | Hydro1k; ~30 arc sec, global coverage | SRTM + GTOPO; 30 arc sec, global coverage; correction for river bottom level estima-tion and vegetation correction (17 m except for areas with low vegetation (Eva et al. 2004)) | SRTM; 3 arc sec, near global coverage (±60°N); vegetation correction (23 m for areas where forest is the predominant vegeta-tion type (Eva et al. 2004; Hess et al. 2003)) | Hydro1k; ~30 arc sec, global coverage | ACE (Ob), SRTM (Amazon); ~30 arc sec (100 m); vegetation correction in Amazon region (data obtained doing fieldwork) |
| **Floodplain area (CDF - cumula-tive distribu-tion function of subgrid surface eleva-tions)** | CDF, cumulative distribution of sub-grid elevations | No | CDF, cumulative distribution of sub-grid elevations (36 points) | Optionally fixed or variable area option. If variable: floodplain storage is distributed over subgrid cells based on a CDF - cumulative distribu-tion of relative eleva-tions | As a function of water level (sum of surface water pixels inside a floodplain catchment that is lower than the water level) | CDF (only the value if half of the grid cell is flooded is used); to avoid runaway flood-ing maximum flooda-ble area is used as input (unpublished data from Hess et al.) | CDF (using only the mean and the stand-ard deviation of the logarithm of eleva-tion). A prorated fraction of the preex-isting surface types is converted to have an "open water" land cover type. | The values of water depth at each cross-section are overlain onto a DEM (or the inundation extents at each cross section are linearly interpo-lated). |
| **Routing** | Kinematic wave | Kinematic wave for first-order tributary channels, | Diffusive wave | Kinematic wave | Hydrodynamic model in flat reaches of the main rivers, Musk- | Kinematic wave, diffusive wave for floodplains | Kinematic wave | Diffusive wave for channels and flood-plains |

| Features | ISBA-TRIP | WBM-WTM/ WBMplus | CaMa-Flood | PCR-GLOBWB | MGB- IPH | THMB | JULES-G2G | LISFLOOD/ LISFLOOD-FP |
|---|---|---|---|---|---|---|---|---|
| | | Muskingum-Cunge for interbasin channels and floodplains | | | ingum-Cunge method in upstream areas | | | |
| **Flood routing direction** | No floodplain flow routing | Along the river network; channel and floodplain gradients identical | No floodplain flow routing | No floodplain flow routing; floodplains treated as regular river stretches with increased resistance | No floodplain flow routing; the floodplains act only as storage areas | According to the maximum water slope between neighboring grid cells | No floodplain flow routing | According to the maximum water slope between neighboring grid cells |
| **Flow velocity v (including specifications of the roughness coefficient n)** | Variable in time and space; $n_r$ varies arbitrary from upstream areas to the river mouth (0.04-0.06), $n_f$ according to the vegetation type (0.035 - 1.0); slope taken from STN-30p DEM (0.5° resolution) | Variable in time and space; $n_r$=0.04, $n_f$=0.07 | Variable in time and space; n=0.03 for the Amazon river basin | Variable in time and space; increased wetted perimeter and Manning's n in case of flooding --> increased hydraulic resistance (decreased $v_r$) $n_r$=0.04, $n_f$=0.1 | Constant in time, variable in space; $n_r$= 0.035-0.04 (different values for different large river basins aiming at fitting hydrographs) | Constant in time, variable in space | Constant in time and space: $v_r$=1.0 m/s, $v_f$=0.2 m/s | Not explicitly considered by the model, $v_r$ [m/s] at high/ low water: Solimoes 1.3/ 0.77, Purus 0.86/ 0.26; $n_r$ usually 0.01 - 0.04, $n_f$ usually 0.03 - 0.15. Can be set individually for each grid cell. |
| **Soil and Groundwater dynamics** | Vertical soil, groundwater reservoir | Vertical soil, groundwater reservoir | Vertical soil, groundwater reservoir (MATSIRO) | Vertical soil, groundwater reservoir or lateral groundwater (optional) | Soil reservoir and groundwater reservoir | Vertical soil, groundwater reservoir | Vertical soil | Vertical soil, groundwater reservoir |
| **Floodplain-groundwater interaction** | Yes | No | No | No | No | No | No | No |
| **Institutes responsible for model development** | Centre National de Recherchés Météorologiques, France | University of New Hampshire (USA), City University of New York (USA) | IIS, University of Tokyo (Japan) | Utrecht University (Netherlands), Deltares (Netherlands) | Instituto de Pesquisas Hidráulicas – IPH, Universidade Federal do Rio Grande do Sul – UFRGS (Brasil) | SAGE, University of Wisconsin-Madison (USA) | Centre for Ecology and Hydrology (UK), Met Office (UK) | University of Bristol (UK) |

All of the models listed in Table 2.1 except MGB-IPH – which uses catchment units – run in a grid format, most of them with a spatial resolution from 0.25 degree to 1.0 degree (WBM-WTM, PCR-GLOBWB, JULES-G2G with 0.5 degree, CaMa-Flood with 0.25 degree, and ISBA-TRIP with 1 degree); 0.5 degree is approximately 3100 km² at the equator. Only two models – THMB and LISFLOOD-FP – have a finer spatial resolution ($\leq$ 5 minutes). The temporal resolution of the model outputs is one day, except JULES-G2G, which gives outputs on a monthly time step.

Although GHMs run on global or continental-scales, the simulated floodplain inundation is validated only for limited regions of the globe. Only CaMa-Flood and ISBA-TRIP show results on modeled floodplain area on a global-scale (Yamazaki et al. 2011; Decharme et al. 2012). Most models validate floodplain area and/or floodplain height for the Amazon River basin (WBM-WTM, CaMa-Flood, PCR-GLOBWB, MGB-IPH, THMB). Modeled floodplain area in the Niger inland delta is validated using JULES-G2G and LISPLOOD-FP (Dadson et al. 2010; Neal et al. 2012). The latter also simulates water heights in relatively small regions located in the Amazon (Wilson et al. 2007; Trigg et al. 2009) and Ob river basins (Biancamaria et al. 2009).

Due to its enormous size, the limited number of hydraulic restrictions along its reaches, and the critical role of its extensive floodplain system, the Amazon River basin is of special interest in simulating water storage and transmission of the flood wave (Richey et al. 1989), with major impacts on ecology and biogeochemistry (Melack and Forsberg 2001; Richey et al. 2002; Melack and Hess 2004).

Although an explicit representation of inland water bodies is important for the calculation of, for example, evapotranspiration within a grid cell, most of the models do not account for inland water bodies (ISBA-TRIP, MGB-IPH) or consider them as static (WBM-WTM, CaMa-Flood, THMB, JULES-G2G). Only two models calculate the area of inland water bodies as a function of storage (PCR-GLOBWB) or lake level (LISFLOOD-FP). As Coe et al. (2008) have suggested, an over-prediction of discharge may be, among other causes, attributed to an underestimation of evaporation from the land surface. Similar errors could arise when man-made reservoirs due to dam construction are not represented within the model (Decharme et al. 2012).

River flow is highly affected by human activities such as dam construction, water withdrawals and irrigation (Dadson et al. 2010; Yamazaki et al. 2011; Decharme et al. 2012). Human water use is simulated by most of the GHMs listed in Table 2.1 except ISBA-TRIP, CaMa-Flood, and MGB-IPH. However, due to the lack of data on a global-scale, there are still uncertainties in modeling human water use; these include the verification of regulated groundwater pumping, artificial channel networks and the amount of water transferred, as well as the amount of water recycled to estimate consumptive water use (Wada et al. 2014).

GHMs use multiple datasets to represent drainage network and surface elevation. The main differences between the datasets and their application are the various spatial resolutions and the correction against hydrology and vegetation. The models use the datasets with a spatial resolution of either 3 arc seconds or 30 arc seconds, and a global or near global coverage. When only elevation data from the Shuttle Radar Topography Mission (SRTM) is used (WBM-WTM, THMB), latitudes north of 60°N and south of 60°S are not covered (the same is true for HydroSHEDS, as it is based on SRTM data). Most GHMs (except WBM-WTM, MGB-IPH, and LISFLOOD-FP) use drainage networks, which were corrected for hydrological applications, whereas only two of the models listed in Table 2.1 – PCR-GLOBWB and JULES-G2G – apply hydrologically corrected surface elevations (Hydro1k and HydroSHEDS). Paiva et al. (2013) have corrected SRTM and GTOPO30 data for river bottom level estimation in the MGB-IPH model. Three models (MGB-IPH, THMB, LISFLOOD-FP) correct surface elevations against vegetation, at least in areas with high and dense vegetation (Table 2.1).

It is important to emphasize, as most authors do, that the data input from digital elevation models (DEMs) is a possible source of major errors within GHMs. Currently, due to recent advances in remote sensing technologies enhancing the collection of topographic data, various types of DEMs have become available.

The Global 30 Arc-Second Elevation data set (GTOPO30) provided from the U.S. Geological Survey (USGS) was derived from several raster and vector sources of topographic information, which imply differing vertical accuracy and possible errors (e.g. caused by map digitizing and elevation surface interpolation). The vertical accuracy is stated as $\pm 30\,\text{m}$ (absolute error at 90% confidence interval; http://webgis.wr.usgs.gov/globalgis/gtopo30/gtopo30.htm).

Similar to GTOPO30, spaceborne DEMs such as ASTER GDEM (Rauter et al. 2009) and the SRTM dataset also suffer from random noise (artifacts, holes, gaps) caused by operating platform maneuver errors. Additionally, spaceborne DEMs are affected by surface objects such as trees, buildings, and bridges. The SRTM has a linear vertical absolute height error of less than 16 m (Farr et al. 2007), which includes errors related to vegetation. The SRTM data is based on an interferometric SAR technique, and returns the majority of its signal from near the top of the canopies in areas with dense vegetation (Farr et al. 2007). Because ASTER GDEM is not as sharp as the SRTM data, and because it appears to contain less spatial detail (Rauter et al. 2009; Jacobsen 2010; Chang et al. 2010), it is preferential to use SRTM data in GHMs.

Another DEM used in GHMs (Table 2.1) is the Altimeter Corrected Elevations (ACE2) dataset (Smith and Berry 2009). This DEM is a combination of SRTM and altimetry data. As ACE2 replaces SRTM pixels over rainforest areas, it corrects SRTM errors caused by dense vegetation. In contrast to the SRTM, the altimeter data is able to penetrate vegetation cover and reflects the signal from the underlying ground surface.

Furthermore, altimetry data is used for high latitudes north of 60°, which are not covered by SRTM.

Several authors (Beighley et al. 2009; Paiva et al. 2013; Wilson et al. 2007; Neal et al. 2012; Yamazaki et al. 2012a) have stated that in order to improve the accuracy of the hydrodynamic simulations, it is essential to correct raw DEM data against vegetation and other artifacts. For the DEMs GTOPO30 and SRTM, hydrologically corrected products are available; these products are HYDRO1k (USGS product) and HydroSHEDS (Hydrological data and maps based on SHuttle Elevation Derivative at multiple Scales; Lehner et al. 2008b). The hydrological corrections particularly imply stream burning and void filling to ensure that the flow stays within the river channel, but there is no vegetation correction. Yamazaki et al. (2012a) have presented another method for correcting raw SRTM data in floodplain modeling. Nevertheless, further improvements to the DEM adjustment algorithm are still essential. The typical resolutions and accuracies of spaceborne DEMs may not be fine enough to represent small channels that connect floodplains and local depressions in floodplains, or to derive channel slopes and relationships among water storage, water level and inundated area (Wilson et al. 2007; Beighley et al. 2009; Yamazaki et al. 2011). Improvements in Light Detection And Ranging (LiDAR) technology have made the acquirement and application of high-resolution DEM data increasingly popular, especially within the field of flood inundation modeling. Airborne LiDAR DEMs are preferred due to their higher horizontal resolution, vertical accuracy (~0.1 m), and ability to separate the bare-ground from vegetation and built structures (Sanders 2007; Shen et al. 2015). However, the availability of high resolution LiDAR DEMs is generally limited to few locations, and thus they are not applicable in continental-scale or even global-scale hydrological models (Yamazaki et al. 2012b).

In GHMs, the channel geometry is usually calculated as either a function of river discharge with constant or basin specific coefficients to approximate hydraulic relationships, or a function of drainage area (Table 2.1). Flooding occurs in all of the GHMs when the river channel reaches its maximal capacity. The GHMs use a threshold for flood initiation, which is either bankfull discharge, bankfull height, or bankfull storage. It is important to note that the estimation and calculation of channel geometry, channel slope, and the flood initiation parameter are challenging tasks in GHMs that contain macro-scale floodplain modeling. In general, model results are highly sensitive to these parameters, and their uncertainty has been described as a possible source of errors by many authors (Coe et al. 2008; Yamazaki et al. 2011; Decharme et al. 2012; Paiva et al. 2013). Especially river width and river bankfull depth are critical parameters because they define the water holding capacity of a river channel during flooding. A number of studies have begun to use satellite observations to determine river channel width and water depth (Durand et al. 2008; Pavelsky and Smith 2008; Durand et al. 2010). Recently, a Global Width Database for Large Rivers (GWD-LR) which contains time constant river width calculated from satellite-based water masks and flow direction

maps with a near global (60°N-60°S) coverage has become available (Yamazaki et al. 2014). Corroboration with newly remote sensing techniques is a challenging task, and the implementation of satellite-derived channel parameters could be an alternative to parameter estimation based on empirical equations.

In almost all of the models, the water spilling from the river channel flows completely or proportionately into the floodplain. An exception to this is MGB-IPH, in which there is no interaction between river and floodplain. Here the lowest surface elevation of the digital elevation model is assumed to represent the river bottom (not the bankfull stage), so that the calculated flooded area includes the river and the floodplain. Once on the floodplain, most models use a cumulative distribution function (CDF) of the surface elevations to determine the floodplain extent and water height.

The water exchange between the channel and the floodplain is known to be complex (Alsdorf et al. 2005; Alsdorf et al. 2007), and its simulation ought to be improved in several models (e.g. Yamazaki et al. 2011; Decharme et al. 2012). However, in order to further enhance the simulation of mass transfer between rivers and floodplains, it would be necessary to consider the detailed physics of floodplain infilling and draining (Yamazaki et al. 2011).

An important difference among GHMs lies in the method of routing, which can be divided broadly into two categories: 1) separate routing in rivers and floodplains (WBM-WTM, THMB, LISFLOOD-FP) and 2) floodplains acting only as storage areas and treated as regular river stretches (ISBA-TRIP, CaMa-Flood, PCR-GLOBWB, MGB-IPH, JULES-G2G). All GHMs of the first category allow a backflow of water from the floodplain to the river in the same grid cell if the flood initiation threshold is not reached. In addition, all of them – with the exception of WBM-WTM – allow backwater flows to upstream grid cells (THMB only for floodplains, not for rivers) or a diffuse routing of floodwater to all neighboring grid cells according to maximum water slope (THMB, LISFLOOD-FP). From the second category, only ISBA-TRIP includes backflow from the floodplain to the river and only CaMa-Flood allows backwater effects (Table 2.1). Backwater flows are especially important in the Amazon river basin (Meade et al. 1991) and, if not considered, they may be a reason for underestimation of flooding (Coe et al. 2008) or overestimation of flow velocity (Han et al. 2009).

There are three different methods for processing flow velocity: 1) constant in space and time (JULES-G2G), 2) constant in time but variable in space according to various relationships with the topography or aiming at fitting hydrographs at basin or subbasin-scale (MGB-IPH, THMB), and 3) variable in time and space according to the river and floodplain geomorphology and the water level gradient using the Manning-Strickler equation (ISBA-TRIP, WBM-WTM, CaMa-Flood PCR-GLOBWB).

Because flow velocity changes in accordance with actual river discharge (Leopold and Maddock 1953), it is meaningful to transport the water within a hydrological model that has a river flow velocity variable in space and time. Among all of the models described

in Table 2.1, only WBM-WTM explicitly distinguishes between river and floodplain flow velocity. ISBA-TRIP and PCR-GLOBWB reduce flow velocity in rivers if flooding occurs (Table 2.1). Within the Manning-Strickler equation, river flow velocity is calculated as a function of actual discharge, river bed roughness, and river slope. Nevertheless, observations have revealed that flow velocities differ between rivers and floodplains (Alsdorf et al. 2007) and should, therefore, be modeled separately.

Except for ISBA-TRIP, none of the GHMs include floodplain-groundwater interactions. ISBA-TRIP calculates infiltration of water from floodplains to soil, and from soil the water drains to the groundwater reservoir (Decharme et al. 2008). As demonstrated by Wolski et al. (2006), Fan and Miguez-Macho (2010), and Miguez-Macho and Fan (2012), a rising groundwater table can support surface water bodies, thus floodplains as well, by maintaining a saturated substrate. Nevertheless, none of the GHMs include detailed groundwater table depth information to be able to calculate water flows from groundwater to floodplains. It is important to emphasize that a lack of infiltration from rivers and floodplains to soil and groundwater may cause an over-prediction of discharge and prevent floodplain dewatering (Wilson et al. 2007; Dadson et al. 2010). Such a lack of infiltration is also a major source of soil moisture in semi-arid and arid regions and may cause an underestimation of evapotranspiration if not considered within the model (Wolski et al. 2006).

In summary, the GHMs listed in Table 2.1 have several strengths but also some weakness. None of the models includes together the following features:

- inland water bodies with variable area

- high resolution and hydrologically corrected surface elevation

- vegetation correction of surface elevations in areas with high and dense vegetation

- the two-way exchange between river and floodplain

- separate routing in rivers and floodplains, simulating backwater effects for both rivers and floodplains

- flow velocity for rivers and floodplains, both variable in time and space

- floodplain - groundwater interactions

The purpose of this PhD work, as described in more detail in the objectives (Section 1.2), is to develop a floodplain algorithm for the global hydrology model WaterGAP. The WaterGAP model which contains macro-scale floodplain modeling will implement all of these characteristics within a single model.

## 2.2 WaterGAP

### 2.2.1 Overview and model history

The freshwater model WaterGAP (Water Global Assessment and Prognosis) was created to assess water availability and water use on a global-scale. It comprises two main components: a Global Hydrology Model (WGHM, e.g. Döll et al. 2003, Müller Schmied et al. 2014) to simulate the continental water cycle, and a Global Water Use Model to estimate water consumption and water withdrawals for agriculture (livestock and irrigation; Döll and Siebert 2002), industry (manufacturing and cooling of thermal power plants; Vassolo and Döll 2005; Voß and Flörke 2010), and domestic water use (Voß et al. 2009). Additionally, a sub-module (GWSWUSE - Ground Water Surface Water Use) computes the fractions of total water use, abstracted from either surface waters (lakes, reservoirs, and rivers) or groundwater (Döll et al. 2012).

WaterGAP has been developed at the Center for Environmental Systems Research (CESR) of the University of Kassel (Germany) since 1996, and since 2003 also at the Institute of Physical Geography of the University of Frankfurt/Main (Germany). Since the initial publications of WaterGAP (Alcamo et al. 2003; Döll et al. 2003), it has been continuously improved.

WaterGAP calculates flows and storages of water for the whole land area of the globe, except Antarctica, at a spatial resolution of 0.5 geographical latitudes by 0.5 geographical longitudes (55 km by 55 km at the Equator) and a temporal resolution of one day. Model input includes spatially distributed physiographic information such as characteristics of soil type, land cover, topography, hydrogeology, and the location and area of surface water bodies (wetlands, lakes, and reservoirs) as well as time series of climate data like temperature, precipitation, and solar radiation, among others.

The model is able to compute both historical developments and future projections of different hydrological variables, water availability and water use. It is applied to assess water scarcity and water stress (Smakhtin et al. 2004; Alcamo et al. 2007), quantify the impact of human actions on freshwater (Döll et al. 2009), and study climate change effects on the global freshwater system (Döll 2009; Döll and Zhang 2010; Döll and Müller Schmied 2012), irrigation water requirements (Döll and Siebert 2002), and droughts and floods (Lehner et al. 2006b).

WaterGAP has been applied in a number of international projects such as the Millennium Ecosystem Assessment, the UN Global Environmental Outlooks, the UN World Water Development Reports, the EU-funded Projects SCENES and WATCH, and projects funded by the German Research Foundation (DFG) like REGHYDRO. With regard to the latter project, global hydrological modeling and regional geodetic estimation using GRACE data were combined in order to improve the characterization of regional gravity field features using WaterGAP and global-scale hydrological modeling of water

storage variations (and flow) using information on the variation of the gravity field from GRACE (Adam et al. 2010; Döll et al. 2012).

## 2.2.2 Simulation of hydrological processes within WaterGAP

The simulation of hydrological processes within WaterGAP is done by the WaterGAP Global Hydrology Model (WGHM). It computes time-series of water flows and storages – e.g. groundwater recharge, evapotranspiration, river discharge and water storages variations in canopy, snow, soil, lakes, wetlands, rivers, and groundwater – considering the anthropogenic water demand.

Figure 2.1 provides a schematic representation of the major vertical and lateral hydrological processes of WGHM.
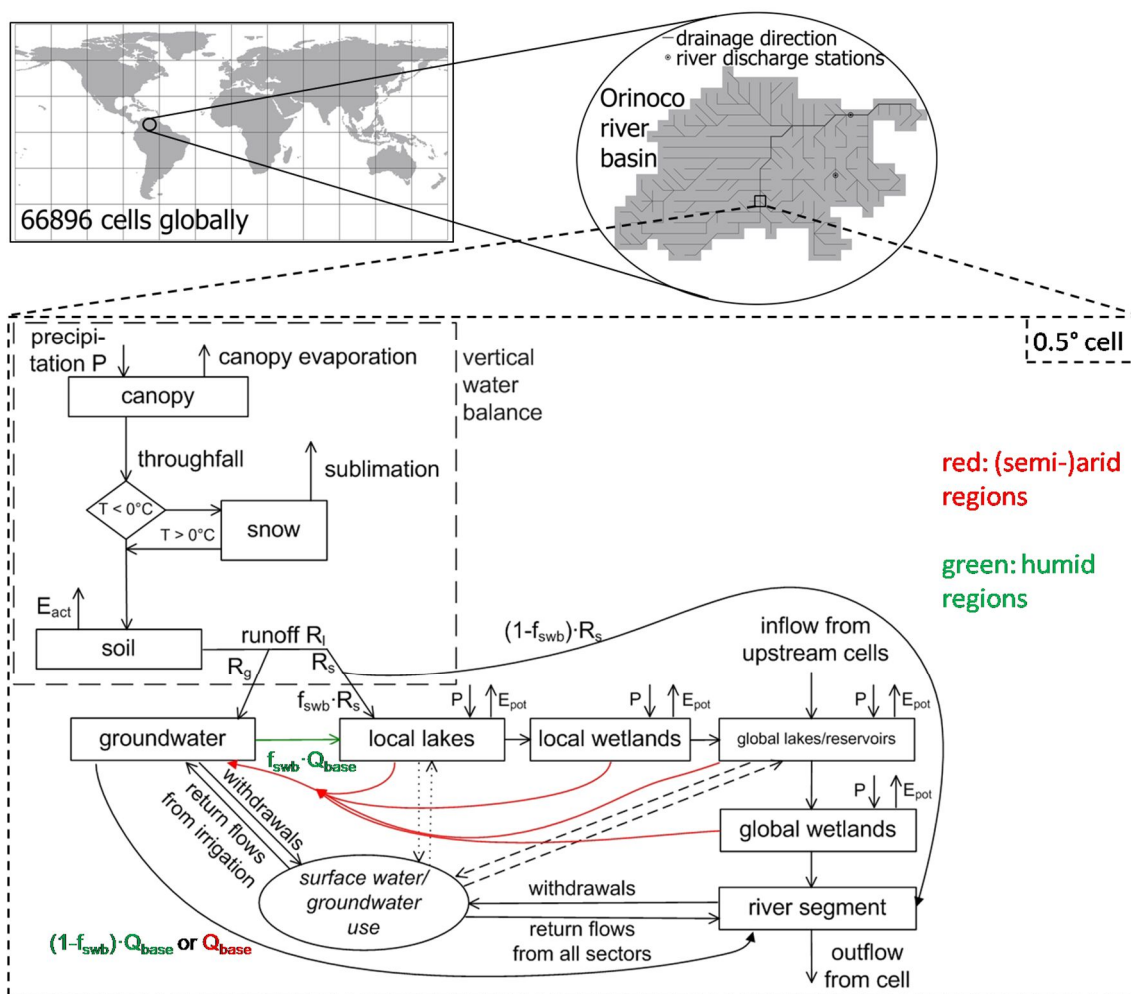


**Figure 2.1** Schematic representation of the vertical and lateral water balance as computed by the WaterGAP Global Hydrological Model (WGHM) (modified from Döll et al. 2012), including human water use. In the flow chart, boxes represent the water storage compartments, and arrows the water fluxes (inflows, outflows); $E_{pot}$: potential evaporation, $E_a$: actual evaporation, $E_c$: evaporation from the canopy, $R_l$: runoff from land, $R_g$: groundwater recharge, $R_s$: surface runoff, $Q_{base}$: baseflow, $f_{swb}$: fraction surface water body.

A daily water balance is calculated for the fraction of continental area for each of the 66896 grid cells (Figure 2.1). A vertical water balance simulates interception by canopy, snow accumulation, and water throughfall to soil. The resulting runoff is routed within the grid cell in a lateral water balance through a groundwater store and various surface water stores, and finally, contributes to river discharge. Grid cell discharge (river and floodplain discharge) is routed with a variable flow velocity (Section 4.6) to the next downstream cell (kinematic wave, Section 4.5.1) according to a river network derived from the global drainage direction map DDM30 (Döll and Lehner 2002). The location and maximum size of lakes, reservoirs and wetlands are based on the Global Lakes and Wetland Database (GLWD) (Lehner and Döll 2004), with an addition of more than 6000 man-made reservoirs (Döll et al. 2009; Lehner et al. 2011). Whereas so-called 'local' surface water bodies are only fed by runoff produced within the grid cell, so-called 'global' surface water bodies also receive water inflow from upstream cells (Section 4.4.2). For each surface water body, precipitation and evapotranspiration are computed. Groundwater storage is affected by groundwater recharge beneath lakes, wetlands and floodplains in (semi-)arid regions, and diffuse groundwater recharge (Figure 2.1), which is calculated as a function of total runoff, soil texture, hydrogeology, relief and the existence of permafrost or glaciers (Döll and Fiedler 2008). Water withdrawal from the hydrological system as well as consumptive water use of the different sectors, computed by the Water Use Model of WaterGAP, can optionally be taken out of the grid cell. Since water requirements cannot always be satisfied in any grid cell at any time, WGHM allows for the extraction of the unsatisfied portion from a neighboring grid cell.

Each grid cell of WGHM is provided with information from different datasets. Important inputs include static input maps of soil and land cover (see Table 2.2 in Verzano 2009) as well as time series of climate data for precipitation, temperature, cloudiness, and number of wet days. Monthly climate data are downscaled to daily data; in the case of precipitation, the available number of wet days per month are used. The current model version WaterGAP 2.2b uses monthly climate data, except for precipitation, from the Climate Research Unit CRU TS 3.2 (Harris et al. 2014). Monthly time series of 0.5° gridded precipitation is provided by the Global Precipitation Climatology Center GPCC version 6 (Schneider et al. 2014).[1]

WaterGAP 2.2b is tuned in a basin-specific manner against long-term average observed discharge at 1323 gauging stations around the world (WaterGAP 2.1g and WaterGAP 2.1h at 1235 gauging stations) by adjusting one to three model parameters (Hunger and Döll 2008). The discharge data is provided by the Global Runoff Data Center (GRDC).

---

[1] Climate data input for the former WaterGAP model versions 2.1g and 2.1h (applied for the analysis presented in Chapter 3) is CRU TS 2.1 Mitchell and Jones 2005 and GPCC v3 Rudolf and Schneider 2005.

A thorough model description of the WaterGAP 2.2 version, including 1) the Global Hydrology Model, 2) the calibration and regionalization approach upon which WaterGAP is based, and 3) the Global Water Use Model can be found in the appendix of Müller Schmied et al. (2014). The homogenization approach of the climate forcing is described in Müller Schmied et al. (2016). Changes to WaterGAP 2.2, leading to the version 2.2a, are documented in Döll et al. (2014). No publication is yet available which concerns the latest version WaterGAP 2.2b. This version contains – in addition to minor modification (e.g. to inland sinks) – an adapted calibration scheme (that allows up to 10% uncertainty of measured river discharge).

Former model versions and developments that have been made since the first publication on WaterGAP in 2003 are described, for example, in Kaspar (2004), Verzano (2009), Hunger and Döll (2008), Döll and Fiedler (2008), Döll et al. (2012), and Döll and Müller Schmied (2012).

### 2.2.3 Model version applied in this thesis

WaterGAP 2.2b has been developed within the timeframe of this PhD work. Therefore, it was used to implement the final floodplain algorithm, as well as for the more recently performed final results.

The development and testing of the floodplain algorithm as well as the preliminary tests of surface water extension and surface water storage variations (Chapter 3) were accomplished at an earlier stage of this PhD work. For this reason, WaterGAP 2.1g and WaterGAP 2.1h were applied for these analyses.

CHAPTER 3

# Analysis of satellite-derived naturally inundated areas and surface water storage as a basis for floodplain modeling

## 3.1 Global-scale analysis of satellite-derived time series of naturally inundated areas as a basis for floodplain modeling[1]

### 3.1.1 Introduction

Wetlands play an important role in the terrestrial water cycle, influencing evapotranspiration, water storage, and river discharge dynamics. In addition, they are the habitat of a large number of animals and plants. Thus, to assess the Earth's system and its changes, a good understanding of the dynamics of wetlands, including inundated areas, water storages, and water flows is required. Global hydrological and land surface models simulate wetlands and seasonally inundated areas with strongly varying degrees of complexity, and some do not simulate them at all. Decharme et al. (2008) described an advanced approach for simulating the inundation of floodplain within a global land surface model, at a spatial resolution of 1° by 1°. In this model, the floodplain reservoir fills when the river height exceeds a critical value. The flooded fraction of the grid cell is determined based on the 1 km by 1 km Digital Elevation Model HYDRO1k (http://edcdaac.usgs.gov/gtopo30/hydro). With a spatial resolution of 5' by 5', Coe et al. (2008) computed the dynamics of flooded areas in the Amazon basin, using basin-specific information on river width, and river stage at which flooding begins as a function of upstream drainage area. To represent subgrid-scale morphology, a cumulative distribution function was derived from the Shuttle Radar Topography Mission (SRTM) 90m elevation data (Farr et al. 2007) (aggregated to 1 km resolution), and a quantitative relation between inundated areas and water stored in the inundated floodplain was derived.

While the models of Decharme et al. (2008) and Coe et al. (2008) aim at simulating the inundation of floodplains that occurs when river channels can no longer contain all the flowing water, the WaterGAP Global Hydrology Model WGHM (Döll et al. 2003), with a spatial resolution of 0.5° by 0.5°, simulates all types of inland wetlands (including floodplains, freshwater marshes, swamp forests, bogs, fens and salt pans) but does not distinguish between the different types. The location of wetlands and their extent are

---

[1] Based on Adam, L., Döll, P., Prigent, C. and Papa, F.: Global-scale analysis of satellite-derived time series of naturally inundated areas as a basis for floodplain modeling, Advances in Geosciences, 2010.

prescribed by the Global Lakes and Wetlands Database GLWD (Lehner and Döll 2004). The size of wetlands does not vary explicitly over time. However, in the current version of WGHM, evaporation is modeled as a function of water storage, so that wetland area is implicitly assumed to reduce with decreasing storage. Wetland evaporation is reduced by 10% when actual storage is half of the maximum storage and becomes zero when storage is zero (Hunger and Döll 2008).

In the Amazon basin, which is characterized by seasonal large-scale inundations of floodplains, WGHM was found to overestimate the lateral transport velocity of water. Because of that, the modeled seasonal discharge peaks too early in the year ( Döll et al. 2003; Fiedler and Döll 2010). In addition, compared to seasonal water storage variations as obtained from satellite-derived gravity fields, WGHM underestimates the amplitude of the seasonal water storage variations in the Amazon basin (Fiedler and Döll 2010; Werth and Güntner 2010). This may be explained by an underestimation of wetland storage capacity, because maximum storage height of wetlands is assumed to be 2 m globally, a value that is probably too small for the wetlands in the Amazon basin. Therefore, wetland storage in the Amazon basin is fully exploited throughout most of the year. If the river flow velocity is decreased by a factor of 3 (or more, depending on the discharge station), a good agreement between observed and simulated seasonality of river discharge and water storage is obtained. This indicates that WGHM might underestimate the storage capacity of the wetlands in the Amazon, and is a motivation for improving the dynamic modeling of wetlands in WGHM, in particular, the modeling of floodplains and other wetlands which depend on seasonal river flooding. The development of a new model algorithm requires data of the dynamics of inundation areas, in addition to discharge data and data on total water storage variations in the river basin as provided by satellite-derived gravity fields.

The objective of this study was to analyze time series of inundated areas derived from satellite observations, as the first step towards improved floodplain inundation modeling in WGHM. In Section 2, we present a global-scale data set of time series of naturally inundated areas that can be used for developing and validating a floodplain inundation model for WGHM. This data set is based on a monthly time series of inundated areas that was derived from multiple satellites for the time period 1993-2004 ( Prigent et al. 2007; Papa et al. 2010). In Section 3, we compare this time series with the static wetland extent in the Global Lakes and Wetlands Database GLWD. In Section 4, we show a first analysis of the relation between the dynamics of observed river discharge and inundation extent for selected 0.5° grid cells located in the Amazon and Ob river basins, to identify how flooding can be modeled as a function of computed river discharge. Additionally, inundation extent is compared to modeled river discharge of WGHM for three large river basins: Amazon, Mississippi, and Ob.

### 3.1.2 Naturally inundated areas

A monthly time series of inundated areas for 1993-2004, in percent of the total land area, was derived from a multisatellite method employing passive microwave land surface emissivities obtained from SSM/I and ISCCP observations, ERS scatterometer responses, and AVHRR visible and near-infrared reflectances. The satellite observations are mapped to an equal area grid with a cell size of 773 km² (0.25° x 0.25° resolution at the equator) (Prigent et al. 2007; Papa et al. 2010). Inundated areas detected by satellites include man-made inundations, in particular, those from irrigation of paddy rice. A preliminary exercise was performed by Prigent et al. (2001), subtracting the monthly mean rice field extents provided by Matthews et al. (1991) from the initial satellite-derived estimates. Here, to obtain time series of naturally inundated areas (NIA) that can serve as a basis for validating modeled floodplain inundation dynamics, the extent of irrigated rice as estimated in the MIRCA2000 data set by Portmann et al. (2010) was subtracted from the 1993-2004 time series of monthly satellite-derived inundated areas. MIRCA2000 is a global data set of monthly irrigated and rainfed crop areas, with a spatial resolution of 5 arc minute. The data set provides growing areas of 26 crop classes for each month of the year, covering all major food crops, cotton, crop categories (perennial, annual, and fodder grasses) as well as multicropping systems and maximizes consistency with census-based national and subnational statistics (Portmann et al. 2010). Irrigated rice areas are not available as time series, but as 12 monthly values that are representative of the situation around the year 2000, such that the same monthly rice area was subtracted for all of the years. The satellite derived inundated areas of Papa et al. (2010) were upscaled from their original resolution of an equal area grid with a cell size of 773 km² to the 0.5° grid cells of WGHM (by intersecting the two grids and calculating an area weighted sum for each 0.5° cell), while rice areas were upscaled from 5' grid cells (by aggregation). Please note that the basic statistical information used to derive the seasonality of growing areas in MIRCA2000 is mostly at the spatial scales of countries or regions. Coastal cells (cells not included in the data set of inundated areas (Papa et al. 2010) or not totally covered by the 0.5° cells of WGHM) have been excluded from the data set due to the fact that satellites observations cannot distinguish between oceans (or large permanent inland water bodies) and inundation areas. Figure 3.1a shows the mean annual growing area of irrigated rice, with a global value of 0.61 x 10⁶ km². Subtracting monthly irrigated rice areas from of satellite-derived inundated areas leads to a reduction of up to 7.8% in August (the month where the maximum global inundation occurs). Figure 3.1b shows the resulting annual mean of NIA. The overall spatial pattern appears to be plausible, with floodplain inundation of some large rivers like the Amazon and the Paraná being clearly recognizable. Temporal variability of wetlands varies strongly, with low coefficients of variation of the monthly values between 1993 and 2004 occurring in the Amazon basin (Figure 3.1c). Very high

21

values of the coefficient of variation generally correlate with low mean annual inundation values.
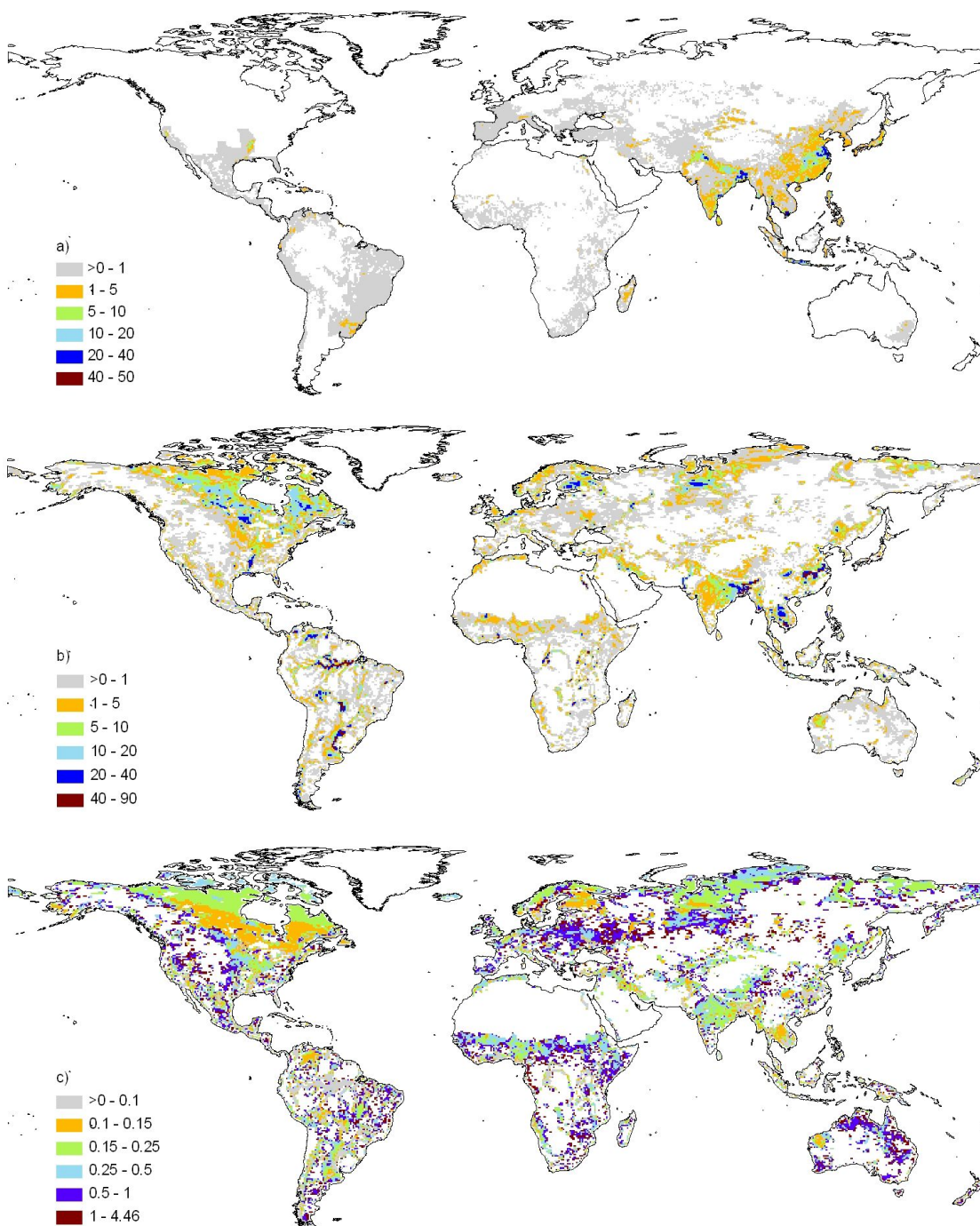


**Figure 3.1** Annual average growing area of irrigated rice, in percent of cell area **(a)**, annual average naturally inundated area (average over all months between January 1993 and December 2004) based on Papa et al. (2010) and Portmann et al. (2010), in percent of cell area **(b)**, and variability of naturally inundated areas as expressed by the coefficient of variation **(c).** Irrigated rice and surface water extent values are aggregated to 0.5° cells.

### 3.1.3 Comparison between satellite-based inundated areas and GLWD

The wetlands in GLWD encompass "freshwater marshes, floodplains", "swamp forest, flooded forest" and "intermittent wetland/lake" as well as rivers, bogs, coastal wetlands, saline wetlands, and three classes of wetland complexes (Lehner and Döll 2004). They cover approximately 9 million km$^2$ or 7% of the global land area excluding Antarctica and Greenland. The first three types are seasonally inundated, covering 4.4 million km$^2$ or 3.3% of the global land area. According to GLWD, lakes and reservoirs cover 2.7 million km$^2$ or 2% of the global land area (Lehner and Döll 2004). To compare GLWD to the satellite-derived NIA data set, GLWD was aggregated to 0.5° grid cells, and all coastal cells, large lakes not included in NIA, and wetland complexes of GLWD were removed. All wetland classes were aggregated and expressed as open water area in percent of cell area.
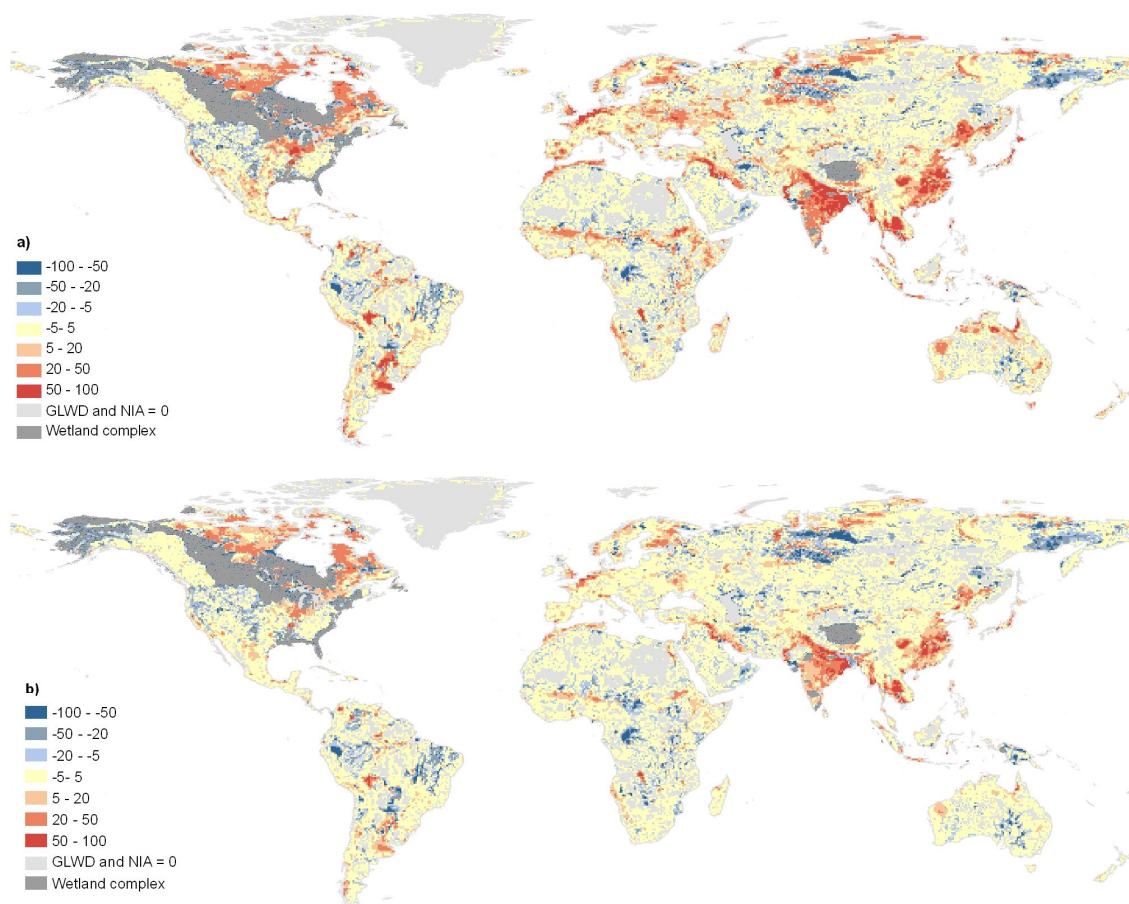


**Figure 3.2** Difference between the maximum value of naturally inundated areas (NIA) for each grid cell during 1993-2004 and the wetland extent of GLWD, in percent of cell area **(a)**, and the difference between the mean annual maximum of NIA and the wetland extent of GLWD, in percent of cell area **(b)**.

GLWD is expected to represent a certain maximum extent of inundation as it is based on mapping of wetlands. Inundation extent of NIA should always be below the open water area of GLWD except possibly in the case of extreme events. We compared

23

GLWD areas to the maximum value of NIA for each grid cell during 1993 and 2004 (3.2 a) and to the mean annual maximum of NIA (mean of the maximum grid cell value of NIA of each of the 12 years) (Figure 3.2 b). For the considered 48574 0.5° grid cells, GLWD includes 6.2 million km$^2$ of open water, as compared to 10.1 million km$^2$ for the maximum grid-specific NIA and 6.1 million km$^2$ for the mean annual maximum of NIA. For 62% of the grid cells, GLWD and maximum NIA differ by less than 5% (in units of percent of cell area), while GLWD areas are smaller than NIA for 26% of the grid cells (red areas in Figure 3.2a). For the remaining 12%, maximum NIA is smaller than GLWD areas (blue areas in Figure 3.2a). When GLWD is compared to the mean annual maximum of NIA, in which extreme outliers are excluded and typical seasonal maxima are represented, the area with good agreement increases to 70%, while the area where GLWD is smaller than NIA decreases to 16% (Figure 3.2b).

The NIA values may be considerably smaller than GLWD if the maximum inundation extent during the time span in which the map representation of the wetland had been done was not reached during 1993-2004. This is likely the case in central Australia, where large salt lakes are included in GLWD that are flooded only once in a few decades. But there are also other reasons. For example, NIA does not include the extensive wetlands in the Congo basin, in particular, the 60,000 km$^2$ large RAMSAR Grands Affluents wetland at the middle reaches of the Congo (www.ramsar.org). This may be due to the presence of highly dense vegetation in the region which limits the ability of the multi-satellite technique to clearly capture the inundations.

Where NIA is larger than GLWD, this may be caused either by the omission of wetland areas in GLWD or by an erroneous identification of inundation by remote sensing. Satellite observation may overestimate the extent of actual open water areas because very wet soils may be wrongly identified as inundated. This is likely the case in Northwestern Europe (Netherlands, Belgium, Northern Germany, England and Norway). In South and Southeast Asia, the problem of wet soils may contribute to the overestimation but it appears equally likely that GLWD is missing some wetlands there. For four selected grid cells in these problematic areas in Northwestern Europe and South Asia, GLWD open water extent (a constant) was compared to the satellite-derived time series of naturally inundated areas (Figure 3.3). For the two cells over Europe, the satellite values appear to be implausibly high. Even though there are a considerable amount of lakes in the cell close to the Baltic (Figure 3.3a), the open water surface increases much less in spring as the satellite data, and it appears to be likely that the satellite algorithm misinterprets wet spring soils (after melting of snow) as inundated. The cell in Northwestern Germany (Figure 3.3 b) has an average of the satellite-derived inundated area that exceeds the size of Lake Constance or Lake Balaton, such that these large areas may also represent wet soils. To understand the comparison for the two South Asian cells, please note that in GLWD, approximately the areas of Bangladesh is indicated as one large floodplain. The cell shown in Figure 3.3 c is located inside this GLWD floodplain area, the cell of Figure 3.3 d just outside. According to the satellite data, the latter is less ex-

tensively inundated during the monsoon season than the former, but it appears plausible that significant inundation during the monsoon season occurs also outside the floodplain area indicated in GWLD.
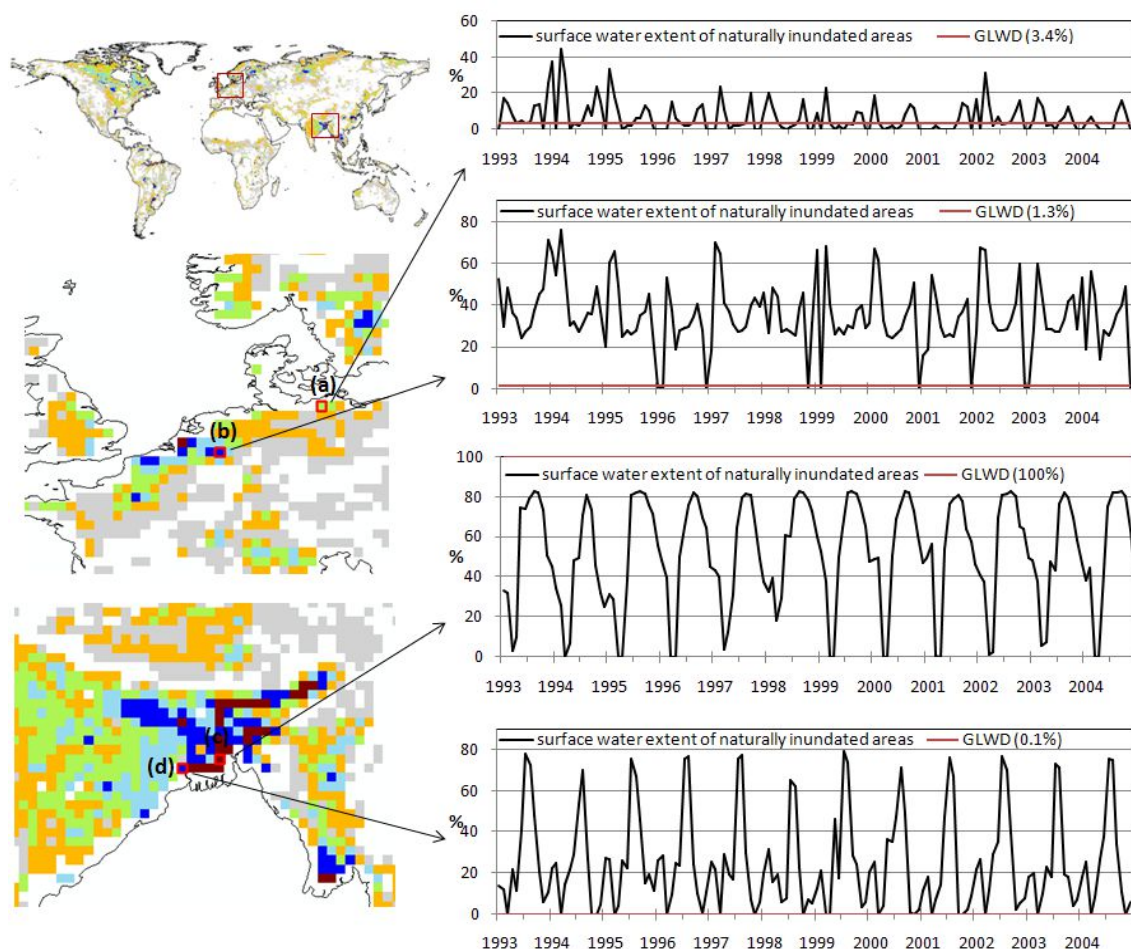


**Figure 3.3**  Comparison of inundation extent (in percent of 0.5° grid cell) of the time series of satellite-derived naturally inundated areas (1993-2004) and the wetland extent of GLWD (a constant) for four selected grid cells in Northwestern Europe and South Asia (right column). The left-hand column shows the location of the selected cells and the annual average of NIA (for legend see Figure 3.1 b).

### 3.1.4   Relation between inundation area and river discharge

Flow dynamics in floodplains are expected to depend on river discharge. In order to develop an algorithm that simulates the flow of water between the channel and the floodplain, it is useful to first analyze the relation between river discharge and inundation in the same grid cell as well as on a basin wide scale. We compared the extent of naturally inundated areas to 1) observed river discharge obtained from the Global Run-off Data Centre GRDC (grdc.bafg.de) at three gauging stations in the Amazon and Ob river basins (Figure 3.4) and to 2) modeled river discharge of WGHM for three large river basins (Figure 3.5 and 3.7).

Prigent et al. (2007) showed for the Amazon that their inundation estimates fit well to higher resolution SAR estimates, even though the number of pixels with low inundated area fraction was underestimated, and the number of pixels with very high fractions was overestimated. As expected from several prior investigations in different areas (Papa et al. 2006, 2007, 2008b and 2010, Prigent et al. 2007, Azarderakhsh et al. 2011), the temporal variation of natural inundation exhibits a close correlation with in situ, but as well with modeled river discharge variations. For the mainstream Amazon at Obidos, there is a high correlation of river discharge and inundated area in the grid cell. In the driest months, at least 20% of the cell area remains inundated. For a much smaller tributary, the Rio Jari at São Francisco, flooding only occurs, typically during one month of the year, which is approximately the month with the highest discharge (time lag 0-1 month) (Figure 3.4). On the basin-scale, natural inundation extent correlates well with modeled river discharge from WGHM (R = 0.86). The variability is relatively low in both data sets with the standard deviation being less than 30% of the mean values (Table 3.2). The results show strong seasonal cycles with highest values from March to May and lowest values from October to November as illustrated in Figure 3.5 and Figure 3.5.
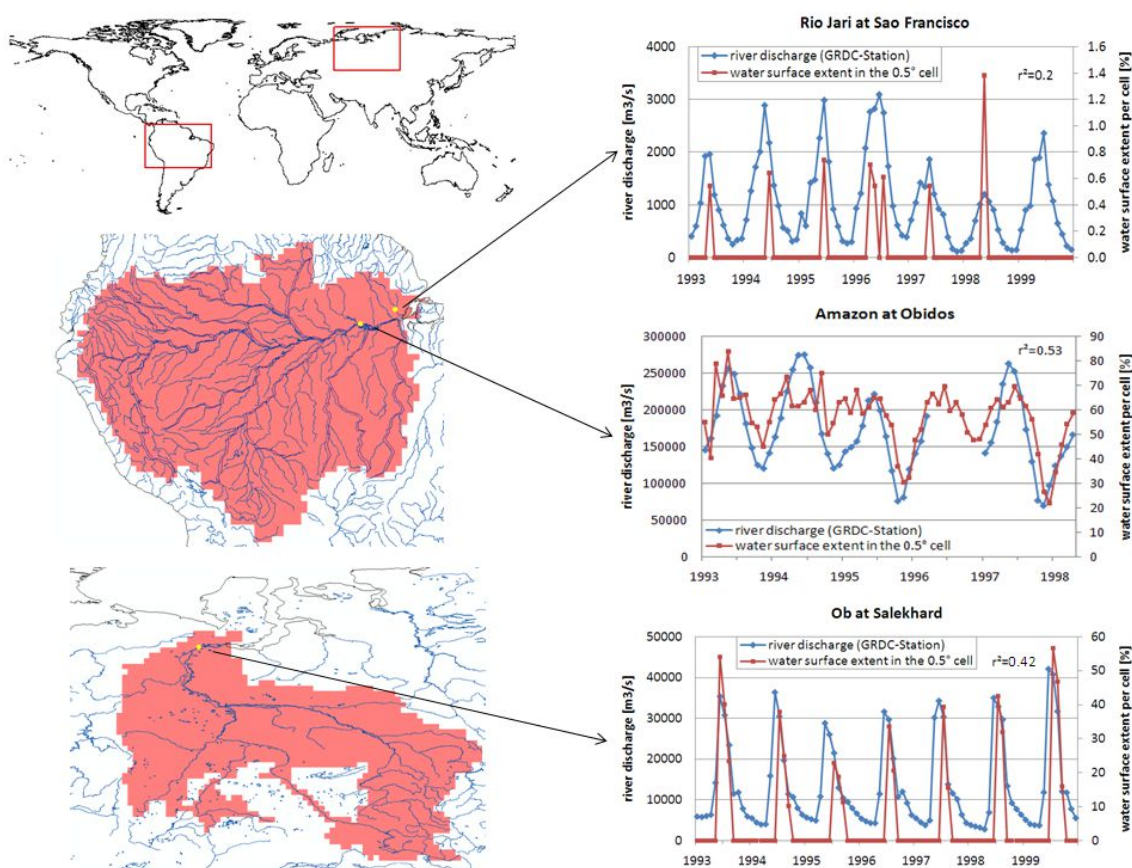


**Figure 3.4** Comparison of time series of observed river discharge (GRDC) at three gauging stations in the Amazon and Ob river basins, and the extent of naturally inundated areas in the same 0.5° grid cell.

The station Salekhard at the Ob River is located in the permafrost region and is dominated by snow. In the case of snow, satellite estimates cannot be obtained. Open surface

water is visible only from July to September (Figure 3.4), when also meltwater discharges are high and snowmelt accumulates at the surface due to the low relief. Here, a high correlation between river discharge and open water extent can be observed but the largely inundated areas may be primarily a function of temperature than of river discharge. Similar seasonal cycles can be observed for the whole river basin (Figure 3.5). Flooding occurs only in the summer month from May to September (Figure 3.6) with a maximum in June, which coincides with the maximum of modeled discharge. In the southern part of the basin, the maximum inundation extent happens two months earlier than at Salekhard station in the northern part of the basin (Figure 3.7). Papa et al. (2008b) had already shown the close correlation of snow melt with inundation extent in arctic river basins. Here, this is also confirmed by the large difference in variability of the datasets. Whereas the standard deviation of modeled river discharge is only 40% of the mean discharge, the variability of inundation extent rises up to 130% of the mean monthly inundation extent (Table 3.2).

The time series of natural inundation extent and modeled river discharge also agree well for the Mississippi river basin, although the correlation coefficient (R = 0.77) is lower than in the Amazon and Ob river basins. River discharge slightly decreases from 1993 to 2000 and increases from 2001 to 2004. This development cannot be observed from the values of inundation extent (Figure 3.5). The variability of inundation extent is about 20% higher than the variability of modeled river discharge (Table 3.2). Looking at the monthly averages and differences in the monthly cycle (Figure 3.5 and 3.6), river discharge peaks in April, one month earlier than inundation extent.

Maximum inundation shows a time lag of 0–2 months with respect to river discharge. On a basin-scale the maximum lag correlation for the two time series is zero months. Similar correlations between the temporal dynamics of surface water extent and river discharge have also been identified in previous studies cited above.
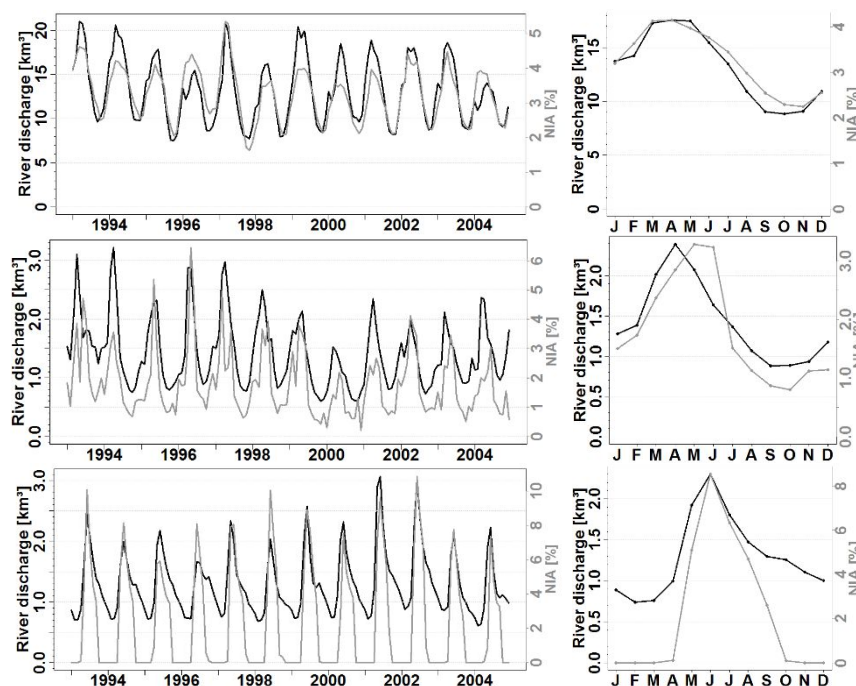
**Figure 3.5** Comparison of time series (1993-2004) and seasonal cycles (monthly averages 1993-2004) between modeled river discharge and the extent of naturally inundated areas for the three river basins: Amazon, Mississippi, and Ob (from top to bottom).
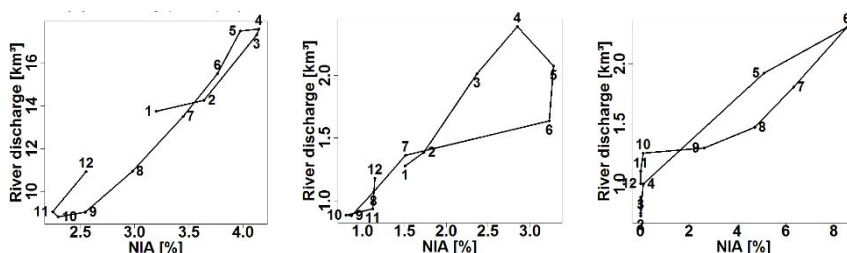


**Figure 3.6** The mean monthly cycle of discharge responses to inundation extent for the three river basins: Amazon, Mississippi, and Ob (from left to right). The numbers in the figures represent the months of the year.

**Table 3.2** Comparison of monthly values of NIA with modeled river discharge from 1993 to 2004 for different river basins and on a global-scale. The table contains values of the Coefficient of Correlation (R), the Coefficient of Determination (r²), the maximum correlation when lag times are considered (Rmax), the time lag at maximum correlation between inundation extent and river discharge in month (TimeLag), the mean (Mean) and standard deviation (sd) of NIA and modelled river discharge in percent of grid cell area and km³ respectively, and the standard deviation in percent to the mean (Var [%]).

| River | | | | Time | NIA | | | River Discharge | | |
| Basin | R | r² | Rmax | Lag | Mean | sd | Var [%] | Mean | sd | Var [%] |
|---|---|---|---|---|---|---|---|---|---|---|
| Ganges | 0.94 | 0.88 | 0.94 | 0 | 8.09 | 8.11 | 100 | 3.27 | 2.84 | 87 |
| Mekong | 0.91 | 0.82 | 0.91 | 0 | 6.19 | 5.03 | 81 | 3.28 | 2.66 | 81 |
| Ob | 0.87 | 0.75 | 0.87 | 0 | 2.29 | 3.09 | 135 | 1.30 | 0.52 | 40 |
| Amazon | 0.86 | 0.75 | 0.86 | 0 | 3.24 | 0.77 | 24 | 13.18 | 3.61 | 27 |
| Parana | 0.86 | 0.73 | 0.86 | 0 | 4.67 | 1.53 | 33 | 2.63 | 0.74 | 28 |
| Nil | 0.57 | 0.32 | 0.83 | -1 | 1.56 | 0.57 | 36 | 1.29 | 0.80 | 61 |
| Mississippi | 0.77 | 0.59 | 0.77 | 0 | 1.80 | 1.12 | 63 | 1.42 | 0.58 | 41 |
| Euphrates | 0.59 | 0.34 | 0.59 | 0 | 2.86 | 1.91 | 67 | 0.43 | 0.28 | 65 |
| Danube | 0.32 | 0.10 | 0.32 | 0 | 0.33 | 0.33 | 101 | 1.78 | 0.77 | 43 |
| Global | 0.80 | 0.64 | 0.93 | 1 | 1.41 | 0.90 | 64 | 1.08 | 0.21 | 20 |

Figure 3.7 shows the geographical structures of the three river basins for natural inundation extent (a) and river discharge (b), in which the first map always displays the maximum values, the second map the variability, and the third map the month during which the maximum value occurred.

Spatial patterns in the Amazon River basin of inundation extent and river discharge, for both maximum values and variabilities, are very similar (Figure 3.7). For the most part, high values occur along the main stem and the big tributaries. The inundation in the southern part of the river basin, at the Mamore river, does not coincide with high river discharge values. The month of the maximum of both datasets depends mainly on precipitation (Papa et al. 2010). South of the Equator, maximum values occur in the months of the northern hemisphere winter, whereas the northern part of the basin is characterized by high values in months of northern hemisphere summer.

The Mississippi River basin is characterized by a humid eastern part and a semiarid western part with almost no inundation and very low river discharge. Inundation extent and variability are highest along the lower and middle Mississippi, with a large inundation area north of the inflow of the Ohio River. Maximum variation in river discharge is along the main stem of Mississippi and along large tributaries. Spatial patterns of the month of maximum coincide very well between inundation extent and modeled river discharge. In most areas, river discharge peaks about one month earlier than inundation extent. Maximum values occur from late summer to December in the area of the Arkansas River draining the Rocky Mountains, to January/ February in the southern part of the basin and until May/ June in the northern part of the basin.

Inundation extent and river discharge in the Ob River basin are high along the main rivers of Ob and Irtysh. Unlike river discharge, there is an area of large inundation with high variability located around the inflow of the Irtysh into the Ob River. Because of latitude depending snow melting, we found equally to Papa et al. (2008b) the propagation from south to north regarding the month during which maximum inundation occurs. General spatial patterns of inundation extent and river discharge agree well, with maximum values from April to May in the southern part of the basin, and from May to June in the northern part of the basin. Even though, the river discharge for some grid cells in the center part of the basin occurs in the winter month, which cannot be explained.
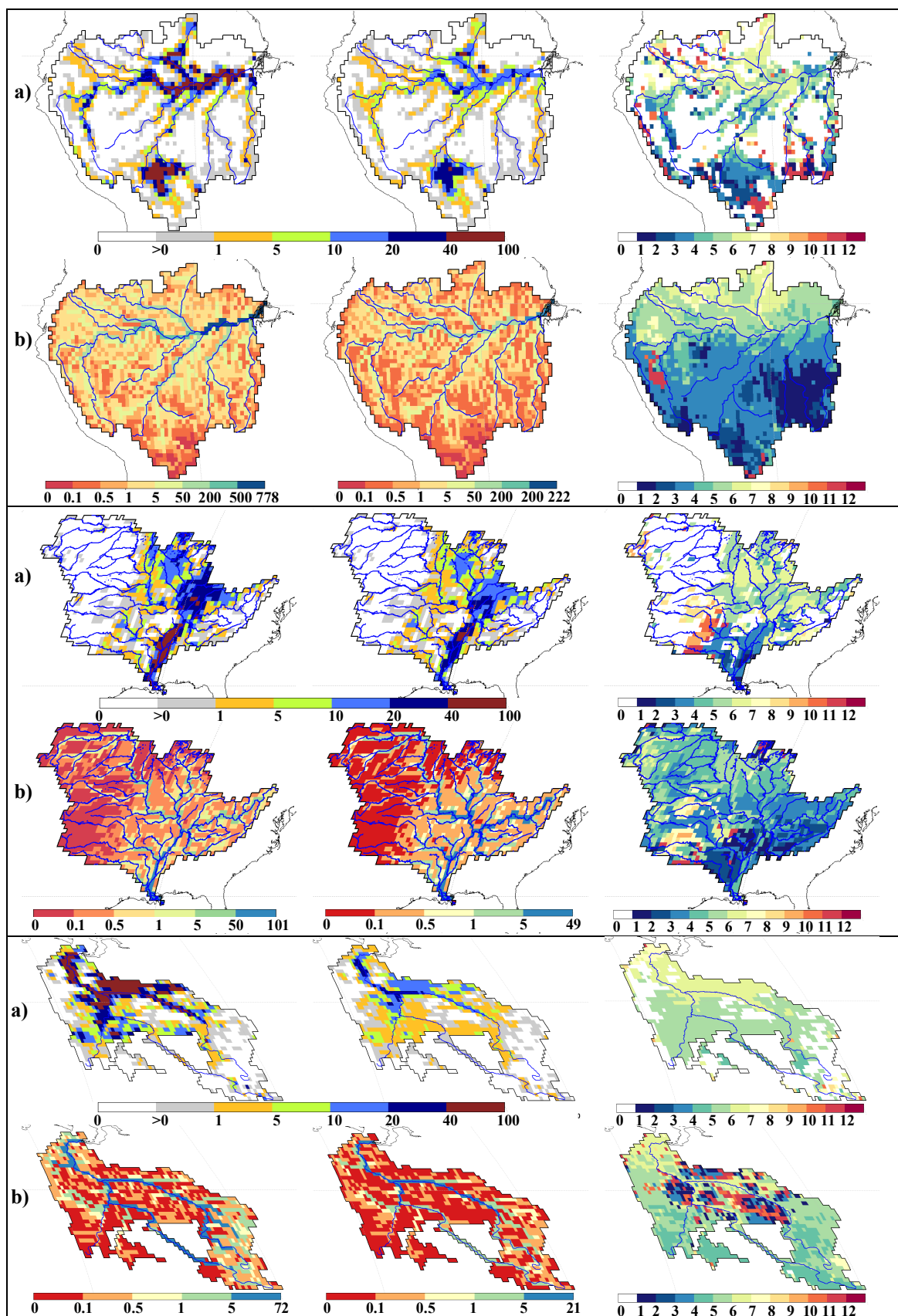
**Figure 3.7** Comparison between the extent of naturally inundated areas (a) and modelled river discharge (b) for the three river basins: Amazon, Mississippi and Ob. From left to right: mean annual maximum [%, km³], mean monthly variation [%, km³] and average month of maximum for each year [month], in the time period 1993-2004.

### 3.1.5 Conclusions

In order to support the improved modeling of floodplain inundation in the global hydrological model WGHM, we combined a multisatellite data set of inundated areas (Papa et al. 2010) for the time period 1993-2004 with data on monthly irrigated rice areas around the year 2000 (Portmann et al. 2010). The resulting global-scale time series of monthly naturally inundated areas (NIA) (spatial resolution 0.5°) was compared to the static wetland extent in GLWD (used as input to WGHM) to better understand the validity and applicability of both data sets. We conclude that NIA can be used as an independent validation data set for dynamic floodplain models, but future work is required to identify areas where NIA overestimates inundation extent due to very wet soils, and where the satellite retrieval algorithm may not be able to identify inundated areas (e.g. in densely vegetated areas). GLWD mostly represents the maximum of surface water extent except in cases of extreme flooding, but in some regions (e.g. South Asia) is quite possible that wetland areas need to be added. To determine how flooding can be modeled as a function of computed river discharge, the relation between the dynamics of naturally inundation extension and both observed and modeled river discharge was analyzed. In summary, a correlation between inundated area and river discharges was found, with certain phase shifts of the maxima. Very good agreement was determined particularly in the seasonal and interannual variations of the data sets. The comparison of spatial patterns of inundation extent and modeled river discharge in the three river basins show similar distributions of monthly variations, maximum values, and the month when the maximum occurs. However, in some regions inundation spreads over large areas, whereas changes in river discharge are principally limited to the main streams.

This study allows for a better understanding of the dynamics of naturally inundated areas, which contributes to the development of an improved model algorithm for dynamic floodplain inundation in WGHM. The results of the comparison between natural inundation extent, in situ river discharge, and modeled river discharge allow a cross-validation of the data sets, and encourage the use of the satellite-derived time series of naturally inundated areas for model validation.

## 3.2 Analysis of surface water storage compartments in WGHM: A comparison to GRACE for the Amazon

### 3.2.1 Background

Compared to seasonal total water storage (TWS) variations as derived from GRACE (see Section 4.7.1 for details on GRACE data), TWS variations from WGHM are strongly underestimated for the Amazon basin (Figure 3.8). The underestimation is

comparable to that of the GLDAS-NOAH model (by a factor of 1.8), which does not consider any groundwater or surface water storage at all (Landerer and Swenson 2012). As the Amazon River basin is characterized by its massive floodplain system, this underestimation may be due to the inappropriate modeling of floodplain dynamics, because globally, TWS variations of WGHM are higher as compared to GPS analyses (Fritsche et al. 2012). To obtain improved estimates of inundation extent and water storage variations in large floodplains, a dynamic floodplain model will be developed and included into WGHM. As a basis for floodplain modeling, the current model output of surface water storages in WGHM are analyzed in this study (focusing on the Amazon River basin).
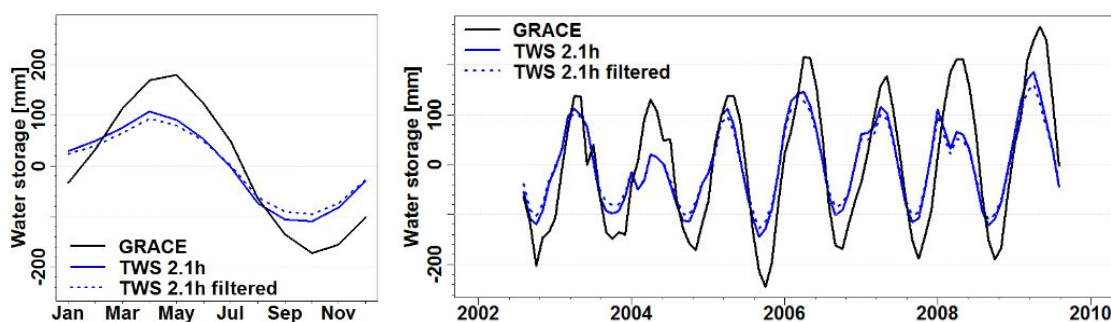


**Figure 3.8**  Total water storage of WGHM (version 2.1h) and GRACE in the Amazon River basin in the time period 08/2002-08/2009 (left: mean of time series).

"GRACE solutions were smoothed using the non-isotropic filter DDK3 (Kusche et al. 2009). To allow a consistent comparison to WGHM results, the filtered results were interpolated to the WGHM 0.5° grid such that basin averages of TWS variations could be computed as averages over the respective WGHM grid cells. In order to compare TWS variations modeled with WGHM to GRACE-derived TWS variations, WGHM model output was smoothed using the same procedure" (Döll et al. 2012, p. 5). The filtering leads to reduced amplitudes of TWS variations of WGHM (Figure 3.8 and 3.9).

In this study, two model versions of WGHM are used. Version 2.1g is used to analyze water storage variations in the individual surface water storage compartments of WGHM. This analysis was done at an earlier stage of the PhD work, when version 2.1h was still under development. The improved model version 2.1h was then used to compare model results to GRACE. In version 2.1g the demand on water use is satisfied only from surface water, whereas in version 2.1h withdrawals are taken also from groundwater. As there is very little water use in the Amazon basin, the difference between both model versions is small, and the differences between 2.1g and 2.1h shown in Figure 3.9 (solid black and blue lines) are due to the different time periods evaluated (2.1g: 1961-90, 2.1h: 8/2002-8/2009).

### 3.2.2 Analysis and Results

In this section, I analyze the water storage variations in the individual surface water storage compartments of WGHM for the Amazon River basin.

The main research questions are:

1) Do wetland storage and TWS variations increase with increasing wetland storage capacity?
2) What are the differences in spatial distribution of seasonal water storage variations of WGHM compared to GRACE?

Please note that in WGHM, $S_{max}$ serves to normalize outflow from wetlands, such that with higher $S_{max}$, outflow $Q_{out}$ is reduced for the same actual water storage $S$ in the wetland, with

$$Q_{out} = k * S * (\frac{S}{S_{max}})^{2.5} \qquad \text{3.1}$$

where $k$ is the outflow coefficient and $S$ can exceed $S_{max}$.

First, water storage was calculated with the standard version of WaterGAP 2.1g, which assumes a maximum wetland storage capacity $S_{max}$ of 2 m. The total water storage variation in WGHM 2.1g is mainly attributed to river channel storage (Figure 3.11). Wetlands and lakes hardly show seasonal water storage variations. It seems that wetlands and lakes are always at full capacity and this might be the reason for missing seasonal variations. In addition to the surface water storages, WGHM considers canopy, snow, soil, and groundwater storage for the contribution to TWS; however, these four other storages should be independent of $S_{max}$.

In a second step, the maximum wetland storage capacity in the model was increased by a factor of 2.5 and 10.

The absolute values of water storage in surface water compartments and of TWS, and the average normalized long-term mean (1961-1990) values – calculated with different maximum wetland storage capacities (2 m, 5 m, 20 m) in WaterGAP and averaged over the Amazon River basin – are shown in Figure 3.10 and 3.11. The average values for wetland and total water storage increase with higher wetland $S_{max}$ (Figure 3.10). When $S_{max}$ is increased by a factor of 10, TWS increases on average by a factor of 2.7 (wetland storage by a factor of 8.4). Wetland and total water storage variations increase; wetland storage variations on average by a factor of 4.2, and total water storage variations by a factor of 1.2 (Figure 3.11). The higher maximum wetland depth has almost no effect on lake and reservoir water storage and their variations. River water storage variation

slightly decreases with higher wetland storage capacities (Figure 3.11). With the creation of more wetland storage capacity, less water is stored in the river channel. This strengthens the assumption that in the standard version of WGHM, wetlands are always full of its capacity. Furthermore, there is a noticeable shift in time of maximum and minimum water storage. By increasing the maximum wetland storage capacity by factor 10, maximum and minimum water storages occur about one month later than in the standard version of WGHM (Figure 3.11), and the phase of TWS from WGHM and GRACE become more similar (Figure 3.9). Then, both GRACE and WGHM show the lowest TWS in October. However, since the model output of WaterGAP 2.1g is not filtered, the results should be interpreted with caution when compared to GRACE.
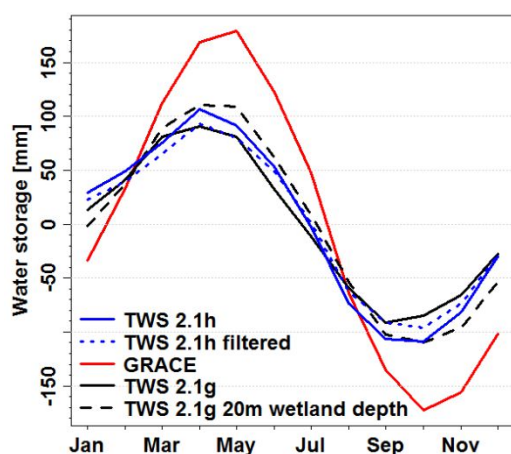


**Figure 3.9** TWS variation of WGHM (different model versions) and GRACE in the time period 2002-2009 in the Amazon River basin.

This study shows that with higher wetland storage capacity, the seasonal variation of floodplain/wetland storage and of TWS increases (Figure 3.10 – Figure 3.12). Due to the increased water retention in the wetlands, there is a time shift of maximum and minimum TWS, such that WGHM fits better to GRACE. In addition, interannual variation of TWS is increased (Figure 3.12).
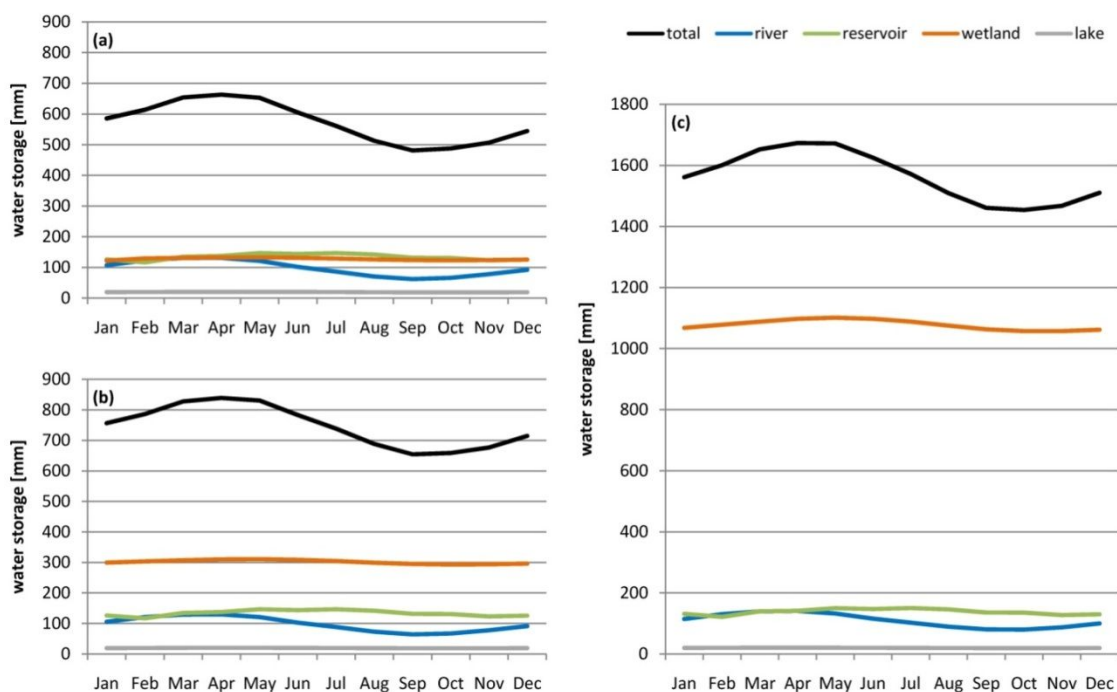
**Figure 3.10** Basin-averaged time series of individual surface water storage compartments and of TWS. Calculated with WGHM 2.1g with 2 m (a), 5 m (b) and 20 m (c) wetland storage capacity. Long-term average 1961-1990 for the Amazon basin.
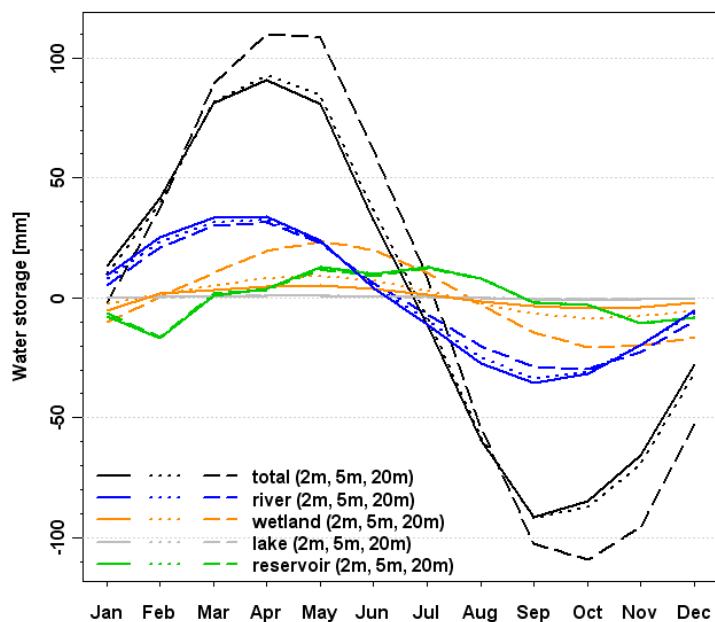


**Figure 3.11** Average normalized long-term mean (1961-1990) monthly values of surface water storages and of TWS, for the Amazon Basin with different maximum wetland storage capacities (2 m, 5 m, 20 m).
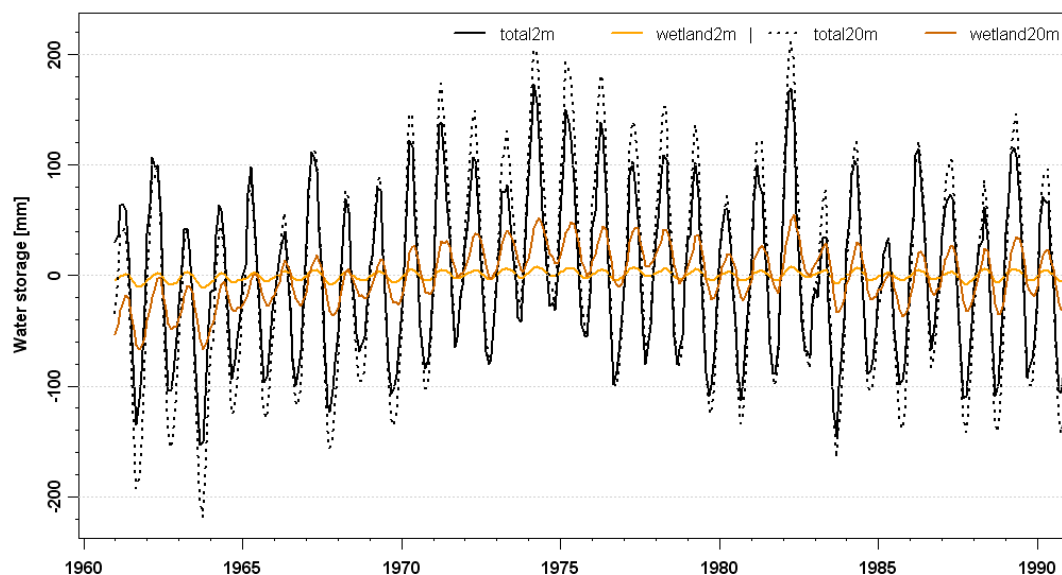
**Figure 3.12** Average normalized monthly wetland and total water storages for the Amazon Basin with different maximum wetland storage capacities (2 m, 20 m), for 1961-1990.

To assess the spatial distribution of TWS variation, TWS variation was quantified in two ways. Seasonal TWS variation was determined from mean monthly TWS values, as the difference between TWS in the calendar month with the highest TWS and TWS in the calendar month with the lowest TWS. In addition, the mean interannual variability of monthly TWS was determined by computing, from the time series, the difference between the highest and the lowest TWS value of each calendar month, and then averaging over the 12 calendar months.

The spatial distribution of total water storage variation of WGHM (version 2.1h filtered) compared to GRACE is shown in Figure 3.13 (seasonal TWS variation) and Figure 3.14 (mean interannual variability of monthly TWS). Interannual variability is approximately half of the seasonal variability. In both cases, WGHM and GRACE storage variations are highest along the Amazon mainstream. Generally, water storage variations are strongly underestimated by WGHM compared to GRACE (already shown in Figure 3.8), and there is a spatial shift of maximum total water storage variation in WGHM. Whereas the maximum seasonal total water storage variation in GRACE is located in the central part of the Amazon River basin, where the main tributaries flow into the mainstream, the maximum in WGHM is located in the most downstream part of Amazon (Figure 3.13). The GRACE maximum occurs where there is a high density of seasonal wetlands/floodplains, while the WGHM maximum occurs where, due to flow accumulation, the highest river discharges and thus the highest river storages variations occur. According to remote-sensing data on inundation extent (Papa et al. 2010), a par-

36

ticularly high density on seasonal floodplains can be observed along the main river near the water mouths of the tributaries Rio Purus, Rio Negro and Rio Madeira, and in the Llanos de Mojos, a flat area in the southern part of the Amazon river basin (rivers Beni and Mamore). In the static GLWD, seasonal flooded areas are located mainly along the main river and their tributaries, as well as in a big area in the western part of the Amazon basin (Rio Marañon). The maximum of the mean interannual variability of monthly TWS of WGHM is also shifted downstream as compared to GRACE, but only a little bit, much less than the maximum of seasonal TWS variation (Figure 3.14). However, in the upstream areas of the basin, seasonal TWS variations of WGHM fit rather well to those of GRACE, while the interannual variability is strongly underestimated everywhere.
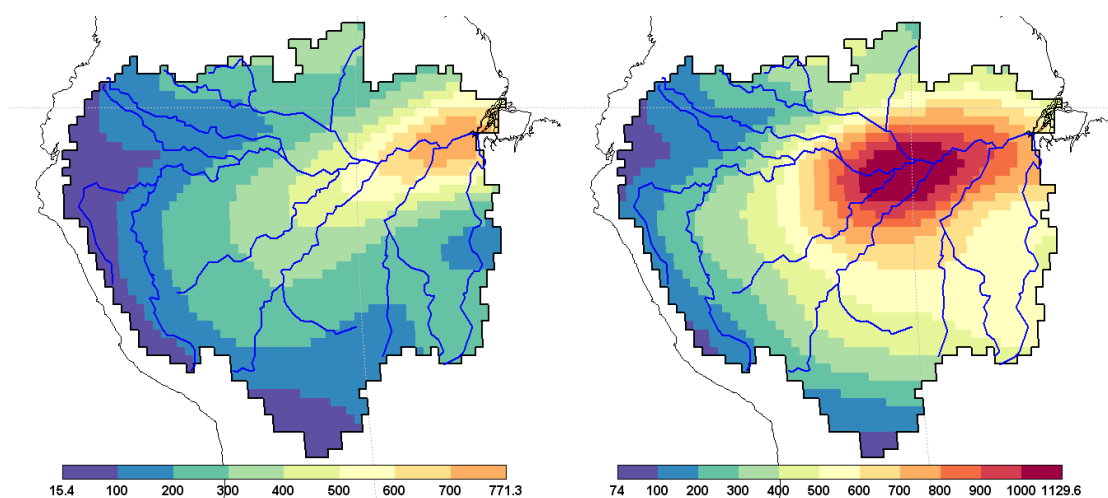


**Figure 3.13** Seasonal TWS variation [mm] in the Amazon River basin (2002-2009) of WGHM (left) and GRACE (right). WGHM version: 2.1h filtered.
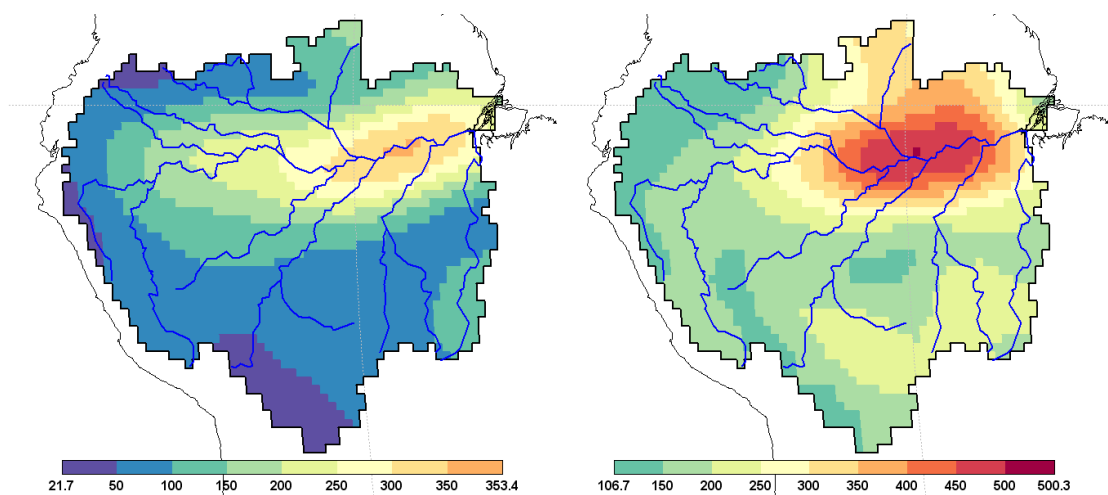


**Figure 3.14** Mean interannual variability of monthly TWS [mm] in the Amazon River basin (2002-2009) of WGHM (left) and GRACE (right). WGHM version: 2.1h filtered.

37

### 3.2.3 Outlook

In the current version of WGHM, the distribution and extent of surface water compartments are based on a static Global Lakes and Wetland Database (GLWD) (Lehner and Döll 2004). It is quite possible that in some areas GLWD does not represent the maximum of surface water extent as it should (Adam et al. 2010). The water (inflow from upstream grid cells and runoff produced inside the grid cell) in WGHM is always transported through all storage compartments. Therefore, storage variations in WGHM mainly depend on river discharge and flow accumulation. The floodplain/wetland depth (maximum storage capacity) is set to 2 m in the standard version of WGHM.

With the new approach of modeling dynamic floodplain inundation, water is stored on floodplains only if river discharge exceeds a certain threshold, the bankfull flow. The floodplain extent and the maximum storage capacity of floodplains/wetlands are not static but variable, based on water storage above bankfull flow and the surface elevation of the floodplain. Furthermore, the flow velocity on floodplains is smaller than in the river channel, as we assume a higher roughness coefficient on floodplains.

Floodplain wetlands are complex ecosystems and highly variable in flooding time, extent and duration of flooding. With the new approach to model dynamic floodplain inundation in WGHM, the spatial distribution, as well as the amplitude of seasonal water storage variations, is expected to be improved. By merging a digital elevation model (DEM) with the hydrological model, WGHM will be able, for the first time, to model flood inundation extent and water heights. As floodplains are inundated when the rivers overflow their banks, and the inundation extent is based on surface elevation, the location and spatial distribution of floodplains should be improved. This study shows, that with increasing wetland storage capacity in WGHM, wetland storage and TWS variations in the Amazon River basin increase. Since in the new approach, storage capacity of floodplain wetlands depends on their elevation profile, it is expected to obtain a better result of seasonal water storage variations, when compared to GRACE.

CHAPTER 4

## Methods - A new approach to simulate dynamic floodplain inundation on a global-scale

### 4.1 Introduction

In this chapter, I introduce the methods of simulating dynamic floodplain inundation within WaterGAP, with a focus on the changes in the water balance of rivers and floodplains. First of all, I present the overall equations for modeling the water balance for rivers and floodplains, and I also give an overview of the relevant parameters and variables; the most important are represented in a schematic figure (Section 4.2). Then, in the subsequent sections I explain how the variables used in the water balance equations are calculated and derived. These sections are composed of: the flood initiation with river-floodplain interaction (Section 4.3), the estimation of floodplain area and area of other surface water bodies (Section 4.4), the flow routing among grid cells (Section 4.5), and the calculation of flow velocities for rivers and floodplains (Section 4.6). Finally, in Section 4.7 I explain how the model validation data and the model efficiency criteria are applied.

### 4.2 Water balance equations for rivers and floodplains

The Global Hydrology Model of WaterGAP (WGHM) calculates daily water balances for the land areas and for the open water bodies of the individual grid cells. Within each grid cell, the runoff produced inside the cell and the inflow from the upstream cell(s) are transported through a series of storage compartments. The resulting cell outflow then becomes the inflow of the downstream cell (Figure 4.1).
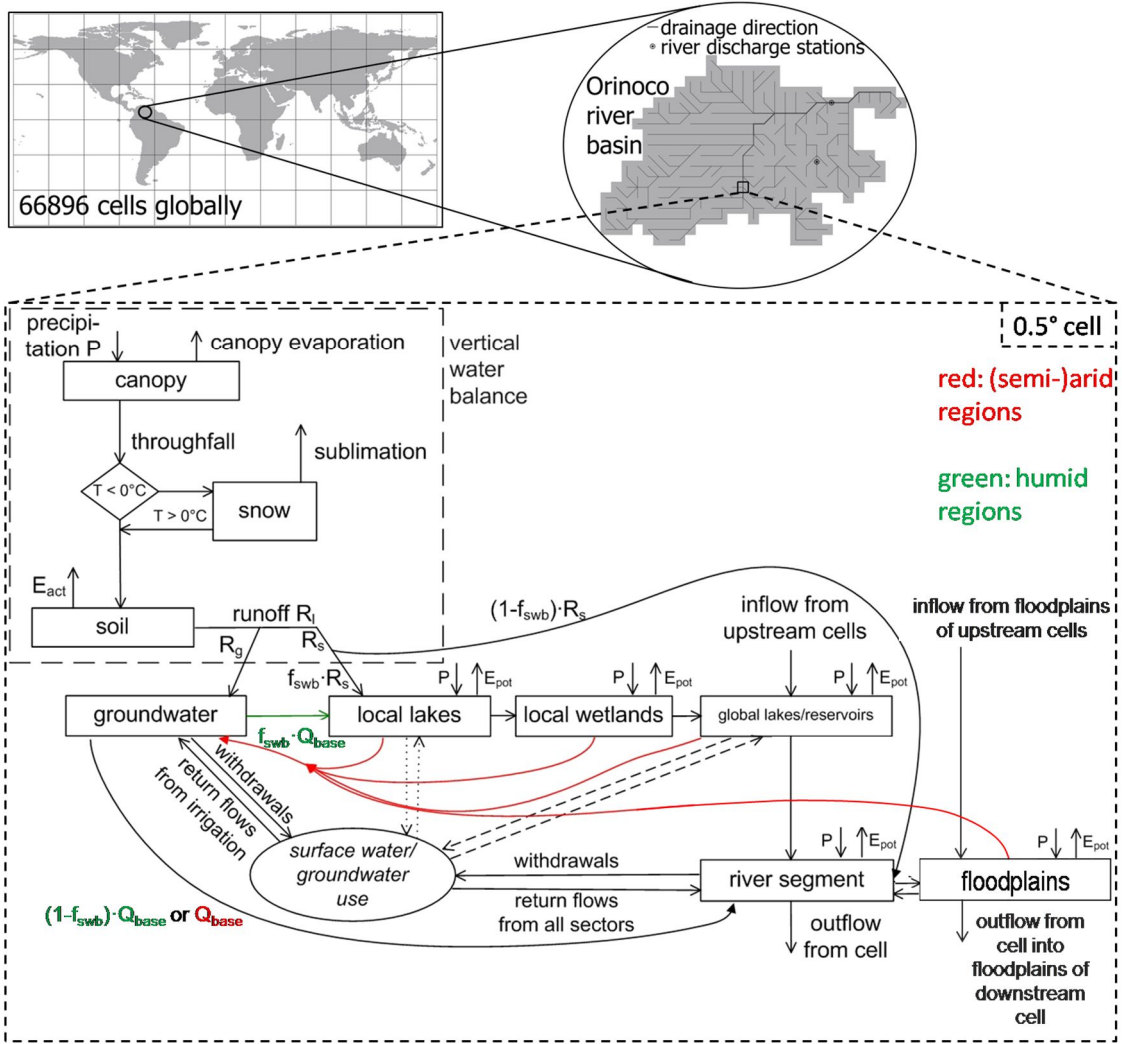
**Figure 4.1** Schematic representation of the vertical and lateral water balance as computed by the WaterGAP Global Hydrological Model (WGHM) (modified from Döll et al. 2012), including human water use. In the flow chart, boxes represent the water storage compartments and arrows the water fluxes (inflows, outflows); $E_{pot}$: potential evaporation, $E_a$: actual evaporation, $E_c$: evaporation from the canopy, $R_l$: runoff from land, $R_g$: groundwater recharge, $R_s$: surface runoff, $Q_{base}$: baseflow, $f_{swb}$: fraction surface water body.

The major vertical and lateral hydrological processes of WGHM are explained in detail in Section 2.2. In the scope of this PhD work, I implemented a new storage compartment into the WaterGAP code: the floodplain storage. Thus, the former model processes (shown in Figure 2.1) change by replacing the global wetland storage based on GLWD with the floodplain storage compartment (Figure 4.1).

The water balance equations for rivers (*r*) and floodplains (*f*) are formulated as ordinary differential equations:

$$\frac{dS_{r,f}}{dt} = F_{r,f} - K_{r,f} * S_{r,f} \qquad\qquad 4.2$$

The change of water volume in the storage compartment ($S$) [$km^3$] for each time step ($t$) is calculated as the net inflow to the compartment ($F$) [$km^3/d$] reduced by the water storage times an outflow coefficient ($K$) [$1/day$].

The analytical solution of Equation 4.2 provides the storage at the end of each time step $t$ as a function of the storage at the end of the last time step ($t$-$1$):

$$S_{r,f}(t) = S_{r,f}(t-1) * e^{-K_{r,f}*t} + \frac{1}{K_{r,f}} * F_{r,f} * (1 - e^{-K_{r,f}*t}) \qquad 4.3$$

As the time step is 1 day, each analytical solution has the form:

$$S_{r,f}(t) = S_{r,f}(t-1) * e^{-K_{r,f}} + \frac{1}{K_{r,f}} * F_{r,f} * (1 - e^{-K_{r,f}}) \qquad 4.4$$

The outflow coefficient ($K$) is calculated as the ratio between the flow velocity of the river or floodplain ($v$) [$km/d$] and the river channel length in the grid cell ($l$) [$km$]:

$$K_{r,f} = \frac{v_{r,f}}{l} \qquad 4.5$$

The calculation of flow velocity of rivers and floodplains is explained in detail in Section 4.5. In order to represent real river channel length ($l$), the direct distance between grid cells is multiplied by an individual meandering factor for each 0.5° grid cell, derived from HydroSHEDS 15 arc-sec river network (Verzano 2009).

The net inflow of the river compartment ($F_r$) and floodplain compartment ($F_f$) respectively is calculated as the sum of all prescribed inflows and outflows of the compartments:

$$F_r = Q_{ir} - Q_{rf} + (P - PET) * A_r - NA_s \qquad 4.6$$

$$F_f = Q_{if} + Q_{rf} + (P - PET) * A_f - R_{gf} * A_f \qquad 4.7$$

where $Q_i$ [$km^3/d$] is the inflow into the river/floodplain from upstream cell including runoff produced within the cell and the outflow of global lakes and reservoirs, $Q_{rf}$ [$km^3/d$] is the flow from the river channel into the floodplain (+) or vice versa (-) (see Equation 4.8, Section 4.3.2), $P$ and $PET$ is precipitation and potential evaporation on grid cells in km³ (for calculation/ data sources see Section 2.2.2), $NA_s$ [$km^3/d$] are the net water abstractions from the river (for calculation see Döll et al. 2012), $R_{gf}$ [$km/d$] represents groundwater recharge beneath floodplains[2]. Precipitation, potential evaporation, and groundwater recharge are calculated for river and floodplain area respectively. Because of that, these variables are multiplied by the area fraction of the water bodies. The way in which river area fraction ($A_r$) [$\%/100$] is calculated is explained in Section 4.4.2. The floodplain area fraction ($A_f$) [$\%/100$] is determined by applying the hypsographic approach (Section 4.4.1).

---

[2] Groundwater recharge is calculated only in semi-arid areas with 10 mm per day (Döll et al. 2014).

**Table 4.3** List of parameters and variables. The gray lines represent variables which are visualized in Figure 4.2.

| Symbol | Name | Unit |
|---|---|---|
| $A_f$ | Dynamic flooded area (fractional area of a grid cell inundated) | %/100 |
| $A_r$ | River area fraction per grid cell | %/100 |
| d | Distance between target and downstream grid cell | m |
| $D_b$ | River channel water depth at $Q_b$ | m |
| $D_f$ | Floodplain water depth | m |
| $D_r$ | River channel water depth | m |
| $H_f$ | Floodplain water height | m |
| $H_r$ | River water height | m |
| F | Sum of all prescribed inflows and outflows of the storage compartment | km³/d |
| K | Outflow coefficient | d |
| l | L*meandering factor | m, km |
| L | River channel length in the grid cell | m |
| $NA_s$ | Net water abstraction from surface water | km³/d |
| $n_r$, $n_f$ | Roughness coefficient for river and floodplain | - |
| p | Percentage of water flowing from river to floodplain or vice versa (if $Q_i > Q_b$) | % |
| $p_{min}$ | Minimum percentage of water flowing from river to floodplain or vice versa (if $Q_i > Q_b$) | % |
| P | Precipitation | mm |
| PET | Potential evaporation | mm |
| $Q_r$ | River discharge | km³/month, km³/d, m³s⁻¹ (gauging stations) |
| $Q_b$ | Bankfull flow | m³s⁻¹, km³/d |
| $Q_f$ | Floodplain discharge | m³s⁻¹, km³/d |
| $Q_i$ | Inflow from river from upstream cell including runoff produced within the cell | m³s⁻¹, km³/d |
| $Q_{if}$ | Inflow from floodplain from upstream cell including runoff produced within the cell | m³s⁻¹, km³/d |
| $Q_{ra}$ | Actual river channel flow (≥$Q_b$) (maximum river channel capacity at a given time) | m³s⁻¹, km³/d |
| $Q_{rf}$ | Flow from river channel to floodplain or vice versa | m³s⁻¹, km³/d |
| r | Area reduction factor for surface water bodies and river | - |
| $r_{Qb}$ | Bankfull flow reduction factor | - |
| R | Hydraulic radius for river and floodplain | m |
| $R_g$ | Groundwater recharge | mm/d, km/d |
| s | Water surface slope | m/m |
| $S_r$, $S_f$ | Water storage for river and floodplain | km³ (WGHM-output), m³ (in WGHM) |
| $S_b$ | Water storage at bankfull | m³ |
| $v_r$, $v_f$ | Flow velocity of river or floodplain | ms⁻¹ |

| Symbol | Name | Unit |
|---|---|---|
| W | River channel width | m |
| x | River discharge above or below actual river channel flow ($Q_i$-$Q_{ra}$) | m³/s |
| z | Land surface elevation | m |
| $z_{min}$ | Minimum land surface elevation per 0.5° grid cell (bank height, outflow level of the grid cell) | m |
| □ | 0.5° grid cell | |
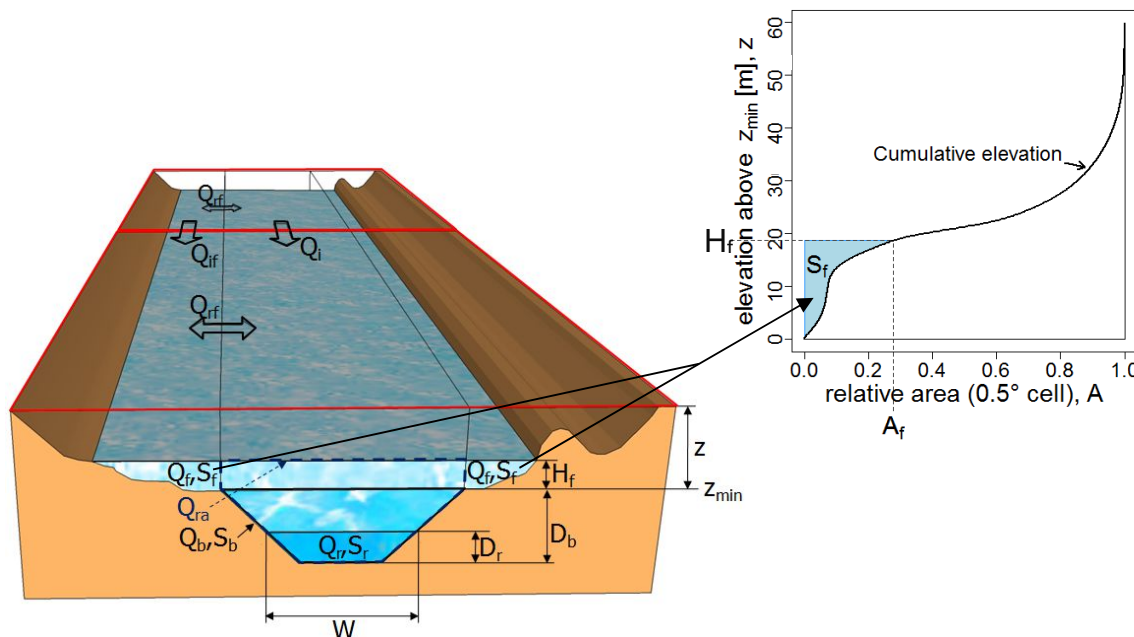


**Figure 4.2** Schematic figure of model parameters and variables, and hypsographic curve; for legend see gray lines in Table 4.3

## 4.3 Flood initiation and river - floodplain interaction

### 4.3.1 Flood initiation

Flood initiation is determined by bankfull flow, which is defined as the point at which the river channel is at full capacity and the flow just begins to enter the active floodplain (Leopold 1994). "In order to estimate bankfull flow on a global-scale, an approach needed to be found, which does not depend on in-situ measurements. A number of studies worldwide have proven a relation between a certain flood return period and the bankfull stage" (Verzano 2009, p. 98). Bankfull flow, as it is used as input for WaterGAP, is a time constant value estimated on a global-scale for each of the 0.5° grid cells of WaterGAP. It is based on a statistical approach on flood frequency analysis, the Partial Duration Series (PDS) approach, which was calculated and validated for Europe by Verzano (2009) and Schneider et al. (2011a). For Europe, modeled bankfull flows are consistent with observed bankfull flows at gauging stations, but overestimate flood peaks (Schneider et al. 2011a).

Until WaterGAP 2.2b, bankfull flow was only used to estimate river width and depth for the calculation of river flow velocity (Section 4.6) and it had been validated only for Europe (Verzano 2009; Schneider et al. 2011a). In order to implement dynamic flood-plain modeling in WaterGAP, it was necessary to analyze the bankfull flow and the number of months and the volume of water where this threshold for flood initiation is passed over on a global-scale.

In the current model version WaterGAP 2.2b, bankfull flow, when used as a threshold for flood initiation, seems to be too high. It is known from observations, that for instance in the middle and downstream Amazon or in the large Siberian river systems there are largely endured inundations every year (Papa et al. 2007, 2008b). Figure 4.3 shows the number of days per year from 1971 to 2009 where river inflow is above bankfull flow at Obidos (Amazon River basin) and Salekhard (Ob River basin). The mean annual duration of flooding is 46 and 7 days at Obidos and Salekhard respectively, which appears to be too short compared to observations (Papa et al. 2007; Junk 1997). In several years there is even no inundation modeled (Figure 4.3).
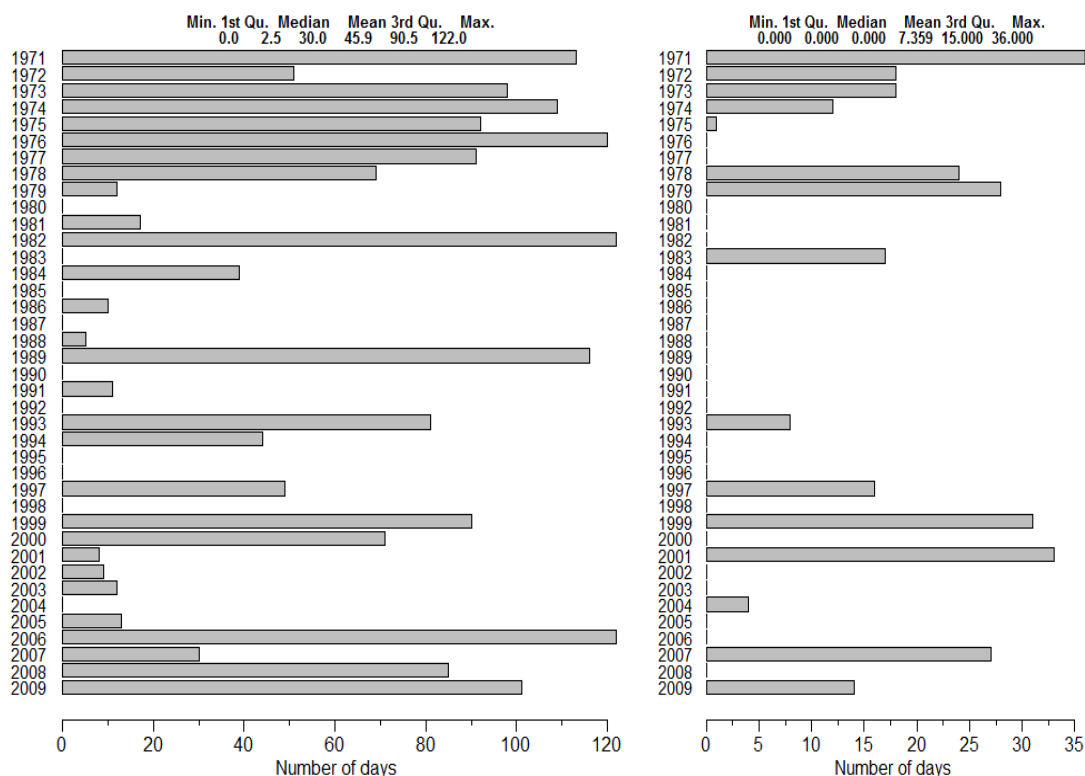


**Figure 4.3**   Number of days per year where river inflow is above bankfull flow at Obidos (left) and Salekhard (right).

The analysis of bankfull flow used as flood initiation value in WaterGAP 2.2 demonstrates that the duration of flooding and the return period in many regions is too short

(Figure 4.3). Therefore, for modeling dynamic floodplain inundation within WaterGAP, the bankfull flow from Schneider et al. (2011b) is multiplied by a reduction factor ($Q_b*r_{Qb}$). WaterGAP 2.2b_fpl was tested for the Amazon river basin by applying different bankfull flow reduction factors ($r_{qb} = 0.9, 0.8, ..., 0.5$). The best model fit regarding modeled river discharge and water surface extension, compared to observed river discharge at gauging stations and satellite derived observed surface water extension, was achieved with a bankfull flow reduced to 70%, $r_{qb} = 0.7$ (for sources of model validation data see Section 4.7).

For Europe, modeled bankfull flows are in agreement with the observed bankfull flow at gauging stations, but overestimate flood peaks (Schneider et al. 2011a). By implementing river-floodplain interactions in WaterGAP, the overestimation of flood peaks could be reduced, as floodplains act as temporal water storage and, thereby, reduce flood peaks and flow velocity (Schneider et al. 2011a). Note, that the reduced bankfull flow to 70% represents the flood initiation threshold. River discharge and river stage are still rising in the case of flooding, so that maximum river flow should still agree well with observed maximum stage discharge; just the flood peaks in WaterGAP are smoothed out (Section 4.3.2).

## 4.3.2 River - floodplain interaction

The water flows from the river into the active floodplain if inflow into the river component of a cell $Q_i$ exceeds the bankfull flow $Q_b$ (Figure 4.2). If flooding occurs, the water level height on the river equals that on the floodplain and is thus above bank height ($B$). River storage is above the storage at bankfull ($S_b$). River discharge during flood events, here called actual river channel flow $Q_{ra}$ ($Q_{ra} \geq Q_b$), which is, in the state of flooding, the maximum river channel flow at a given time. From the amount of water above river channel capacity $x$ ($x>0$) not all flows into the floodplain; some of the water stays on the river channel. Or vice versa, from the amount of water below river channel capacity $x$ ($x<0$) not all flows back into the river; some of the water remains on the floodplain. The flow between river and floodplain ($Q_{rf}$ [$m^3/s$]) is, thus, calculated as a portion of $x$ and can be either positive (from river to floodplain, if $x>0$) or negative (from floodplain to river, if $x<0$):

$$Q_{rf}(t) = x * \frac{p}{100} \quad , \quad x(t) = Q_i(t) - Q_{ra}(t-1) \qquad 4.8$$

whereas the portion $p$ [%] depends on the relation of $x$ to $Q_{ra}$ and is calculated by using an exponential function with a predefined minimum ($p_{min} = 60\%$) (Figure 4.4):

$$p(t) = f(x) = 100 - \frac{100 - p_{min}}{e^{10*\frac{|x(t)|}{Q_{ra}(t-1)}}} \qquad 4.9$$

45

When flooding starts, $Q_{ra}$ equals bankfull flow ($Q_b$ [$m^3/s$]). During flooding $Q_{rf}$, the flow between river and floodplain is taken into account:

$$Q_{ra}(t) = \max\left(Q_i(t) - Q_{rf}(t), Q_b\right) \qquad\qquad 4.10$$

Furthermore, the floodplain discharge $Q_f$ is calculated by adding (or subtracting) $Q_{rf}$ to the floodplain inflow $Q_{if}$ from upstream grid cells:

$$Q_f(t) = Q_{if}(t) \pm Q_{rf}(t) \qquad\qquad 4.11$$

If *x<0* and the floodplain storage $S_f$ is less than the difference of river water storage from last time step *S$_r$(t-1)* to current time step *S$_r$(t)*, all of the water on the floodplain flows back into the river. In that case, the flow between river and floodplain $Q_{rf}$ is negative and equals *x* (*Q$_{rf}$ = min(x, S$_f$)*).

In order to find a method to calculate *p*, I tested several equations (some of them shown in Figure 4.4) and values for *p$_{min}$* (*p$_{min}$ = 0, 20, 50, 60, 70, 80*). To do that, I compared 1) modeled river discharge to observed river discharge at gauging stations, and 2) modeled surface water extent to satellite derived observed surface water extent; both in the testing region, the Amazon river basin (for sources of model validation data see Section 4.7).

Regarding *p$_{min}$*, best model results are achieved if at least 60% of the water above river channel capacity flows into the floodplain. Up to a value of *p$_{min}$ = 60*, the larger *p$_{min}$* the better the WaterGAP results for both river discharge and surface water extent. With *p$_{min}$*-values larger than 60%, modeled river discharge starts getting worse compared to observations, due to a decrease in peak flows.

To find an appropriate equation to calculate *p*, it was required that the equation complies with the following characteristics:

1) p depending on the relation from *x* to $Q_{ra}$: Given that larger rivers have larger water storage capacity than small rivers, with equal *x* the portion of water entering in the floodplain (*p*) is less for large rivers than for small rivers. With equal $Q_{ra}$, the larger the amount of water above river channel capacity (*x*), the larger the portion of water flowing into the active floodplain.

2) The portion of *x* being relatively large already with small amounts of water above river channel capacity to ensure a rapid and extensive river-floodplain interaction. Thus, the function is required to have a steep gradient right from the beginning of the curve (Figure 4.4).

3) If flooding occurs, at least always some amount of water staying additionally to the bankfull flow in the river channel (*p* approximates to 100%, but never reaches 100%).

Figure 4.4 shows three of the tested equations for calculating *p*, whereas only the exponential function fulfills the above-mentioned requirements.
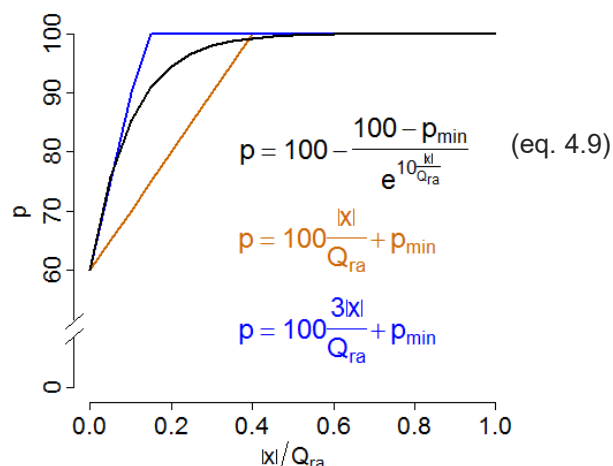
**Figure 4.4** Portion $p$ [%] of $x$ (water flow exceeding the river channel capacity, $x = Q_i - Q_{ra}$); $p_{min}$ is a predefined minimum percentage (set to 60%) and $Q_{ra}$ is the actual river channel flow $Q_{ra}$ in the case of flooding ($Q_{ra} \geq Q_b$, maximum river channel capacity at a given time). In addition, two other equations are shown, where the model has been tested for.

## 4.4 Water surface extent

Water surface extent is the sum of the inundation area on the floodplain, determined by applying the hypsographic approach (Section 4.4.1), and the area of other water bodies in WGHM, which are based on the Global Lakes and Wetland Database GLWD (Section 4.4.2).

### 4.4.1 Hypsographic Approach

A cumulative distribution function (CDF) of relative elevations – a hypsographic curve – is used to describe the floodplain elevation profile, assuming that flooding starts from low regions in a grid cell. Thus, with the volume of water on the floodplain ($S_f$), the floodplain height ($H_f$) and the corresponding dynamic floodplain extent ($A_f$) can be determined for each 0.5° grid cell (Figure 4.2).

Low values of floodplain storage imply that less volume of water is necessary to flood a certain area of a 0.5° grid cell. These grid cells are characterized by a low slope of the CDF and, therefore, also by a relatively small floodplain height compared to grid cells with rough terrain and large elevation differences.

The hypsographic approach with the underlying data is explained in more detail in the following paragraphs and figures.

The CDF for each 0.5° grid cell on a global-scale is derived from two digital elevation models: HydroSHEDS (Hydrological data and maps based on SHuttle Elevation Derivatives at multiple Scales, Lehner et al. 2008b) and ACE2 (Altimeter Corrected Eleva-

47

tions, Smith 2009), both with a spatial resolution of 3 seconds. HydroSHEDS covers the region within ±60°N and ACE2 is applied for latitudes outside these bounds.

HydroSHEDS DEM is based on high-resolution (3 seconds = ~90 m) elevation data of the Shuttle Radar Topography Mission (SRTM), which were corrected for hydrological applications. SRTM data were obtained on a near-global-scale (±60°N) by a specially modified radar system flown onboard the Space Shuttle Endeavour in February 2000 (Farr et al. 2007). The hydrological correction implies particularly the assurance that "the surface of each river pixel was lower than that of the directly adjacent land pixels" (Lehner et al. 2006a, p. 6) and the void-filling of SRTM data by filling the no data voids "by means of an iterative neighborhood analysis" (Lehner et al. 2006a, p. 8). This tends to force the flow to stay within river channels (Lehner et al. 2008a).

The ACE2 dataset is a DEM on a global-scale. Within the region bounded by ±60°N, the elevation data of SRTM was synergistically merged with Satellite Radar Altimetry. Especially over the rainforest, SRTM data was replaced by multi-mission satellite altimeter data. Unlike the SRTM radars, where elevation measurements are produced from near the top of the canopies (Farr et al. 2007), the radar altimetry is able to sense the surface beneath vegetation canopies. "For regions outside the latitude bounds of SRTM, all available altimeter data were fused with a range of existing ground truth" (Smith and Berry 2009, p. 13). These data include GLOBE (Global Land One-km Base Elevation Project) and the original ACE DEM (Topex KU Band, ERS-1, Envisat RA-2 Ku Band, Jason-1 Ku Band). The overall time span of the used altimeter missions reaches from March 1994 to July 2005 (Smith and Berry 2009). Unlike HydroSHEDS, ACE2 is not hydrologically corrected.

When combining HydroSHEDS and ACE2 data to get data on surface elevation on a global-scale, 512 of 66896 WaterGAP grid cells could not be covered (155 grid cells north of 60°N and 357 south of 60°N), including the regions of Alaska, southeast Greenland and some islands like Reunión and Mauritius, Cape Verde, Hawaii and other Pacific islands (red regions in Figure 4.7). Furthermore, the Caspian Sea is with 108 grid cells included in the WaterGAP land mask, but there is no information on surface elevation. In these grid cells – with no information on the floodplain elevation profile – the algorithm to simulate dynamic floodplain inundation cannot be applied. Instead, global wetlands based on GLWD are kept in WaterGAP. This concerns 20 grid cells (of total 66896), all of them located in Alaska.

The SRTM dataset, based on an interferometric SAR technique, returns the majority of its signal from near the top of the canopies in areas with dense vegetation (Farr et al. 2007). The highest accuracy losses due to vegetation are in the tropics in dense rainforest areas, also because SRTM was flown in northern hemisphere winter. In contrast, the altimeter data is able to penetrate vegetation cover and reflects the signal from the underlying ground surface. In the ACE2 DEM, SRTM pixels over rainforest areas – espe-

cially in the Amazon and Congo River basins – were replaced with multi-mission satellite altimeter data. The HydroSHEDS DEM is based only on the radar-derived product SRTM and, thus, more strongly influenced by vegetation than ACE2.

Several authors (Beighley et al. 2009; Paiva et al. 2013; Wilson et al. 2007; Neal et al. 2012; Yamazaki et al. 2012a) have stated that it is essential to correct raw DEM data against vegetation and other artifacts for improving the accuracy of the hydrodynamic simulations. This requires detailed information about land use or vegetation cover, to be able to distinguish abrupt rises in elevation caused by vegetation or by natural landscape effects, like river banks.

Within the scope of this PhD work, I tested different methods for vegetation correction: a) some of them based on the implementation of a global vegetation data set into WGHM and b) others based on the correction of vegetation only in areas with high and dense vegetation. In any case, the correction is done for entire river basins to conserve the hydrological corrections of the HydroSHEDS DEM. That means that all surface elevations within all grid cells of one river basin are lowered by the same value of vegetation height (negative surface elevations are set to zero).

The global vegetation map from Simard et al. (2011) maps forest canopy heights derived from laser altimetry – also referred to as LIDAR (light detection and ranging) – using 2005 data from the Geoscience Laser Altimeter System (GLAS) aboard ICESat (Ice, Cloud, and land Elevation Satellite). The spatial resolution is 1 km. The average canopy height in the Amazon river basin is 26 m with a standard deviation of 6 m. Vegetation correction within WaterGAP was tested using the mean, mean minus standard deviation, and mean minus twice the standard deviation of Simard et al. (2011) for each river basin respectively. For the vast majority of the river basins the model fit was best, compared to observed river discharge and surface water extent data, with no vegetation correction. But the Amazon River basin differs considerably. The large seasonal flooding in the Amazon River basin can only be achieved when vegetation correction is applied. According to that finding, two additional model runs were tested, applying vegetation correction of 23 m and 17 m only for the Amazon River basin. These values are used in the hydrological models THMB (Coe et al. 2008) and MGB-IPH (Paiva et al. 2011) respectively. Finally, the best model fit of WaterGAP 2.2b_fpl compared to observation data is achieved when correcting the DEM by a vegetation height of 17 m, and only in the Amazon River basin.

Figure 4.5 shows schematically the generation of input data for WGHM derived from the digital elevation models.

- Cumulative sorting of sub grid elevation points of each 0.5° grid cell.
- Omission of the 0.001% lowest elevation values (value 361 = **minimum elevation of the 0.5° grid cell ($z_{min}$)**).
- Each of the remaining 359640 elevation points represents a relative grid cell area $A$ of 0.000278% of the 0.5° grid cell area.
- Determination of **floodplain height $H_f$** for each $A$, potential **floodplain area $A_f$** by using the cumulative elevation function (hypsographic curve).
- Determination of **floodplain storage $S_f$** by calculating $H_f$ times $A_f$ minus the area under the hypsographic curve.

Extraction of 100 elevation points ($m$) from total 359640 ($n$) per 0.5° grid cell using a quadratic function (point visualization on the hypsographic curve).

Storage of $z_{min}$ and the corresponding values of $A_f$, $H_f$ and $S_f$ for each of the 100 sub grid elevation points in a Table (the final input into WGHM is in form of arrays).

**Inputs for WGHM derived from DEMs:**

| m | $A_f$ | $H_f$ | $S_f$ | $z_{min}$ |
|---|---|---|---|---|
| 1 | 0 | 0 | 0 | Value 361 |
| . | . | . | . | |
| . | . | . | . | |
| . | . | . | . | |
| 100 | 99.99 | Value 360000 | . | |

**Figure 4.5** Scheme of input generation for WGHM, derived from DEMs using a cumulative distribution function of relative elevations (hypsographic curve) of a 0.5° grid cell. $S_f$ is the water storage above bankfull which flows on the active floodplain, $A_f$ is the floodplain area, $H_f$ the floodplain height and $z_{min}$ is the minimum elevation of the 0.5° grid cell (outflow level). To reduce computational load, only 100 elevation points per grid cell (0.028%) were used in the program code to describe the hypsography of each grid cell (dots and vertical black lines on the cumulative elevation curve).

First of all, the DEM elevation data with a spatial resolution of 3 seconds is assigned to the 66896 0.5° grid cells of WaterGAP, with each grid cell including 360000 subgrid elevation points.

In a second step, the minimum elevation (outflow level, $z_{min}$) of a grid cell is defined and the subgrid elevation points are sorted cumulatively. In that way the surface eleva-

50

tion profile of the floodplain for each of the 0.5° grid cells in WGHM is described by its hypsographic curve, assuming that low regions in a grid cell flood first. In the hypsographic approach, it is assumed that the minimum elevation in the 0.5° cell ($z_{min}$) represents the water height in the river channel at the bankfull stage and is defined as the outflow level of the 0.5° grid cell (Figure 4.7). Figure 4.6 shows the subgrid elevation in an example grid cell in the Amazon River basin with its flow accumulation, derived from HydroSHEDS. It can be seen that the water level height in the river channel is quite inhomogeneous. To avoid errors – like negative elevation values or low elevation values over surface water caused by void filling of SRTM and/or altimetry data – I discard the lowest 0.001% of the elevation values (value 361 = $z_{min}$). This assumes that at least one part per thousand of each grid cell remains always covered by water. Each of the remaining 359640 elevation points represents 0.000278% of the total 0.5° grid cell area $A$. Floodplain height $H_f$ and floodplain storage $S_f$ are determined for each state of flooding (floodplain area $A_f$) of the grid cell area $A$ by using the cumulative elevation curve (Figure 4.5). Whereas floodplain storage $S_f$ is calculated as $H_f$ times $A_f$ minus the area under the curve in the limits from zero to $A_f$.

In a third step, to reduce computational load, only a fraction of the subgrid elevation points per 0.5° grid cell are extracted (Figure 4.5). The hypsographic curve is approximated using only 100 points per grid cell (0.028%). As flooding in lower regions is more frequent, the elevation profile is represented with more data points in the first part of the CDF, while higher elevation values are represented with less detail. Considering this, the extraction of $m$ number of elevation points ($m = 1,2,3,...,100$; $m_{max} = 100$) from the total number of elevations points per grid cell ($n(100) = 359640 = n_{max}$) is done by using a quadratic function; the equation can be solved by using the method of substitution knowing that $n(1) = 1$ and $n(100) = 359640$:

$$n(m) = \lfloor am^2 + b + 0.5 \rfloor$$

$$= \left\lfloor \frac{n_{max} - 1}{m_{max}^2 - 1} m^2 + \frac{n_{max} - m_{max}^2}{1 - m_{max}^2} + 0.5 \right\rfloor \qquad 4.12$$

The first elevation value ($m = 1$) is the minimum elevation – considered as bankfull height – and the last elevation value ($m = 100$) is the maximum elevation of the 0.5° cell. The floor ($\lfloor \quad \rfloor$) plus 0.5 in Equation 4.12 ensures integer values.

Finally, as shown in Figure 4.5, the corresponding values of $A_f$, $H_f$ and $S_f$ for each of the 100 subgrid elevation points are, in addition to $z_{min}$, stored in a table. As the data is tabulated for the same area in each grid cell (each of the 100 subgrid elevation points represents a certain cell area) $A_f$ in percent of cell area is the same for all of the grid cells, with a first value of zero and a last value of 99.99 (100% minus the area of the outflow subgrid). In contrast, $H_f$ and $S_f$ are different for each of the 66896 grid cells globally, as these variables depend on each grid cells unique floodplain elevation profile. The varia-

bles in the table (Figure 4.5) are an additional input to the global hydrology model WGHM and are supplied in the format of arrays[3].

Within WGHM, the floodplain storage (water volume above the river channel capacity) is distributed over the cell according to the hypsographic curve, starting from the minimum elevation of the grid cell. The dynamic floodplain area ($A_f$) and height ($H_f$) is determined by interpolating between the values in the previously prepared table. However, $A_f$ and $H_f$ would be overestimated if the SRTM digital elevation values were derived during low water periods where the water in the river channel is below the bankfull stage, and there would be an underestimation of these variables if at the time of obtaining SRTM data, part of the cell area had already been flooded.
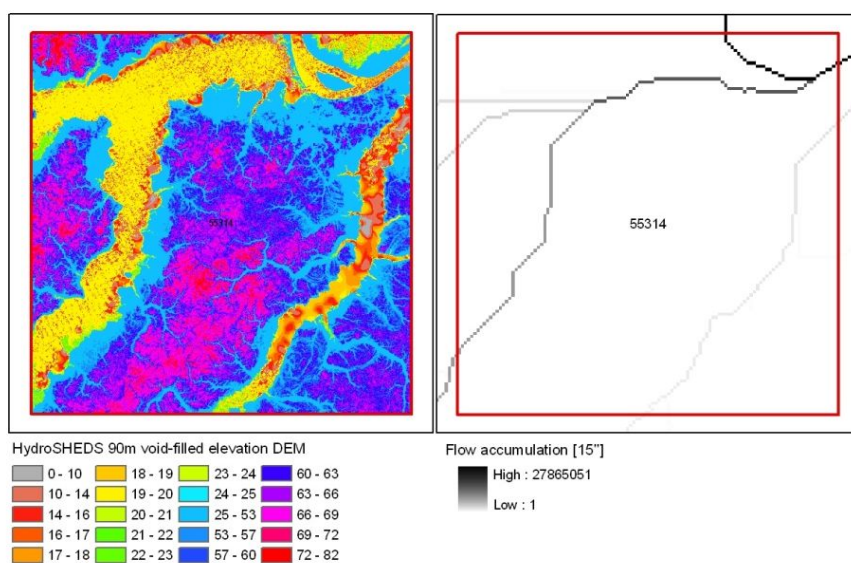


**Figure 4.6** HydroSHEDS elevation [m a.s.l.] (left) and flow accumulation (right) in an example of 0.5° grid cell located in the Amazon River basin, demonstrating the inhomogeneity of the water level height in river channels.

---

[3] Details about the tools for WGHM input data preparation, including downscaling of sub grid elevation data, CDF generation, determination of flood regarded variables, data extraction, and array input generation are described in the appendix.
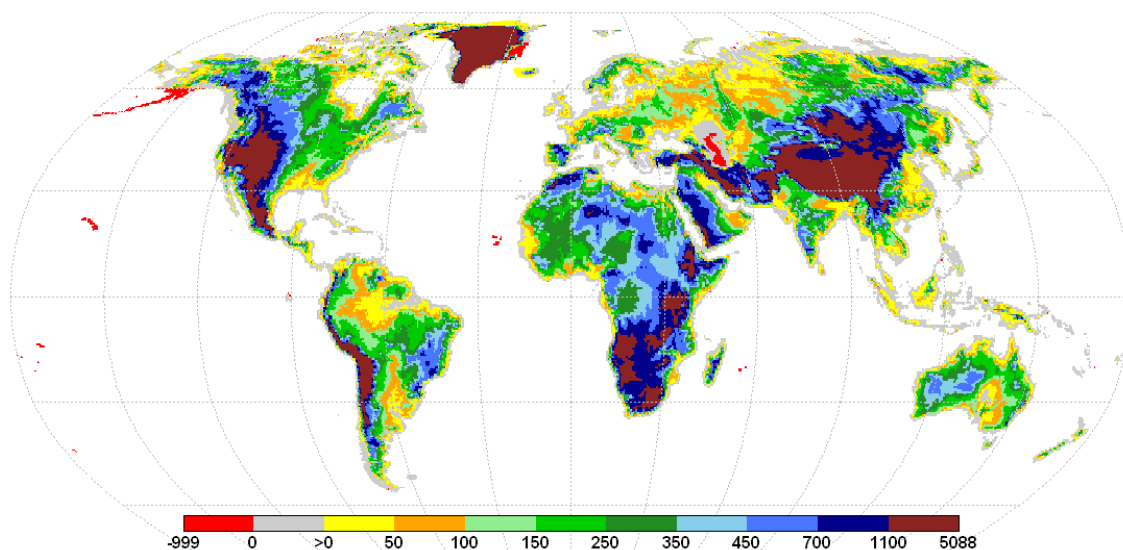
**Figure 4.7** Minimum Elevation $z_{min}$ [m a.s.l] per 0.5° grid cell derived from HydroSHEDS and ACE2 digital elevation models. Negative elevations are set to zero. No data value is the -999.

Negative elevation values of the DEMs are set to zero. Negative values may occur due to sink cells or erroneous classification of surface elevations in HydroSHEDS and ACE2. These errors might lead to artificial rapids, as high changes in surface water slope lead to higher flow velocities. However, by correcting these values, real sinks (e.g. Dead Sea, Caspian Sea depression) get missed. Setting negative values to zero leads, in the case of the Caspian Sea depression, to a completely flat floodplain elevation profile (all elevation values are zero). For these grid cells, and also for those not indicated as lake or wetland/floodplain in GLWD, WaterGAP would produce a 100% inundated cell as soon as bankfull flow is reached. This would result in a strong overestimation of evapotranspiration. In case the results showed an overestimation of floodplain extent in areas of natural depressions, these areas should be excluded from the correction of negative elevations.

### 4.4.2 Permanent surface water bodies in WGHM

In WGHM the location of lakes, reservoirs and wetlands, and their extent are static, prescribed by the Global Lakes and Wetland Database GLWD (Lehner and Döll 2004). Wetlands include all types of inland wetlands like floodplains, freshwater marshes, swamp forests, bogs, fens, and salt pans. In the model, all types of surface water bodies from GLWD are merged into 4 categories: local lakes, local wetlands, global lakes/reservoirs, and global wetlands (Figure 4.7). Whereas surface water bodies defined as local are only fed by precipitation of the grid cell itself, surface water bodies defined as global also receive inflow from upstream grid cells.

In WaterGAP 2.2b the areal fraction of land and surface water bodies is temporally varying (except for global lakes and reservoirs). The area of each storage compartment of

surface water bodies ($A_m$) is equal to maximum area ($A_{max}$) times a temporally varying area reduction factor ($r$) which is a function of water storage at the previous time step ($S_m(t-1)$):

$$A_m(t) = A_{max} * r_m(t)$$
$$r_m(t) = f(S_m(t-1)) \qquad \qquad 4.13$$
$$A(0) = A_{max}$$

The maximum area of surface water bodies (lakes, reservoirs, and wetlands) is based on the global land and wetland database GLWD (Lehner and Döll 2004) and is about 7.5% (10133912 km²) of the continental area (Figure 4.8). The surface water bodies area reduction factor $r$ implies values between 0 and 1.

For modeling dynamic floodplain inundation, global wetlands (2.9% (3872986 km²) of the continental area) are removed and floodplain storage is added as a new storage compartment to WGHM; whereas floodplain area is calculated at each time step based on the hypsographic approach (Section 4.4.1).[4] Local wetlands from GLWD are kept; as they do not receive inflow from other grid cells and flooding from the main river of a 0.5° grid cell, it is not likely that they reach floodplains of small tributaries (Coe et al. 2008).

In case lakes and local wetlands become inundated by river flooding, evaporation may be overestimated. To avoid this, it is assured that total area of open surface water (lakes, reservoirs, local wetlands, rivers, and floodplains) does not exceed 100% of the continental area of a grid cell, i.e. the area that is not the ocean.

---

[4] Global Wetlands based on GLWD are kept in WaterGAP only in grid cells with no available data on surface elevation (Hydrosheds and ACE2; see Chapter 4.4.1). This concerns 20 grid cells (of total 66896), all of them located in Alaska.
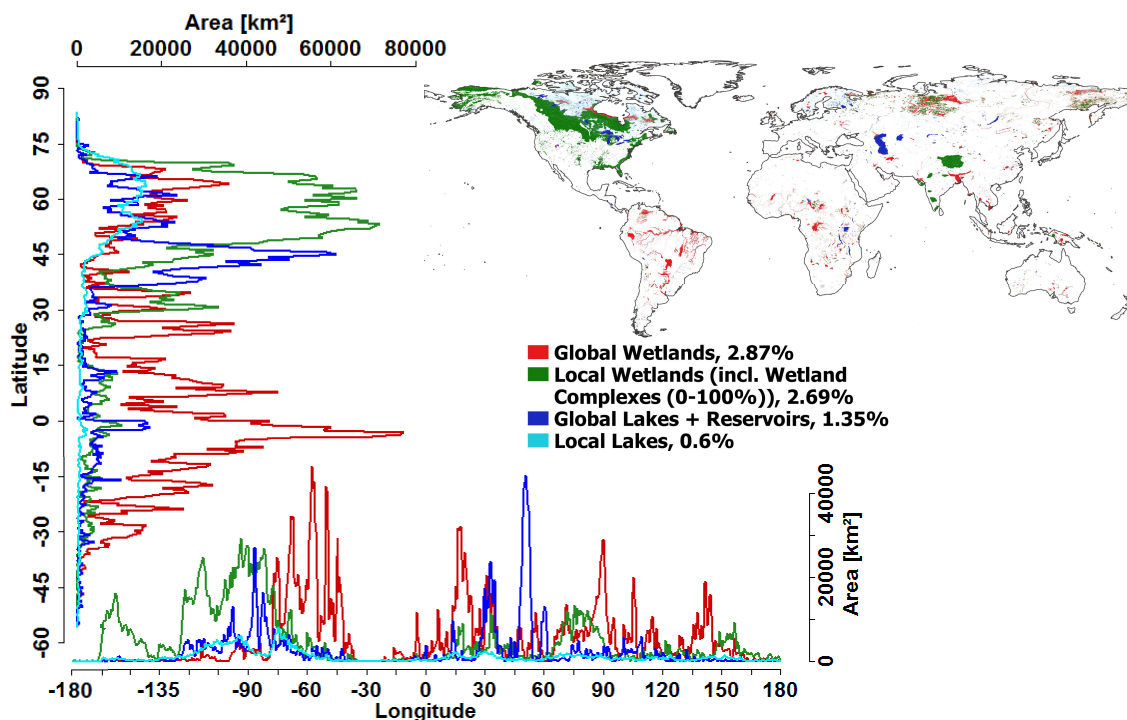
**Figure 4.8** Distribution of surface water from the Global Lakes and Wetland Database GLWD (Lehner and Döll 2004) merged in 4 categories: local lakes, local wetlands, global lakes/reservoirs, and global wetlands. The area in km² of each of the 4 Categories is summarized for latitudes and longitudes. The location of the continents is shown on the spatial map. The percent information in the legend is the area related to the global continental area of all WaterGAP grid cells.

## 4.5 Flow routing

The lateral transport of water between grid cells (upstream/ downstream relation) is based on the global drainage direction map DDM30 (Döll and Lehner 2002). By implementing the floodplain algorithm into WaterGAP, water transport between grid cells is calculated not only for river channels but also for floodplains.

The flow direction and the flow velocity depend on the water level slope $s$. Until WaterGAP model version 2.2 the slope was time constant and water was always routed downstream (kinematic wave). By implementing subgrid surface elevation into WaterGAP, WaterGAP 2.2_fpl is able to calculate water level heights for each grid cell and time step. These water level heights are used to calculate a time variable slope with either solely downstream routing or downstream with proportional upstream routing (backwater effects). Flow routing is calculated with one time step per day applying the kinematic wave routing and with 72 time steps per day (20 minutes) applying the routing option allowing backwater flows, for rivers as well as for floodplains.

In WaterGAP 2.2_fpl the user can decide whether to use the kinematic wave water flow routing with or without backwater flows. By implementing the calculation of water lev-

55

el, WaterGAP is able, for the first time, to represent backwater effects (i.e. the water stage downstream affects flow velocity upstream). Especially in the Amazon river basin backwater effects are very important (Meade et al. 1991). If they are considered, modeled river discharge and flow velocities should improve when compared to observations. Large tributaries that drain the southern Amazon River basin (especially the Madeira, Tapajós, and Xingu rivers) reach their peak discharges in April, two months earlier than the main stem does, which results in backwater conditions in the lowermost 800 km of the Amazon main stem. The peak stage at Obidos usually precedes the peak stage 750 km upriver at Manacapuru (Meade et al. 1991).

In the following two subchapters I explain in detail both routing approaches: kinematic wave and backwater flows.

### 4.5.1 Kinematic wave

In the kinematic wave routing approach, the water channel slope is time constant and always positive. This implicates positive flow velocities and immediately discharged downstream waters.

In the kinematic wave approach, the slope $s$ [-] for both rivers and floodplains is calculated by dividing the difference between the land surface elevation at the outflow ($z_{min}$) of the target grid cell $i$ and the downstream grid cell $j$ by the river length between these grid cells (cell center to cell center):

$$s = \frac{z_{mini} - z_{minj}}{d_i * mf}$$ 
4.14

Whereas $d_i$ [$m$] is the direct distance to the downstream grid cell and $mf$ [-] is the meandering factor (sinuosity).

The meandering factor $mf$ [-] was derived from the HydroSHEDS 15 arc-second river network and ranges from 1 to 6.41 globally with an average sinuosity of 1.17 (Verzano 2009). The minimum elevation $z_{min}$ [$m$] is the lowest sub elevation (outflow level) of a grid cell and was derived from HydroSHEDS and ACE2 (±60N) (see Section 4.4.1). Due to possible errors of the DEMs and the coarse resolution schematic drainage direction map, minimum elevation of the target grid cell $z_{mini}$ [$m$] might be below the minimum elevation of the downstream grid cell $z_{minj}$ [$m$]. In this case, $z_{mini}$ is set equal to $z_{minj}$. If the slope is zero, it is set to a minimum slope of 0.0001.

### 4.5.2 Diffusion wave - backwater effects

Contrary to the kinematic wave, the diffuse wave equation routes water according to the slope of the water surface, allowing an upstream flow of water. Positive flow velocity indicates forward flow from upstream to downstream, whereas negative velocity indicates backward flow from downstream to upstream (Figure 4.9). In the case of a nega-

tive water level gradient and more than one upstream grid cell, water is routed either to the grid cell with the largest water level gradient or, if gradients are equal, to the grid cell with the biggest drainage area. Water always flows downstream in grid cells where no upstream grid cell exist and in grid cells of river mouths (no backwater effects from the ocean). The flow direction depends on the water level gradient, in other words, whether the slope $s$ [-] is positive or negative. For the diffusion wave approach, Equation 4.14 is therefore modified and river slope $s$ [$m$] is calculated by dividing the water level gradient between the target grid cell $i$ and the downstream grid cell $j$ by the river length (cell center to cell center):

$$s = \frac{(z_{mini} + H_{fi}) - (z_{minj} + H_{f_j})}{x_i * mf} \text{ , if } Q_i > Q_b$$

$$s = \frac{(z_{mini} - D_{bi} + D_{ri}) - (z_{minj} - D_{rbj} + D_{r_j})}{x_i * mf} \text{ , if } Q_i < Q_b$$

4.15

The minimum elevation of a grid cell $z_{min}$ [$m$] represents the outflow level of a grid cell (bank height) and is obtained from digital elevation models (Section 4.4.1). In the case of flooding (if $Q_i > Q_b$), the water level of the river is equal to that of the floodplain and is above bank height ($z_{min} + H_f$, $H_r = H_f$). Floodplain height $H_f$ [$m$] is determined by using the hypsographic approach (Section 4.4.1). In case of no flooding (if $Q_i < Q_b$), the water level of the river is calculated by adding the river depth ($D_r$) to the river bottom height, which is approximated by subtracting the river depth at bankfull state ($D_b$) from the bank height $z_{min}$. The river depth under bankfull and non-bankfull conditions is calculated using Equation 4.25 (Section 4.6).

If $z_{mini}$ is equal to $z_{minj}$, slope depends only on floodplain height or river depth. In the case the slope is zero, it is set to 0.0001 and water is routed downstream. Backwater effects are calculated for both rivers and floodplains.
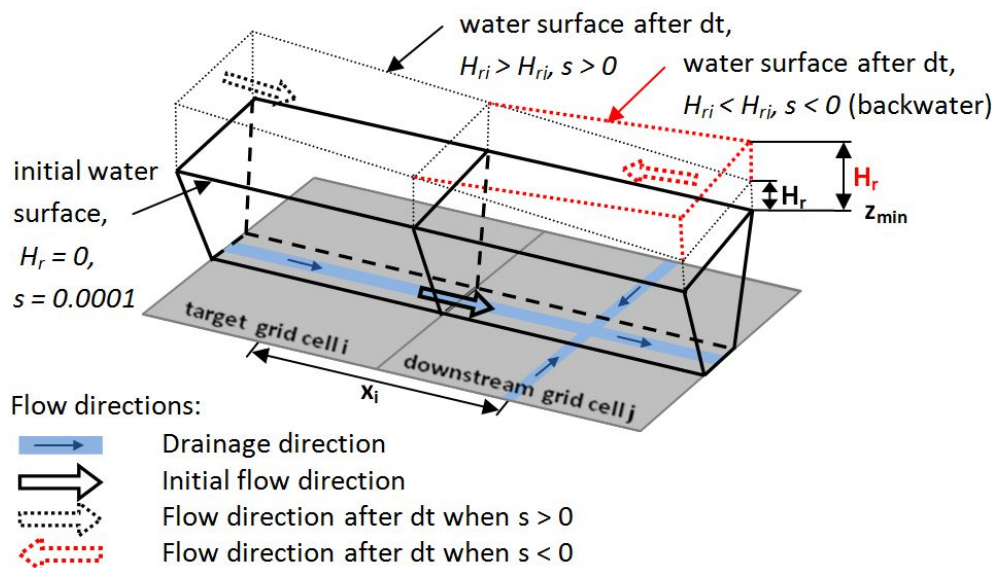
**Figure 4.9** Sketch of flow routing between grid cells. The slope $s$ specifies the flow direction in rivers and floodplains. It is based on the outflow level of the grid cell $z_{min}$, the river height $H_r$, and the river length between the target and the downstream grid cell (cell distance $x_i$ times a meandering factor).

If water is routed always downstream (kinematic wave routing), river storage is calculated using an ordinary differential equation containing one independent variable: time ($dS/dt$). This equation is solved analytically in WaterGAP 2.2b. In the diffusive wave routing, or rather if backwater flows are allowed, the river storage equation is solved using a partial differential equation, as it contains two independent variables: time and space. Since this is not solved analytically, a higher temporal model resolution is necessary to avoid numerical instability.

To avoid numerical instability, Yamazaki et al. (2011) have selected a higher temporal resolution for computing diffusion wave (20 minutes) compared to kinematic wave (30 minutes) in the CaMa-Flood model. The temporal resolution of WaterGAP 2.2b with kinematic wave routing is daily. For computing backwater flows, WaterGAP runs stable with a time step of 20 minutes (tested with 40, 30, 20, 15, 10, and 5 minutes).

A diffusion wave assumes that the direction as well as the flow velocity depend on the water level gradient. At this moment, unfortunately, this works only in a restricted way for WaterGAP 2.2b_fpl. Actually, river and floodplain depth should be equal when flooding occurs. This is not the case in WaterGAP because river and floodplain depth are calculated in different ways. The floodplain depth is determined from the floodplain elevation profile based on a high resolution digital elevation model (by applying the hypsographic approach, Section 4.4.1). On the contrary, due to the lack of data on river bathymetry, the river depth is estimated from river storage, transposing the equation of cross-sectional area times river length in the grid cell (Equation 4.26). Since river storage is relatively variable in time (not very steady), depending mainly on river inflow, river depth and thus the water level gradient and the slope can change strongly within only a few days. The flow velocity is highly sensitive to the slope and fluctuates when

applying the river slope, depending on the daily water level gradient per grid cell (Equation 4.15). The latter is therefore only used to derive the flow direction in WaterGAP 2.2b_fpl. Whereas the slope within the flow velocity equation keeps being calculated like in WaterGAP 2.2b, which is time constant and depends on the water level gradient of the outflow level of the target and the downstream grid cell (Equation 4.14). Once the flow direction has been defined and indicates upstream routing, the total outflow of the grid cell should flow to an adjacent upstream grid cell. Unfortunately, if this is applied to WaterGAP, river discharge in downstream areas of the river basin gets extremely low and huge water masses get stored on floodplains rising into infinity with time. Figure 4.10 shows the average water slope for each grid cell in $10^3$ [m/m] for the year 2003 (left) and the number of months in which the water slope is negative (right; e.g. 2 month means more than 59 days with negative water slopes in the year 2003). Grid cells with average negative water slopes, indicating backwater routing, are accumulated along the main river, an area where backwater conditions have been observed (Meade et al. 1991). Anyway, in many of these grid cells, the water slope is negative almost the whole year. To circumvent a permanent upstream routing caused by endured negative water slopes in some grid cells, I decided to route only a percentage of the cell outflow upstream and the remaining amount of water outflow downstream. Best model results are achieved by routing only 5 percent (tested with 50, 20, 15, and 5%) of the grid cell outflow backward in case water slope is negative.
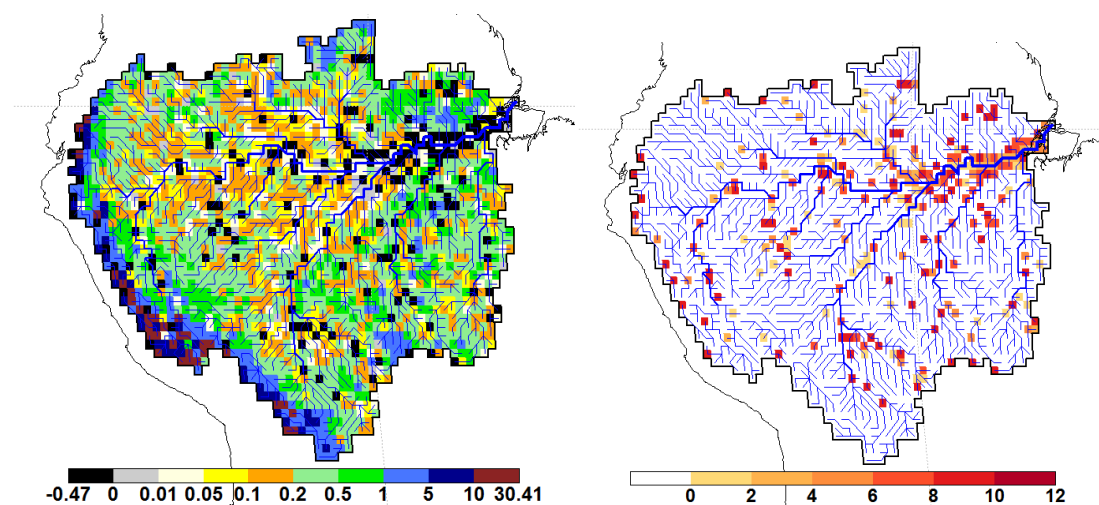


**Figure 4.10** Annual mean daily water slope [$10^3$ m/m] in the Amazon River basin in 2003 as computed by WaterGAP 2.2b_fpl with kinematic wave routing (left) and the number of months in which the water slope is negative (right).

In summary, WaterGAP 2.2b_fpl with backwater flows differs from that without backwater flows (kinematic wave routing) in its higher temporal resolution of 20 minutes (compared to 1 day) and 5% backwater flow in case water slope is negative.

## 4.6 Flow velocity on rivers and floodplains

In WaterGAP 2.2b, a variable flow velocity in rivers was applied. In WaterGAP 2.2b with floodplain algorithm, the variable flow velocity is not only calculated for rivers but also for floodplains.

Flow velocity for rivers and floodplains is calculated using the Manning-Strickler equation, which is one of the best-known and most used equations to calculate river flow velocities:

$$v_{r,f} = n_{r,f}^{-1} * R_{r,f}^{2/3} * s_{r,f}^{1/2} \qquad\qquad 4.16$$

The advantage of this equation is that the required parameters can be derived from available data and it is, nevertheless, sophisticated enough to deliver realistic flow velocity values for a large variety of environmental conditions on a global-scale (Verzano 2009). In Equation 4.16, for rivers and floodplains respectively, $v$ is the flow velocity in m/s, $n$ is the roughness coefficient [-], $R$ [$m$] is the hydraulic radius, and $s$ is the water surface slope [-].

Verzano (2009) has estimated different river roughness coefficients for each grid cell of WaterGAP, ranging from 0.033 to 0.0598 with a global mean of 0.0359, using topographic and/or geologic information (this requires the definition of mountainous and urban areas and the use of additional datasets: GTOPO 30, GRUMP). In previous model versions up to WaterGAP 2.1f, a constant river roughness coefficient of 0.044 was applied (Schulze et al. 2005). In this study, the roughness coefficient for floodplains ($n_f$) was set to a constant value of 0.07, recommended by Mays (1996) for floodplains with medium to dense brush.

Wilson et al. (2007) have used the hydrodynamic model LISFLOOD-FP to predict floodplain inundation in the central Amazon, applying different roughness coefficients for rivers and for floodplains. They noticed that changing $n_f$ makes small difference in model performance.

The hydraulic radius, $R$ [$m$], of a specific river cross section or floodplain section, changes with actual discharge and, hence, it is the dynamic variable within the Manning-Strickler equation. The hydraulic radius depends on the actual water level and the shape of the river bed or floodplain profile, and is calculated dividing cross-sectional area *CSA [m²]* by the wetted perimeter *WP [m]*:

$$R = \frac{CSA}{WP} \qquad\qquad 4.17$$

Assuming that the floodplain profile is shaped as a rectangle, *CSA* and *WP* can be calculated as a function of floodplain width $W_f$ [*m*] and depth $D_f$ [*m*]:

$$R_f = \frac{CSA_f}{WP_f} = \frac{D_f * W_f}{2D_f + W_f} \qquad\qquad 4.18$$

"For a small floodplain, characterized by a flat bottom and steep sides, the initial increase in stored volume occurs as a rapid increase in area; at higher water levels, volume increases in the floodplain result in an increase in water depth without much increase in flooded area" (Wolski et al. 2006, p. 65). In Equation 4.18 the floodplain width $W_f$ [*m*] is calculated by the ratio of flooded area $A_f$ [*m²*] and the river channel length in flow direction (without meander) (*L* [*m*]), and floodplain depth $D_f$ [*m*] is a function of water Storage on the floodplain $S_f$ [*m³*] and flooded area $A_f$ [*m²*]:

$$W_f = \frac{A_f}{L} \qquad\qquad 4.19$$

$$D_f = \frac{S_f}{A_f} \qquad\qquad 4.20$$

Flooded Area $A_f$ [*m²*], used in Equation 4.19 and 4.20, is determined on the basis of the CDF for each grid (see Section 4.4.1). Contrary to floodplains, in WaterGAP 2.2 the shape of the river channel is assumed to be trapezoidal, not rectangular. Given the fact that under natural conditions, in a flat and broad river bed, depth would decrease faster than width with falling discharge, Equation 4.18 for calculating the hydraulic radius *R* is modified assuming a trapezoidal river channel:

$$R_r = \frac{CSA_r}{WP_r} = \frac{D_r(2D_r + W_{bottom})}{W_{bottom} + 2D_r\sqrt{1 + 2^2}} \quad , \quad W_{bottom} = W_r - 2 * 2D_r \qquad 4.21$$

Whereas the side slope is 0.5, $W_{bottom}$ [*m*] is the width of the ground of the river channel and $D_r$ [*m*] is the river channel depth.

Verzano (2009) has described how river width and depth are calculated in WaterGAP 2.2b. Since these equations and their derivations are also important for the methods applied in WaterGAP 2.2b with floodplain algorithm, I quote this relevant paragraphs:

"Continuous data on river width and depth is lacking on the global-scale. Based on the close relationship between channel form and discharge (*Q*, [*m/s*]), Leopold and Maddock (1953) introduced equations, which estimate these parameters as a function of discharge:

$$W_r = a * Q^b \qquad\qquad 4.22$$

$$D_r = c * Q^f \qquad\qquad 4.23$$

Equations 4.22 and 4.23 can be found in hydrology textbooks (e.g. Mosley and McKerchar 1993, (p. 8.4.); Dunne and Leopold 1978, (p. 637)) and are frequently applied.

Allen et al. (1994) carried out a regression analysis with a dataset of 674 river cross sections across the USA and Canada to quantify the best-fit coefficients (*a*, *c*) and exponents (*b*, *f*) in the equations, valid for bankfull discharge ($Q_b$):

$$W_r = 2.71 * Q_b^{0.557}$$ 
<div align="right">4.24</div>

$$D_r = 0.349 * Q_b^{0.341}$$
<div align="right">4.25</div>

During regression analysis, Allen et al. (1994) obtained high coefficients of determination ($R^2$) of 0.88 and 0.75 for width and depth. In this approach of modeling river velocity, it is assumed that the hydraulic radius of a non-bankfull river follows the same geometric rules as bankfull discharge" (Verzano 2009, p. 64; Schulze et al. 2005, p. 134).

The standard version of WaterGAP 2.2b calculates river depth and width after Allen et al. (1994), as a function of actual river discharge, even though coefficients are only valid for bankfull discharge, not for all of the river discharges.

Within the scope of this thesis, I implemented a new method into WaterGAP, which computes river depth $D_r$ as a function of river storage of previous time step $S_{r(t-1)}$ *[m³]* instead of actual river discharge:

$$D_r = -\frac{W_{bottom}}{4} + \sqrt{\frac{(W_{bottom})^2}{16} + \frac{CSA_r}{2}} \quad , \quad CSA_r = \frac{S_{r(t-1)}}{l}$$
<div align="right">4.26</div>

Equation 4.26 was derived by transposing the equation of river cross sectional area $CSA_r$ (see Equation 4.21) to river depth. Where $CSA_r$ is calculated by dividing the river storage of previous time step $S_{r(t-1)}$ *[m³]* by the river length in the grid cell *l [m]*.

At the initialization time step, river storage is calculated by multiplying river length, river depth and river width:

$$S_r = l * D_r * W_r$$
<div align="right">4.27</div>

For the calculation of river storage at the initialization time step, both river depth and width are determined using the equations after Allen et al. (1994), inserting the river discharge at bankfull (Equation 4.24 and 4.25).

Coe et al. (2008) have calculated river width $W_r$ *[m]* as a function of upstream area *A* *[m²]*:

$$W_r = 0.421 * A^{0.592}$$
<div align="right">4.28</div>

The coefficients are estimated using observed river discharge data from the National Water Agency of Brazil (www.ana.gov.br). Within the framework of this thesis, I tested different methods for calculating river width (Schulze et al. 2005; Coe et al. 2008; Beighley et al. 2009). By doing that, I calculated long term average flow velocities (1971-2000) in the Amazon River basin, with the result that a change in river width has

small influence on river velocity (differences are less than 0.01 m/s in almost two-thirds of the grid cells).

The standard version of WaterGAP 2.2b_fpl computes river width as a function of river discharge (according to Allen et al. 1994), and river depths as a function of river storage of previous time step. Chapter 5.1 presents the effect of changing flow velocity – using different equations to calculate river depth – on the results of river discharge and water storages in WaterGAP 2.2b_fpl.


The slope $s$ [-] for rivers and floodplains is calculated by dividing the water level gradient between the target grid cell $i$ and the downstream grid cell $j$, by the river length between these grid cells (cell center to cell center) (Equations 4.14 and 4.15).

In the standard version of WaterGAP 2.2, a time constant channel slope is applied, in which water is routed always downstream (kinematic wave approach, Section 4.5.1). In WaterGAP 2.2_fpl, backwater flows in river channels are permitted for the first time (diffusion wave approach, Section 4.5.2). In that case, river water level slope and thus river velocity can be negative. The water level slope is variable in time.


## 4.7 Validation Data and model efficiency criteria


### 4.7.1 Validation Data

Model outputs of WaterGAP hydrology model were validated with the following data sets:

1) Total water storage variations: The Gravity Recovery and Climate Experiment (GRACE) is a twin-satellite mission of NASA and DLR launched in 2002. GRACE measures changes in Earth's gravity field by making accurate measurements of the distance between the two satellites due to gravitational acceleration, using a microwave ranging system and GPS. The spatial resolution is about 400 km. GRACE data with the time period from 2002 to 2009 provided by University of Bonn (ITG-Grace 2010) was used to validate total water storage variations as calculated by the WaterGAP hydrology model. To compare WGHM data with GRACE data, the WGHM data was filtered with the same decorrelation filter as the GRACE data (non-isotropic filter DDK3, Kusche et al. 2009).

2) River discharge: Time series of daily and monthly values of river discharge observed at gauging stations provided by the Global Runoff Data Centre (GRDC) were used for comparison to modeled river discharge and surface water extent from WGHM. The GRDC provides river discharge data for more than 9000 stations and data up to 200 years old (grdc.bafg.de). In this study, generally, a 30-year time series (1971-2000) was used for validation.

3) Water surface extent: The validation of surface water extent was done by comparing the modeled surface water extent with the global data set of naturally inundated areas (Adam et al. 2010) and observed inundation extent for the central Amazon region provided by Hess et al. (2003). The global-scale time series of monthly naturally inundated areas (NIA) (spatial resolution 0.5°) is a combination of the multisatellite data set of inundated areas (Papa et al. 2010) available for the time period 1993-2004 and data on monthly irrigated rice areas around the year 2000 (Portmann et al. 2010) (Section 3.1). The information on surface water extent from Hess et al. (2003) is based on 100-m resolution L-band SAR observations from the Japanese Earth Resources Satellite-1 (JERS-1) and represents low-water (September–October 1995) and high-water (May–June 1996) conditions in the central Amazon.

4) Water levels: Observed river water heights were provided from hydroweb (Crétaux et al. 2011). These time series are mainly based on altimetry data from Topex/Poseidon. The data is available from 1993-2011 and was used for validating river and floodplain water heights as simulated by WaterGAP.

## 4.7.2   Efficiency criteria for model performance

In order to evaluate the quality and the behavior of the hydrological model, I compared the model output to observed data on river discharge, water surface extent, water heights, and water storage. To provide objective assessment, mathematical measures – i.e. efficiency criteria – of how well the model simulation fits the observed data are required. This PhD work addresses comparisons of model-simulated data ($M$) with the observed data ($O$) for the same set of conditions (i.e., a pairwise comparison) over a given time period. Such time period is divided into $n$ time increments that can be of arbitrary duration (e.g. monthly or daily time steps). Missing values in observed and/or simulated values are removed before computations.

Numerous model evaluation statistics have been used in hydrological modeling studies and reported in the literature (Nash and Sutcliffe 1970; Willmott et al. 1985; Willmott 1981; Legates and McCabe 1999; Krause et al. 2005; Moriasi et al. 2007; Criss and Winston 2008). The quantitative statistics can be classified into three major categories: 1) Error index statistics, for example Mean Absolute Error (MAE), Root Mean Square Error (RMS), and Normalized Root Mean Square Error (NRMS), 2) standard regression statistics, for example Pearson product-moment correlation coefficient (r) and Coefficient of Determination ($R^2$) and 3) dimensionless statistics, for example Nash-Sutcliffe efficiency (NSE), Modified Nash-Sutcliffe efficiency (mNSE), Kling-Gupta efficiency (KGE), Index of Agreement (d), Modified Index of Agreement (md), Percent Bias (pbias), and volumetric efficiency (VE).

Error index statistics have the advantage that they quantify the error in the units of interest, which makes interpretation easier, but it is difficult to qualify what is considered

a low or high error. Standard regression statistics determine the strength of the linear relationship between modeled and observed data. They are almost always discussed in basic statistics texts and are, consequently, familiar to most scientists, but suffer from limitations that make them poor measures of model performance – i.e. insensitivity to over- or underestimation. Dimensionless statistics provide a relative model evaluation assessment, so that the resulting statistic and reported values can apply to various constituents (Legates and McCabe 1999).

As none of the methods for quantifying the goodness-of-fit of observations against model-calculated values is free of limitations, a combination of different efficiency criteria is currently recommended (Krause et al. 2005; Legates and McCabe 1999). To evaluate model efficiency, Moriasi et al. (2007) suggest to use three quantitative statistics in addition to the graphical techniques.

In this PhD work, I operationally determined model efficiency by calculating the coefficient of determination R², the Nash-Sutcliffe Efficiency NSC (Nash and Sutcliffe 1970), and the volumetric efficiency VE (Criss and Winston 2008). Furthermore, I use graphical methods – scatter plots and hydrographs – for a visual inspection of model performance. The reasons why I selected these three statistics to evaluate model performance are the following: 1) robustness in terms of applicability to various types of observations (e.g. discharge and water height) and different locations (e.g. discharge at multiple gauges, in various river basins and climatic conditions), 2) widespread use, acceptance, and recommendation in published literature, and 3) information on performance ratings.

The coefficient of determination R² describes how much of the variance in the observed data is explained by the variance of the modeled data. R² is defined as the squared value of the covariance between the two variables divided by the product of their standard deviations, and can range from zero to one (Equation 4.29).

$$R^2 = \left( \frac{\sum_{i=1}^{n}(O_i - \bar{O})(M_i - \bar{M})}{\sqrt{\sum_{i=1}^{n}(O_i - \bar{O})^2} \sqrt{\sum_{i=1}^{n}(M_i - \bar{M})^2}} \right)^2 \qquad 4.29$$

R² is independent of model bias and oversensitive to model outliers; serious defects already pointed out by Legates and McCabe (1999) and many others. Only the dispersion is quantified. "A model which systematically over- or underpredicts all the time will still result in good R² values close to 1.0 even if all predictions were wrong" (Krause et al. 2005, p. 90). However, due to the fact that standard regression statistics are almost always discussed in basic statistical texts and, consequently, they are familiar to virtually all scientists, R² continues to be used to determine how well a model simulates the observed data. R² is assumed to provide fundamental information on how well the sequence of higher and lower values in an observed time series is represented by the model (Hunger and Döll 2008).

The model efficiency proposed by Nash and Sutcliffe (1970) (NSE) is defined as one minus the mean squared error between modeled and observed data, normalized by the variance of the observed data (Equation 4.30).

$$NSE = 1 - \frac{\sum_{i=1}^{n}(O_i - M_i)^2}{\sum_{i=1}^{n}(O_i - \bar{O})^2}$$ 4.30

The efficiencies can range from $-\infty$ to 1. An efficiency of $NSE = 1$ represents a perfect fit of modeled and observed discharge. An efficiency of NSE lower than zero ($NSE < 0$) indicates that the average of the observed time series would be a better estimation than the model (Schaefli and Gupta 2007; Gupta et al. 2009).

In hydrological modeling, NSE is a very commonly used statistic coefficient to measure the goodness-of-fit of a model, which provides extensive information on reported values. Its use is recommended by Moriasi et al. (2007) among others. NSE is considered to be more appropriate than $R^2$ as it considers, besides the correlation, the standardized bias (Legates and McCabe 1999; Krause et al. 2005) and thus reflects the overall fit of a hydrograph. One of the main concerns about NSE is the use of the mean observed value as a reference, which may lead to an overestimation of the model success for strongly seasonal time series and, otherwise, oddly large negative NSE values do not necessarily indicate that some model is extremely poor, but only that the time series of observation is very steady. A comparison of NSE across basins with different seasonality should be, therefore, interpreted with caution (Criss and Winston 2008; Gupta et al. 2009). Another problem of NSE, and also $R^2$, is that it overemphasizes high values and neglects low values (Legates and McCabe 1999; Krause et al. 2005).

Criss and Winston (2008) proposed a volumetric efficiency (VE) to circumvent several disadvantages of NSE. VE is calculated by subtracting the ratio between the mean absolute error and the mean of the observations from one (Equation 4.31).

$$VE = 1 - \frac{\sum_{i=1}^{n}|M_i - O_i|}{\sum_{i=1}^{n} O_i}$$ 4.31

Similar to NSE, VE is dimensionless and ranges from minus infinite to one. Since VE is based on the absolute error, not the squared error like NSE, it emphasizes neither high nor low values, and reflects a more dynamic sensitivity. In studies where VE has been applied for model evaluation, it was found to be effective and robust, and has been recommended for use (Birkel et al. 2010; Cheng 2015). Especially during low flows or for time series with small standard deviation, VE should be preferred over NSE. However, as the volumetric efficiency is relatively new, information on value ranges is less available than for NSC. Furthermore, VE is only applicable for observations with positive values; therefore VE is not suitable for evaluating the model performance of average normalized data (e.g. average normalized total water storage variations).

Only if two of the tree model evaluation statistics exceed certain threshold efficiencies, the model is assumed to work well in terms of its internal contribution to the output of interest. In general, model simulation is considered to be acceptable when NSE > 0.5 (Moriasi et al. 2007; Ritter and Muñoz-Carpena 2013). Birkel et al. (2010) set the same efficiency thresholds for VE as for NSE and higher efficiency thresholds for $R^2$. In this PhD thesis, the model performance is quantified by using four grades with ratings listed in Table 4.4.

**Table 4.4**   Criteria for a goodness-of-fit evaluation.

| Performance rating | $R^2$ | NSE, VE |
|---|---|---|
| Very good | > 0.85 - 1 | > 0.75 - 1 |
| Good | > 0.75 - 0.85 | > 0.65 - 0.75 |
| Acceptable | > 0.6 - 0.75 | > 0.5 - 0.65 |
| Unsatisfactory | 0 - 0.6 | -Inf - 0.5 |

Nevertheless, the listed ratings are taken only as a guideline for interpreting the goodness-of-fit of model predictions, as they may differ depending on model applications (Beven 2007). Besides that, model performance always depends on the quality of the validation data, which is discussed in Chapter 6.

CHAPTER 5

# Results

## 5.1  Introduction

In this chapter, I present the results of the global hydrological model WaterGAP with an integrated floodplain algorithm (WaterGAP 2.2b_fpl); the algorithm I developed as part of this PhD thesis.

The results of WaterGAP 2.2b_fpl are mainly influenced by three changes compared to the former WaterGAP model version 2.2b:

1) the methods for calculating flow velocities,
2) the implementation of dynamic floodplain inundation, and
3) the adjusted model calibration parameters.

For a better understanding and interpretation of the final results of WaterGAP 2.2b_fpl (Section 5.4), I present separately in Section 5.2 and 5.3, the effect on model results of the three main differences to the former WaterGAP version 2.2b.

Section 5.2 displays the effect of changing the method for calculating flow velocity on modeled river flow velocity, water storage, and river discharge (using WaterGAP 2.2b_fpl, not calibrated). The model results are compared to ground observations on river flow velocities and river discharge.

With the implementation of dynamic floodplain inundation into WaterGAP, cell discharge is separated into river and floodplain discharge, and the former static global wetlands area of GLWD (see Section 4.4.2) is replaced by the temporally and spacially varying floodplain area. This is described, illustrated and compared to WaterGAP 2.2b in Section 5.3 (calculating river depth within the equation of flow velocity as a function of river storage at previous time step, as applied in WaterGAP 2.2b_fpl, enables direct comparison). Furthermore, the effect of calibrating the floodplain model WaterGAP 2.2b_fpl on model outputs is also shown.

Finally, Section 5.4 presents the results of WaterGAP 2.2b_fpl, including the new flow velocity method, the floodplain algorithm, and appropriate calibration parameters. This section also highlights the overall improvement of WaterGAP 2.2b_fpl with respect to the former WaterGAP 2.2b version (in WaterGAP 2.2b river depth within the equation of flow velocity is calculated as a function of river discharge) and compares and validates model output to a number of observed data sets, as well as to a number of studies made by other global hydrological and large-scale models which include floodplain algorithms. Furthermore, WaterGAP 2.2b_fpl with kinematic wave routing is compared to WaterGAP 2.2b_fpl allowing backwater flows (no separate calibration was done for the backwater model, as it was assumed that the change in river discharge is – for the

majority of regions on the globe – not significant; WaterGAP 2.2b_fpl backwater is run with the calibration parameters from WaterGAP 2.2b_fpl kinematic).

For the sake of simplicity, the names of the single WaterGAP model versions are often abbreviated. WaterGAP 2.2b is named shortly "WG22b" or even shorter "22b", WaterGAP 2.2b_fpl (fpl for floodplain) is named "WG22b_fpl" or "22bfpl". For the floodplain model, when referred to either kinematic routing or kinematic routing allowing backwater flows, the abbreviation of the model version is followed by "k" for kinematic or "b" for backwater.

## 5.2   Flow velocity

In previous model versions of WGHM (WaterGAP 2.1g and earlier versions) the flow velocity was constant, 1 m/s. In WaterGAP 2.2b, a variable flow velocity is applied, in which both river width and river depth are computed as a function of discharge, based on the close relationship between channel form and discharge (Leopold and Maddock 1953, Equation 4.21 and 4.22). The coefficients used in WaterGAP 2.2b were quantified by Allen et al. (1994) during a regression analysis with river cross sections in North America; these coefficients are valid for bankfull conditions (Equation 4.23 and 4.24).

Within the scope of this thesis, I implemented a new method into WaterGAP, which computes river depth as a function of river storage of previous time step instead of actual river discharge (Equation 4.26). In the reminder of this section, I present the results of variable river flow velocity modeled by WaterGAP 2.2b with floodplain algorithm and kinematic wave routing, applying the two methods of river depth calculation. For brevity, I named "old flow velocity method" (oldFV) the river flow velocity based on river depth, which is calculated as a function of river discharge, and "new flow velocity method" (newFV) the river flow velocity based on river depth, which is calculated as a function of river storage at previous time step. For a direct comparison of modeled results with the different flow velocity methods, I applied for both model variants the same calibration parameters (from WaterGAP 2.2b oldFV). This has to be kept in mind when comparing WaterGAP 2.2b newFV with observed data, because model performance might change slightly with a new calibration.

Figure 5.1 compares modeled flow velocities and observed flow velocity in the Amazon River basin. The comparison was done at 39 gauging stations, with data available from 1994 to 2009 with 3 to 13 years of ADCP (Acoustic Doppler Current Profiler) measures, depending on gauging station (www.ore-hybam.org/, Table 5.5). The map on the top of the figure shows the locations of the gauging stations and the spatial distribution of average monthly river flow velocity (1971-2000) in the Amazon River basin, after having applied the new flow velocity method. The calculated average river flow velocity for the Amazon basin is 0.97 m/sec. "It can be seen that river flow velocities in

mountains are significantly higher compared to lower regions [Figure 5.1], due to the comparably steep river bed slopes" (Verzano 2009). More than half of the Amazon basin grid cells (59%) have a lower flow velocity than 1 m/sec, the value which was used as a constant in previous WaterGAP model versions (26% of the grid cells are below 0.5 m/s and 16% > 1.5 m/s). The Amazon mainstream sticks out with a slightly higher flow velocity compared to the surrounding areas (Figure 5.1). Compared to the old method of flow velocity calculation, the new flow velocity is higher in flat regions and along major rivers (up to 0.64 m/s higher), and is almost half of the speed in mountain areas. The river flow velocity at gauging station locations is reproduced considerably better when applying the new versus the old flow velocity method. For 32 of 39 stations, the average modeled flow velocity is closer to the average observed flow velocity. In 85% of the stations, two of three efficiency criteria show better values when applying the new flow velocity compared to the old one (Table 5.5).

The improvement of model performance can also be stated by looking at the mean monthly river flow velocity (1971-2000) at 4 example stations located in the Amazon River basin (Figure 5.2).

However, WaterGAP still underestimates river flow velocity at 24 stations, and the fit in seasonality is slightly worse with the new flow velocity method; a statement which can be deduced from the lower R² values in almost two-thirds of the stations (Table 5.5).

When WaterGAP 2.2b with floodplain algorithm is compared to WaterGAP 2.2b without floodplain algorithm, the change in modeled performance regarding river flow velocities is small (slightly better when floodplain algorithm is applied). The grid cells average values are a bit higher in WaterGAP 2.2b_fpl compared to WaterGAP 2.2b. The spatial pattern of high and low river flow velocities is almost equal within the two model variants.

A comparison of modeled and observed river flow velocities in the Yukon River basin leads to similar results to that of the Amazon River basin and is illustrated in the appendix (Appendix 2).
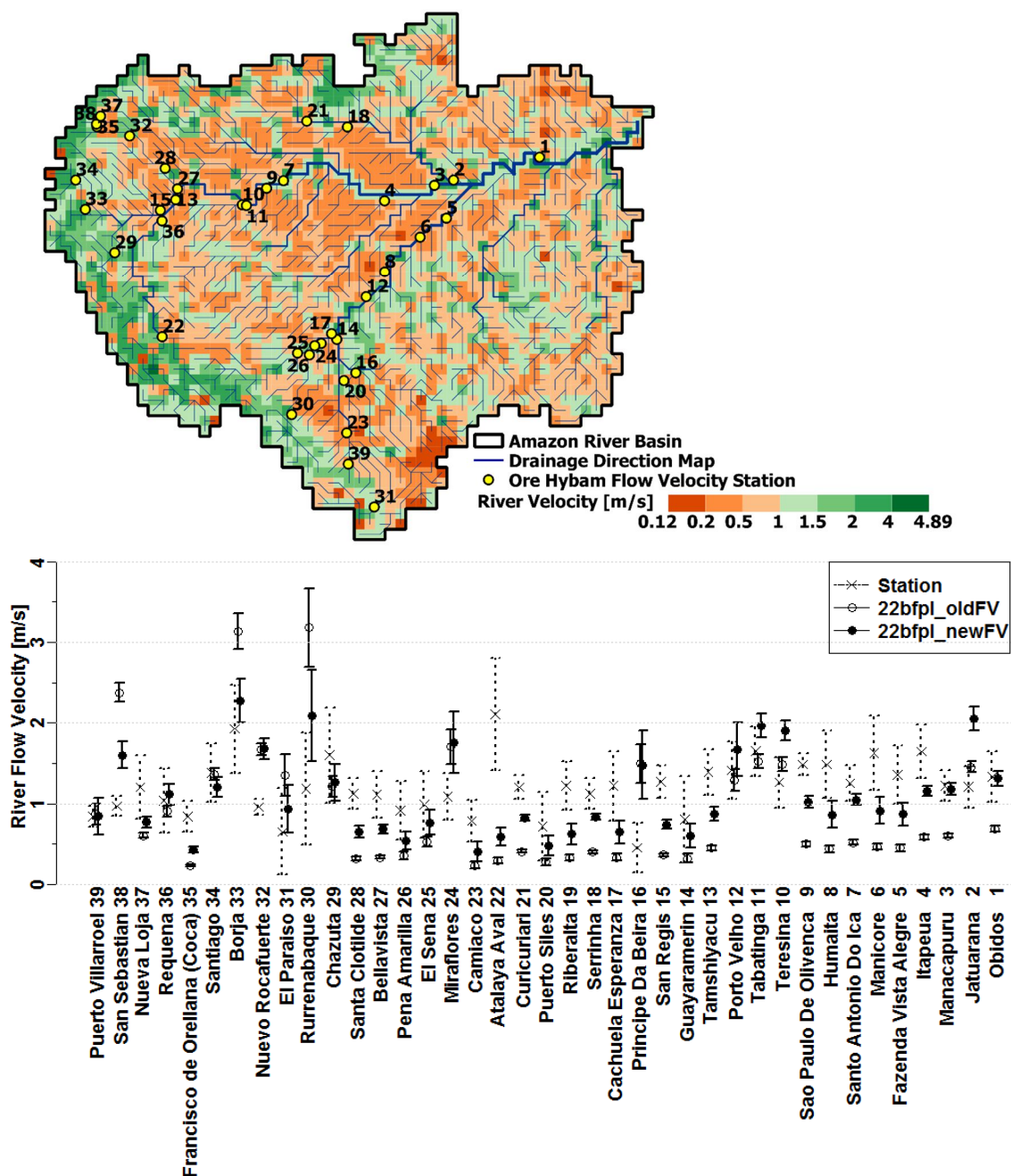
**Figure 5.1**   River flow velocity [m/s] of WaterGAP 2.2b_fpl with kinematic wave routing in the Amazon River basin. Top: Mean river flow velocity [m/s] 1971-2000 (newFV) and location of gauging stations. Bottom: Comparison of average simulated (WaterGAP 2.2b_fpl with the old and new method of calculating river flow velocity) and measured river flow velocity at 39 gauges in the Amazon River basin. The error bars indicate the standard deviations. Observed river flow velocity for the 39 gauges was available from 1994 to 2009 with 3 to 13 years of ADCP measures depending on gauging station (see Table 5.5). Data source: ORE HYBAM (www.ore-hybam.org/).
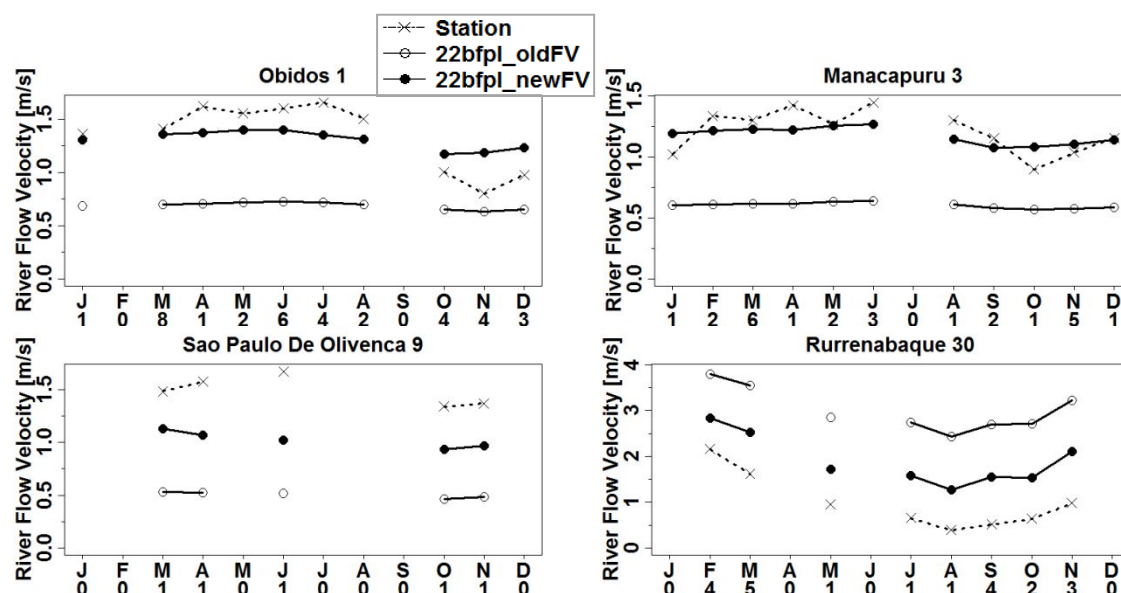
**Figure 5.2** Mean monthly (1971-2000) river flow velocity at 4 stations located in the Amazon River basin. The numbers on the x-axis are the number of observations per month in the time period 1994-2009. Modeled river flow velocity has been computed by WaterGAP 2.2b with floodplain algorithm (22bfpl (kinematic)), applying variable flow velocity with river depths based on 1) river discharge (old flow velocity (oldFV)) and 2) river storage of previous time step (new flow velocity (newFV). Data source: ORE HYBAM (www.ore-hybam.org/).

**Table 5.5** Gauging stations with flow velocity data: Characteristics and quality criteria. Observed monthly river flow velocity is compared to modeled river flow velocity computed by WaterGAP 2.2b_fpl (kinematic), calculating variable flow velocity with river depths based on 1) river discharge (old flow velocity (oldFV)) and 2) river storage of previous time step (new flow velocity (newFV). Source of observed data: ORE HYBAM (www.ore-hybam.org/); for station names and station locations see Figure 5.1.

| Station | Catchment area [$10^3$ km³] | ADCP start | ADCP end | No. of obser-vations | Mean flow velocity[m/s] obs/oldFV/newFV | R² oldFV/newFV | NSC oldFV/newFV | VE oldFV/newFV |
|---|---|---|---|---|---|---|---|---|
| 39 | 5.88 | 1997 | 2008 | 16 | 0.85/0.87/0.84 | 0.48/0.49 | -0.08/-1.41 | 0.48/0.07 |
| 38 | 6.15 | 2001 | 2009 | 25 | 0.97/2.38/1.61 | -0.12/-0.08 | -144.50/-31.12 | -0.83/-0.32 |
| 37 | 9.23 | 2002 | 2009 | 17 | 1.21/0.61/0.77 | 0.30/0.31 | -2.46/-1.25 | -0.26/-0.14 |
| 36 | 21.41 | 2002 | 2007 | 15 | 1.04/0.90/1.12 | 0.69/0.70 | 0.06/0.30 | 0.09/0.25 |
| 35 | 21.54 | 2001 | 2009 | 27 | 0.85/0.23/0.43 | 0.26/0.25 | -10.77/-4.91 | -0.40/-0.21 |
| 34 | 30.73 | 2001 | 2009 | 22 | 1.38/1.36/1.21 | 0.67/0.60 | 0.23/0.03 | 0.14/0.22 |
| 33 | 36.87 | 2003 | 2008 | 12 | 1.93/3.14/2.27 | 0.50/0.47 | -5.09/-0.21 | -0.01/0.25 |
| 32 | 46.16 | 2001 | 2009 | 18 | 0.96/1.67/1.68 | 0.35/0.40 | -52.79/-54.37 | -0.02/-0.01 |
| 31 | 55.49 | 2002 | 2006 | 7 | 0.65/1.35/0.94 | 0.84/0.79 | -1.40/0.25 | -0.19/0.35 |
| 30 | 68.20 | 1996 | 2008 | 21 | 1.19/3.18/2.10 | 0.85/0.86 | -7.87/-1.03 | -0.71/0.20 |
| 29 | 73.19 | 2003 | 2008 | 9 | 1.60/1.21/1.27 | 0.88/0.88 | -0.15/0.17 | 0.17/0.34 |
| 28 | 86.15 | 2001 | 2006 | 5 | 1.13/0.32/0.65 | 0.75/0.71 | -22.00/-7.41 | -0.16/0.20 |
| 27 | 98.44 | 2001 | 2008 | 17 | 1.11/0.33/0.68 | 0.75/0.72 | -7.81/-2.15 | -0.19/0.08 |
| 26 | 101.19 | 2003 | 2008 | 13 | 0.92/0.36/0.54 | 0.93/0.92 | -2.33/-0.67 | -0.07/0.19 |
| 25 | 123.21 | 2003 | 2008 | 12 | 0.99/0.53/0.77 | 0.96/0.96 | -1.10/0.26 | 0.04/0.34 |
| 24 | 126.23 | 1996 | 2005 | 13 | 1.09/1.71/1.76 | 0.85/0.84 | -4.26/-5.38 | 0.36/0.28 |
| 23 | 161.65 | 2004 | 2008 | 10 | 0.79/0.24/0.40 | 0.95/0.94 | -4.73/-1.79 | -0.09/0.27 |
| 22 | 192.24 | 2003 | 2007 | 5 | 2.11/0.30/0.59 | 0.93/0.93 | -8.38/-5.66 | -0.28/-0.11 |
| 21 | 212.27 | 1996 | 2005 | 3 | 1.21/0.41/0.83 | 0.88/0.99 | -41.45/-9.02 | -0.12/0.21 |
| 20 | 218.32 | 2004 | 2008 | 13 | 0.72/0.28/0.48 | 0.95/0.93 | -0.95/0.12 | -0.08/0.21 |

| Station | Catchment area [10³ km³] | ADCP start | ADCP end | No. of observations | Mean flow velocity[m/s] obs/oldFV/newFV | R² oldFV/newFV | NSC oldFV/newFV | VE oldFV/newFV |
|---|---|---|---|---|---|---|---|---|
| 19 | 272.68 | 1996 | 2008 | 20 | 1.22/0.33/0.62 | 0.71/0.72 | -8.87/-3.69 | -0.17/0.19 |
| 18 | 283.04 | 1996 | 2005 | 3 | 1.13/0.40/0.84 | 1.00/0.96 | -20.95/-3.06 | -0.12/0.15 |
| 17 | 305.73 | 2002 | 2008 | 15 | 1.22/0.33/0.65 | 0.91/0.90 | -4.38/-1.43 | -0.16/0.17 |
| 16 | 353.19 | 2004 | 2008 | 8 | 0.46/1.50/1.48 | 0.98/0.96 | -12.58/-12.30 | -1.29/-1.28 |
| 15 | 367.59 | 2003 | 2008 | 17 | 1.28/0.37/0.74 | 0.81/0.72 | -20.95/-6.98 | -0.18/0.12 |
| 14 | 613.77 | 1996 | 2008 | 18 | 0.81/0.32/0.61 | 0.95/0.93 | -0.68/0.30 | -0.08/0.24 |
| 13 | 745.93 | 2002 | 2008 | 20 | 1.40/0.45/0.88 | 0.86/0.76 | -11.49/-3.14 | -0.13/0.18 |
| 12 | 980.13 | 1995 | 2002 | 3 | 1.41/1.29/1.67 | 1.00/1.00 | 0.43/0.19 | 0.38/0.81 |
| 11 | 982.33 | 1995 | 2003 | 5 | 1.65/1.52/1.97 | 0.62/0.50 | 0.05/-1.09 | 0.18/0.25 |
| 10 | 982.33 | 1995 | 2001 | 3 | 1.27/1.49/1.91 | 0.99/1.00 | -0.26/-5.64 | 0.26/0.22 |
| 9 | 1022.21 | 1995 | 2003 | 5 | 1.49/0.50/1.02 | 0.76/0.54 | -61.43/-13.50 | -0.05/0.29 |
| 8 | 1101.29 | 1995 | 2002 | 3 | 1.49/0.44/0.87 | 0.84/0.88 | -9.32/-2.81 | -0.15/0.25 |
| 7 | 1151.38 | 1995 | 2003 | 6 | 1.25/0.52/1.05 | 0.80/0.60 | -13.28/-0.79 | -0.07/0.19 |
| 6 | 1156.27 | 1995 | 2002 | 3 | 1.63/0.47/0.91 | 0.99/0.98 | -9.27/-2.99 | -0.16/0.22 |
| 5 | 1305.17 | 1995 | 2002 | 6 | 1.36/0.45/0.87 | 1.00/0.95 | -7.18/-1.57 | -0.10/0.29 |
| 4 | 1807.65 | 1995 | 2003 | 6 | 1.65/0.59/1.16 | 0.88/0.90 | -12.25/-2.34 | -0.13/0.13 |
| 3 | 2228.52 | 1994 | 2006 | 25 | 1.22/0.60/1.18 | 0.76/0.70 | -10.89/0.35 | -0.04/0.33 |
| 2 | 2926.70 | 1995 | 2003 | 19 | 1.21/1.46/2.06 | 0.94/0.93 | -0.52/-10.50 | 0.23/0.18 |
| 1 | 4658.80 | 1995 | 2007 | 35 | 1.34/0.69/1.31 | 0.94/0.88 | -4.03/0.42 | -0.02/0.28 |
| Mean | 639.47 | | | 13 | 1.21/0.90/1.09 | 0.78/0.75 | -13.48/-5.02 | -0.10/0.15 |
| Median | 218.32 | | | 13 | 1.21/0.53/0.91 | 0.85/0.86 | -7.18/-1.79 | -0.09/0.21 |

To investigate the effect of variable flow velocity on water storage and river discharge, I ran WaterGAP with the old and new method of river flow velocity calculation and compared both model outputs.

Figure 5.3 shows mean monthly values of modeled river flow velocity, river discharge, and water storages (total, surface and river water storage) with both old and new flow velocity, within the Amazon River basin. River flow velocities in the Amazon River basin are highest at peak flow (March) and decline during low discharge (minimum discharge and river flow velocity in September). In the basin average, the new river flow velocity is lower compared to the old river flow velocity (in mountain areas flow velocity is almost halved, but nearly doubled along the main stem). The seasonal variation is higher, because of the lower minima flow velocities in most of the grid cells. As in the old method, the coefficients in the equation of river depth are valid for bankfull conditions. The old method is, in times of low flows, less suitable. The new river flow velocity leads to lower river water storage and consequently to a lower surface and total water storage (Figure 5.3). The other storage compartments computed by WaterGAP, like lake water or groundwater storage, show no significant change by applying the new instead of the old flow velocity. The river discharge – the timing of maximum and minimum – is shifted to one to two month earlier compared to the model simulation with the old flow velocity method.
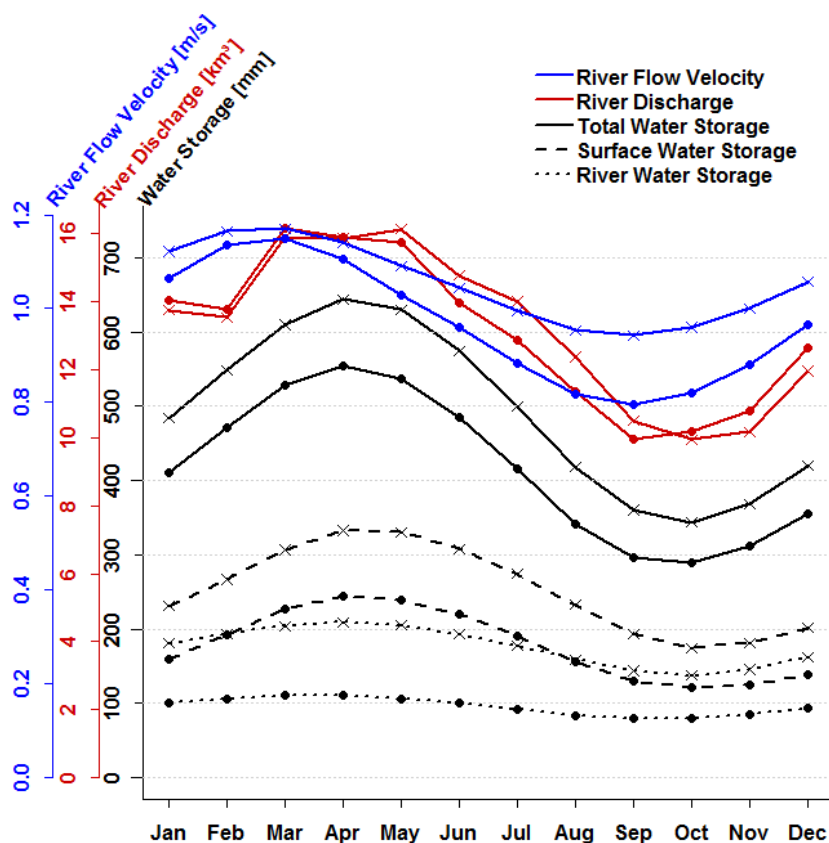
**Figure 5.3** Averaged variable river flow velocity, river discharge and water storage compartments for the Amazon River basin (1971-2000). Simulated by WaterGAP 2.2b_fpl applying old (x) and new (filled dots) river flow velocity.

Furthermore, in order to evaluate the effect of changing river flow velocity on modeled river discharge, I compared modeled river discharge of both model versions (WaterGAP 2.2b_fpl kinematic with old and new flow velocity) at 40 gauging stations located in the Amazon River basin for the period 1961-1996 (depending on data availability; for some stations, shorter time series had to be applied; Data source GRDC). These stations are part of the 1235 discharge stations worldwide, which were used for WaterGAP model calibration. Figure 5.4 exemplifies the comparison for five discharge stations.

The differences between the two model simulations are, for the most part, quite small. Compared to the observed data, both show slightly lower mean discharge values (7 to 8 percent lower) and lower standard deviations (about one third). The seasonal variability fits well with the observed data in most of the stations (about three-quarter of the stations have a $R^2$ value of at least 0.6). Nevertheless, the model performance increases in only 20% of the stations applying the new flow velocity instead of the old flow velocity. In 24 of 40 stations, at least two of the three efficiency criteria ($R^2$, NSE, VE) are worse when applying the new flow velocity method. Most notably is the shift in maximum discharge to one or two months earlier in some stations (Figure 5.4), which results in poorer $R^2$ values.

75
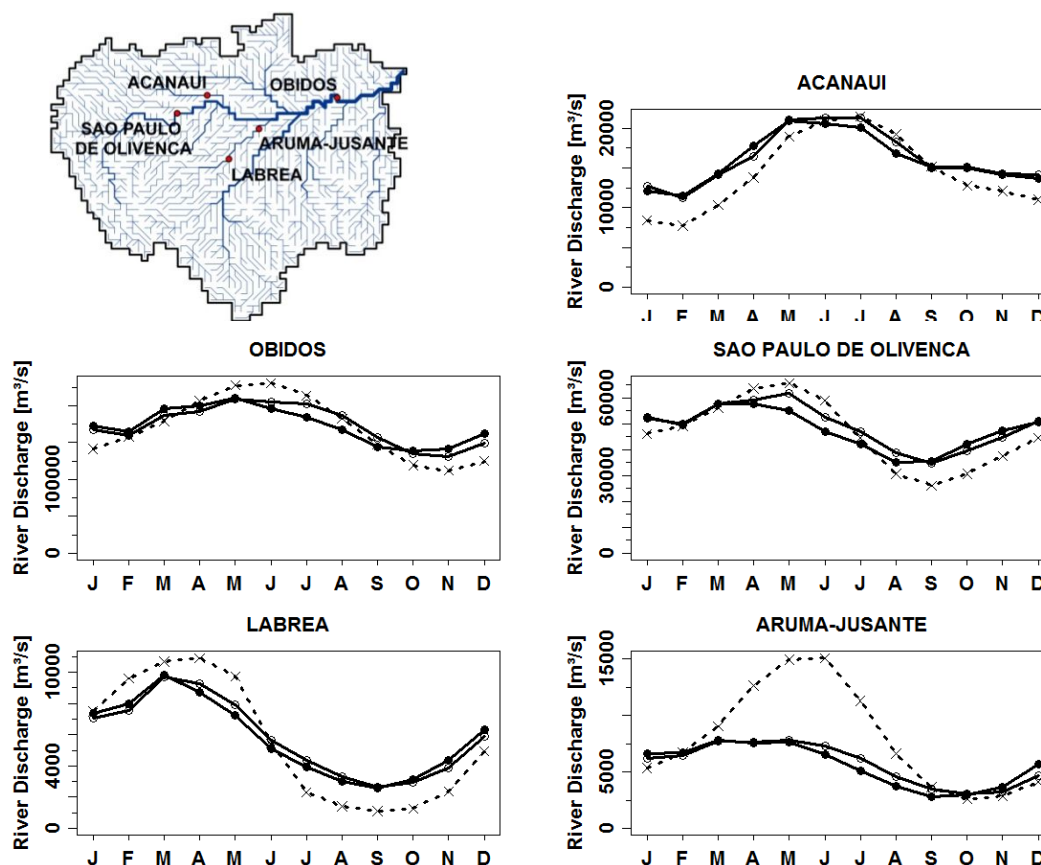
**Figure 5.4** Effect of the variable flow velocity on average long term monthly discharges (1971-2000) at five gauging stations in the Amazon River basin. The dotted lines are observed values (GRDC 2013) and the solid lines are the WaterGAP simulations applying dynamic flow velocity with river depths based on 1) river discharge (circles) and 2) river storage at previous time step (filled circles).

It can be concluded that the calculation of river depth within the flow velocity equation as a function of previous river water storage, instead of river discharge, leads to significant improvement of modeled river flow velocities when compared to observation data. The effect of a change in flow velocity is also meaningful for river water storage, which is lower, but less important for river discharge.

## 5.3 Dynamic floodplain inundation and model calibration

WaterGAP 2.2 is calibrated in a basin-specific manner against mean annual observed river discharge at 1319 gauging stations (WaterGAP 2.1g at 1235 gauging stations). The adjusted calibration factor is regionalized to grid cells outside the calibration basins (Müller Schmied et al. 2014). The observed discharge data is provided by the Global Runoff Data Center (GRDC). The calibration routine in WaterGAP 2.2b forces the long-term annual simulated discharge to be equal (within ±1 %) to the observed long-term annual discharge at grid cells representing calibration stations, for the period of observations (with a maximum of 30 years of observation being considered) (Müller

Schmied et al. 2016). This force is done by varying one soil parameter and up to two correction factors within WaterGAP (Döll et al., 2003; Hunger and Döll, 2008).

To analyze the effect of implementing the floodplain algorithm into WaterGAP and the calibration of the final model WaterGAP 2.2b_fpl, I compared three WaterGAP runs one another:

1) WaterGAP 2.2b (WG22b),
2) WaterGAP 2.2b_fpl, including floodplains and with kinematic wave routing using the calibration parameters of WG22b (kNoCal), and
3) WaterGAP 2.2b_fpl, including floodplains with kinematic routing and new (accurate) calibration parameters (kCal).

To enable a direct comparison, all three models, including WG22b, were calculated applying the new flow velocity method (computing river depth as a function of river storage of previous time step instead of actual river discharge; see Section 5.2).

Figure 5.5 illustrates monthly averaged modeled discharge in the time period 1971-2000 in eight major river basins. For the WaterGAP runs with floodplain algorithm both river discharge and total discharge (river + floodplain discharge) are shown. By implementing dynamic floodplain inundation, river discharge peak flows are reduced because water flows into the adjacent floodplain when the bankfull flow is reached. The sum of river and floodplain discharge (total cell discharge) differs from that in WG22b. This is mainly due to the fact that water storage on the static GLWD global wetlands differs from that on active floodplains in terms of total volume and seasonality. While the wetlands of GLWD implemented in WGHM are almost always full of its capacity (Section 3.2), the dynamic floodplains show a high variation in storages. In WaterGAP with floodplain algorithm, river discharge diminishes slower after peak flow because water from the floodplains still drain back into the rivers when river discharge is below bankfull flow (see e.g. Amazon and Nile in Fig 5.5). With the calibration of the floodplain model, mean river discharge and also total discharge rises in four of the eight analyzed river basins and stays almost equal in the other four river basins (Figure 5.5). The effect of calibration on water storage is proportional to that on river discharge.
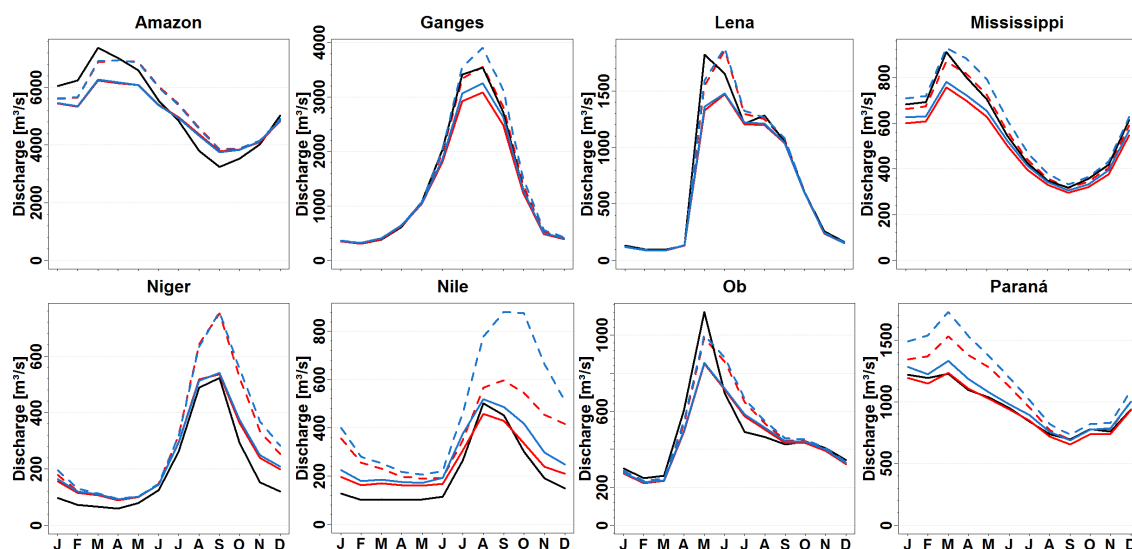
**Figure 5.5** Monthly average modeled river (solid lines) and total discharge (river + floodplain discharge, dotted lines) in eight major river basins in the time period 1971-2000. The black lines represent WaterGAP 2.2b, the red lines WaterGAP 2.2b_fpl NoCal, and the blue lines WaterGAP 2.2b_fpl Cal. For a better comparison, all of them calculated with the new flow velocity method.

The box plot in Figure 5.6 gives an overview of the model efficiency values $R^2$, NSE, and VE. Modeled river discharge was compared to observations from 248 gauging stations (GRDC 2013) located within the eight major river basins (Figure 5.6 left); among them, 40 stations located in the Amazon River basin (Figure 5.6 right). The box plots represent the median (bold line), the 25% and the 75% quartile (box), and the maximum and minimum of the data within 1.5 times the interquartile range (whiskers). Outliers are not drawn. It can be clearly seen that with the implementation of the floodplain algorithm into WaterGAP, the model performance increases. Average model performance is almost equal for the non-calibrated and the calibrated version. The medians of standard deviation and mean river discharge are very similar to the observed discharge in all of the three models (not shown).
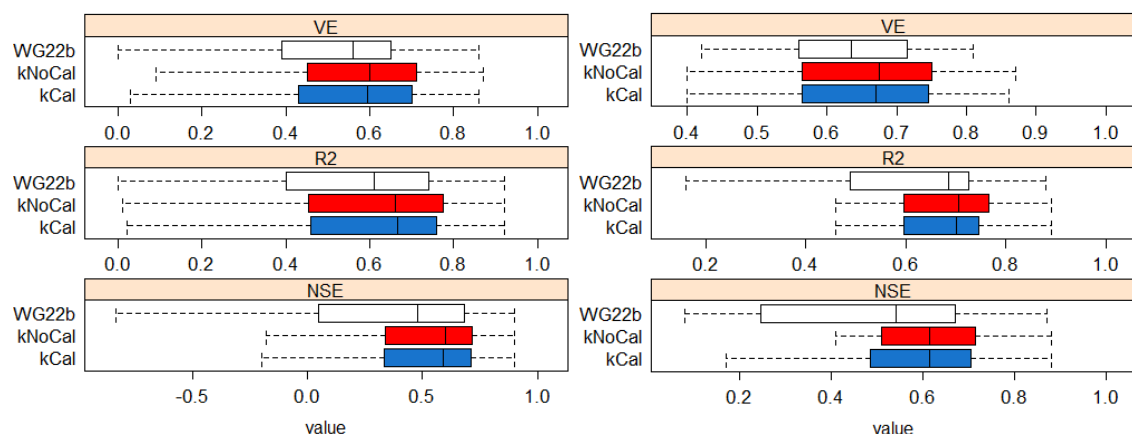


**Figure 5.6** Box plot of model performance simulating river discharge at 248 locations within eight major river basins (**left**); among them, 40 locations within the Amazon River basin (**right**). Simulated river discharge of WaterGAP 2.2b (WG22b), WaterGAP 2.2b_fpl kinematic not calibrated (kNoCal) and WaterGAP 2.2b_fpl kinematic calibrated (kCal) compared to observed

river discharge from GRDC (GRDC 2013) in the time period 1971-2000 (occasional missing data in some stations). All WaterGAP runs apply the new method for calculating river flow velocity. Location and additional information of the discharge gauging stations are listed in the appendix (Figure A.11, Table A.1). The box plot represents the median, 25% and 75% quartile (box), and the 1.5xIQR (whiskers). Outliers are not shown.

With the implementation of dynamic floodplain inundation into WaterGAP, the former static global wetlands area of the Global Lakes and Wetland Database GLWD (see Section 4.4.2) is replaced by the temporally and spatially varying floodplain area. Figure 5.7a shows monthly average (1971-2000) floodplain area (dashed lines) and total surface water extent in the Amazon River basin. The total surface water extent consists of the sum of the inundation area on the floodplain, determined by applying the hypsographic approach (Section 4.4.1), and the area of other water bodies in WGHM, which are based on the GLWD (Section 4.4.2). Here, the Amazon River basin is illustrative for all of the river basins. The seasonal variation of the inundation area in the floodplains, and consequently the total surface water extent as well, is higher or even much higher than that of the former global wetlands of GLWD; the mean surface water extent is lower in all river basins. Note, that the mean value is very much dependent on the presence and extent of other surface water bodies than floodplain area, for example, local wetlands and lakes; by contrast, the seasonality is mainly driven by the dynamic floodplain inundation. Floodplain/wetland storage and total water storage behave similar to surface water extent, with higher seasonality and lower mean values in WaterGAP 2.2b_fpl compared to WaterGAP 2.2b (Figure 5.7b). The effect of model calibration on surface water extent and water storages is similar to that on river discharge, with equal or higher values in the calibrated model version compared to the non-calibrated one.
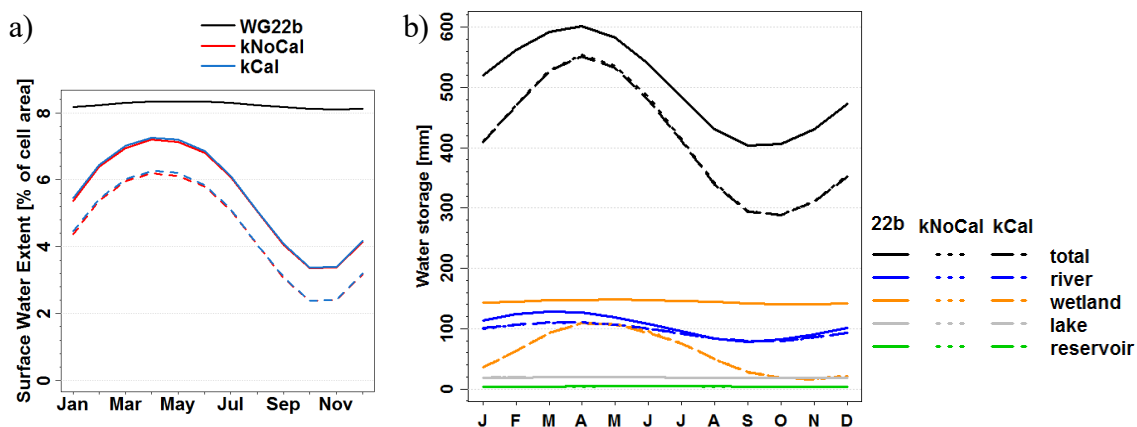


**Figure 5.7** Modeled mean surface water extent (a) and water storages (b) of the Amazon River basin in the time period 1971-2000. Plotted lines are labeled in the figure legends. The dashed lines in figure (a) represent the floodplain extent only and the solid lines the total surface water extent including all surface water bodies.

## 5.4 Final results of calibrated WaterGAP 2.2b floodplain model

### 5.4.1 Water Level

Water level and water level changes are evaluated using the HYDROWEB hydrological database (Crétaux et al. 2011). The water level time series are mainly based on Topex/Poseidon GDRs (Geophysical Data Records). The data is available at a 10 days' time step (the duration of an orbital cycle) from 1993 to 2011 (with occasional missing data). The basic data for rivers are the 10 Hz altimetry data. Virtual stations are defined corresponding to the intersection of the satellite track with the river (http://www.legos.obs-mip.fr/soa/hydrologie/hydroweb/General_Info.en.html). Modeled and observed water levels are compared at 80 sites located in 6 major river basins (Figure A.11).

WaterGAP computes relative water heights for rivers and floodplains, in which river water levels equal the floodplain water levels in case of flooding. To compare with the altimetry data, the minimum elevation of a grid cell ($z_{min}$) was added to the relative water heights of WaterGAP 2.2b_fpl kinematic (WG22b_fpl k) and WaterGAP 2.2b_fpl backwater (WG22b_fpl b).

The modeled water levels are in quite good agreement with the observations. The overall R² for the time series of monthly values (1993-2010, if available), averaged over all sites per river basin, ranges from 0.8 (Ganges) to 0.98 (Niger and Paraná) in WG22b_fpl k; and from 0.36 (Niger) to 0.98 (Amazon and Paraná) in WG22b_fpl b. The R² averages over all river basins are 0.94 and 0.78 in WG22b_fpl k and WG22b_fpl b respectively. The volumetric efficiency (VE) reaches acceptable values only in WG22b_fpl b, ranging from 0.45 (Niger) to 0.9 (Paraná) with an average of 0.72. NSE values are high only for Ganges (0.95) and Paraná (0.64) in WG22b_fpl b.

The model performance varies strongly from basin to basin and site to site. At most sites the performance of the mean water level is poor, resulting in very low NSE and low VE values. The difference of modeled and observed mean water levels is lower in regions with elevations close to sea level than at higher altitudes, suggesting that the minimum elevation of the grid cells, derived from digital elevation models, does not agree with the altimetry measured elevations.

In both WaterGAP 2.2b_fpl models, the simulated seasonality and interannual variability of water heights are in good agreement with the observations (Figure 5.9 and Figure 5.8). The seasonality is represented slightly better in WG22b_fpl k than in WG22b_fpl b, but it overestimates the magnitude. Especially low water levels are extremely low in WG22b_fpl k compared to observations.

The interannual variability of water levels is well simulated with both models in most of the six analyzed river basins (Figure 5.8); low water years and high water years (in the Amazon River basin, 1993 and 2002, respectively) agree with the observations.
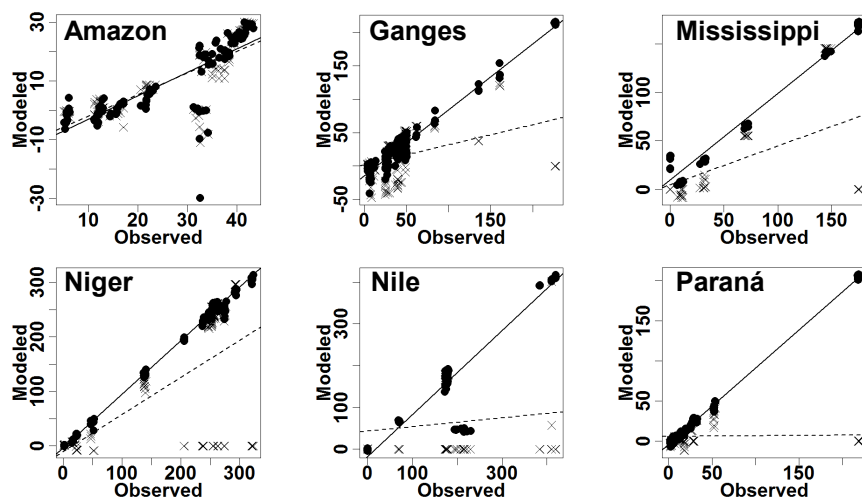


**Figure 5.8** Scatter diagram of observed versus modeled mean annual water levels [m a.s.l.] for 80 locations in 6 river basins for the years 1993 to 2010 (for location of altimetry gauging stations and additional station information see Figure A.11 and Table A.2 in the appendix). Modeled water levels are from WG22b_fpl k (filled circles and solid regression line) and WG22b_fpl b (crosses and dashed regression line).

Figure 5.9 shows water level changes at five altimetry sites located in the Amazon River basin. Site 1 shows the overestimation of magnitude in WG22b_fpl k exemplarily for many of the analyzed 80 observation sites in the six river basins. In contrast, the magnitude of water levels is smoothed allowing backwater flows. At some stations, where backwater flows last over several months of the year, water level change gets close to zero (site 5 in Figure 5.9). The model efficiency of average monthly water levels at the five sites is listed on the bottom of Figure 5.9, indicating a good agreement between simulated and observed data (two of three efficiency criteria are within acceptable range). On average WG22b_fpl b performs slightly better than WG22b_fpl k.

| Nr. | Station | River | Mean Water Level [m] observed | k | b | R² k | b | NSE k | b | VE k | b |
|-----|---------|-------|----------|-------|-------|------|------|--------|--------|-------|------|
| 1 | T228 | Amazon | 11.96 | -1.16 | 2.47 | 0.69 | 0.88 | -81.91 | -35.28 | -0.12 | 0.20 |
| 2 | 822_03,822_02 | Amazon | 33.30 | 34.91 | 34.19 | 0.65 | 0.63 | -2.65 | -3.56 | 0.9 | 0.89 |
| 3 | 493_01 | Amazon | 41.24 | 49.76 | 51.20 | 0.92 | 0.79 | -26.87 | -37.71 | 0.79 | 0.76 |
| 4 | 951_01,908_01 | Jupura | 38.96 | 47.78 | 47.13 | 0.81 | 0.76 | -22.4 | -19.44 | 0.78 | 0.79 |
| 5 | 493_03,493_02 | Jupura | 42.47 | 56.90 | 57.67 | 0.63 | 0.77 | -55.03 | -61.83 | 0.66 | 0.64 |
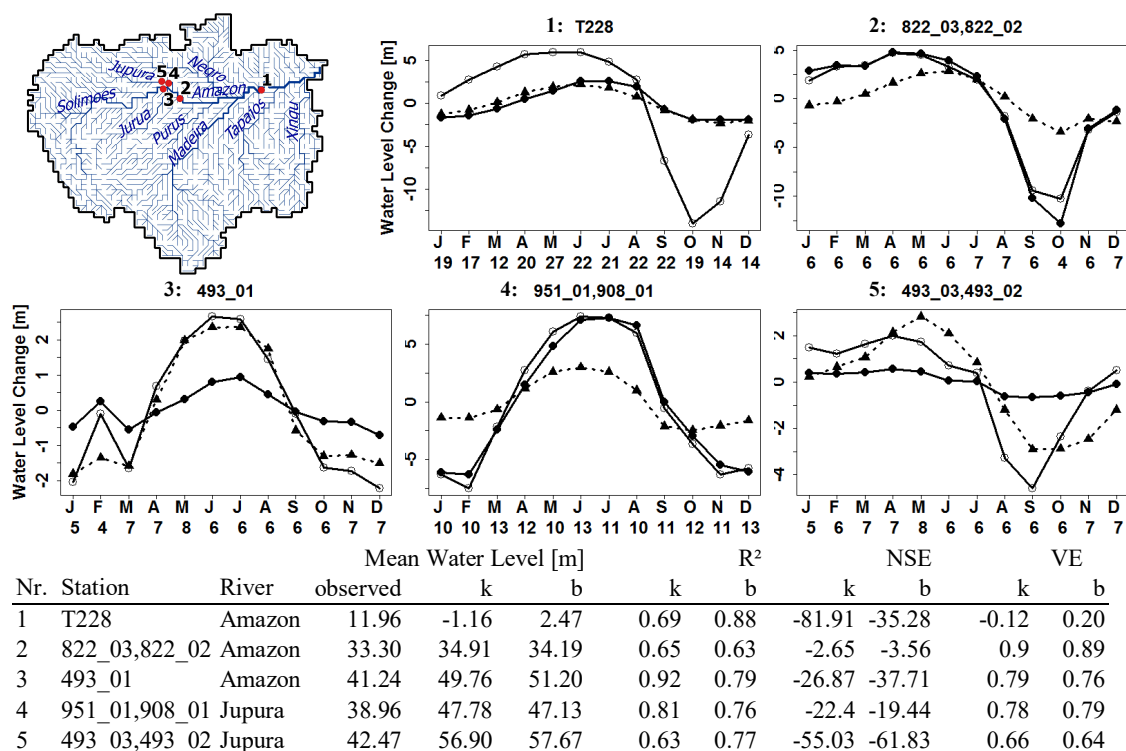
**Figure 5.9** Observed and modeled mean monthly water level changes (1993-2010) at five altimetry gauging stations in the Amazon River basin. The dashed line indicates observed values (Hydroweb) and the solid lines represent WG22b_fpl k (circles) and WG22b_fpl b (filled circles). Mean water levels and model efficiency of average monthly water levels for WG22b_fpl k (k) and WG22b_fpl b (b) are listed at the bottom.

## 5.4.2 River discharge

To analyze modeled river discharge of WaterGAP 2.2b, including the algorithm for dynamic floodplain inundation (WG22b_fpl), I compared model outputs of both WG22b_fpl with kinematic wave routing and WG22b_fpl allowing backwater flows to observed river discharge, as well as to modeled river discharge of the former WaterGAP version 2.2b (WG22b). The observed data are from the Global Runoff Data Centre (GRDC 2013), collected at 248 gauging stations located within eight major river basins: Amazon, Ob, Mississippi, Paraná, Ganges, Nile, Niger, and Lena (for locations and station information see Figure A.11 and Table A.1).

In addition to the visual inspection of the hydrographs, the performance of the different model simulations were quantified by using the three efficiency criteria: R², NSE, and VE (see Section 4.7.2). Modeled river discharge agrees well with observations at most of the 248 gauging stations. Model efficiency is highest in the WaterGAP model variant with floodplain algorithm and kinematic wave routing (WG22b_fpl k), and lowest in model variant allowing backwater flows (WG22b_fpl b). The median model efficiency values (R²/NSE/VE) for the three model variants are: 0.67/0.56/0.58 (WG22b), 0.67/0.59/0.60 (WG22b_fpl k) and 0.64/0.55/0.57 (WG22b_fpl b). Note that

82

WG22b_fpl b is not calibrated (calibration parameters are used from WG22b_fpl k); NSE and VE values might change with calibration.

The differences in model performance between the model variants become more noticeable when looking at the number of stations improved or worsened with the implementation of the floodplain algorithm. Comparing WG22b_fpl k with WG22b, from the total 248 stations, R² values increase at only 91 stations and decrease at 144 stations. In contrast, NSE and VE values increase at 124 and 121 stations, and decrease at only 113 and 106 stations, respectively. At 117 stations, at least two of the three efficiency criteria are higher in WG22b_fpl k compared to WG22b, 114 stations are lower, and 17 are equal. The model efficiency is illustrated in more detail (for single river basins) in Figure A.12 in the appendix.

Figure 5.10 shows average monthly river discharge at 7 gauging stations located in the Amazon River basin. The simulated monthly river discharge shows similar seasonal cycles. The hydrographs illustrate reduced peak flows in WG22b_fpl compared to WG22b because water flows from the river into the floodplain when the bankfull flow is reached. Also, the fact that river discharge diminishes slower after peak flow – as well as the high low flows at downstream locations – can be attributed to the implementation of the floodplain algorithm into WaterGAP, due to the drainage from the floodplain to the river in case river discharge is below bankfull flow and there is still water in the floodplain (see Section 5.3). At some stations, usually at locations with larger floodplain inundation, the reduced seasonal amplitude in WG22b_fpl compared to WG22b fits better to GRDC data, resulting in higher NSE and VE values.
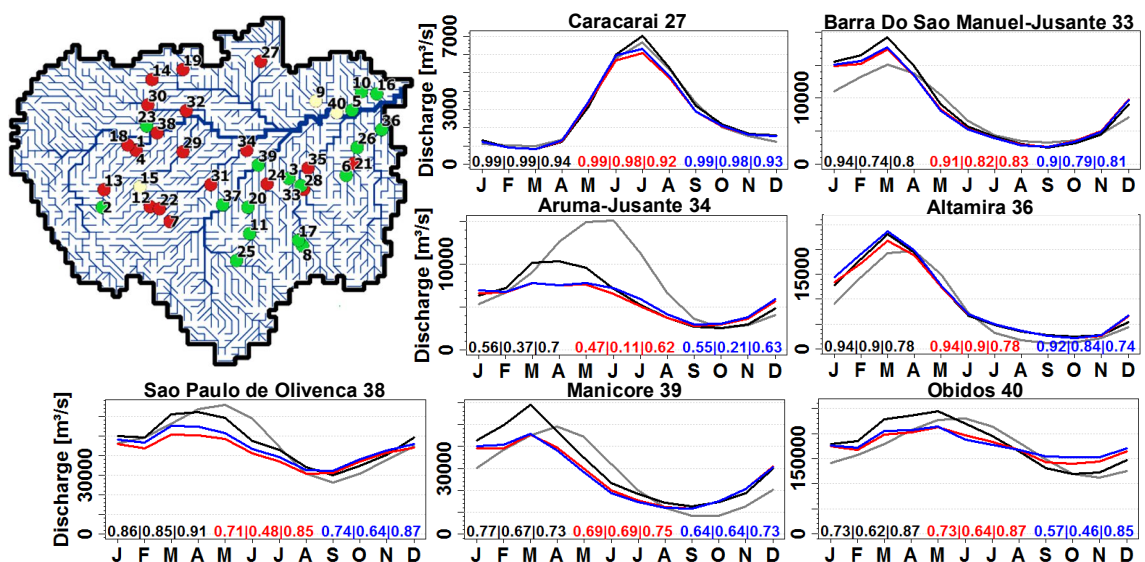


**Figure 5.10** Monthly average modeled and observed river discharge at seven gauging stations in the Amazon River basin in the time period 1971-2000. The gray lines indicate observed data from GRDC (2013), the black, red, and blue lines represent modeled data of WG22b, WG22b_fpl k, and WG22b_fpl b, respectively. The numbers at the bottom of each plot are the model efficiency values for the three model variants compared to GRDC, each with R²|NSE|VE. The map on the top left shows the change in model performance between WG22b_fpl k and the former WG22b at 40 river discharge stations when at least two of the three efficiency criteria are higher (green), equal (yellow), or lower (red).

Furthermore, at many stations river discharge in WG22b_fpl rises faster after reaching its minimum (e.g. at Sao Paulo de Olivenca, Figure 5.10), which is probably the main reason for the poorer R² values compared to WG22b. This fact can be attributed to the application of the new river flow velocity calculation, in which river depth in the equation of flow velocity is now calculated as a function of river storage at previous time step, instead of current river discharge (Section 5.2).

For most of the 248 stations, the timing of maximum and minimum river discharge agree well with GRDC data. However, WaterGAP tends to model the maximum of river discharge too early compared to observations. In the Amazon River basin, peak flow is shifted to one or two months earlier at 30% of the stations (12 of 40 stations in all model variants), whereas maximum river discharge is one month later than the observed at only 3 of the 40 stations.

The correlation of modeled and observed river discharge is on average almost equal for WG22b_fpl k and WG22b_fpl b, with an R² of only 0.02 better in the kinematic wave model (both at all 248 stations and at the 40 stations in the Amazon River basin).

"The Amazon main stem has tributaries in both hemispheres. In the south, peak rainfall periods occur between December and February, up to 6 months earlier than peak rainfall in the northern regions" (May to August) (Birkett et al. 2002). This geographical factor accounts for the different timing in maximum river discharge which occurs in the southern gauging stations from February to April and in the northern stations from May to July (e.g. station Caracarai in Figure 5.10). Meade et al. (1991) have found that the Amazon main stem is subject to backwater effects. Large tributaries which drain the southern Amazon River basin (especially the Madeira, Tapajós, and Xingu rivers) reach their peak discharges in April, two months earlier than the main stem does, resulting in backwater in the lowermost 800 km of the Amazon main stem, when they flow into it. The peak stage at Obidos usually precedes the peak stage 750 km upriver at Manacapuru (Meade et al. 1991). The effect of backwater flows can also be seen when looking at the hydrographs in Figure 5.10. Different from other southern gauging stations, the observed river discharge at Aruma-Jusante (located at the Purus River approximately 100 km south of where the Purus flows into the Amazon main stem) peaks in May, being similar to the gauging station Obidos located at the Amazon main stem 837 km downstream (http://www.grdc.sr.unh.edu/html/Polygons/P3625310.html). This fact is well simulated if backwater effects are applied in WaterGAP. Only in the model variant WG22b_fpl b, the river discharge at the station Aruma-Jusante peaks in May.

Many authors have reported the attenuation of peak discharge and flood wave due to the presence of floodplains (Sippel et al. 1998; Hamilton et al. 2004; Hamilton et al. 2007; Alsdorf et al. 2010; Lininger and Latrubesse 2016). At peak discharge, the excess water is absorbed by the floodplain so that river discharge increase slows or even stops as the

river water spreads onto the floodplain. The water stored on the floodplain by the end of the flooding season returns to the channel.

This observed attenuation of river flow peaks is represented also in WaterGAP, in the version including the floodplain algorithm. The effect of floodplains on river discharge can be seen in Figure 5.10 (station Obidos and Aruma-Jusante) but becomes even more noticeable when looking at daily river discharge. Figure 5.11 shows daily river discharge at stations Caracarai and Manicore, located in the Amazon River basin. The daily-scale fluctuations of river discharge at Manicore are suppressed. Manicore is a station at the Madeira River, with a large upstream area and extensive floodplains, which store water during floods and release it after the flood peaks (Alsdorf et al. 2010). In contrast, at Caracarai station, located at Branco River – a smaller tributary with less floodplain inundation – each flood wave is not fully attenuated by the floodplains, resulting in higher oscillations of daily river discharge.
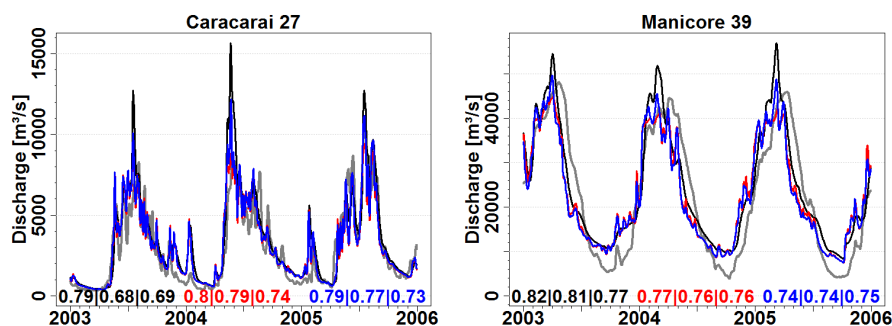


**Figure 5.11** Time series of modeled and observed daily river discharge at two gauging stations in the Amazon River basin (2003-2005). The gray lines indicate observed data from GRDC (2013), the black, red, and blue lines represent modeled data of WG22b, WG22b_fpl k, and WG22b_fpl b, respectively. The numbers at the bottom of each plot are the model efficiency values for the three model variants compared to GRDC, each with $R^2$|NSE|VE.

### 5.4.3 Surface Water Extent

Modeled surface water extent of WaterGAP 2.2b (WG22b), WaterGAP 2.2b_fpl kinematic (WG22b_fpl k), and WaterGAP 2.2b_fpl backwater (WG22b_fpl b) are compared with each other as well as to observations. Modeled surface water extent refers to the sum of the inundation area on the floodplain, determined by applying the hypsographic approach (Section 4.4.1), and the area of other water bodies in WGHM, which are based on the Global Lakes and Wetland Database GLWD (Section 4.4.2). The observations used for model validation are the global-scale time series of monthly naturally inundated areas (NIA) available for the time period 1993-2004, and the data set from Hess et al. (2003) representing low and high-water conditions in the central Amazon in the years 1995 and 1996. Both data sets are based on satellite observations. The first one is a combination of multisatellite data (Papa et al. 2010) and monthly irrigated rice areas (Portmann et al. 2010), used to obtain naturally inundated areas excluding man-made surface waters (Adam et al. 2010). The second one is a dual-season map for the central

Amazon region representing inundation extent under low- and high-water conditions (September/ October 1995 and May/ June 1996). This data was derived from high resolution SAR observations by Hess et al. (2003).

The terms "inundated area" and "surface water extent" are used more or less as synonyms in this study; although the term "inundated area" would be more appropriate for areas with higher seasonal change in extent, such as floodplains and wetlands, and "surface water extent" would be more appropriate when referred to the whole area of surface water bodies, including also lakes and reservoirs with less seasonality in their extent.

Before comparing the datasets among each other, the following characteristics of the datasets must be mentioned:

1) The NIA dataset excludes inland seas (Caspian Sea, Aral Sea), large lakes such as the Great Lakes in North America, for instance, and coastal pixels that are likely contaminated by the ocean (Papa et al. 2010; Adam et al. 2010).

2) GLWD is expected to represent a certain maximum extent of surface water bodies as it is based on mapping of wetlands (Lehner and Döll 2004). Within WaterGAP this maximum area can shrink (except for global lakes and reservoirs) due to a temporally varying area reduction factor that is a function of water storage at previous time step (Section 4.4.2).

3) The wetland mask from Hess et al. (2003) represents a certain maximum wetland area in the central Amazon. Additional to the real time flooded areas at high-water stage in May/ June 1996, non-flooded areas were also defined as wetlands – areas adjacent to or surrounded by flooded areas and displaying landforms consistent with wetlands geomorphology (Hess et al. 2003).

Figure 5.12 and 5.13 display global maps of average surface water extent and annual average seasonal variation as observed by NIA and as modeled by WG22b and WG22b_fpl k, as well as difference maps among one another. Due to the fact that the model results of WG22b_fpl k and WG22b_fpl b appear quite similar on a global map, only the differences between the two floodplain model variants (WG22b_fpl k and WG22b_fpl b) are mapped. All data are averaged for the time period 1993-2004, in which observations were available. For all of the WaterGAP grid cells, the average area of open water is 2.15 million km² for NIA, and 7.59, 5.83, and 5.85 million km² for the three model variants WG22b, WG22b_fpl k, and WG22b_fpl b, respectively.

**Average SWE 1993-2004:**
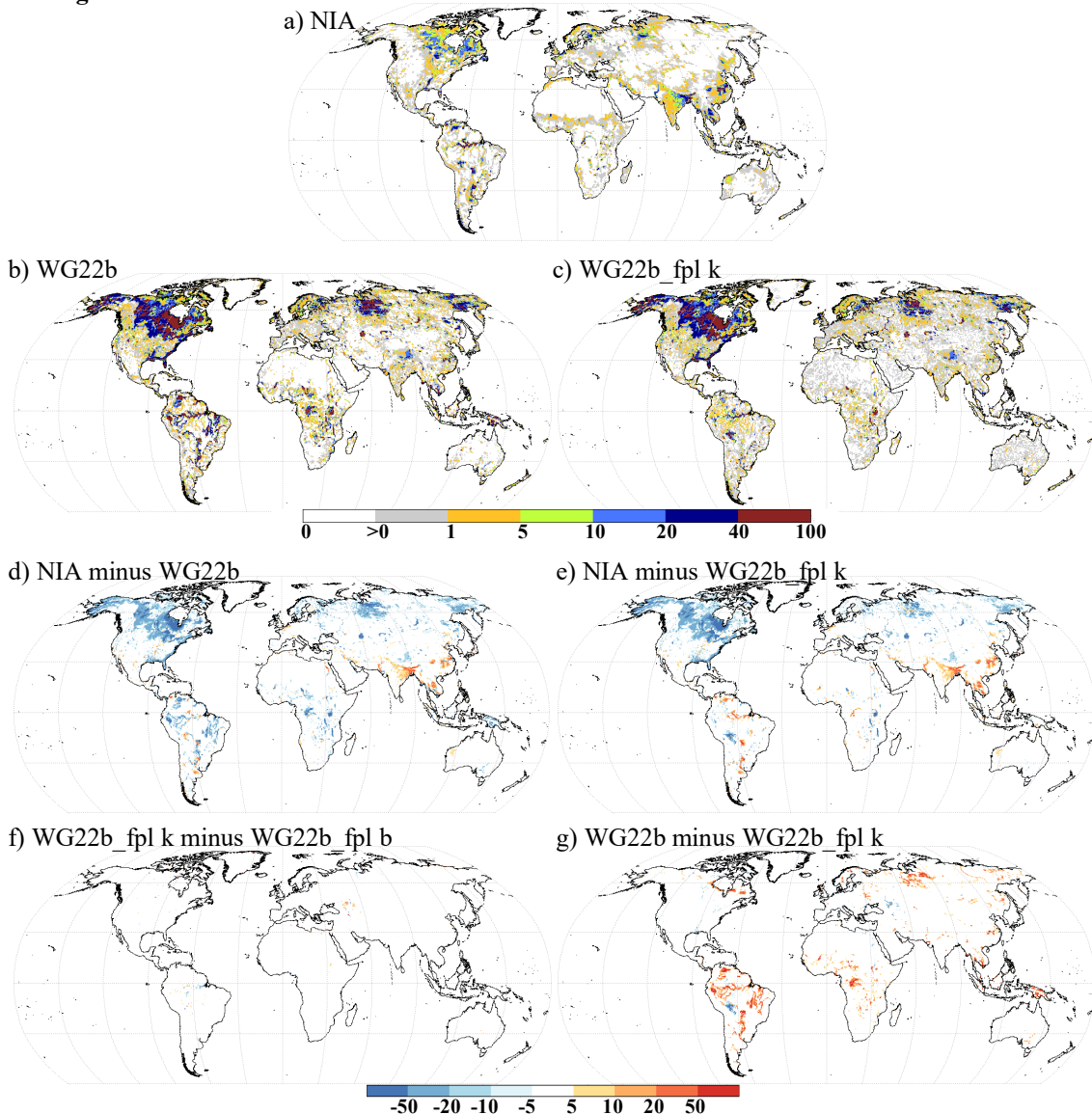


**Figure 5.12** Average observed and modeled surface water extent in percent of cell area in the time period 1993-2004, and differences between observations and model outputs.

**Seasonal Variation SWE 1993-2004:**
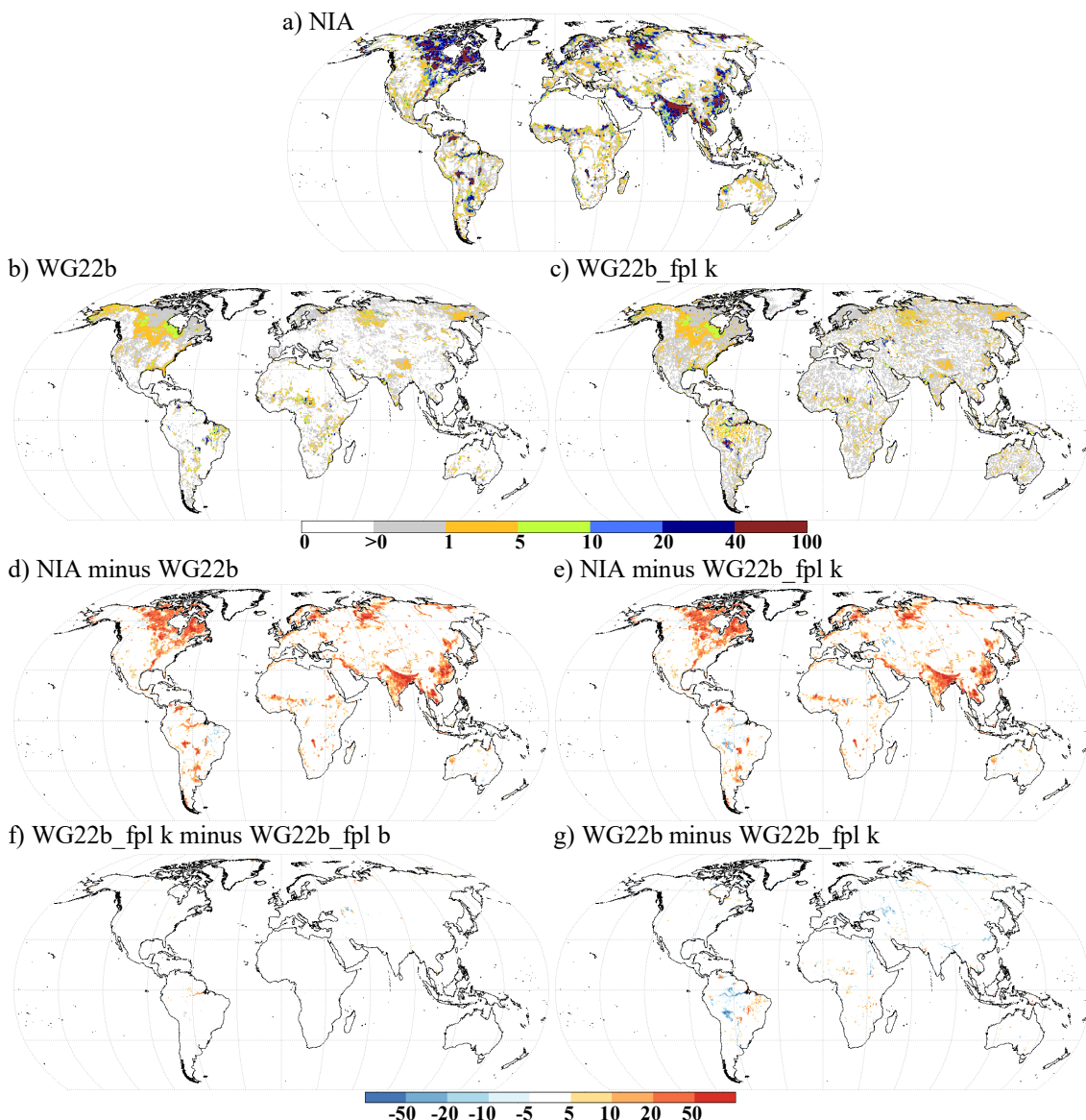


**Figure 5.13** Annual average of observed and modeled seasonal variation of surface water extent in percent of cell area (1993-2004), and differences between observations and model outputs.

With regard to Figure 5.12 and 5.13, it is striking that the model results show, in general, higher average SWE and lower seasonal variation than NIA. With modeling dynamic floodplain inundation within WaterGAP, average SWE decreases and the seasonal variation increases; thus model results are closer to observations than the results of WG22b. Average modeled SWE in all model variants is very high in northern latitudes of North America and Siberia, caused by many local lakes and local wetlands included in GLWD. Average observed SWE is especially high in Southeast Asia. NIA and modeled average surface water extent differ by less than 5 percent (in units of percent of cell area) in 79% of the grid cells of WG22b and 81% of the grid cells of WG22b_fpl (k and b), while average NIA is smaller than modeled areas for 19 and 16 percent of the grid cells for WG22b and WG22b_fpl, respectively (red areas in Figure 5.12d and e). Comparing the three model variants, average SWE of WG22b is higher than in WG22b_fpl,
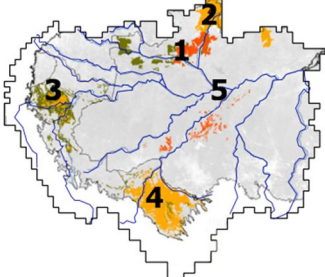
except for the Beni savanna in southern Amazon and the Caspian Depression (and some smaller scattered locations). Allowing backwater flows causes slightly higher average values of SWE in the central and lower Amazon and slightly lower values in the Caspian Depression compared to the kinematic wave routing.

With the exception of some isolated grid cells, the seasonal variation of WG22b is smaller than observed NIA all over the world. In contrast, WG22b_fpl shows a higher seasonal variation in the Amazon River basin and the Caspian Depression. Within the lower Amazon seasonal variation slightly decreases by modeling backwater effects.

Modeled and observed surface water extent within the Amazon River basin is drawn spatially in Figure 5.14 and shown as basin average time series in Figure 5.15.

Due to the fact that the data from Hess et al. (2003) represent a certain maximum extent of inundated areas, its spatial distribution is compared to the mean annual maximum of NIA and modeled SWE. The mean annual maximum is here preferred to the absolute maximum of the monthly time series because extreme outliers are excluded and thus typical seasonal maxima are represented. All of the datasets include, more or less intensively, the major interfluvial Amazonian wetlands as classified by Junk et al. (2011) (Table 5.6).

**Table 5.6**   Important areas of interfluvial wetlands in the Amazon River basin (modified from Junk et al. 2011).

| No. | Wetland name/ type | Location |
|-----|--------------------|----------|
| 1 | Negro river campina/ campinarana | |
| 2 | Roraima/ Rupununi savannas | |
| 3 | Central Peru savannas and palm forest | |
| 4 | Beni savannas | |
| 5 | Central floodplains | |



Campinas and campinaras in central Amazonia

Large hydromorphic savanna complexes on variable soil types

Forests associated with interfluvial wetlands

Hess et al. (2003) have shown higher SWE than NIA in all regions in the Amazon River basin. Especially noteworthy are the many grid cells with no SWE at all within NIA, as well as the much lower SWE in the central Peru savanna. Values of SWE modeled by WG22b_fpl (both b and k) are in general in between the two observation datasets, except the central Amazon region upstream the Purus tributary flows into the main stem, with little lower modeled SWE than observed. On the contrary, the former model version WG22b seems to miss wetlands in the region of the Negro River campina, the Roraima/ Rupununi savannas, the Beni savannas, and along the Madeira River, where modeled SWE is lower than in both of the observation data sets. When comparing WG22b_fpl k and WG22b_fpl b, differences of mean annual maximum SWE are quite

small. Allowing backwater flows leads to slightly lower values in the central Amazon and slightly higher values in the Beni savannas.
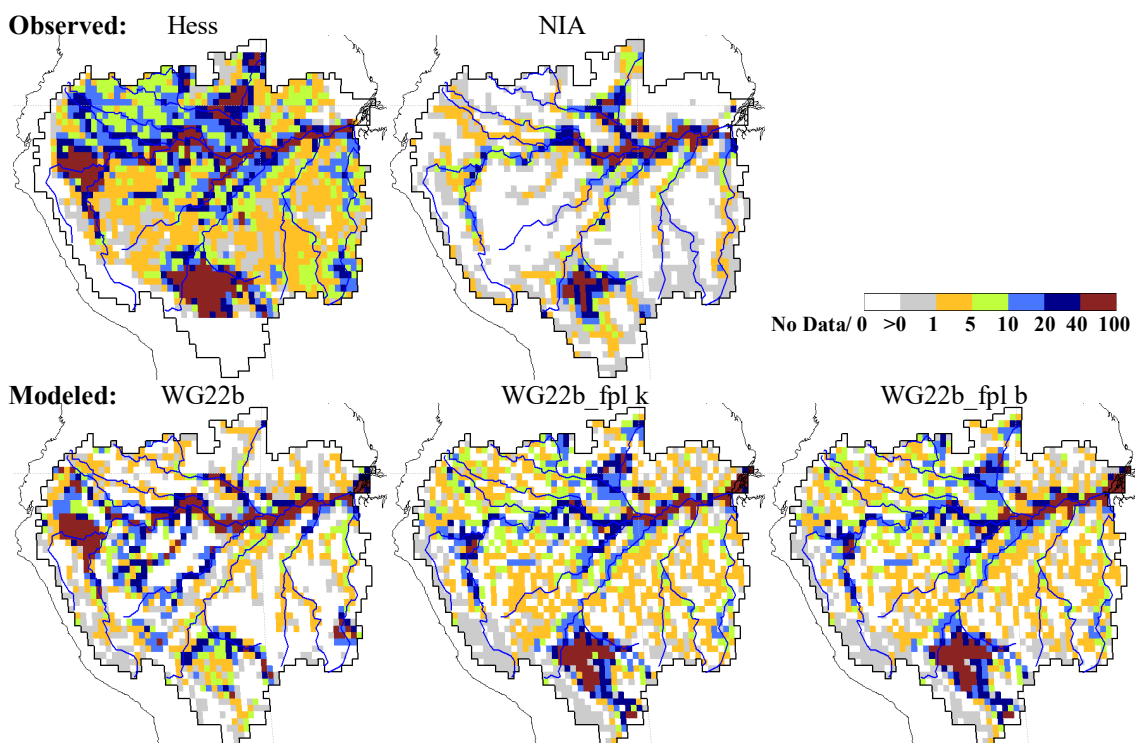


**Figure 5.14** Maximum surface water extent in percent of cell area within the Amazon River basin as observed by Hess et al. (2003) (wetland mask at high water conditions in May/ June 1996) and NIA (mean annual maximum 1994-2004) **(top)**, and as simulated by WG22b, WG22b_fpl k and WG22b_fpl b (mean annual maximum 1994-2004) **(bottom)**.

Whereas the maxima of SWE diminish when allowing backwater flows, the mean SWE increases (Figure 5.15). The basin average time series of modeled SWE (Figure 5.15) indicate the huge improvement of model performance achieved by the implementation of the dynamic floodplain algorithm into WaterGAP. Only the WG22b_fpl models agree well with observations in their seasonal variation and in the timing of low and high inundation. Compared to NIA, the mean modeled SWE is higher in the total Amazon, resulting in low model efficiency values of NSE and VE. This is because of the lower observed SWE in the region of the central Peru savanna and the Beni savanna, as well as the many grid cells where NIA has no inundation and modeled SWE is up to 5% of the grid cell area (Figure 5.14). In the central Amazon WG22b_fpl k and WG22b_fpl b agree well with NIA, with highest model efficiency when including backwater effects ($R^2$ = 0.8, NSE = 0.86, VE = 0.91). In WG22b_fpl b minimum SWE is higher and the seasonal amplitude lower, which agrees better to the observed NIA. When comparing WaterGAP 2.2b_fpl to SWE under low- and high-water conditions (September/ October 1995 and May/ June 1996) as observed from Hess et al. (2003), as well as when comparing WaterGAP 2.2b_fpl to SWE modeled by the CaMa-Flood model from Yamazaki et al. (2011) (black and green crosses in the bottom left of Fig-

ure 5.15, respectively), WaterGAP 2.2b_fpl shows lower mean SWE and, in the backwater model, also lower seasonal variation.
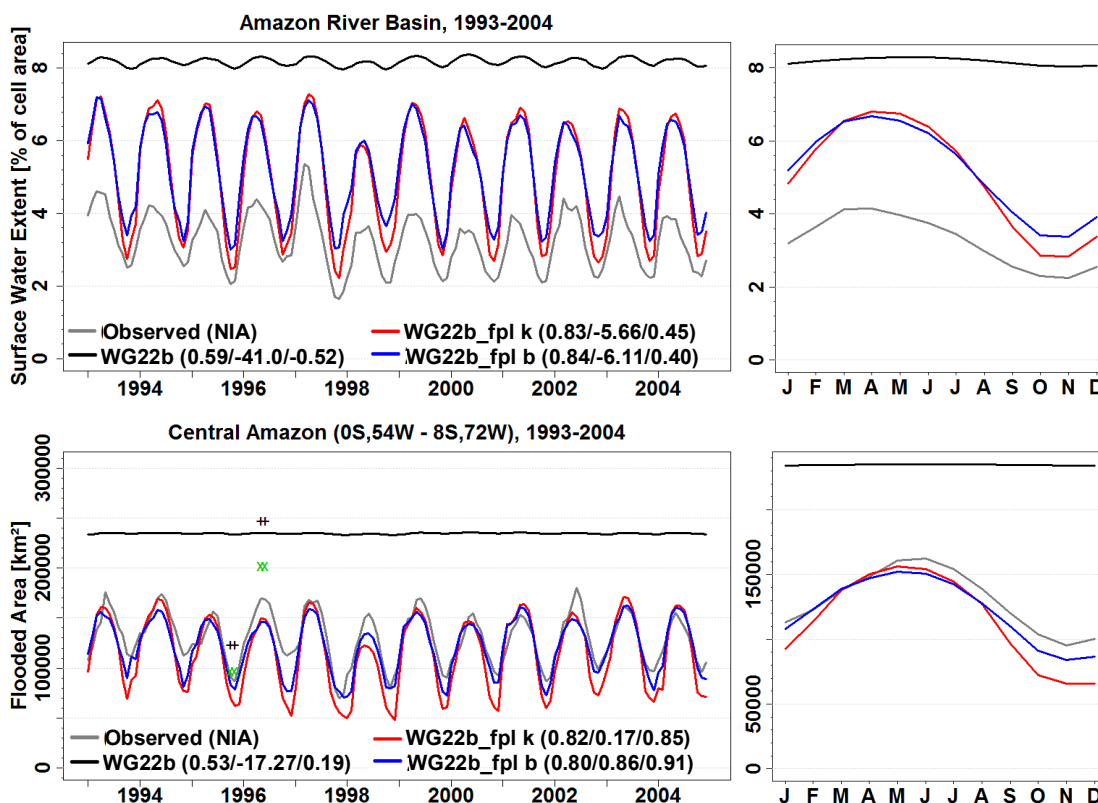


**Figure 5.15** Time series of modeled and observed surface water extent in the Amazon and central Amazon River basin (1993-2004). The gray lines represent surface water extent as observed by NIA. Modeled SWE of WG22b, WG22b_fpl k, and WG22b_fpl b is shown with black, red, and blue lines, respectively. The black crosses in the bottom left figure represent the inundation extent under low- and high-water conditions from Hess et al. (2003), and the green crosses represent SWE as modeled by Yamazaki et al. (2011) at the same time as the observations from Hess et al. (2003) (September/ October 1995 and May/ June 1996).

The results in other major river basins on the globe show, similar to the results in the Amazon, a clear improvement of SWE modeled by WG22b_fpl compared to WG22b. This implies flood localization, timing (month of maximum SWE), seasonal variation, and average values of SWE. However, compared to NIA, seasonal variation is still too low. Contrary to the Amazon River basin, in other river basins there is often no significant change in model performance when backwater effects are applied.

Changes in surface water extent affect the actual evapotranspiration (AET). Global AET within WaterGAP is calculated as the sum of evapotranspiration from canopy, snow, soil, and surface water. It does not include additional evapotranspiration caused by irrigation and other human water use. This part of evapotranspiration is called actual water

consumption (WCa) (Müller Schmied et al. 2014). "AET has large uncertainties/variability both at global and continental-scale (esp. in Europe and North America). As AET is not calibrated directly (but water balance is closed and thus influenced by calibration), this is related to the differences in climatic variables" (Müller Schmied et al. 2016, p. 22).

On a global-scale, mean AET are highest around the Equator, consistent with available energy (Figure5.16a and b). The change in AET by implementing the floodplain algorithm into WaterGAP (Figure 5.16c) is highly correlated with the change in SWE (Figure 5.12g). With lower SWE, less water evaporates. The same is true for the differences when applying kinematic wave routing (WG22b_fpl k) or when allowing backwater flows (WG22b_fpl b) (Figure 5.16d versus Figure 5.12f). The global sums of simulated AET in km³ per year for the three model variants during 1971–2000 are: 69448 (WG22b), 66235 (WG22b_fpl k), and 66280 (WG22b_fpl b). All these values are within the range of estimates reported in the literature (see values in Müller Schmied et al. (2014), Table 5).

a) AET of WG22b

c) WG22b minus WG22b_fpl k

b) AET of WG22b_fpl k

d) WG22b_fpl k minus WG22b_fpl b
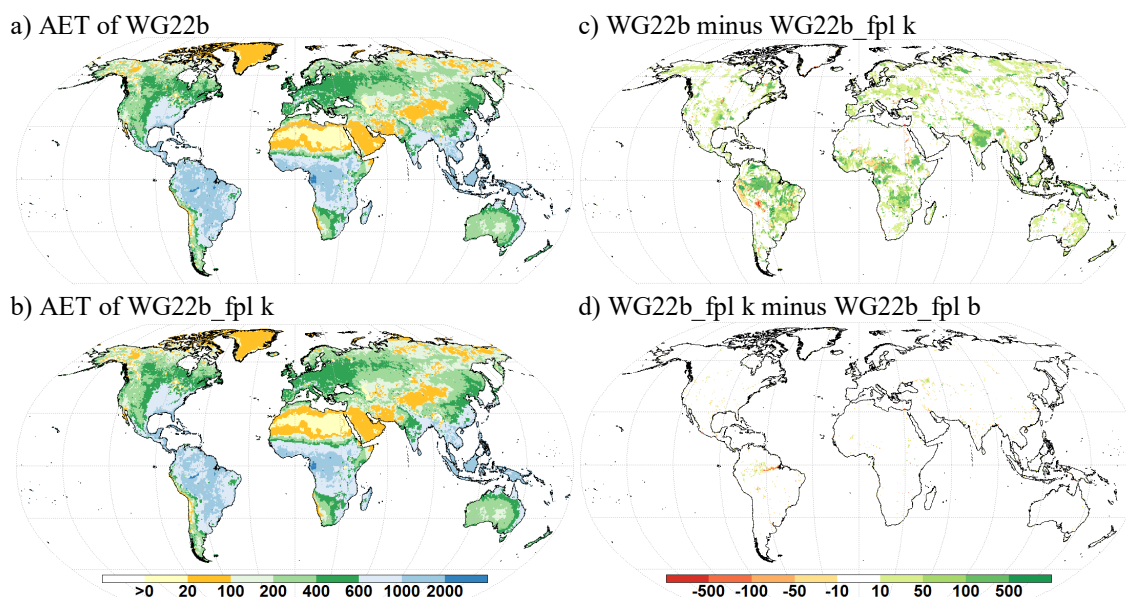


**Figure 5.16** Mean modeled actual evapotranspiration AET [mm/yr] (1971-2000) of WG22b (a) and WG22b_fpl k (b) and differences between the models WG22b and WG22b_fpl k (c) and WG22b_fpl k and WG22b_fpl b (d) in mm/yr.

### 5.4.4 Water Storage Variations

The Gravity Recovery and Climate Experiment (GRACE; Tapley et al. 2004), launched in 2002, measures mass variation on and near the Earth's surface based on monthly gravity field estimates at spacial scales down to ~400 to 600 km (Tapley et al. 2004). Mass variations within the continental water cycle are a major signal component after removal of signals from atmosphere and oceans. To evaluate TWS simulated by the WaterGAP Global Hydrological Model (WGHM), I use variations of total continental

water storage (TWS) from GRACE for the time period from August 2002 to August 2009, provided by the Institute of Theoretical Geodesy (ITG) at University of Bonn (ITG-Grace2010). GRACE data must be filtered, or smoothed, to minimize errors from spatial noise (Wahr et al. 1998; Swenson and Wahr 2006). Here, for this evaluation, ITG-Grace2010 is decorrelated/smoothed using the non-isotropic filter DDK3 (Kusche et al. 2009). For a direct comparison of observed and modeled water storage variations, modeled TWS variations must be filtered in the same way as the GRACE data (Güntner et al. 2009). The filtering in hydrological models leads to reduced TWS variations in river basins, possibly due to leakage errors from surrounding areas (Chen et al. 2007; Alkama et al. 2010). This is also true for WGHM (see Figure 3.10) and is discussed in Section 6.4.

To compare with GRACE data, the monthly TWS variations modeled by WaterGAP are calculated as the sum of water storage variations in canopy, snow, soil, groundwater, lakes, reservoirs, wetlands/floodplains, and rivers. After filtering both data sets, GRACE and WGHM, the data sets are mapped (back) into spatial grids – the original 0.5° grid cells of WaterGAP.

Figure 5.17 illustrates the seasonal and interannual TWS variations of GRACE and three WaterGAP model variants (WaterGAP 2.2b (WG22b), WaterGAP 2.2b including floodplains (WG22b_fpl k), and WaterGAP 2.2b including floodplains and allowing backwater flows (WG22b_fpl b) on the global-scale.

The seasonal TWS variation is the range of variation for each year (8 values) in the time period 08/2002 to 08/2009 and the interannual TWS variation is range of variation for each month (12 values) in the given time period.
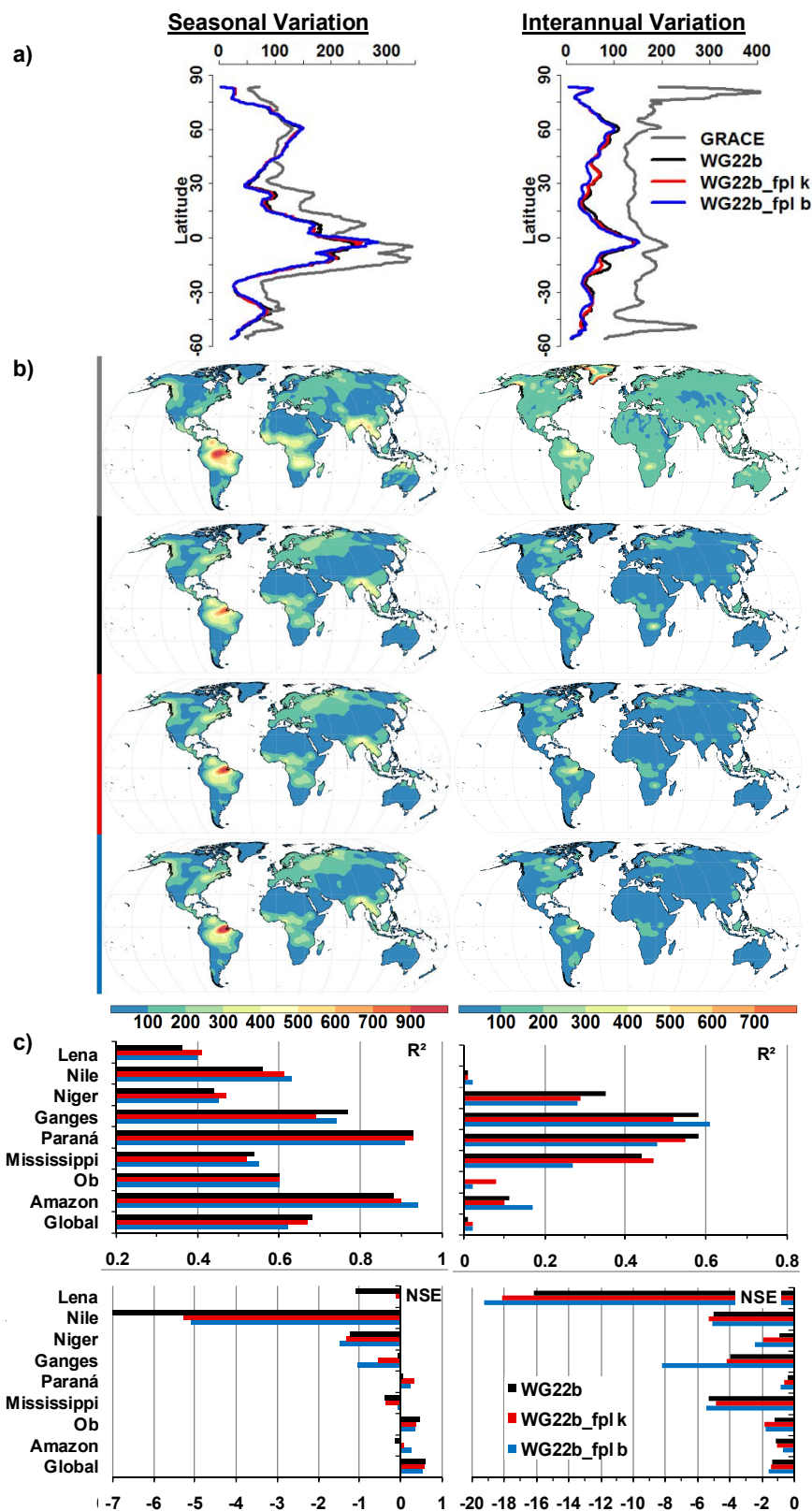
**Figure 5.17** Seasonal **(left)** and interannual **(right)** variation of TWS anomalies [mm EWH] for the products: GRACE (grey), WG22b (black), WG22b_fpl k (red), and WG22b_fpl b (blue). For each of the three values and each TWS product, the zonal average **(a)** and the spatial distribution on a global-scale **(b)** are shown. The model performance of TWS anomalies compared to GRACE (spatial averaged time series 08/2002 to 08/2009) is shown for eight major river basins and for the global-scale **(c)**.

In general, modeled TWS anomalies agree well with observations from GRACE, with a similar spatial distribution of high and low values (Figure 5.17a and b). However, the seasonal and annual amplitudes are globally underestimated, resulting in very low NSE values (Figure 5.17c).

The spatial maps show that the seasonal variation of TWS is overestimated compared to the GRACE (Figure 5.17b) in western North America (Mississippi, St. Laurence), parts of Europe, Western Siberia (Ob) and Northwest of South America (River mouth of the Amazon River, Orinoco). In contrast, in central South America (west and south Amazon, Tocantis) and the Congo, TWS is underestimated. Largest underestimation of both seasonal and interannual TWS variation occurs in the central Amazon and the Congo River basin. These findings are confirmed by Figure 5.17a, representing the zonal average of modeled and observed TWS variations, as well as by Figure 5.19 (Amazon) or Figure A.13 (eight major river basins), showing basin averaged monthly TWS variations.

The model performance, determined by calculating the correlation coefficient ($R^2$) and the Nash-Sutcliff Efficiency (NSE) on a global-scale and for eight major river basins, is shown in Figure 5.17c. The statistical measures are determined from the spatially averaged time series of monthly TWS variations in the time period from 08/2002 to 08/2009 (seasonal variation is calculated for each year (8 values) and the interannual variation is calculated for each month (12 values)). The highest efficiency values regarding the seasonal variation of TWS can be recorded in the Paraná and Amazon River basin, and the lowest in the Niger and Lena River basin. The model performance regarding the interannual variation of TWS anomalies is relatively low for all of the regions on the globe, but particularly low in northern latitudes.

With the implementation of dynamic floodplain inundation into WaterGAP, the seasonal variation of wetland/floodplain storage increases. At the same time, the dynamic in the river storage compartment decreases (exemplarily shown for the Amazon River basin in Figure 5.20). The change of variation within the other storage compartments is negligibly small compared to that in rivers and wetlands/floodplains. Merely in the Niger, Nile, and Paraná River basin the change of variation in groundwater storage (increment) is likewise important to that in the river (see Figure A.14). These three river basins have larger arid or semiarid areas where groundwater is recharged from surface water bodies (see Figure 4b in Döll et al. 2014). In almost all regions, the reduction of seasonal variation in river storage is less than the gain in wetland/floodplain and groundwater dynamic (except in the Mississippi and Ganges River basin), so that the seasonal variation of TWS increases. With the implementation of the floodplain algorithm into WaterGAP, the model performance improves in four of the eight in detail analyzed river basins regarding the annual variation of TWS change, and in five of the eight river basins regarding the seasonal variation of TWS changes (Figure 5.17c). The results and the model efficiency of the three model variants are very different according

to the region. In only one river basin, the Ob, an overall worsening of model results (regarding seasonal and interannual TWS variations) was obtained when applying WG22b_fpl (both k and b). On the contrary, a clear overall improvement was achieved for the Amazon and Mississippi River basin, with highest efficiency values using WG22b_fpl b.

Because of its high seasonal amplitude of TWS (see Figure 5.17b center), the Amazon River basin is of special interest and its spatial pattern of observed and modeled seasonal TWS variations is enlarged in Figure 5.18. The model results agree well with observations from GRACE, confirmed by the high to very high values of $R^2$ and VE (volumetric efficiency). However, basin average seasonal TWS variation is still too low compared to GRACE, resulting in low NSE values, and maximum variation is located in the downstream, not in the central, Amazon.

The implementation of the floodplain algorithm into WaterGAP leads to a clear improvement of model performance when compared to GRACE. The amplitude of seasonal TWS increases (highest in WG22b_fpl b) and the maximum seasonal TWS variation is shifted about 100 km upstream (in both WG22b_fpl k and WG22b_fpl b). The better performance of WG22b_fpl b compared to WG22b_fpl k can be mainly attributed to its higher seasonal TWS variation located at the mouth of the rivers Tapajos and Madeira in the Amazon main stem.
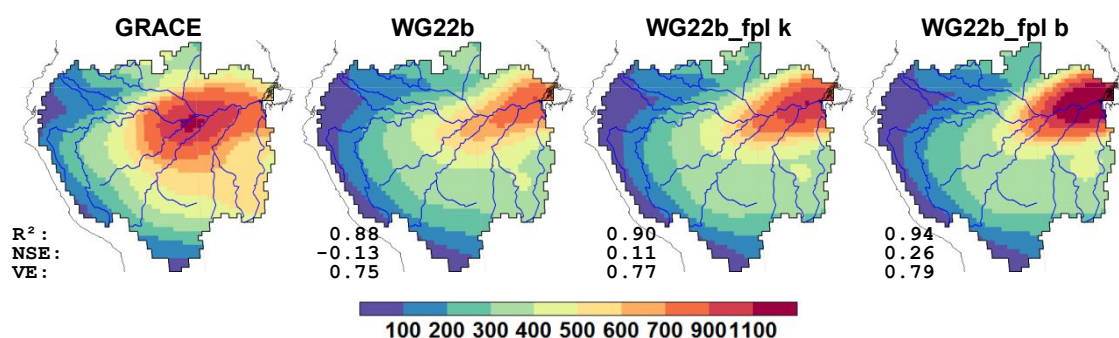


**Figure 5.18** Seasonal variation of TWS anomalies [mm EWH] in the Amazon River basin observed by GRACE and modeled by WG22b, WG22b_fpl k, and WG22b_fpl b.

The time series of basin averaged monthly TWS variations confirm the good overall agreement of the filtered model results with GRACE (Figure 5.19 for the Amazon and Figure A.13 for eight major river basins).
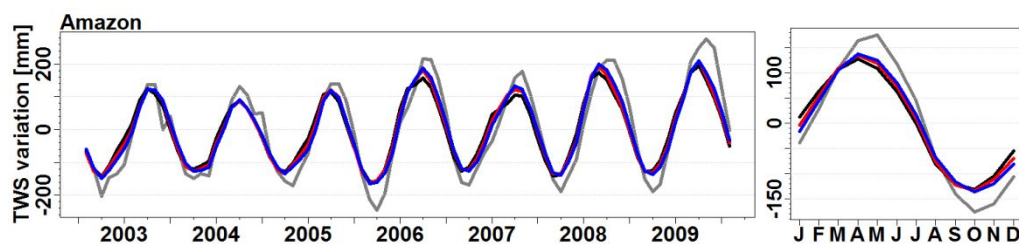
**Figure 5.19** Basin-scale mean monthly (right) and monthly TWS variations (left) in millimeter equivalent water height (EWH) observed by GRACE (gray) and modeled by WG22b (black), WG22b_fpl k (red), and WG22b_fpl b (blue).

In tropical river basins (Amazon, Paraná, Ganges, Niger) the time series of modeled TWS variations are well correlated to the GRACE data ($R^2$ ranging from 0.68 to 0.93 depending on river basin and model version). The correlation over arctic and temperate river basins (Lena, Ob, Mississippi) is lower ($R^2$ ranging from 0.54 to 0.68) but still acceptable ($R^2 > 0.6$) in at least one of the three model variants (model efficiency values of major river basins and its subbasins are listed in Table A.4 in the appendix). At a basin-scale WaterGAP underestimates the GRACE signal over tropical basins and tends to overestimate over arctic and temperate basins (Figure A.11). In more than half of the analyzed river basins the annual cycle of TWS variation (and also river discharge) occurs one month earlier compared to observations. In the Amazon River basin this shift is diminished by modeling dynamic floodplain inundation (Figure 5.19). The Amazon is the only river basin in which wetland/floodplain storage variation within WG22b_fpl is the dominant contributor to variations in TWS.

The underestimation of TWS variation in the Amazon River basin is, at subbasin-scale (subbasins illustrated in Figure A.11), highest in the southern Amazon (downstream the river discharge station Porto Velho) and lowest in the central Amazon (upstream the river discharge station Obidos). Best model performance is achieved when applying backwater effects.

Figure 5.20 shows the mean annual cycle of variations in single water storage components and TWS (unfiltered average values 1971-2000) exemplarily for the Amazon River basin (for other river basins see Figure A.16).
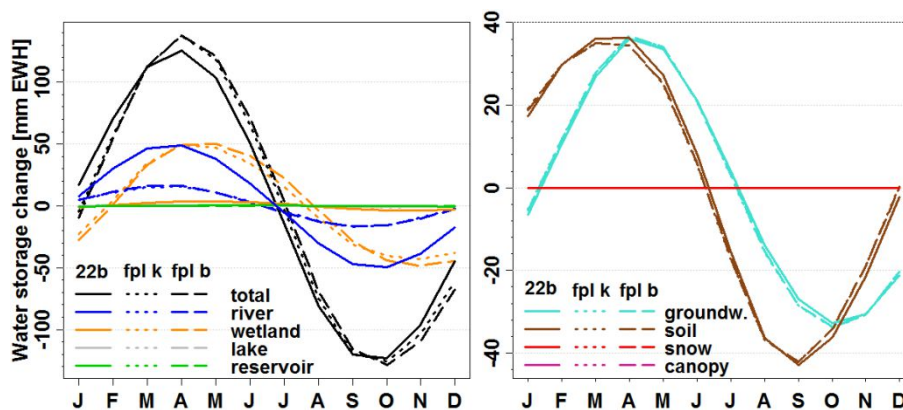
**Figure 5.20** Monthly average variation in TWS and single water storage compartments (1971-2000) in the Amazon River basin modeled by WG22b, WG22b_fpl k, and WG22b_fpl b (unfiltered).

It becomes clear that the river and wetland storage compartments (wetlands include floodplains) are the ones most affected by the implementation of dynamic floodplain inundation into WaterGAP. In general (not only in the Amazon River basin), the seasonal variation of wetland storage gets significantly larger and the seasonal variation in river storage significantly smaller. This is also confirmed when looking at the portions of seasonal water storage variations from single storage compartments within eight major river basins (Figure 5.21). The portions refer to the summarized seasonal variation of the single storage compartments, not to TWS, enabling a better comparison among the model variants and among different river basins. Note, that because of possible phase shifts, seasonal TWS variation is not necessarily equal to the sum of seasonal variation from the single storage compartments (e.g. in the Lena River basin snow storage peaks in April, and river storage variation in June).
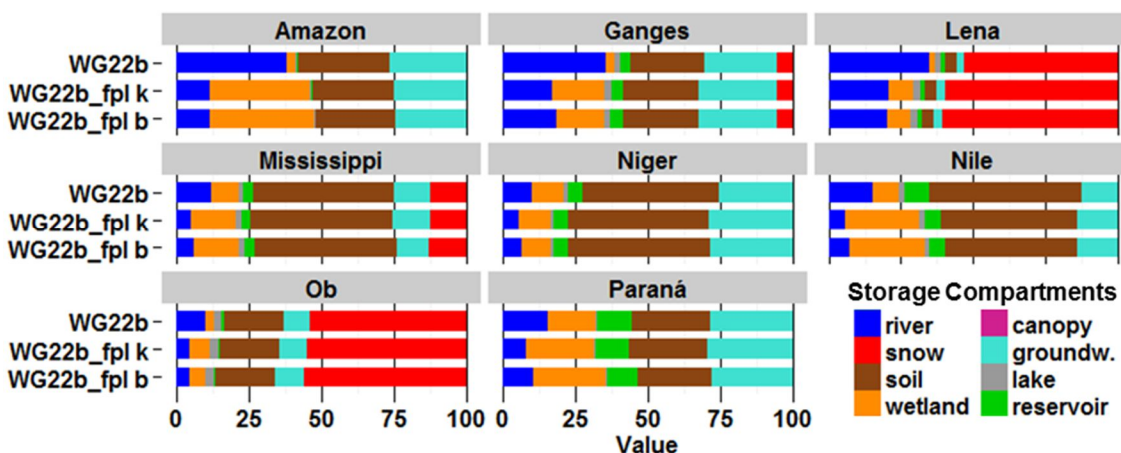


**Figure 5.21** Average seasonal water storage variations (1971-2000) of single storage compartments in percent. 100% represents the sum of single storage variations of the individual model version (unfiltered data) and specific river basin.

Within the eight major river basins analyzed in more detail, the contribution of wetland storage variation to TWS variation ranges in WG22b only from 3% (Amazon) to 19% (Paraná), whereas in WG22b_fpl k/WG22b_fpl b the contribution ranges from 12%/9% (Ob) to 38%/39% (Amazon). With the algorithm of dynamic floodplain inundation within WaterGAP, wetland storage variation is now under the major four contributors to TWS variations (besides variation in soil, groundwater, and snow storage compartments); in the Amazon River basin even the most important contributor. For the majority of the river basins, the dominant signal on TWS variations is attributed to soil moisture. Over boreal river basins, snow mass plays the major role.

CHAPTER 6

# Discussion

## 6.1 Introduction

As mentioned in Chapter 1, this PhD thesis is contained within the research project REGHYDRO, in which global hydrological modeling and regional geodetic estimation of water storage variations using GRACE data are combined to achieve an improved characterization of water storage (and flow), as well as of the gravity field in large river basins. Our working group – the working group of hydrology at the University of Frankfurt am Main – focused on the hydrological component of gravity variations. As previously stated, the main purpose of this PhD thesis is to improve water flows and storage variations as estimated by the global hydrological model WaterGAP.

To simulate large floodplains and wetlands inundated by overbank flooding of river water, I developed and applied a new algorithm within the WaterGAP Global Hydrology Model (WGHM). Introducing this algorithm for dynamic floodplain inundation into WaterGAP significantly improved the simulation of river discharge, surface water extent and storage variations. Through the implementation of subgrid-scale topography, WaterGAP is, for the first time, able to represent surface water stages – such as water height and inundated area – and simulate backwater effects.

In this chapter, answers to the four research questions (stated in Section 1.2) are provided and the methods and results are discussed.

The first question concerns the overall improvement of the model. Special attention is paid to the discussion of the results regarding surface water extent and possible causes for discrepancies to the validation data sets.

The second question deals with backwater flows. This implies discussing the methods of estimating channel geometry, water levels, and water routing within WaterGAP and other hydrological models.

Finally, the third and fourth questions address storage and discharge variations and include the discussion on the differences between the model results and GRACE.

## 6.2   General model improvement with emphasis on surface water extent

Research question 1: *Does the implementation of dynamic floodplain inundation in WaterGAP lead to improvements in model performance regarding river discharge, surface water extent, and/or total water storage variations? If so, which specific geographic areas are improved most?*

On a global-scale, WaterGAP model performance significantly increased due to the implementation of the algorithm for modeling dynamic floodplain inundation. The improvements comprise all of the analyzed model output variables: river discharge (also river flow velocity), water storage variations, and surface water extent. Model improvement is most noticeable in the Amazon River basin. Indeed, more than any other river basin it is characterized by its vast floodplains and wetlands, which occupy ~20% of the watershed (Melack and Forsberg 2001), and affect storage and transmission of the flood wave (Richey et al. 1989).

Compared to the former WaterGAP model version 2.2b (WG22b), river discharge improved in WaterGAP which includes the floodplain algorithm (WG22b_fpl), particularly with regard to seasonal variation and timing of high and low flows (attenuation of peak discharge and flood wave). In addition to the implementation of the algorithm for modeling dynamic floodplain inundation, I implemented a new method for calculating river depth in WaterGAP. River depth is now calculated as a function of river storage at previous time step, instead of as a function of actual river discharge as it was in WG22b (Section 4.6). The change in river depth leads to higher river flow velocity along the main stem and large tributaries. A comparison of modeled to observed river flow velocities in the Amazon River basin exibits higher model efficiency at 85% of the stations when the new method for calculating river depth within the river flow velocity equation is applied. Nevertheless, the river discharge tends to peak earlier, when applying the new river depth, resulting in a lower correlation with the observed discharge. In WG22b_fpl, the time lag in peak discharge is balanced by the presence of floodplains, absorbing water at peak flows and releasing it afterward. Finally, when comparing modeled and observed (GRDC) monthly discharge (1971-2000) between WG22b_fpl – including the floodplain algorithm and the new calculation of river depth – and the former model version WG22b, the average correlation (averaging the 248 analyzed gauging stations) remains unchanged.

In WG22b_fpl, unlike in WG22b, the presence of large floodplains is reflected in the daily river discharge. Daily-scale fluctuations in river discharge diminish, the larger the floodplain is, due to the attenuation of the flood wave (Section 5.4.2, Figure 5.11).

The implementation of the floodplain algorithm in WaterGAP led to better estimates of total water storage (TWS) variations for the majority of the eight river basins investigated with more detail. TWS variations increase in most regions of the globe due to higher floodplain/wetland storage variation. Indeed, the larger TWS variations fit better to the TWS variations derived from GRACE. Compared to GRACE, the model improvement is most evident in the Amazon and Mississippi River basin. In the Amazon River basin model performance is better, not only for seasonal and annual TWS variation, but also for the timing and location of maximum seasonal TWS variation. Compared to GRACE however, the seasonal and annual amplitudes of TWS are still underestimated on a global-scale. Moreover, the model efficiency for arctic river basins (Ob and Lena) remains relatively poor or even decreases (Ob) when the floodplain algorithm is applied. The reasons for the discrepancies between model results and GRACE are discussed in detail under research questions three and four.

The model improvement from WG22b_fpl to the former WG22b is particularly evident when simulating surface water extent (SWE), which improved in all respects – flood localization, timing (month of maximum), seasonal variation, and average values – for all of the eight analyzed major river basins. In the Amazon River basin the correlation between modeled and observed (satellite-derived naturally inundated areas – NIA) monthly SWE (1993-2004) rose from $R^2 = 0.59$ for WG22b to $R^2 = 0.83$ for WG22b_fpl. Although the seasonal variation of SWE increases when applying the floodplain algorithm in WaterGAP, it remains too low – except for the Amazon River basin – when compared to the satellite-derived observations.

On a global-scale, modeled SWE was compared to the monthly time series of NIA (Section 5.4.3). This data set has been found capable of serving as an independent data set for model validation of hydrological models (Adam et al. 2010, König 2011). In some regions, however, NIA tends to overestimate the actual fraction of inundation due to difficulties of the multi-satellite method to accurately discriminate between very wet soils and open water. Comparisons between the multi-satellite data set and high-resolution SAR images reveal that the former often overestimates SWE in areas with large inundation extent as well as after heavy rain; small areas of inundation, conversely, are underestimated or even not detected (Papa et al. 2007; König 2011). Compared to WaterGAP, NIA exhibits especially high values of both average SWE and seasonal variation in the region of the Ganges River basin. In this region (also the region of the Sudd Swamps, characterized by a distinct dry season and clear rainy season), NIA was found to be not suitable for model validation (König 2011). Not only single values of NIA show differences to the higher resolution remote sensing images of Landsat 7 (ETM+ band5), but also the seasonal variation of NIA. NIA strongly overestimates SWE in the region of Bangladesh; only interannual variations are represented in agree-

ment to Landsat 7 images and data from the Bangladesh Water Development Board (BDWB; www.ffwc.gov.bd), although with much lower amplitude (König 2011).

On a global-scale, the average modeled SWE remains too high and the seasonal variability too low (except in the Amazon) when compared to NIA, suggesting that local wetlands and/or local lakes in WaterGAP (based on GLWD) are overestimated. Especially in northern latitudes (North America, Siberia), WaterGAP exhibits a vast extent of surface water with almost no seasonal variation. GLWD represents the maximum area of surface water bodies in WaterGAP, which shrinks in function of water storage (Section 4.4.2). Section 3.2.2 explored the behavior of wetland storage variations in WG22b was explored, with the result that by increasing maximum storage capacity, seasonal variation in wetlands increases as well. The very low seasonal variation and high average values of SWE in high latitudes suggest that local wetlands and local lakes are, similar to global wetlands in WG22b, almost always full of its capacity.

In the Amazon River basin, the seasonal variation of modeled SWE agrees well with the seasonal variation of NIA. This was achieved by correcting the vegetation of the digital elevation model, which represents the floodplain profile in WG22b_fpl (Section 4.4.1). The flatter the floodplain profile of a grid cell, the more area is flooded when water enters the floodplain. The flat floodplain profile is also the reason for the very high seasonal variation in SWE in the region of the Caspian Sea depression. As described in Section 4.4.1, correcting the negative elevation values of the DEMs to a value of zero leads to a completely flat floodplain elevation profile in areas with real sinks (Dead Sea, Caspian Sea depression); thus, even a miniscule amount of water entering the floodplain is enough to cover the entire grid cell.

Seasonal variation of modeled SWE is highly sensitive, not only to the value of vegetation correction, but also to the parameter of bankfull flow reduction, and is influenced by the parameter of river-floodplain interaction (Sections 4.3.1 and 4.3.2; see Appendix 3.1 for the sensitivity of model output to model parameters). These parameters are constant in space and time; adjusting them at basin-scale or subbasin-scale should result in higher model efficiency in specific regions.

The Amazon River has the largest floodplain in the world along its main stem. This aspect has made it the object of numerous research studies (Melack 1984; Richey et al. 1989; Meade et al. 1991; Sippel et al. 1998; Hess et al. 2003; Alsdorf et al. 2007). WaterGAP-simulated SWE in this region was compared to satellite observations (NIA and data from Hess et al. 2003) as well as to SWE modeled by the catchment-based macro-scale floodplain model CaMa-Flood (Yamazaki et al. 2011). Compared to NIA, WaterGAP model efficiency is very high when applying the floodplain algorithm including backwater effects ($R^2 = 0.8$, NSE = 0.86, VE = 0.91). However, compared to Hess et al. (2003) and CaMa-Flood, the average SWE of WG22b_fpl b (b for backwater) is much lower. Whereas the minimum SWE is in good agreement (only slightly underestimated) with two of the data sets (NIA and CaMa-Flood), the maximum SWE is underestimated

when compared to all of the data sets. In the lower and central Amazon, backwater effects from the major tributaries Madeira, Tapajos and Xingu are especially important (Meade et al. 1991). Backwater flows in WaterGAP improve the model performance in the central Amazon. However, further improvement of the method to model backwater effects in WaterGAP and/or parameter adjustment of WG22b_fpl b should lead to a better approximation of model output to observations (see Section 6.3). The slightly lower minimum values could also be explained by the possibility that a number of local lakes are missing in GLWD. Melack (1984) has observed, via remote sensing, that approximately 10000 km² along the Amazon River are covered by thousands of permanent lakes that range in size from less than a hectare to over 600 km.

## 6.3    Backwater effects – river channel geometry – water levels

Research question 2: *What is the effect of backwater flows on modeled river discharge, surface water extent and water storage variations? How does the spatial distribution of large floodplains/wetlands and total water storage variations in the Amazon River basin change when modeling backwater effects?*

To analyze the effect of backwater flows on WaterGAP model outputs, WaterGAP 2.2b including the floodplain algorithm (WG22b_fpl), was run twice: one time applying kinematic wave routing (WG22b_fpl k; k for kinematic), and one time applying kinematic wave routing allowing for backwater flows (WG22b_fpl b; b for backwater).

Compared to WG22b_fpl k, modeling backwater effects within WG22b_fpl, using the method described in Section 4.5.2, leads to a significant improvement in model results for the Amazon River basin. For other river basins, the effect of modeling backwater flows varies: model efficiency improves for some output variables, worsens for others, and in many cases, displays no significant change.

Backwater effects in the Amazon River basin cause an attenuation and delay of the flood wave when compared to WG22b_fpl with kinematic wave routing. The peak stage at the downstream gauging station Obidos precedes the peak stage of the 750 km upstream station Manacapuru (Meade et al. 1991). WaterGAP river discharge agrees with this observation in the model variant where backwater flows are allowed. The modeled peak flow at Obidos is in May. In WG22b_fpl k, modeled peak flow at the 800 km upstream station Aruma-Jusante is too early (March); whereas in WG22b_fpl b is in May, likewise for Obidos (Section 5.4.2).

The correlation between modeled and observed monthly river discharge is, on average, almost equal for both WG22b_fpl k and WG22b_fpl b ($R^2$ value 0.02 better in the kinematic wave model). At the Amazon downstream station Obidos, not only are there reduced peak flows, but also higher low flows when the floodplain algorithm is applied in WaterGAP, with the highest low flows displayed in WG22b_fpl b. However, this

increment might be overestimated either due to an overabundance of water on the floodplains during low flow periods (which drains back to the river) or because of a too low flood-wave speed, or as a result of both. In the first case, the reason for overestimation could be an inadequate parameter for the river-floodplain interaction. In WG22b_fpl, this parameter is a function of water exceeding the bankfull flow and the actual river channel flow (Section 4.3.2). Alsdorf et al. (2007) have demonstrated, in their analysis of interferometric SAR data, that river and floodplain water levels cannot be assumed to be the same, unlike the way it is modeled in WG22b_fpl. The water level gradient between floodplain and river is currently not considered in WG22b_fpl and might influence the amount of water being exchanged. In the second case, the reason for overestimation could be attributed to errors in locations and the frequency at which backwater flows occur as a result of uncertainties in modeled river channel geometry and thus water levels (discussed further down).

The effect of backwater flows with regard to surface water extent is characterized by an improvement of the timing in which SWE reaches its maximum. This is true for all of the analyzed river basins (with more or less significance). Furthermore, the spatial patterns of seasonal variation of SWE improved for many regions of the globe (most notably in the Amazon and Paraná River basin). In the case of the Amazon River basin, seasonal variation of SWE decreased, especially in the very downstream part of the basin. This observed decrease leads to a better agreement with the spatial distribution of observed NIA when compared to WG22b_fpl k. The improvement in model performance allowing backwater flows regarding the monthly time series of SWE at basin and subbasin-scale can be attributed to reduced seasonal amplitudes. Especially during low flows (in the dry season), the values of wetland/floodplain extent remain higher.

One of the main expectations of modeling backwater effects was to improve the spatial distribution of seasonal total water storage variations in the Amazon River basin. Whereas GRACE observes the maximum seasonal TWS variation at the central Amazon, WaterGAP simulates the highest seasonal TWS variations close to the river mouth (Section 5.4.4, Figure 5.18). The expectations were met; compared to GRACE, WG22b_fpl b achieves the best values in model performance out of all of the WaterGAP model variants. The improvements were, however, smaller than were initially expected. The inclusion of backwater flows in WG22b_fpl increases the seasonal TWS variation at the mouth of the Amazon tributaries Tapajos and Madeira. However, the influence on seasonal TWS variations in the central Amazon (where the Purus and the Negro River flow into the Amazon main stem) is small. There are several possible reasons for the discrepancies between GRACE and WaterGAP model results: uncertainties in the GRACE solutions, errors caused by filtering the data products, and inadequate modeling of the hydrological processes in WaterGAP, among others. This section dis-

cusses the last point; possible uncertainties of the GRACE data are discussed under the research question three and four (Section 6.4).

The modeling of backwater effects, or even diffusion wave routing, within hydrological models is based on slope, which requires the simulation of water levels and water level gradients from a target grid cell to the adjacent grid cell(s). The simulation of water levels, in turn, requires the estimation of the river channel geometry or the floodplain profile – in case water is above river channel bank height and floods the surrounding areas.

The lack of globally available data remains a major obstacle in calculating the geometry – river widths and depths – of river channels. Channel geometry is highly important to hydrological modeling since it significantly influences the cross-sectional area, hydraulic radius, river slope, and river flow velocity. Existing GHMs estimate river width and depths as a function of actual river discharge or upstream drainage area (Section 2.1). The parameters used in such equations are typically only verified for a limited area and for bankfull conditions. Likewise, in WaterGAP 2.2b_fpl river width (and depth at the initial time step) is estimated as a function of river discharge by using an equation derived by Allen et al. (1994) from a regression analysis of 674 river cross sections in the USA and Canada (Section 4.6). Although this relationship is only valid for bankfull conditions, it is used in WaterGAP for all of the river discharges below or above bankfull, which may cause inconsistencies in the relation between river channel geometry and river flow velocity or river storage. WG22b_fpl uses the river storage simulated at the initial time step to calculate the river depth at the next time step.

The calculation of the river water level gradient from one cell to another requires, not only an estimation of river depth, but also the absolute river elevation. In WG22b_fpl, the absolute river elevation is defined as the outflow level, also called minimum elevation, of a grid cell ($z_{min}$). This minimum elevation of a grid cell, as well as the floodplain elevation profile, are obtained by implementing 100 subgrid elevations for each 0.5° grid cell based on a combination of two digital elevation models (DEMs: HydroSHEDS and ACE2; see Section 4.4.1). The data input from a DEM is a possible source of major errors in global hydrological models (an overview of DEMs used in GHMs is provided in Section 2.1). Possible sources of errors, depending on the DEM, include: random noise (artifacts, holes, gaps), surface objects (trees, buildings, bridges), and hydrological correction (steam burning, void filling). Furthermore, the correction of the DEM input data for WaterGAP against vegetation and negative elevations (Section 4.4.1) might not be adequate for all of the regions where the correction is applied. To remove vegetation artifacts from the DEM data, a constant value of 17 m is subtracted in all of the DEM pixels in the Amazon River basin. However, vegetation height may vary even in forested areas.

The comparison of modeled to observed water levels from Topex/Poseidon (see Section 5.4.1 for more details) at 80 altimetry gauging stations located in 6 major river basins indicates that WG22b_fpl performs well with regard to both seasonal and interannual water level variations. However, WaterGAP overestimates the absolute values of the altimetry observed water levels for most of the 80 stations. Allowing backwater flows led to a significant model improvement compared to WG22b_fpl k, with less seasonal variation, and mean water levels much closer to the observed means; although mean values are still overestimated. The difference between modeled and observed mean water levels is smaller in regions with elevations close to sea level than at higher altitudes, suggesting that the minimum elevation of the grid cells, derived from DEMs, is not in agreement with the altimetry measured elevations.

Other studies that compare modeled to observed altimetry data present a variety of outcomes (Coe et al. 2002; Yamazaki et al. 2011; Yamazaki et al. 2012b; Paiva et al. 2013; Wilson et al. 2007). Paiva et al. (2013) and Yamazaki et al. (2012b), for example, have compared ENVISAT data to water levels of the MGB-IPH model and the CaMa-Flood model in the Amazon River basin. Whereas MGB-IPH strongly underestimates the amplitude of modeled water levels, CaMa-Flood results in an overestimation. In contrast to the results of WG22b_fpl, Yamazaki et al. (2012b) obtains higher water level peaks in their model including backwater flows than in their kinematic wave model, and mean water levels, in general, performed well. The model CaMa-Flood has a higher model resolution than WaterGAP (0.25° compared to 0.5°), which might be one of the reasons for its better performance regarding the simulation of absolute water levels. Another reason may be the different methods for extracting errors from the DEM. All of the authors agree that uncertainty in river and floodplain geometry and errors in the topographic data cause inaccuracies in simulated water levels. However, some discrepancies between modeled and observed water levels might also be attributed to errors in the altimetry data. Especially low water estimates derived from radar altimetry are associated with the largest uncertainty (Birkett et al. 2002).

The effect of backwater flows on model outputs is related to the distribution and duration of negative water slopes, as illustrated in Figure 4.10 (Section 4.5.2) for the Amazon River basin. The longer the duration of negative slopes, the larger the difference in model outputs between WG22b_fpl b and WG22b_fpl k. In the Amazon River basin, most of the grid cells with negative water slopes are located along the main stem in the downstream part of the river basin; fewer grid cells are located in central Amazon (where the Purus and the Negro River flow into the main stem), the part in which the GRACE signal of seasonal TWS variation is highest and satellite observations (NIA and Hess et al. 2003) exhibit an average inundation extent of more than 40% per grid cell.

The duration of negative water slopes, indicating backwater flows, appears to be too high for most of the grid cells. Backwater flows, lasting more than six months of a year,

appear to be unrealistic, even in the Amazon. For this reason, at present moment – with the methods developed and presented in this PhD thesis – a diffusion wave routing is not applicable to WaterGAP (Section 4.5.2). Indeed, diffusion wave routing (routing the entire outflow of a grid cell in a direction according to its water slope, as well as adapting flow velocity corresponding to its water slope) requires a better simulation of the river geometry (width and depth) within WaterGAP and a higher accuracy of the minimum surface elevation (outflow level) per grid cell. Ideas regarding how this can be improved are stated in the outlook of this thesis (Chapter 7).

Large-scale hydrological models where a diffusion wave routing is implemented are CaMa-Flood (Yamazaki et al. 2011), THMB (Coe et al. 2000; diffusion wave only for floodplains, not for rivers, and with a time constant flow velocity), and LISFLOOD-FP (Bates and De Roo 2000). The clearest difference in model structure between these models and WaterGAP is the higher spatial resolution (Table A.5). They also differ in other features, such as the estimation of the channel geometry and the methods for extracting errors from the DEM.

## 6.4 Storage and discharge variations

Research question 3: *What is the contribution of water storage in floodplains and wetlands to total water storage variation and variations in river discharge?*

The most influential factor for river discharge variation in WaterGAP is the surface runoff, which is primarily driven by precipitation. Other factors include water withdrawals, groundwater return flows and, in WaterGAP 2.2b with floodplain algorithm (WG22b_fpl; fpl for floodplain), also floodplain return flows to the river. The proportion in which each factor contributes to variations in river discharge differs greatly from region to region. In WG22b_fpl, the contribution of floodplains/wetlands water storage to variations in river discharge is high in areas with large and endured flooding; the variation in river discharge decreases with the presence of floodplains due to the attenuation of peak discharges (see Section 5.4.2).

In WG22b_fpl (both, applying kinematic wave routing and allowing backwater flows), the storage variation in floodplains/wetlands is one of the four major contributors to seasonal total water storage (TWS) variations; in the Amazon River basin this contributor is even the most important one. In the majority of river basins, seasonal TWS variations are dominated by variations in the soil storage compartment. For boreal and arctic river basins, snow mass plays a major role.

Research question 4: *What are the river basin-specific causes of the observed discrepancies between variations in total water storage, such as variations derived by GRACE, and by the WaterGAP Global Hydrological Model (WGHM)?*

Global-scale comparisons between WGHM and first results of GRACE (between 2002 and 2004), which were carried out by Ramillien et al. (2005) and Schmidt et al. (2006), have already presented a good agreement in terms of geographical location of storage anomalies, but also revealed differences in the amplitudes of storage variations. Ramillien et al. (2005) have stated that there is no systematic underestimation by the model, but that the underestimation clearly depends on the region. These findings are in agreement with the present study.

The global-scale comparison of monthly to seasonal TWS variations between WG22b_fpl and GRACE displays overall similar spatial patterns and temporal storage variations. For most of the regions on the globe the correlation is high. Nevertheless, on a global average the seasonal and interannual amplitudes are smaller for WaterGAP than for GRACE. With regard to the monthly time series of TWS variations at river basin-scale, the model efficiency is highest in tropical river basins (Amazon, Paraná, Ganges, Niger) and relatively low in arctic and temperate river basins (Ob, Lena, Mississippi) (see Section 5.4.4).

There are several reasons that could account for the discrepancies between TWS variations computed by WG22b_fpl and TWS variations derived from GRACE.

The three major error sources of GRACE when resolving hydrological signals are measurement errors, leakage errors, and atmospheric pressure errors (Seo and Wilson 2005). GRACE signals suffer from leakage errors from one region to another. When analyzing specific regions such as river basins, the signals are influenced by leakage from surrounding areas. The atmospheric pressure is closely linked to the total mass of the atmosphere. GRACE signals are subject to residual signals and aliasing effects of variations from other masses removed during the GRACE data processing (mainly atmosphere and ocean mass; e.g. Seo et al. 2008). Gravity field errors – measurement and processing errors – are reduced by applying a post-processing filter technique (Swenson and Wahr 2006; Werth et al. 2009), whereas a desirable filter technique minimizes both GRACE gravity field errors and signal leakage across the border of the region of interest (Werth et al. 2009). GRACE uncertainties are higher over small to medium scale river basins than over major basins. Moreover, GRACE uncertainties are high over desert regions and relatively small over high latitudes (Alkama et al. 2010).

For a direct comparison between TWS variations derived from GRACE and modeled TWS variations, the model data must be filtered in the same way as the GRACE data (Güntner et al. 2009). This filtering, however, significantly affects the seasonal amplitudes of basin-scale water storage changes (Section 3.2) and might be one reason for the underestimation of seasonal TWS variation from WaterGAP when compared to

GRACE. The analysis of Chen et al. (2007) indicates that Gaussian smoothing (filtering) also introduces no-negligible phase changes, possibly due to asymmetric spectral leakage errors from surrounding areas.

By comparing monthly TWS variations from WG22b_fpl to GRACE, a time lag of approximately one month is observed for the majority of the analyzed river basins. WG22b_fpl results also indicate time lags in river discharge for some river basins. This suggests that, besides possible errors due to data filtering, there might also be deficits in modeling hydrological processes within the GHM (global hydrological model). Decharme et al. (2010) have found similar time lags when comparing the model output of the GHM ISBA-TRIP to GRACE data and to some discharges. Over boreal river basins (Ob, Mackenzie), the authors have pointed out the excessive flow velocity in the ISBA-TRIP model as the main cause for the time shift. Over tropical and temperate basins, one reason for the discrepancies between modeled and observed TWS variations could be deficits in simulating groundwater dynamics in the GHM (Decharme et al. 2010). WaterGAP contains a groundwater storage compartment and simulates baseflow and groundwater recharge from surface water bodies. However, it appears important to allow the deep water to re-evaporate via diffusive exchanges with the land surface (Fan et al. 2007; Miguez-Macho et al. 2007). Currently, none of the GHMs include information on water table depth to model groundwater-surface water interactions. Groundwater supports extensive wetlands primarily fed by surface water through river flooding. A steady groundwater drainage from higher grounds maintains the water level in floodplain lakes in the dry season (Fan and Miguez-Macho 2010; Miguez-Macho and Fan 2012). A recent study of de Graaf et al. (2015) presents a new global-scale groundwater model by coupling the dynamic land-surface model PCR-GLOBWB and the steady-state groundwater model MODFLOW. This new groundwater model is able to capture the large-scale distribution of groundwater levels and may serve as a starting point for modeling groundwater fluctuations and interactions with surface water in global hydrological models (de Graaf et al. 2015).

Another reason for discrepancies between modeled TWS variations and TWS variations derived by GRACE may be the uncertainty in modeling evapotranspiration in GHMs (Ramillien et al. 2005; Alkama et al. 2010). When evapotranspiration is underestimated, the model tends to overestimate river discharge and TWS, and vice versa. Furthermore, evaporation is highly correlated to surface water extent; therefore, when surface water extent is over- or underestimated, errors in simulated evapotranspiration are produced.

The simulation of snow and melting processes within large-scale hydrological models have often been mentioned as possible sources of uncertainties (van Beek and Bierkens 2009; Yamazaki et al. 2011; Decharme et al. 2012; Müller Schmied et al. 2016). WG22b_fpl achieves the lowest model performance of simulated TWS variations in the Ob, Lena, and Mississippi river basin. In these river basins modeled TWS variations are overestimated when compared to GRACE data. Snow storage variation is the major

contributor of TWS variation in boreal/arctic river basins, and the third major contributor in the Mississippi River basin (after soil and wetland storage variations). Furthermore, the Ob River basin is the only river basin with significant lower model performance when applying the floodplain algorithm to WaterGAP. In WG22b_fpl, the sum of river and wetland storage variation is lower than in the former model version WaterGAP 2.2b, thus snow storage variation gains proportionally in importance.

CHAPTER 7

## Conclusions and Outlook

The main objective of this PhD thesis was to further develop the global-scale hydrological model WaterGAP, with the purpose of improving the estimation of water flows and water storage variations in different storage compartments. The objective was accomplished.

To simulate dynamic floodplain inundation by overbank flows of river water on a global-scale, I developed a new approach which introduces an algorithm into WaterGAP. The new approach uses subgrid-scale topography, based on high-resolution digital elevation models, to describe the floodplain elevation profile within each half degree grid cell of WaterGAP by applying a hypsographic curve. In order to develop the approach, a detailed analysis of model-internal processes of WaterGAP was conducted. Additionally, for validation purposes, a satellite-derived global data set of naturally inundated areas was generated.

The methodology of the floodplain algorithm in WaterGAP includes the modeling of the flood initiation, a two-way interaction between the river and the floodplain, the extent and the water depth of the floodplain area, the separate transport of river and floodplain water between the grid cells with temporally and spatially different variable flow velocities, as well as the interaction between the floodplains and the groundwater.

For the first time, WaterGAP is now able to compute flood inundation extent and water heights for each 0.5° grid cell. In addition, the calculation of water level gradients allows WaterGAP, also for the first time, to account for backwater effects.

WaterGAP including the floodplain algorithm (WaterGAP 2.2b_fpl) is a state-of-the-art global-scale hydrological model which combines the strength of various existing large-scale hydrological models. The essential characteristics of WaterGAP 2.2b_fpl can be briefly summarized as follows: although WaterGAP 2.2b_fpl does not contain any exclusive feature (i.e. a feature included in no other global hydrological model GHM) – except the unique calibration against long term annual river discharge (Hunger and Döll 2008; Müller Schmied et al. 2014) – WaterGAP is the only GHM that includes together the following features:
- inland water bodies with variable area
- high resolution and hydrologically corrected surface elevation
- vegetation correction of surface elevations in areas with high and dense vegetation
- two-way exchange between river and floodplain
- separate routing in rivers and floodplains, simulating backwater effects for both rivers and floodplains

- flow velocity for rivers and floodplains, both variable in time and space
- floodplain-groundwater interactions

Features of WaterGAP in comparison with other large-scale hydrological models containing floodplain modeling are listed in Table A.15 in the appendix.

The model performance of WaterGAP 2.2b_fpl was analyzed by validating model outputs on river flow velocities, river discharge, water storage variations, water heights, and surface water extent against comprehensive data sets based on ground observations and remote sensing data, as well as by comparing model outputs to the former WaterGAP model version 2.2b.

On the global-scale, WaterGAP model results significantly improved due to the implementation of the algorithm for modeling dynamic floodplain inundation. In particular, the location and extention of floodplains, as well as the seasonal variation of surface water extent and total water storage, are much closer to the observations. The model improvement is most remarkable in the Amazon River basin, which is characterized more than any other river basin by its extensive floodplains and wetlands. However, there are still discrepancies between model outputs and observations. Modeled total water storage variation and surface water extent concur with observations regarding their geographical distribution; although WaterGAP underestimates seasonal variation in most of the regions on the globe. Furthermore, modeled TWS variations, river discharge, and river flow velocities indicate a certain time lag in many regions when compared to observations. The highest discrepancies occur between modeled and observed average water levels, albeit strongly varying from site to site. A detailed analysis of the simulated results suggests that in the Amazon River basin, the introduction of backwater effects is important for realistically simulating water storages and surface water extent.

Further model developments are required to improve the simulation of water levels within WaterGAP. Key issues for achieving this goal are the reduction of errors and artifacts (holes, vegetation, etc.) in digital elevation models (DEMs), and the improvement of river geometry estimations. One way to improve the simulation of river geometry could be by implementing the Global Width Database for Large Rivers (GWD-LR) into WaterGAP (developed by Yamazaki et al. 2014). In the equation of Allen et al. (1994), the coefficient used to calculate river width at bankfull stage (Equation 4.24) could be corrected for each individual grid cell in order to fit with the GWD-LR database. The original resolution of GWD-LR is 3 arc seconds and the coverage is between 80°N and 60°S. It would also be interesting to investigate the effect of different DEMs on model results.

With a better estimation of water levels and water level gradients, a diffusive wave routing in WaterGAP might be applicable. It may also be desirable to compute diffused

flood water flow to all neighboring grid cells, and not only to the adjacent up- and downstream grid cells. This is computed in the model THMB, which includes a boundary condition to avoid run away flooding (Coe et al. 2008). Diffusive wave routing in WaterGAP might require a higher spatial model resolution than the 0.5°.

To improve the modeling of backwater effects in WaterGAP (or in the future, when applying diffusion wave routing), it may be necessary to include ocean tide variation. Yamazaki et al. (2012b) have found that anomalies in river discharge, when either considering or disregarding ocean tide variation in the CaMa-Flood model, reach up to 1000 km upstream from the river mouth (near the confluence of the Madeira River and the Amazon main stem). The differences in river discharge are initiated around the river mouth and then propagated to the inland region (Yamazaki et al. 2012b).

The floodplain algorithm in WaterGAP 2.2b_fpl contains four individual parameters: the flood initiation threshold (reduction of bankfull flow), the value for vegetation correction, the river-floodplain interaction, and the backwater flow. In order to achieve the best fit of model outputs on the global-scale – compared to validation data – these parameters were carefully set to specific values, which remain constant in space and time. Further work is necessary to adjust these parameters, making them variable in space (setting different values for basins or subbasins), and perhaps also in time.

Future efforts could also aim at improving the groundwater-surface water interaction in WaterGAP. Since WaterGAP 2.2b_fpl is now able to compute water level gradients, groundwater recharge could be modeled as a function of water level and ground water table depth. This would require a gradient-based groundwater model. With the information on water table depth, in turn, the diffusive exchange between the groundwater and the land surface could be simulated, allowing for a direct groundwater feeding of floodplains and a re-evaporation of groundwater.

In conclusion, this PhD work significantly contributed to the improvement of the global hydrological model WaterGAP. The improved model allows for a better quantification of freshwater flows and freshwater storage for long historical and future time series. Additionally, the improved model contributes to a better understanding of the global water cycle, and allows a better assessment of freshwater resources and their impact on global change. The modeling of temporal and spatial dynamics of floodplains, in particular, enables a better quantification of surface water extent, evaporation, water storage and river discharge dynamics. Changes in the dynamics of floodplains – e.g. caused by land use changes or climate change – are important for biodiversity, methane emissions, carbon storage, and groundwater recharge. In addition, an improvement of modeling hydrological mass variations by WaterGAP serves for a better understanding of the space-time patterns of GRACE observations and for the assessment of the limits of the

spatiotemporal resolution of gravity fields. WaterGAP has also been used to improve regional gravity field features derived from GRACE.

# References

Adam, Linda; Döll, Petra; Prigent, Catherine F.; Papa, Fabrice (2010): Global-scale analysis of satellite-derived time series of naturally inundated areas as a basis for floodplain modeling. In: *Advances in Geosciences* 27, S. 45-50. DOI: 10.5194/adgeo-27-45-2010.

Alcamo, Joseph; Döll, Petra; Henrichs, Thomas; Kaspar, Frank; Lehner, Bernhard; Rösch, Thomas; Siebert, Stefan (2003): Development and testing of the WaterGAP 2 global model of water use and availability. In: *Hydrological Sciences Journal* 48 (3), S. 317–337. DOI: 10.1623/hysj.48.3.317.45290.

Alcamo, Joseph; Flörke, Martina; Märkel, Michael (2007): Future long-term changes in global water resources driven by socio-economic and climatic changes. In: *Hydrological Sciences Journal* 52 (2), S. 247–275. DOI: 10.1623/hysj.52.2.247.

Alkama, R.; Decharme, B.; Douville, H.; Becker, M.; Cazenave, Anny; Sheffield, J. et al. (2010): Global Evaluation of the ISBA-TRIP Continental Hydrological System. Part I: Comparison to GRACE Terrestrial Water Storage Estimates and In Situ River Discharges. In: *Journal of Hydrometeorology* 11 (3), S. 583–600. DOI: 10.1175/2010JHM1211.1.

Allen, Peter M.; Jeffrey C. Arnold; Bruce W. Byars (1994): Downstream channel geometry for use in planning-level models. In: *Journal of the American Water Resources Association* 30 (4), S. 663–671. DOI: 10.1111/j.1752-1688.1994.tb03321.x.

Alsdorf, Douglas; Bates, Paul D.; Melack, John M.; Wilson, Matthew D.; Dunne, Thomas (2007): Spatial and temporal complexity of the Amazon flood measured from space. In: *Geophys. Res. Lett.* 34 (L08402), S. 1–5. DOI: 10.1029/2007GL029447.

Alsdorf, Douglas; Dunne, Thomas; Melack, John M.; Smith, Laurence; Hess, Laura L. (2005): Diffusion modeling of recessional flow on central Amazonian floodplains. In: *Geophys. Res. Lett.* 32 (21). DOI: 10.1029/2005GL024412.

Alsdorf, Douglas; Han, Shin-Chan; Bates, Paul; Melack, John M. (2010): Seasonal water storage on the Amazon floodplain measured from satellites. In: *Remote Sensing of Environment* 114 (11), S. 2448–2456. DOI: 10.1016/j.rse.2010.05.020.

Alsdorf, Douglas E.; Melack, John M.; Dunne, Thomas; Mertes, Leal A. K.; Hess, Laura L.; Smith, Laurence C. (2000): Interferometric radar measurements of water level changes on the Amazon flood plain. In: *Nature* 404 (6774), S. 174–177. DOI: 10.1038/35004560.

Azarderakhsh, Marzieh; Rossow, William B.; Papa, Fabrice; Norouzi, Hamidreza; Khanbilvardi, Reza (2011): Diagnosing water variations within the Amazon basin using satellite data. In: *J. Geophys. Res.* 116 (D24). DOI: 10.1029/2011JD015997.

Bates, Paul D.; De Roo, A. P. J. (2000): A simple raster-based model for flood inundation simulation. In: *Journal of Hydrology* 236 (1-2), S. 54–77. DOI: 10.1016/S0022-1694(00)00278-X.

Beighley, R. Edward; Eggert, K. G.; Dunne, Thomas; He, Y.; Gummadi, V.; Verdin, K. L. (2009): Simulating hydrologic and hydraulic processes throughout the Amazon River Basin. In: *Hydrological Processes* 23 (8), S. 1221–1235. DOI: 10.1002/hyp.7252.

Beighley, R. Edward; Ray, R. L.; He, Y.; Lee, H.; Schaller, L.; Andreadis, K. M. et al. (2011): Comparing satellite derived precipitation datasets using the Hillslope River Routing (HRR) model in the Congo River Basin. In: *Hydrological Processes* 25 (20), S. 3216–3229.

Beven, K. (2007): Towards integrated environmental models of everywhere: uncertainty, data and modelling as a learning process. In: *Hydrol. Earth Syst. Sci.* 11 (1), S. 460–467. DOI: 10.5194/hess-11-460-2007.

Biancamaria, Sylvain; Bates, Paul D.; Boone, Aaron; Mognard, Nelly M. (2009): Large-scale coupled hydrologic and hydraulic modelling of the Ob river in Siberia. In: *Journal of Hydrology* 379 (1-2), S. 136–150. DOI: 10.1016/j.jhydrol.2009.09.054.

Bierkens, Marc F.P. (2015): Global hydrology 2015: State, trends, and directions. In: *Water Resources Research*, S. n/a. DOI: 10.1002/2015WR017173.

Birkel, C.; Tetzlaff, D.; Dunn, S. M.; Soulsby, C. (2010): Towards a simple dynamic process conceptualization in rainfall-runoff models using multi-criteria calibration and tracers in temperate, upland catchments. In: *Hydrological Processes* 24 (3), S. 260–275.

Birkett, Charon M.; Mertes, L. A. K.; Dunne, T.; Costa, M. H.; Jasinski, M. J. (2002): Surface water dynamics in the Amazon Basin: Application of satellite radar altimetry. In: *J. Geophys. Res.* 107 (D20). DOI: 10.1029/2001JD000609.

Chang, H. C.; Li, X.; Ge, L. (2010): Assessment of SRTM, ACE2 and ASTER-GDEM using RTK- GPS. In: *15th Australasian Remote Sensing & Photogrammetry Conf., Alice Springs, Australia, 13-17 September*, S. 271–279. available at http://www.gmat.unsw.edu.au/snap/publications/chang_etal2010a.pdf.

Chen, J. L.; Wilson, C. R.; Famiglietti, J. S.; Rodell, Matt (2007): Attenuation effect on seasonal basin-scale water storage changes from GRACE time-variable gravity. In: *J Geod* 81 (4), S. 237–245. DOI: 10.1007/s00190-006-0104-2.

Chen, J. L.; Wilson, C. R.; Tapley, Byron D. (2010): The 2009 exceptional Amazon flood and interannual terrestrial water storage change observed by GRACE. In: *Water Resources Research* 46 (12), S. W12526. DOI: 10.1029/2010WR009383.

Cheng, Qinbo (2015): Evaluating the Effect of Objective Functions on Model Calibration. Freie Universität Berlin, Germany.

Coe, Michael T. (2000): Modeling Terrestrial Hydrological Systems at the Continental Scale: Testing the Accuracy of an Atmospheric GCM.

Coe, Michael T.; Costa, Marcos H.; Botta, Aurélie; Birkett, C. (2002): Long-term simulations of discharge and floods in the Amazon Basin. In: *J. Geophys. Res.* 107, S. 8044. DOI: 10.1029/2001JD000740.

Coe, Michael T.; Costa, Marcos H.; Howard, Erica A. (2008): Simulating the surface waters of the Amazon River basin: impacts of new river geomorphic and flow parameterizations. In: *Hydrological Processes* 22 (14), S. 2542–2553. DOI: 10.1002/hyp.6850.

Costa, Marcos Heil; Oliveira, C. H. C.; Andrade, R. G.; Bustamante, T. R.; Silva, F. A.; Coe, M. T. (2002): A macroscale hydrological data set of river flow routing parameters for the Amazon Basin. In: *J. Geophys. Res.* 107 (D20). DOI: 10.1029/2000JD000309.

Crétaux, J.-F; Jelinski, W.; Calmant, Stéphane; Kouraev, A.; Vuglinski, V.; Bergé-Nguyen, M. et al. (2011): SOLS: A lake database to monitor in the Near Real Time water level and storage variations from remote sensing data. In: *Advances in Space Research* 47 (9), S. 1497–1507. DOI: 10.1016/j.asr.2011.01.004.

Criss, Robert E.; Winston, William E. (2008): Do Nash values have value? Discussion and alternate proposals. In: *Hydrological Processes* 22 (14), S. 2723.

Dadson, Simon J.; Ashpole, Ian; Harris, Phil; Davies, Helen N.; Clark, Douglas B.; Blyth, Eleanor; Taylor, Christopher M. (2010): Wetland inundation dynamics in a model of land surface climate: Evaluation in the Niger inland delta region. In: *J. Geophys. Res.* 115 (D23). DOI: 10.1029/2010JD014474.

de Graaf, I. E. M.; Sutanudjaja, E. H.; van Beek, L. P. H.; Bierkens, M. F. P. (2015): A high-resolution global-scale groundwater model. In: *Hydrol. Earth Syst. Sci.* 19 (2), S. 823–837. DOI: 10.5194/hess-19-823-2015.

Decharme, B.; Alkama, R.; Douville, H.; Becker, M.; Cazenave, Anny (2010): Global Evaluation of the ISBA-TRIP Continental Hydrological System. Part II: Uncertainties in River Routing Simulation Related to Flow Velocity and Groundwater Storage. In: *Journal of Hydrometeorology* 11 (3), S. 601–617. DOI: 10.1175/2010JHM1212.1.

Decharme, B.; Alkama, R.; Papa, F.; Faroux, S.; Douville, H.; Prigent, C. (2012): Global off-line evaluation of the ISBA-TRIP flood model. In: *Climate Dynamics* 38 (7-8), S. 1389–1412. DOI: 10.1007/s00382-011-1054-9.

Decharme, B.; Douville, H.; Prigent, Catherine F.; Papa, Fabrice; Aires, F. (2008): A new river flooding scheme for global climate applications: Off-line evaluation over South America. In: *J. Geophys. Res. DOI:* 10.1029/2007JD009376.

Döll, Petra (2009): Vulnerability to the impact of climate change on renewable groundwater resources: a global-scale assessment. In: *Environ. Res. Lett.* 4 (3), S. 035006. DOI: 10.1088/1748-9326/4/3/035006.

Döll, Petra; Fiedler, Kristina (2008): Global-scale modeling of groundwater recharge. In: *Hydrol. Earth Syst. Sci.* 2008 (12), S. 863–885. DOI: 10.5194/hess-12-863-2008.

Döll, Petra; Fiedler, Kristina; Zhang, Jing (2009): Global-scale analysis of river flow alterations due to water withdrawals and reservoirs. In: *Hydrol. Earth Syst. Sci.* 2009 (6), S. 4773–4812.

Döll, Petra; Hoffmann-Dobrev, H.; Portmann, F.T; Siebert, S.; Eicker, A.; Rodell, M. et al. (2012): Impact of water withdrawals from groundwater and surface water on continental water storage variations. In: *Journal of Geodynamics* 59-60, S. 143–156. DOI: 10.1016/j.jog.2011.05.001.

Döll, Petra; Kaspar, Frank; Lehner, Bernhard (2003): A global hydrological model for deriving water availability indicators: model tuning and validation. In: *Journal of Hydrology* 270 (1-2), S. 105–134. DOI: 10.1016/S0022-1694(02)00283-4.

Döll, Petra; Lehner, Bernhard (2002): Validation of a new global 30-min drainage direction map. In: *Journal of Hydrology* (258(1-4)), S. 214–231.

Döll, Petra; Müller Schmied, Hannes (2012): How is the impact of climate change on river flow regimes related to the impact on mean annual runoff? A global-scale analysis. In: *Environ. Res. Lett.* 7 (1), S. 014037. DOI: 10.1088/1748-9326/7/1/014037.

Döll, Petra; Müller Schmied, Hannes; Schuh, Carina; Portmann, Felix T.; Eicker, Annette (2014): Global-scale assessment of groundwater depletion and related groundwater abstractions: Combining hydrological modeling with information from well observations and GRACE satellites. In: *Water Resources Research* 50 (7), S. 5698–5720. DOI: 10.1002/2014WR015595.

Döll, Petra; Siebert, Stefan (2002): Global modeling of irrigation water requirements. In: *Water Resources Research* 38 (4), S. 8-1. DOI: 10.1029/2001WR000355.

Döll, Petra; Zhang, Jing (2010): Impact of climate change on freshwater ecosystems: a global-scale analysis of ecologically relevant river flow alterations. In: *Hydrol. Earth Syst. Sci.* 14 (5), S. 783–799.

Durand, M.; Andreadis, K. M.; de Alsdorf; Lettenmaier, D. P.; Moller, D.; Wilson, Matthew D. (2008): Estimation of bathymetric depth and slope from data assimilation of swath altimetry into a hydrodynamic model. In: *Geophys. Res. Lett.* 35 (20), S. L20401. DOI: 10.1029/2008GL034150.

Durand, M.; Rodriguez, E.; Alsdorf, D. E.; Trigg, M. (2010): Estimating River Depth From Remote Sensing Swath Interferometry Measurements of River Height, Slope, and Width. In: *Selected Topics in Applied Earth Observations and Remote Sensing, IEEE Journal of* 3 (1), S. 20–31. DOI: 10.1109/JSTARS.2009.2033453.

Eva, Hugh D.; Belward, Alan S.; De Miranda, Evaristo E.; Di Bella, Carlos M.; Gond, Valery; Huber, Otto et al. (2004): A land cover map of South America. In: *Global Change Biology* 10 (5), S. 731–744. DOI: 10.1111/j.1529-8817.2003.00774.x.

Evans, T. L.; Costa, M.; Telmer, K.; Silva, T. S. F. (2010): Using ALOS/PALSAR and RADARSAT-2 to Map Land Cover and Seasonal Inundation in the Brazilian Pantanal. In: *Selected Topics in Applied Earth Observations and Remote Sensing, IEEE Journal of* 3 (4), S. 560–575.

Fan, Ying; Miguez-Macho, Gonzalo (2010): A simple hydrologic framework for simulating wetlands in climate and earth system models. In: *Climate Dynamics* 37 (1-2), S. 253–278. DOI: 10.1007/s00382-010-0829-8.

Fan, Ying; Miguez-Macho, Gonzalo; Weaver, Christopher P.; Walko, Robert; Robock, Alan (2007): Incorporating water table dynamics in climate modeling: 1. Water table observations and equilibrium water table simulations. In: *J. Geophys. Res.* 112 (D10), S. n/a. DOI: 10.1029/2006JD008111.

Farr, Tom G.; Rosen, Paul A.; Caro, Edward; Crippen, Robert; Duren, Riley; Hensley, Scott et al. (2007): The Shuttle Radar Topography Mission. In: *Rev. Geophys.* 45 (2), S. RG2004. DOI: 10.1029/2005RG000183.

Fiedler, Kristina; Döll, Petra (2010): Monthly and Daily Variations of Continental Water Storage and Flows. In: L. Stroink, V. Mosbrugger, G. Wefer, Frank M. Flechtner, Thomas Gruber, Andreas Güntner et al. (Hg.): System Earth via Geodetic-Geophysical Space Techniques: Springer Berlin Heidelberg (Advanced Technologies in Earth Sciences), S. 407–415. available at doi: 10.1007/978-3-642-10228-8_35.

Fritsche, Mathias; Döll, Petra; Dietrich, Reinhard (2012): Global-scale validation of model-based load deformation of the Earth's crust from continental watermass and atmospheric pressure variations using GPS. In: *Journal of Geodynamics* 59-60, S. 133–142. DOI: 10.1016/j.jog.2011.04.001.

GRDC (2013): River Discharge Data / Global Runoff Data Centre. Koblenz, Federal Institute of Hydrology (BfG).

Gummadi, Venkat (2008): Hydraulic geometry relations for the Amazon Basin. Thesis (MS), Civil Engineering. San Diego State University.

Güntner, Andreas; Werth, Susanna; Papa, Fabrice; Frappart, Frédéric (2009): Retrieval of surface water storage in large river basins from multi-satellite and topographic data. In: *J. Geophys. Res.* (in preparation).

Gupta, Hoshin V.; Kling, Harald; Yilmaz, Koray K.; Martinez, Guillermo F. (2009): Decomposition of the mean squared error and NSE performance criteria: Implications for improving hydrological modelling. In: *Journal of Hydrology* 377 (1-2), S. 80–91. DOI: 10.1016/j.jhydrol.2009.08.003.

Hamilton, Stephen K.; Kellndorfer, Josef; Lehner, Bernhard; Tobler, Mathias (2007): Remote sensing of floodplain geomorphology as a surrogate for biodiversity in a tropical river system (Madre de Dios, Peru). In: *Geomorphology* 89 (1-2), S. 23–38. DOI: 10.1016/j.geomorph.2006.07.024.

Hamilton, Stephen K.; Sippel, S. J.; Melack, John M. (2004): Seasonal inundation patterns in two large savanna floodplains of South America: the Llanos de Moxos (Bolivia) and the Llanos del Orinoco (Venezuela and Colombia). In: *Hydrological Processes* 18 (11), S. 2103–2116. DOI: 10.1002/hyp.5559.

Han, Shin-Chan; Kim, Hyungjun; Yeo, In-Young; Yeh, Pat; Oki, Taikan; Seo, Ki-Weon (2009): Dynamics of surface water storage in the Amazon inferred from measurements of inter-satellite distance change. In: *Geophys. Res. Lett.* Vol. 36, S. L09403. DOI: 10.1029/2009GL037910.

Harris, I.; Jones, P. D.; Osborn, T. J.; Lister, D. H. (2014): Updated high-resolution grids of monthly climatic observations - the CRU TS3.10 Dataset. In: *Int. J. Climatol.* 34 (3), S. 623–642. DOI: 10.1002/joc.3711.

Hess, Laura L.; Melack, John M.; Novo, Evlyn Márcia Leão de Moraes; Barbosa, Claudio C. F.; Gastil, Mary (2003): Dual-season mapping of wetland inundation and vegetation for the central Amazon basin. Large Scale Biosphere Atmosphere Experiment in Amazonia. In: *Remote Sensing of Environment* 87 (4), S. 404–428. DOI: 10.1016/j.rse.2003.04.001.

Hey, Richard D.; Thorne, Colin R. (1986): Stable channels with mobile gravel beds. In: *J. Hydraul. Eng.* 112 (8), S. 671–689.

Hunger, Martin; Döll, Petra (2008): Value of river discharge data for global-scale hydrological modeling. In: *Hydrol. Earth Syst. Sci. Discuss.* 4 (12), S. 841–861. available at www.hydrol-earth-syst-sci-discuss.net/4/4125/2007/.

Jacobsen, K. (2010): Vergleich von ASTER GDEM-mit SRTM-Höhenmodellen. In: *DGPF Tagungsband 19 / 2010 - Dreiländertagung, Wien*.

Junk, Wolfgang J (1997): The central Amazon floodplain. Ecology of a pulsing system. Berlin: Springer (Ecological studies, 126). available at http://www.gbv.de/dms/bowker/toc/9783540592761.pdf.

Junk, Wolfgang J.; Piedade, Maria Teresa Fernandez; Schöngart, Jochen; Cohn-Haft, Mario; Adeney, J. Marion; Wittmann, Florian (2011): A Classification of Major Naturally-Occurring Amazonian Lowland Wetlands. In: *Wetlands* 31 (4), S. 623–640. DOI: 10.1007/s13157-011-0190-7.

Kaspar, Frank (2004): Entwicklung und Unsicherheitsanalyse eines globalen hydrologischen Modells. Inaugural-Dissertation. Universität Kassel, Kassel. FB Naturwissenschaften.

König, Matthias (2011): Validierung einer globalen Zeitreihe der terrestrischen Wasserbedeckung. Diplomarbeit. Goethe-Universität, Frankfurt am Main.

Krause, P.; Boyle, D. P.; Bäse, F. (2005): Comparison of different efficiency criteria for hydrological model assessment. In: *Advances in Geosciences* (5), S. 89–97.

Kusche, J.; Schmidt, R.; Petrovic, S.; Rietbroek, R. (2009): Decorrelated GRACE time-variable gravity solutions by GFZ, and their validation using a hydrological model. In: *J Geod* 83 (10), S. 903-913. DOI: 10.1007/s00190-009-0308-3.

Landerer, F. W.; Swenson, S. C. (2012): Accuracy of scaled GRACE terrestrial water storage estimates. In: *Water Resources Research* 48 (4). DOI: 10.1029/2011WR011453.

Legates, David R.; McCabe, Gregory J. (1999): Evaluating the use of "goodness-of-fit" Measures in hydrologic and hydroclimatic model validation. In: *Water Resources Research* 35 (1), S. 233–241. DOI: 10.1029/1998WR900018.

Lehner, B.; Verdin, K.; Jarvis, A. (2006a): HydroSHEDS. Technical Documentation. Version 1.0.

Lehner, B.; Verdin, K.; Jarvis, A. (2008a): HydroSHEDS. Technical Documentation. Version 1.1.

Lehner, Bernhard; Döll, Petra (2004): Development and validation of a global database of lakes, reservoirs and wetlands. In: *Journal of Hydrology* 296 (1-4), S. 1–22. DOI: 10.1016/j.jhydrol.2004.03.028.

Lehner, Bernhard; Döll, Petra; Alcamo, Joseph; Henrichs, Thomas; Kaspar, Frank (2006b): Estimating the Impact of Global Change on Flood and Drought Risks in Europe: A Continental, Integrated Analysis. In: *Climatic Change* 75 (3), S. 273–299. DOI: 10.1007/s10584-006-6338-4.

Lehner, Bernhard; Liermann, Catherine Reidy; Revenga, Carmen; Vörösmarty, Charles; Fekete, Balazs; Crouzet, Philippe et al. (2011): High-resolution mapping of the world's reservoirs and dams for sustainable river-flow management. In: *Frontiers in Ecology and the Environment* 9 (9), S. 494–502. DOI: 10.1890/100125.

Lehner, Bernhard; Verdin, K.; Jarvis, A. (2008b): New global hydrography derived from spaceborne elevation data: Eos, Transactions, AGU, 89(10):93-94.

Leopold, L. B.; Maddock, Thomas Jr. (1953): The hydraulic geometry of stream channels and some physiographic implications. - (Professional Paper). available at http://pubs.er.usgs.gov/publication/pp252.

Leopold, Luna Bergere (1994): A View of the River: Harvard University Press.

Lininger, Katherine B.; Latrubesse, Edgardo M. (2016): Flooding hydrology and peak discharge attenuation along the middle Araguaia River in central Brazil. In: *CATENA* 143, S. 90–101. DOI: 10.1016/j.catena.2016.03.043.

Matthews, Elaine; Fung, Inez; Lerner, Jean (1991): Methane Emission From Rice Cultivation: Geographic and   Seasonal Distribution of Cultivated Areas and Emissions. In: *Global Biogeochem. Cycles* 5 (1), S. 3–24. DOI: 10.1029/90GB02311.

Mays, Larry W. (1996): Water resources handbook. New York: McGraw-Hill. available at http://www.gbv.de/dms/bowker/toc/9780070411500.pdf.

Meade, Robert H.; Rayol, José M.; Da Conceicão, Sylvio C.; Natividade, José R. G. (1991): Backwater effects in the Amazon River basin of Brazil. In: *Environmental Geology* 18 (2), S. 105–114. DOI: 10.1007/BF01704664.

Melack, John M. (1984): Amazon floodplain lakes: Shape, fetch, and stratification. In: *Verhandlung Internationale Vereinigung Limnologie* 22.

Melack, John M.; Forsberg, Bruce R. (2001): Biogeochemistry of Amazon floodplain lakes and associated wetlands. In: *The biogeochemistry of the Amazon basin and its role in a changing world*, S. 235–276.

Melack, John M.; Hess, Laura L. (2004): Remote Sensing of Wetlands on a Global Scale. In: *SIL news* 2004 (Vol. 42, May).

Miguez-Macho, Gonzalo; Fan, Ying (2012): The role of groundwater in the Amazon water cycle: 1. Influence on seasonal streamflow, flooding and wetlands. In: *J. Geophys. Res.* 117 (D15). DOI: 10.1029/2012JD017539.

Miguez-Macho, Gonzalo; Fan, Ying; Weaver, Christopher P.; Walko, Robert; Robock, Alan (2007): Incorporating water table dynamics in climate modeling: 2. Formulation, validation, and soil moisture simulation. In: *J. Geophys. Res.* 112 (D13), S. D13108. DOI: 10.1029/2006JD008112.

Mitchell, Timothy D.; Jones, Philip D. (2005): An improved method of constructing a database of monthly climate observations and associated high-resolution grids. In: *Int. J. Climatol.* 25 (6), S. 693–712. DOI: 10.1002/joc.1181.

Mitsch, William J.; Gosselink, James G. (2000): The value of wetlands: importance of scale and landscape setting. In: *Ecological Economics* 35 (1), S. 25–33. DOI: 10.1016/S0921-8009(00)00165-8.

Moriasi, D. N.; Arnold, J. G.; van Liew, M. W.; Bingner, R. L.; Harmel, R. D.; Veith, T. L. (2007): Model evaluation guidelines for systematic quantification of accuracy in watershed simulations.

Müller Schmied, H.; Adam, L.; Eisner, S.; Fink, G.; Flörke, M.; Kim, H. et al. (2016): Variations of global and continental water balance components as impacted by climate forcing uncertainty and human water use. In: *Hydrol. Earth Syst. Sci.* 20 (7), S. 2877–2898. DOI: 10.5194/hess-20-2877-2016.

Müller Schmied, Hannes; Eisner, S.; Franz, D.; Wattenbach, M.; Portmann, F. T.; Flörke, M.; Döll, P. (2014): Sensitivity of simulated global-scale freshwater fluxes and

storages to input data, hydrological model structure, human water use and calibration. In: *Hydrol. Earth Syst. Sci.* 18 (9), S. 3511–3538. DOI: 10.5194/hess-18-3511-2014.

Nash, J. E.; Sutcliffe, J. V. (1970): River flow forecasting through conceptual models part I — A discussion of principles. In: *Journal of Hydrology* 10 (3), S. 282–290. DOI: 10.1016/0022-1694(70)90255-6.

Neal, Jeffrey; Schumann, Guy; Bates, Paul (2012): A subgrid channel model for simulating river hydraulics and floodplain inundation over large and data sparse areas. In: *Water Resources Research* 48 (11), S. n/a. DOI: 10.1029/2012WR012514.

Paiva, Rodrigo C. D.; Collischonn, Walter; Buarque, Diogo Costa (2013): Validation of a full hydrodynamic model for large-scale hydrologic modelling in the Amazon. In: *Hydrological Processes* 27 (3), S. 333–346. DOI: 10.1002/hyp.8425.

Paiva, Rodrigo C. D.; Collischonn, Walter; Tucci, Carlos E.M (2011): Large scale hydrologic and hydrodynamic modeling using limited data and a GIS based approach. In: *Journal of Hydrology* 406 (3-4), S. 170–181. DOI: 10.1016/j.jhydrol.2011.06.007.

Papa, Fabrice; Prigent, Catherine F.; Aires, F.; Jimenez, C.; Rossow, William B.; Matthews, Elaine (2010): Interannual variability of surface waters at global scale, 1993-2004. In: *J. Geophys. Res.* 115, D12111. DOI: 10.1029/2009JD012674.

Papa, Fabrice; Prigent, Catherine F.; Durand, Fabien; Rossow, William B. (2006): Wetland dynamics using a suite of satellite observations: A case study of application and evaluation for the Indian Subcontinent. In: *Geophys. Res. Lett.* 2006 (33, L08401). DOI: 10.1029/2006GL025767.

Papa, Fabrice; Prigent, Catherine F.; Rossow, William B. (2008b): Monitoring Flood and Discharge Variations in the Large Siberian Rivers From a Multi-Satellite Technique. In: *Surveys in Geophysics* 29 (4), S. 297–317. DOI: 10.1007/s10712-008-9036-0.

Papa, Fabrice; Prigent, Catherine F.; Rossow, William B. (2007): Ob' River flood inundations from satellite observations: A relationship with winter snow parameters and river runoff. In: *J. Geophys. Res.* Vol. 112, S. D18103. DOI: 10.1029/2007JD008451.

Pavelsky, T. M.; Smith, Laurence C. (2008): Rivwidth: A software tool for the calculation of river widths from remotely sensed imagery. In: *IEEE Geoscience and Remote Sensing Letters* 5 (1), S. 70. DOI: 10.1109/LGRS.2007.908305.

Pedinotti, V.; Boone, Aaron; Decharme, B.; Crétaux, J. F.; Mognard, N.; Panthou, G. et al. (2012): Evaluation of the ISBA-TRIP continental hydrologic system over the Niger basin using in situ and satellite derived datasets. In: *Hydrol. Earth Syst. Sci.* 16 (6), S. 1745–1773. DOI: 10.5194/hess-16-1745-2012.

Petrescu, A. M. R.; van Beek, L. P. H.; van Huissteden, J.; Prigent, C.; Sachs, T.; Corradi, C. A. R. et al. (2010): Modeling regional to global CH4 emissions of boreal and

arctic wetlands. In: *Global Biogeochem. Cycles* 24 (4), S. n/a. DOI: 10.1029/2009GB003610.

Portmann, Felix T.; Siebert, Stefan; Döll, Petra (2010): MIRCA2000 - Global monthly irrigated and rainfed crop areas around the year 2000: A new high-resolution data set for agricultural and hydrological modeling. In: *Global Biogeochem. Cycles* 24 (1), S. GB1011. DOI: 10.1029/2008GB003435.

Prigent, Catherine F.; Matthews, Elaine; Aires, F.; Rossow, William B. (2001): Remote sensing of global wetland dynamics with multiple satellite data sets. In: *Geophys. Res. Lett.* 28 (24), S. 4631–4634.

Prigent, Catherine F.; Papa, Fabrice; Aires, W. B.; Rossow, William B.; Matthews, Elaine (2007): Global inundation dynamics inferred from multiple satellite observations, 1993–2000. In: *J. Geophys. Res.* 2007 (112, D12107). DOI: 10.1029/2006JD007847.

Ramillien, G.; Frappart, F.; Cazenave, A.; Güntner, A. (2005): Time variations of land water storage from an inversion of 2 years of GRACE geoids. In: *Earth and Planetary Science Letters* 235 (1–2), S. 283–301. DOI: 10.1016/j.epsl.2005.04.005.

Rauter, H. I.; Nelson, A.; Strobl, P.; Mehl, W.; Jarvis, A. (2009): A first assessment of ASTER GDEM tiles for absolute accuracy, relative accuracy and terrain parameters. In: *Proc. IEEE IGARSS* (5), S. V240–V243.

Richey, Jeffrey E.; Melack, John M.; Aufdenkampe, Anthony K.; Ballester, Victoria M.; Hess, Laura L. (2002): Outgassing from Amazonian rivers and wetlands as a large tropical source of atmospheric CO2. In: *Nature* 416 (6881), S. 617–620. DOI: 10.1038/416617a.

Richey, Jeffrey E.; Mertes, Leal A. K.; Dunne, Thomas; Victoria, Reynaldo L.; Forsberg, Bruce R.; Tancredi, Antônio C. N. S.; Oliveira, Eurides (1989): Sources and Routing of the Amazon River Flood Wave. In: *Global Biogeochem. Cycles* 3 (3), S. 191–204. DOI: 10.1029/GB003i003p00191.

Ringeval, B.; Houweling, S.; van Bodegom, P. M.; Spahni, R.; van Beek, R.; Joos, F.; Röckmann, T. (2014): Methane emissions from floodplains in the Amazon Basin: challenges in developing a process-based model for global applications. In: *Biogeosciences* 11 (6), S. 1519–1558. DOI: 10.5194/bg-11-1519-2014.

Ritter, Axel; Muñoz-Carpena, Rafael (2013): Performance evaluation of hydrological models: Statistical significance for reducing subjectivity in goodness-of-fit assessments. In: *Journal of Hydrology* 480, S. 33–45.

Rudolf, Bruno; Schneider, Udo (2005): Calculation of gridded precipitation data for the global land-surface using in-situ gauge observations. Proc. 2nd Workshop of the International Precipitation Working IPWG, Monterey.

Sanders, Brett F. (2007): Evaluation of on-line DEMs for flood inundation modeling. In: *Advances in Water Resources* 30 (8), S. 1831–1843. DOI: 10.1016/j.advwatres.2007.02.005.

Schaefli, Bettina; Gupta, Hoshin V. (2007): Do Nash values have value? In: *Hydrological Processes* 21 (15), S. 2075–2080.

Schmidt, R.; Schwintzer, P.; Flechtner, F.; Reigber, Ch.; Güntner, A.; Döll, P. et al. (2006): GRACE observations of changes in continental water storage. In: *Global and planetary Change* 50 (1–2), S. 112–126. DOI: 10.1016/j.gloplacha.2004.11.018.

Schneider, Christof; Flörke, Martina; Eisner, Stephanie; Voß, Frank (2011a): Large scale modelling of bankfull flow: An example for Europe. In: *Journal of Hydrology* 408 (3-4), S. 235–245. DOI: 10.1016/j.jhydrol.2011.08.004.

Schneider, Christof; Flörke, Martina; Geerling, Gertjan; Duel, Harm; Grygoruk, Mateusz; Okrusko, Tomasz (2011b): The future of European floodplain wetlands under a changing climate. In: *Journal of Water and Climate Change* 2 (2-3), S. 106–122. DOI: 10.2166/wcc.2011.020.

Schneider, Udo; Becker, Andreas; Finger, Peter; Meyer-Christoffer, Anja; Ziese, Markus; Rudolf, Bruno (2014): GPCC's new land surface precipitation climatology based on quality-controlled in situ data and its role in quantifying the global water cycle. In: *Theoretical and Applied Climatology* 115 (1-2), S. 15–40. DOI: 10.1007/s00704-013-0860-x.

Schulze, Kerstin; Hunger, Martin; Döll, Petra (2005): Simulating river flow velocity on global scale. In: *Advances in Geosciences* 5, S. 133–136.

Seo, K.-W.; Wilson, C. R. (2005): Simulated estimation of hydrological loads from GRACE. In: *J Geod* 78 (7), S. 442–456. DOI: 10.1007/s00190-004-0410-5.

Seo, Ki-Weon; Wilson, Clark R.; Chen, Jianli; Waliser, Duane E. (2008): GRACE's spatial aliasing error. In: *Geophysical Journal International* 172 (1), S. 41–48. DOI: 10.1111/j.1365-246X.2007.03611.x.

Shen, D.; Wang, J.; Cheng, X.; Rui, Y.; Ye, S. (2015): Integration of 2-D hydraulic model and high-resolution LiDAR-derived DEM for floodplain flow modeling. In: *Hydrol. Earth Syst. Sci. Discuss.* 12 (2), S. 2011–2046.

Simard, Marc; Pinto, Naiara; Fisher, Joshua B.; Baccini, Alessandro (2011): Mapping forest canopy height globally with spaceborne lidar. In: *J. Geophys. Res.* 116 (G4). DOI: 10.1029/2011JG001708.

Sippel, S. J.; Hamilton, Stephen K.; Melack, John M. (1998): Passive microwave observations of inundation area and the area/stage relation in the Amazon River floodplain. In: *International Journal of Remote Sensing* 1998 (Vol. 19, No. 16, 3055-3074).

Smakhtin, Vladimir; Revenga, Carmen; Döll, Petra (2004): A pilot global assessment of environmental water requirements and scarcity. In: *Water International* 29 (3), S. 307–317.

Smith, Richard G.; Berry, Philippa A. M. (2009): ACE2 3 arc second dataset. Version 1.31: EAPRS Laboratory, De Montfort University, Leicester UK, available from http://tethys.eaprs.cse.dmu.ac.uk/ACE2.

Sood, Aditya; Smakhtin, Vladimir (2015): Global hydrological models: a review. In: *Hydrological Sciences Journal* 60 (4), S. 549–565. DOI: 10.1080/02626667.2014.950580.

Swenson, Sean; Wahr, John (2006): Post-processing removal of correlated errors in GRACE data. In: *Geophys. Res. Lett.* 33 (8), S. n/a. DOI: 10.1029/2005GL025285.

Tapley, Byron D.; Bettadpur, Srinivas; Ries, John C.; Thompson, Paul F.; Watkins, Michael M. (2004): GRACE Measurements of Mass Variability in the Earth System. In: *Science* 305 (5683), S. 503–505. DOI: 10.1126/science.1099192.

Trigg, Mark A.; Wilson, Matthew D.; Bates, Paul D.; Horritt, Matthew S.; Alsdorf, Douglas E.; Forsberg, Bruce R.; Vega, Maria C. (2009): Amazon flood wave hydraulics. In: *Journal of Hydrology* 374 (1-2), S. 92–105. DOI: 10.1016/j.jhydrol.2009.06.004.

van Beek, L. P. H.; Bierkens, Marc F.P. (2009): The Global Hydrological Model PCR-GLOBWB: Conceptualization, Parameterization and Verification. Report. Department of Physical Geography, Utrecht University Utrecht The Netherlands. available at http://vanbeek.geo.uu.nl/suppinfo/vanbeekbierkens2009.pdf.

Vassolo, Sara; Döll, Petra (2005): Global-scale gridded estimates of thermoelectric power and manufacturing water use. In: *Water Resources Research* 41 (4), S. n/a. DOI: 10.1029/2004WR003360.

Verzano, Kerstin (2009): Climate Change Impacts on Flood Related Hydrological Processes: Further Development and Application of a Global Scale Hydrological Model. Dissertation. University of Kassel.

Vörösmarty, Charles J.; Fekete, B.; Tucker, B. A. (1998): Global River Discharge, 1807-1991, Version 1.1 (RivDIS). Data set. Available on-line [http://www.daac.ornl.gov] from Oak Ridge National Laboratory Distributed Active Archive Center, Oak Ridge, Tennessee, U.S.A. DOI: 10.3334/ORNLDAAC/199.

Vörösmarty, Charles J.; Moore, Berrien (1991): Modeling basin-scale hydrology in support of physical climate and global biogeochemical studies: An example using the Zambezi River. In: *Surveys in Geophysics* 12 (1), S. 271–311. DOI: 10.1007/BF01903422.

Voß, F.; Flörke, M. (2010): Spatially explicit estimates of past and present manufacturing and energy water use. In: *Kassel, Germany: Center for Environmental Systems Research* 23, S. 23.

Voß, F.; Flörke, M.; Alcamo, J. (2009): Preliminary spatially explicit estimates of past and present domestic water use. WATCH Technical Report.

Wada, Y.; Wisser, D.; Bierkens, Marc F.P. (2014): Global modeling of withdrawal, allocation and consumptive use of surface water and groundwater resources. In: *Earth Syst. Dynam.* 5 (1), S. 15–40. DOI: 10.5194/esd-5-15-2014.

Wahr, John; Molenaar, Mery; Bryan, Frank (1998): Time variability of the Earth's gravity field: Hydrological and oceanic effects and their possible detection using GRACE. In: *J. Geophys. Res.* 103 (B12), S. 30205–30229. DOI: 10.1029/98JB02844.

Werth, S.; Güntner, A.; Schmidt, R.; Kusche, J. (2009): Evaluation of GRACE filter tools from a hydrological perspective. In: *Geophysical Journal International* 179 (3), S. 1499–1515. DOI: 10.1111/j.1365-246X.2009.04355.x.

Werth, Susanna; Güntner, Andreas (2010): Calibration analysis for water storage variability of the global hydrological model WGHM. In: *Hydrol. Earth Syst. Sci.* 14 (1), S. 59–78. DOI: 10.5194/hess-14-59-2010.

Willmott, Cort J. (1981): On the validation of models. In: *Physical geography* 2 (2), S. 184–194.

Willmott, Cort J.; Ackleson, Steven G.; Davis, Robert E.; Fedemma, Johannes J.; Klink, Katherine M.; Legates, David R. et al. (1985): Statistics for the Evaluation and Comparison of Models. In: *J. Geophys. Res.* 90 (C5), S. 8995–9005.

Wilson, M.; Bates, Paul; Alsdorf, Douglas; Forsberg, Bruce R.; Horritt, M.; Melack, John M. et al. (2007): Modeling large-scale inundation of Amazonian seasonally flooded wetlands. In: *Geophys. Res. Lett.* 34, L15404, S. 1–10. DOI: 10.1029/2007GL030156.

Wolski, P.; Savenije, H. H. G.; Murray-Hudson, M.; Gumbricht, T. (2006): Modelling of the flooding in the Okavango Delta, Botswana, using a hybrid reservoir-GIS model. In: *Journal of Hydrology* 331 (1-2), S. 58–72. DOI: 10.1016/j.jhydrol.2006.04.040.

Yamazaki, Dai; Baugh, Calum A.; Bates, Paul D.; Kanae, Shinjiro; Alsdorf, Douglas E.; Oki, Taikan (2012a): Adjustment of a spaceborne DEM for use in floodplain hydrodynamic modeling. In: *Journal of Hydrology* 436-437, S. 81–91. DOI: 10.1016/j.jhydrol.2012.02.045.

Yamazaki, Dai; Kanae, Shinjiro; Kim, Hyungjun; Oki, Taikan (2011): A physically based description of floodplain inundation dynamics in a global river routing model. In: *Water Resources Research* 47 (4), S. n/a. DOI: 10.1029/2010WR009726.

Yamazaki, Dai; Lee, Hyongki; Alsdorf, Douglas E.; Dutra, Emanuel; Kim, Hyungjun; Kanae, Shinjiro; Oki, Taikan (2012b): Analysis of the water level dynamics simulated by a global river model: A case study in the Amazon River. In: *Water Resources Research* 48 (9). DOI: 10.1029/2012WR011869.

Yamazaki, Dai; O'Loughlin, Fiachra; Trigg, Mark A.; Miller, Zachary F.; Pavelsky, Tamlin M.; Bates, Paul D. (2014): Development of the Global Width Database for Large Rivers. In: *Water Resources Research* 50 (4), S. 3467–3480. DOI: 10.1002/2013WR014664.

# Appendices

# 1 Appendix to Chapter 4

## 1.1 Flood initiation

Average start month of the longest flooding event (river inflow > bankfull) (1971-2000), WaterGAP 2.2
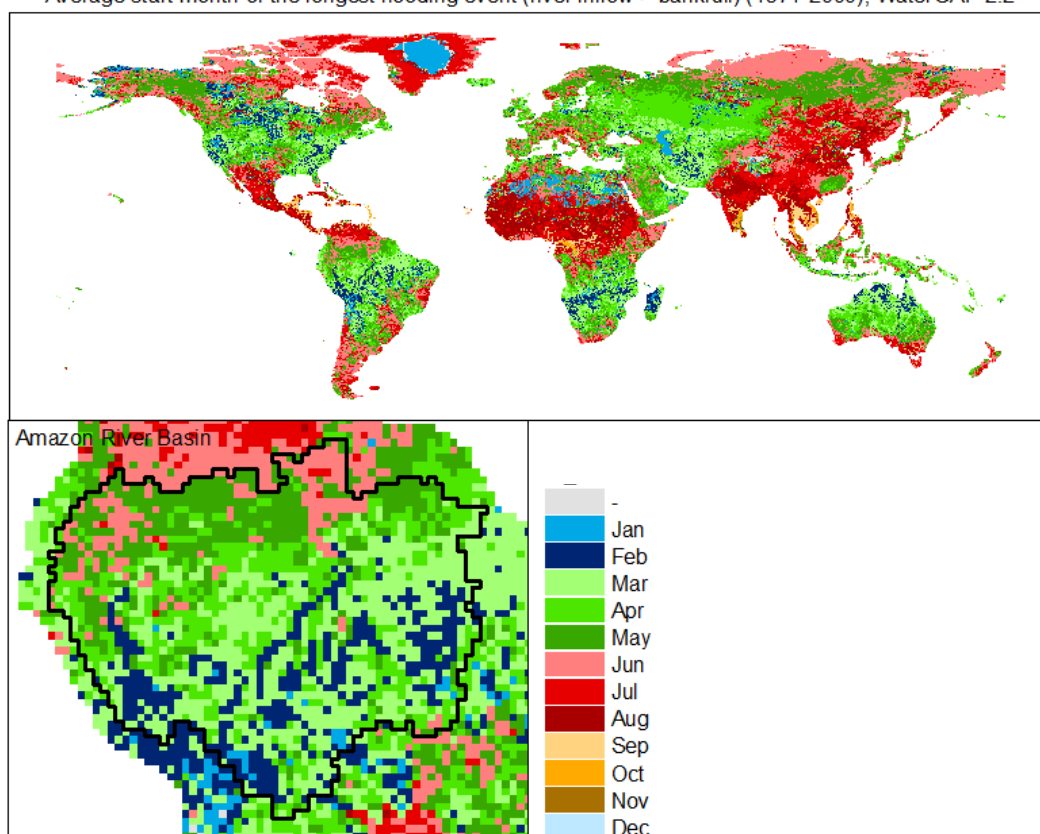


**Figure A.1** Average start month of the longest flood event (river inflow is above bankfull flow) considering daily source data from 1970 to 2000 (e.g. Jan means that the first day where river inflow exceeds bankfull is in January (day 0-31)).

Average duration of the longest flood event (river inflow > bankfull) in month (1971-2000), WaterGAP 2.2



Amazon River Basin

| | |
|---|---|
| | 0 |
| | 1 - 5 |
| | 6 - 15 |
| | 16 - 30 (>0.5 to 1 month) |
| | 31 - 60 (>1 to 2 month) |
| | 61 - 90 (>2 to 3 month) |
| | 91 - 120 (>3 to 4 month) |
| | 121 - 210 (>4 to 7 month) |
| | 211 - 364 (>7 to 12 month) |
| | 365 |
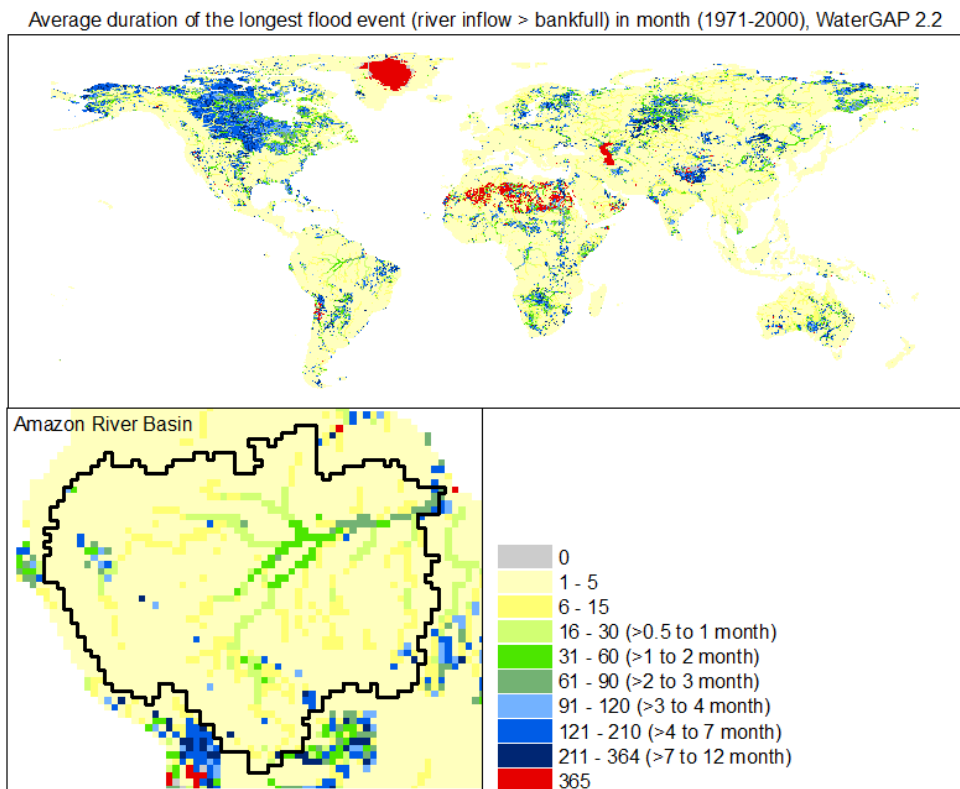
**Figure A.2** Average duration of the longest flood event (river inflow is above bankfull flow) in days (1971-2000).

Average number of flood events per year lasting more than 3 days (1971-2000), WaterGAP 2.2



Amazon River Basin

| | |
|---|---|
| | 0.0000 |
| | 0.0001 - 0.2500 (until every 4 years) |
| | 0.2501 - 0.5000 (every 4 to 2 years) |
| | 0.5001 - 0.7500 (every 2 to 1.5 years) |
| | 0.7501 - 1.0000 (every 1.5 to once a year) |
| | 1.0001 - 2.0000 (once to twice a year) |
| | >2.0 (more than twice a year) |
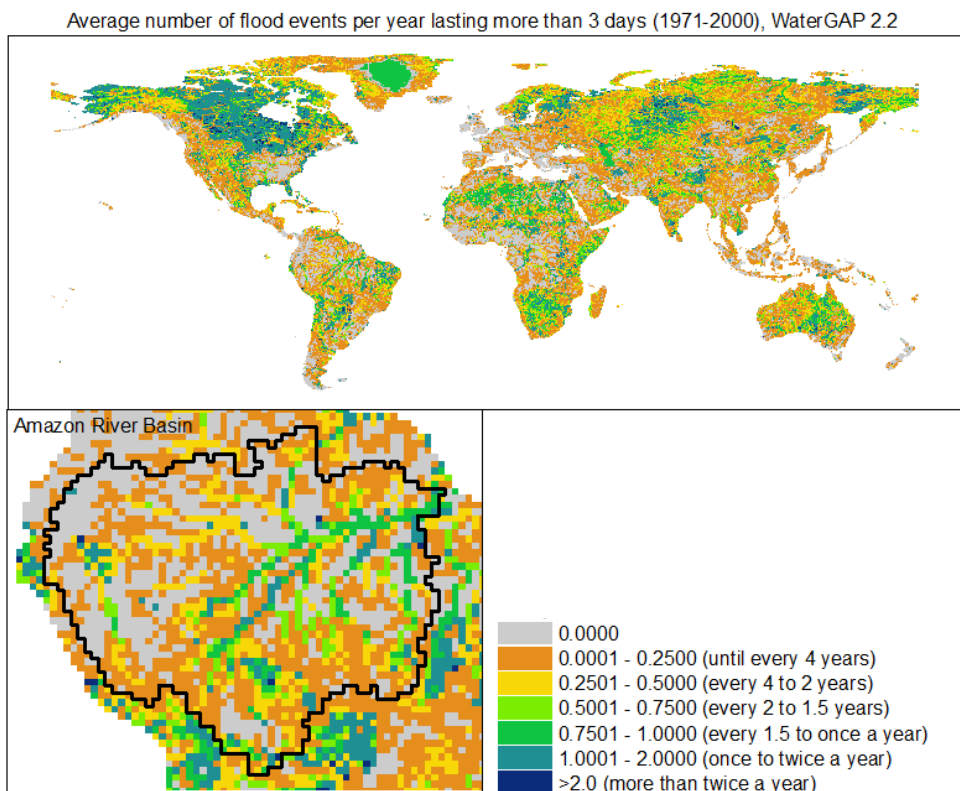
**Figure A.3** Average number of flood events per year where River inflow is at least three days above bankfull flow (1970-2000) (based on daily data source).

132

## 1.2 Data preparation of digital elevation models (DEMs) as model input for WaterGAP

### 1.2.1 HydroSHEDS

**Hydro**logical data and maps based on **SH**uttle **E**levation **D**erivatives at multiple **S**cales (HydroSHEDS):

Data format:
- ARC GRID, BIL (vector)
- projection WGS84

Spatial resolution:
- 3", 15", 30" (approximately 90m, 500m, 1km at the equator)
- global (60N - 60S)

Provided by:
- USGS; developed by the Conservation Science Program of World Wildlife Fund (FFW)

Citation:

Lehner, Bernhard; Verdin, K.; Jarvis, A. (2008): New global hydrography derived from spaceborne elevation data: Eos, Transactions, AGU, 89(10):93-94.

**HydroSHEDS Data preparation as model input for WaterGAP**

General information:
- To facilitate electronic distribution, all raster data at 3 arc-second resolution were divided into five-degree by five-degree tiles. Thus each downloadable HydroSHEDS tile 10 x 10 0.5° cells.
- Raster attribute table columns: 'Rowid' 'Value' 'Count'

Amazon:
- the Amazon basin has 1946 0.5° grid cells
- 30 HydroSHEDS tiles are necessary to cover the whole Amazon basin

World:
- HydroSHEDS includes 775 data tiles for the whole world (southern hemisphere: 245 tiles, northern hemisphere: 530 tiles).
- 276 grid cells of WaterGAP are not covered by HydroSHEDS: 187 cells of Alaska, 34 grid cells located in the Caspian Sea and 55 grid cells islands like Reunión and Mauritius, Cape Verde, Hawaii and other Pacific islands etc.
- Another 81 grid cells are covered by the raster dataset but do not include values (no value after processing raster to txt). Of these cells, 74 are located in the Caspian Sea and 7 are coastal cells (continental area < 20 %).

**Data preparation**

Download the data DEM 3sec void filled elevation from the website
http://gisdata.usgs.net/website/HydroSHEDS/viewer.php. The data format is GRID and
the spacial resolution is 3 arc seconds.

After downloading the data from the website, first of all, the raster data is downscaled
on a spatial resolution of 0.5° or rather related to the 0.5° cells of WGHM. To get one
GRID file for each of the 0.5° cells, the raster files are clipped by the 0.5° cell Polygons
by using GME (Geospatial Modelling Environment, http://www.spatialecology.com/
gme/index.htm). The Arc_ID of the 0.5° cells are written in the file name.

Second, the 0.5° raster files are converted into text files (txt, tab delimited) which are
the required input format for the WaterGAP preprocessing tools to calculate floodplain
depth and floodplain storage capacity. The Raster conversion into txt-files does a Py-
thon Script (*Linda's Tools --> Raster To TXT (multiple)*; Toolbox manual available)
written for ArcMap.

As a third step, the WaterGAP preprocessing tools (Unix Shell Scripts) reduce the data
amount to 100 elevation values per 0.5° grid cell and calculate the floodplain depth and
the storage capacity of the floodplain area for each elevation point. The tools outputs are
one file per 0.5° grid cell for each of the input variables. The statistical software R is
used to merge output files to each one file with global coverage. In doing so WaterGAP
grid cells with no available elevation data are set to -999 or -555 (-999: no DEM Raster
Data available; -555: DEM Raster Data is available but no elevation values for example
including values for land masking).

WaterGAP Input Data:
- $S_f$ – Floodplain Storage [km³]; Source Name: *HS_Storage.sh*
- $D_f$ – Floodplain Depth [m]; relative Elevation of the floodplain. $D_f$ is needed to
  calculate the slope in the diffusive wave equation (if $S_r > S_b$). Source Name:
  *HS_relElev.sh*
- B – Bank height [m]; minimum Elevation of the 0.5° cell. The name of the
  variable in WaterGAP is GALTMOD. Source Name: *HS_minElev.sh*
- $A_f$ – Floodplain Area [%]; constant for all of the 0.5° cells. First value is zero,
  last value is 99.99972101 (100% minus the area of the outflow pixel). No pre-
  processing Tool required.

**Requirements and Tool Descriptions:**

Requirements:
- ArcGIS 9.x or further versions
- GME for ArcGIS 10.x (http://www.spatialecology.com)

- Python 2.5 (with Python extension win32 (http://sourceforge.net/projects/pywin32))
- Excel 2007 or further versions

Using Geospatial Modelling Environment (GME)

- Follow the instructions for downloading and installing GME (http://www.spatial ecology.com/gme/index.htm).
- Start GME.
- Clip HydroSHEDs raster tiles by the 0.5° cell Polygons ("father_polys.shp") using the command cliprasterbypolys (http://www.spatialecology.com/gme/cliprasterbypolys.htm).
- Note that the polygon layer and raster layers must share the same projection.
- For multiple raster inputs, like several HydroSHEDs tiles, you can EITHER
- mosaic multiple tiles to a single raster (ArcGIS: Data Management Tools → Raster → Raster Dataset → Mosaic To New Raster) before clipping it by polygons OR
- use a for loop to clip all the raster tiles located in one folder.
- The for loop requires an index variable name (e.g. i) to define the number of iterations.

  To get simple unique raster tile names including the index variable, I renamed all HydroSHEDs raster to "dem[i]". Rename folders using the awk command under Linux or, for windows, using for example the free software "Flexible Renamer".

GME Syntax Example:

```
for(i in 1:245){
   cliprasterbypol-
   ys(raster=paste("D:\Linda\HydroSHEDS_world\SOUTH\dem",i),
   poly="D:\Linda\WaterGAP\X.ESRI.IPG_home.IPG_data\father_polys.
   shp", uidfield="ARC_ID",
   out="D:\Linda\HydroSHEDS_world\ClipRasterByPolygons_ArcID",
   prefix="r");
};
```

The following paragraphs provide more detailed information about the HydroSHEDS data preparation tool in ArcMap (1), the WaterGAP preprocessing tools for defining the minimum elevation value (2), and the tool for calculating the floodplain Storage capacity (3) per grid cell. These Tools were developed and programmed by the Author of this thesis.:

1) *"LA_raster2txt_ArcMap.py"*: ArcGIS Tool
   - Converts one or more Rasters (DEM or GRID) into text files (txt, tab delimited).
     (First, the tool will convert the rasters into point shape files. Each 0.5°

cell includes 600 x 600 HydroSHEDS elevation values as a maximum (at the Equator; in higher latitude fewer values) which will be stored in the shape files attribute table (dbf-format). This shape is only a temporary file. In a second step the shape files attribute tables (binary files) will be converted into text files (txt), which are the output files)

- The input Rasters can be file Rasters or Geodatabase Rasters. The output parameter will be a workspace.

- The name of the output txt tables will be based on the name of the input Raster but will be unique for the destination workspace.

2) *"HS_minElev.sh"*: Unix Shell Script

- reads the HydroSHEDS elevation files (must be prepared in tab separated text files (txt)), each including 600 x 600 values as a maximum (at the Equator)

- sorts the elevation values according to size

- replaces negative elevations with zero

- defines the lowest permill of all elevation values, which will be deleted (two reasons: a) assuming that at least one part per thousand of each cell is always covered by water, and b) reducing erroneous elevation values, like negative elevations and sink cells). The lowest elevation value of the remaining data represents the minimum elevation of the 0.5° cell.

- joins all files together in a table with 2 columns delimited with '\t' (the first column is the Arc_ID and the second column is the minimum per grid cell)

3) *"HS_Storage.sh"*: Unix Shell Script

- reads the HydroSHEDS elevation files (they must be prepared in tab separated text files (txt)), each including 600 x 600 values as a maximum (at the Equator)

- sorts the elevation values according to size

- replaces negative elevations with zero

- defines the lowest permill of all elevation values, which will be deleted (two reasons: a) assuming that at least one part per thousand of each cell is always covered by water, and b) reducing erroneous elevation values, like negative elevations and sink cells). The lowest elevation value of the remaining data represents the minimum elevation of the 0.5° cell.

- calculates the volume of water [km³] for each elevation point.
    - Transform the unit of elevation from m to km
    - Read in the cell area [km²] of the corresponding 0.5° cell
    - Calculate area of inundation per elevation value and 0.5° cell (transform percent of inundated area in equivalent area inundated per elevation value in km²)

- Sum the volumes up: $(((elev-minElev)/1000)*((cellArea*Area.per.elev.procent)/100)$

  $+ \quad ((elev-minElev)/1000)*((cellArea*Area.per.elev.procent)/100)$

  etc.)

- reduces each file using only 100 elevation points (0.028% of all data points)
- joins all files together in a table with 101 columns delimited with '\t' ( the first column is the Arc_ID and column 2-101 the corresponding flood-plain storage values per grid cell)

### 1.2.2 ACE2

**ACE2** (ACE - Altimeter Corrected Elevations)

Data format:
- ace2 file, convertible in netcdf grd (each download file has a coverage of 15*15 degrees)
- datum: WGS84

Spatial resolution:
- 3", 9",30", 5' (approximately 90m, 280m, 1km, 10km at the equator)
- global

Provided by:
- R. Smith, EAPRS Laboratory, De Montfort University, Leicester UK (supported by European Space Agency (ESA))

Download:
- http://tethys.eaprs.cse.dmu.ac.uk/ACE2/
- Free registration necessary; Download files from ftp

Citation:

Smith, R.: ACE2 3 arc-second dataset, 1.31th edn., EAPRS Laboratory, De Montfort University, Leicester UK, available from http://tethys.eaprs.cse.dmu.ac.uk/ACE2, 22 pp., 2009.

**ACE2 Data preparation as model input for WaterGAP**

General information:
- ACE2 is distributed as 15-degree by 15-degree tiles, with the name referring to the South Western edge of the South Western most pixel. Thus each down-loadable ACE2 tile covers 30 x 30 0.5° cells.
- In the height files the value used for masking (i.e. land/sea mask) is set to -500 and the value for voids in the SRTM which are unable to be corrected are set to -32768 (information on the web page).

World:

- North of 60° there are 155 grid cells with no data (grid cells with only the value -500 (value for land masking)). Except 10 grid cells, all of these are coastal cells. 101 grid cells belong to Greenland, including the 10 non-coastal grid cells.

**Data preparation**

- Download ACE2 altimeter corrected elevations with the spatial resolution of 3 seconds from the ftp-Server (http://tethys.eaprs.cse.dmu.ac.uk/ACE2/).
- Extract files from zip
- Rename the ACE2 file to .raw so 00N000E_3S_ACE2.raw
- Write a header file (ENVI-format) for each of the ACE2 tiles, including the geographic information (upper left corner).
  - There is a C-Script ("GenACEHDR.c ") which generates the header files automatically.
- Convert Raster to ESRI GRID format using ArcCatalog → right Click on .raw-Raster → Export → Raster To Different Format → define the output raster dataset with no extension (default option for ESRI GRID) for example D:\Linda\ACE2_v1.31\60N015E
- By downscaling the Raster data on a spatial resolution of 0.5°, converting 0.5° raster files to text files reduce the data amount to 100 elevation values per 0.5° grid cell and calculate the floodplain depth and the storage capacity of the floodplain area for each elevation point. See the section on data preparation for HydroSHEDS data (Appendix 1.2.1)

## 1.3   Sensitivity analysis

The sensitivity of WaterGAP 2.2b_fpl was analyzed by modeling river discharge and surface water extent (SWE) within eight large river basins (Figure A.4), applying different parameters for: flood initiation threshold (Figure A.5), river - floodplain interaction (Figure A.6), vegetation correction (Figure A.7), calculation of river flow velocity (Figure A.8) and backwater (Figure A.9).
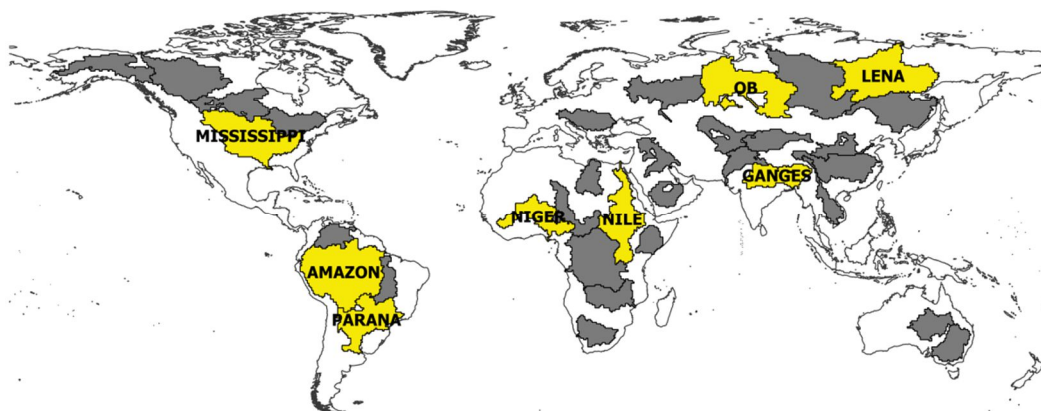
**Figure A.4** Selected river basins for sensitivity analysis.

The dashed and the dotted black lines in Figure A.5 to A.9 represent modeled river discharge and surface water extent from WaterGAP 2.2b without floodplain algorithm and observed data respectively. Both lines serve more as an orientation rather than for comparison, as the focus of this analysis is to show how sensitive are the model outputs of WaterGAP 2.2b_fpl with changing parameters. The data source of river discharge observations is the Global Runoff Data Centre (GRDC 2013), which uses monthly time series from 1971 to 2000 (with occasional missing data depending on gauging station). Observed data on surface water extent is the satellite derived data set on naturally inundated areas (NIA, Adam et al. 2010), which includes monthly values from 1993 to 2004. Model output is only considered in the month and locations of observations (grid cells of gauging station locations for river discharge and whole river basins for surface water extent).

WaterGAP reacts very sensitive to the threshold for flood initiation, the bankfull flow. The lower the bankfull flow, the lower the maxima and thus the amplitude of river discharge for surface water extent, and vice versa (Figure A.5). Which of the bankfull flow achieves the highest model performance vary strongly among the analyzed river basins and among the different model outputs. The average best model fit (considering the 8 river basins and the two model outputs: river discharge and surface water extent) was achieved by applying 70% of the bankfull flow used in WaterGAP 2.2b.

**Bankfull Flow Reduction**
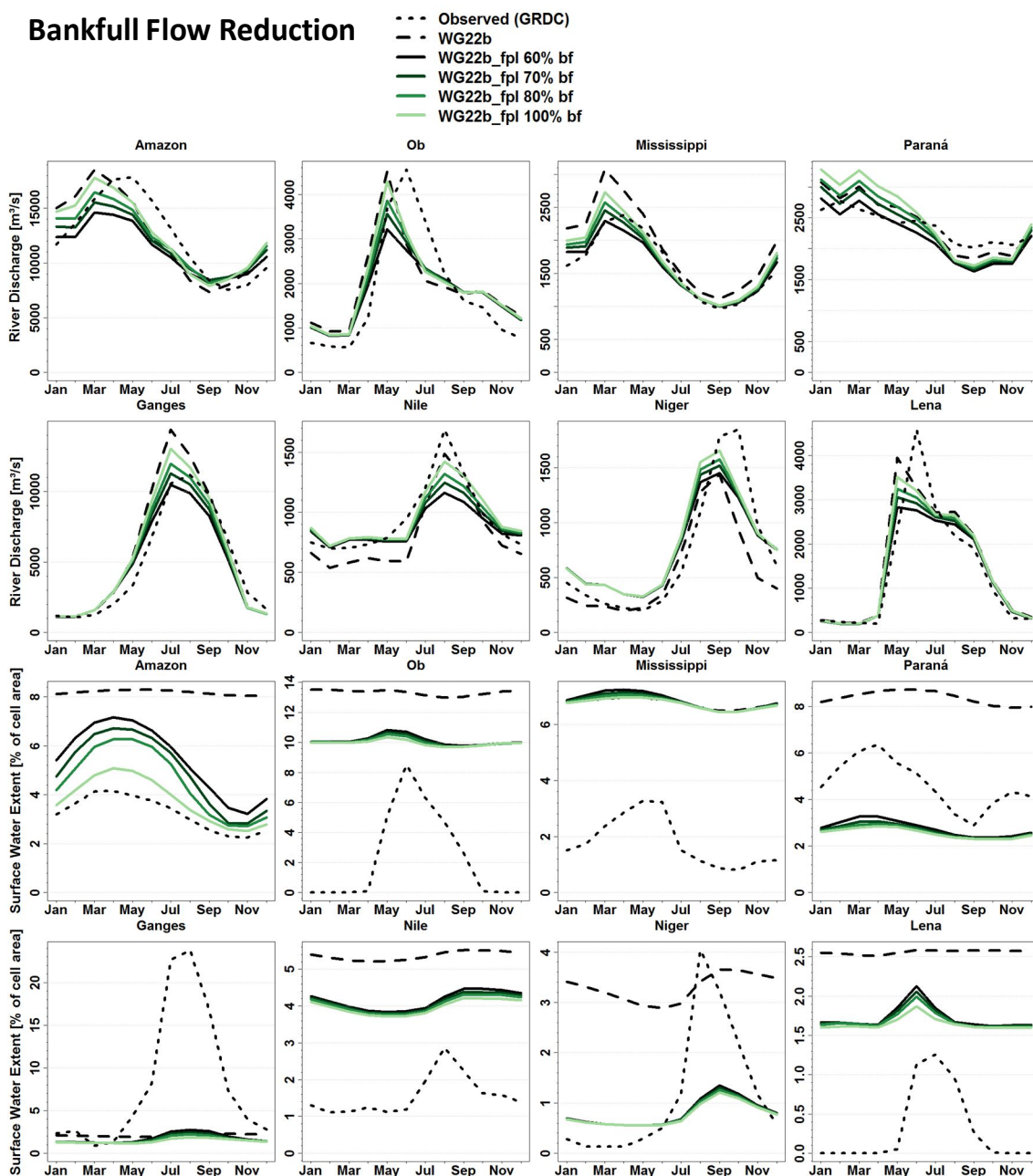


**Figure A.5** Model sensitivity regarding bankfull flow. Average monthly river discharge and SWE for 8 large river basins modelled with WaterGAP 2.2b_fpl kinematic applying the bankfull flow as used in WaterGAP 2.2b (solid light green lines) and reduced bankfull flows using 80%, 70% and 60% of the standard input bankfull flow (solid green to black lines). The dashed and the dotted black lines represent modeled river discharge and SWE extent from WaterGAP 2.2b without floodplain algorithm and observed data respectively; they serve for orientation.

After the bankfull flow, the river-floodplain interaction is the most important parameter for modeling floodplain inundation in WaterGAP. In the majority of the analyzed river basins, best model results were achieved when at least 60% of the water above river channel capacity flows into the floodplain. Up to a value of $p_{min} = 60$, the larger $p_{min}$ the better the WaterGAP results for both, river discharge and surface water extent. With

$p_{min}$-values larger than 60%, modeled river discharge starts getting worse compared to observations, due to a decrease in peak flows (Figure A.6).
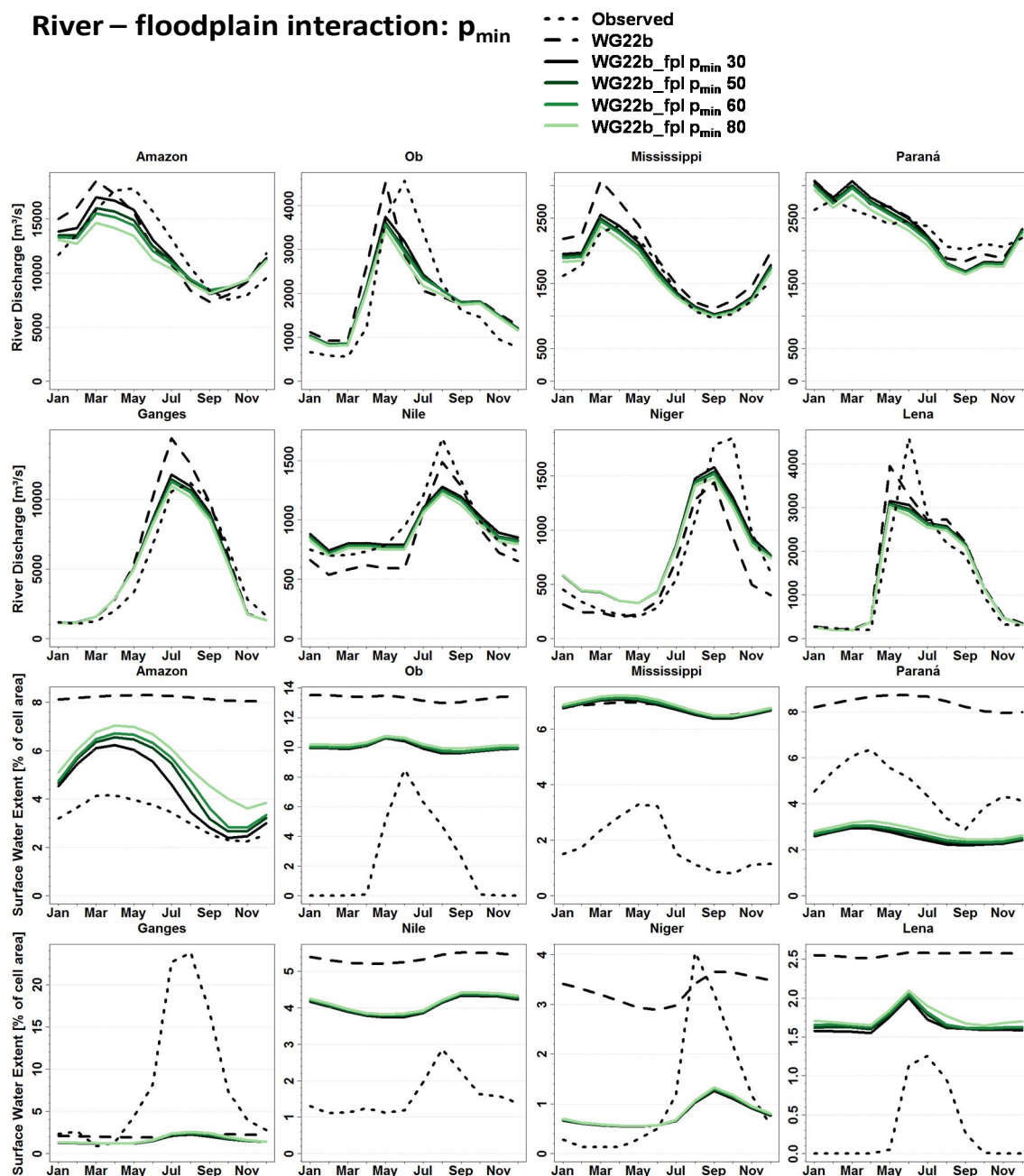


**Figure A.6** Model sensitivity regarding $p_{min}$ (predefined minimum percentage of water flowing from river to floodplain or vice versa, in case bankfull flow is exceeded). Average monthly river discharge and SWE for 8 large river basins modeled with WaterGAP 2.2b_fpl with kinematic wave routing applying a $p_{min}$ of 30, 50, 60 and 80 (black solid lines to light green lines). The dashed and the dotted black lines represent modeled river discharge and SWE from WaterGAP 2.2b without floodplain algorithm and observed data respectively; they serve for orientation.

Vegetation correction is only significant for the WaterGAP model results on surface water extent, not for river discharge (Figure A.7). The elevations of the digital elevation model are corrected (reduced) by the assumed value of vegetation height. Thus, the

floodplain elevation profile gets lower. The higher the value for assumed vegetation height, the flatter the floodplain profile and the faster the water spreads out in the case of flooding and surface water extent rises. The volume of water – and thus discharge – does not change much. It is influenced by precipitation, evapotranspiration and groundwater infiltration, depending on the surface water extent per grid cell.

**Vegetation Correction**

| | Amazon | Ganges | Lena | Mississippi | Niger | Nile | Ob | Paraná |
|---|---|---|---|---|---|---|---|---|
| ···· Observed | | | | | | | | |
| –·– WG22b | | | | | | | | |
| —— WG22b_fpl | 26 | 6 | 15 | 9 | 4 | 5 | 10 | 8 |
| —— WG22b_fpl | 20 | 1 | 11 | 4 | 1 | 2 | 4 | 2 |
| —— WG22b_fpl | 17 | 0 | 0 | 0 | 0 | 0 | 0 | 0 |
| —— WG22b_fpl | 14 | 0 | 8 | 0 | 0 | 0 | 0 | 0 |
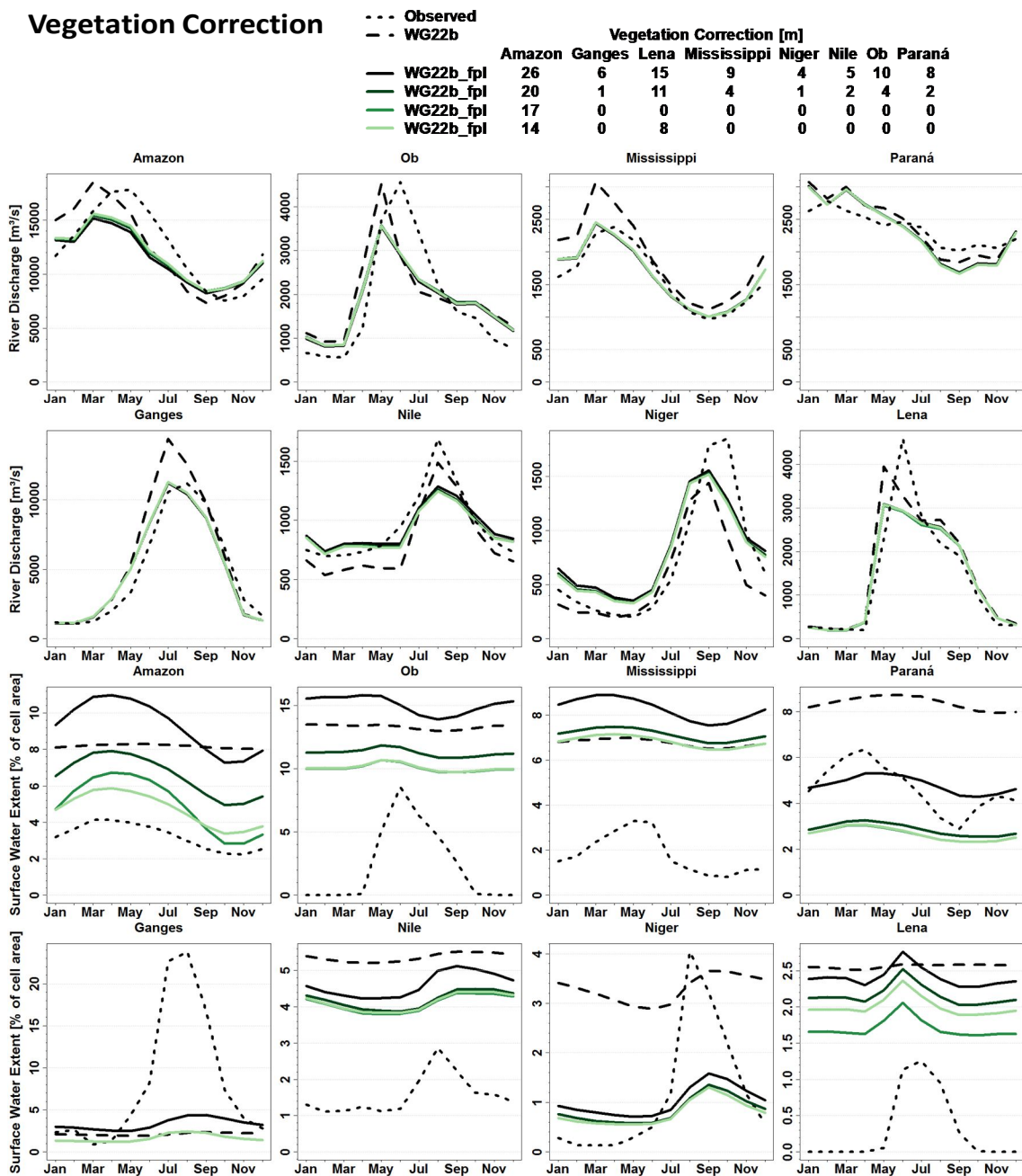


**Figure A.7** Model sensitivity regarding vegetation correction. Average monthly river discharge and SWE for 8 large river basins modeled with WaterGAP 2.2b_fpl with kinematic wave routing applying the different altitude of vegetation correction (see Legend). The dashed and the dotted black lines represent modeled river discharge and SWE from WaterGAP 2.2b without floodplain algorithm and observed data respectively; they serve for orientation.

It is noticeable that by computing river flow velocity as a function of river water storage of previous time step the basin average maximum river discharge occurs earlier than in the other model runs and falls faster after peak flow (Figure A.8). For most of the analyzed river basins, the effect of changing river flow velocity on river discharge and surface water extent is not as high. In Section 5.2 it was shown that the effect on river water storage is much larger. For example in the Amazon River basin, average river water storage is much lower when river flow velocity is calculated as a function of river water storage at previous time step, caused by higher river flow velocities.
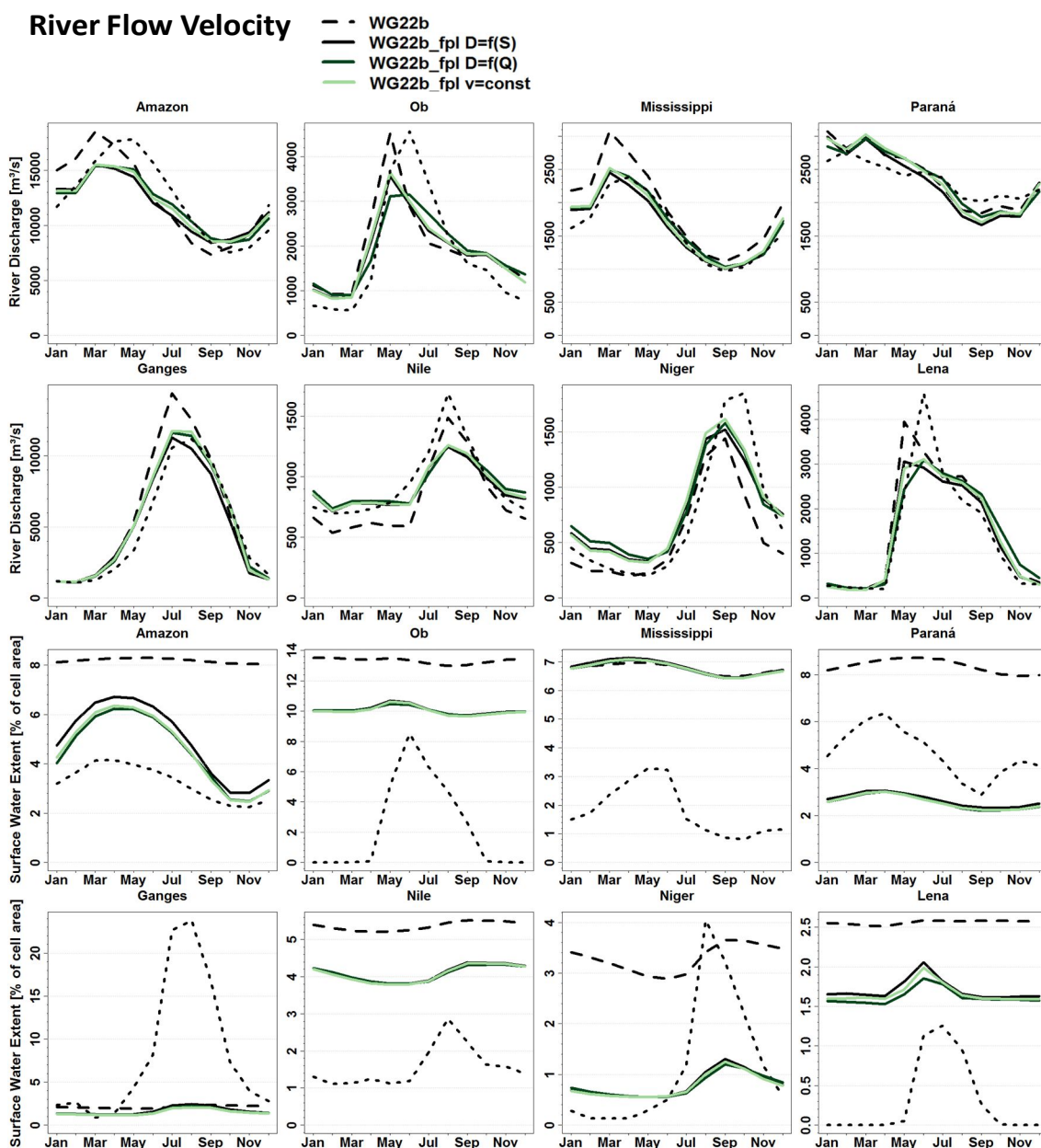


**Figure A.8** Model sensitivity regarding river flow velocity. Average monthly river discharge and SWE for 8 large river basins modelled with WaterGAP 2.2b_fpl kinematic, applying different methods of calculating river flow velocity: 1) as a function of river water storage at previous time step (solid black lines), 2) as a function of river discharge (solid forest green lines) and 3) as a constant value of 1 m/s (solid light green lines). The dashed and the dotted black lines represent modeled river discharge and SWE from WaterGAP 2.2b without floodplain algorithm and observed data respectively; they serve for orientation.

WaterGAP model results are very sensitive to the amount of water flowing upstream in case of a negative water slope (Figure A.9). The more water is allowed to route upstream, the less gets the river discharge in the downstream parts of the river basins (more water is stored on the floodplains). In basin averages, model performance regarding river discharge decreases with higher backwater flows, whereas model performance regarding water surface extent increases. However, the latter is not very significant, while the first is.
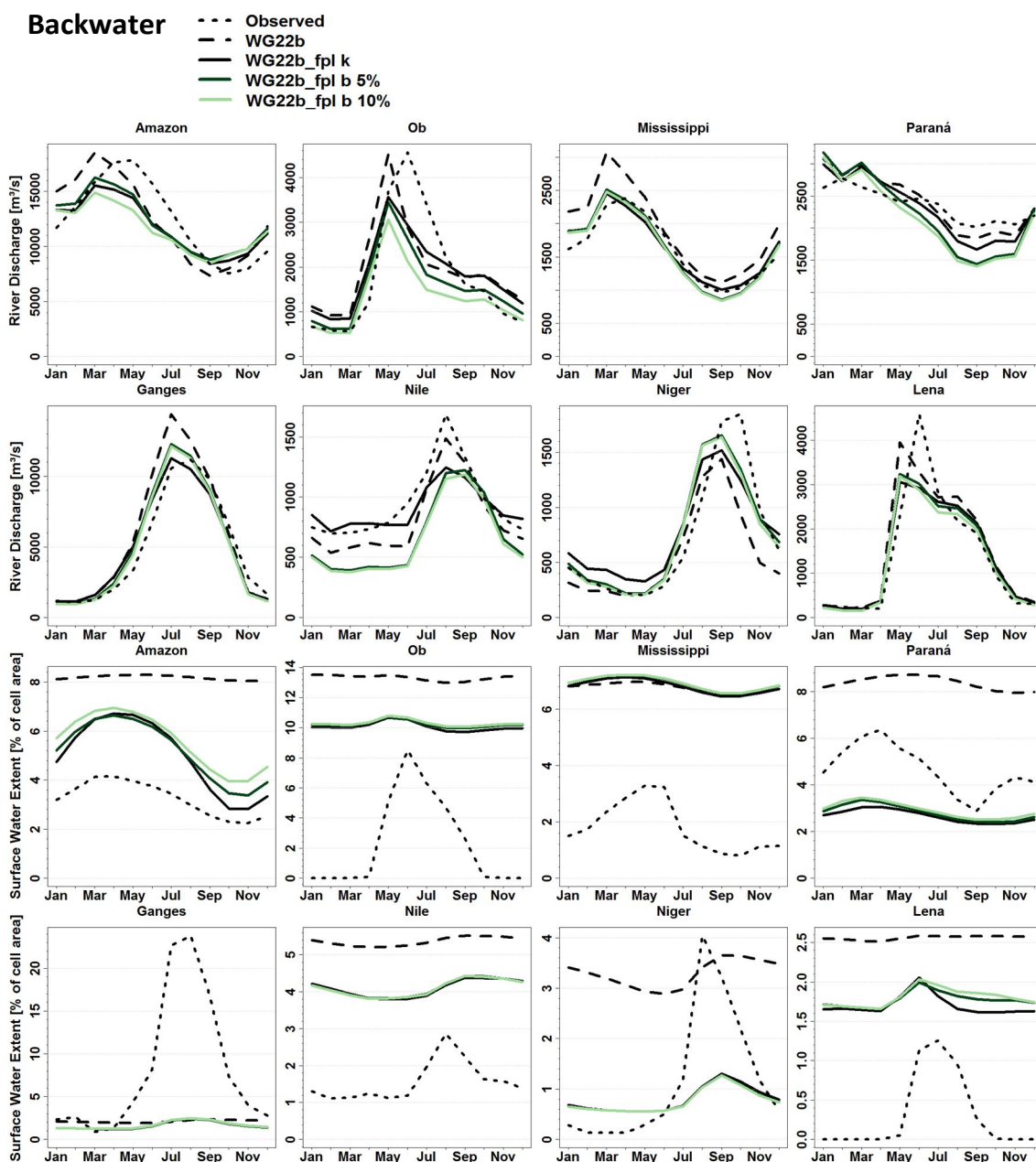


**Figure A.9** Model sensitivity regarding backwater flow. Average monthly river discharge and SWE for 8 large river basins modeled with WaterGAP 2.2b_fpl with no backwater effects (solid black lines) and with 5% (solid forest green lines) and 10% (solid light green lines) backwater routing in case of negative water slopes. The dashed and the dotted black lines represent modeled river discharge and SWE from WaterGAP 2.2b without floodplain algorithm and observed data respectively; they serve for orientation.

# 2 Appendix to Chapter 5

## 2.1 Flow Velocity
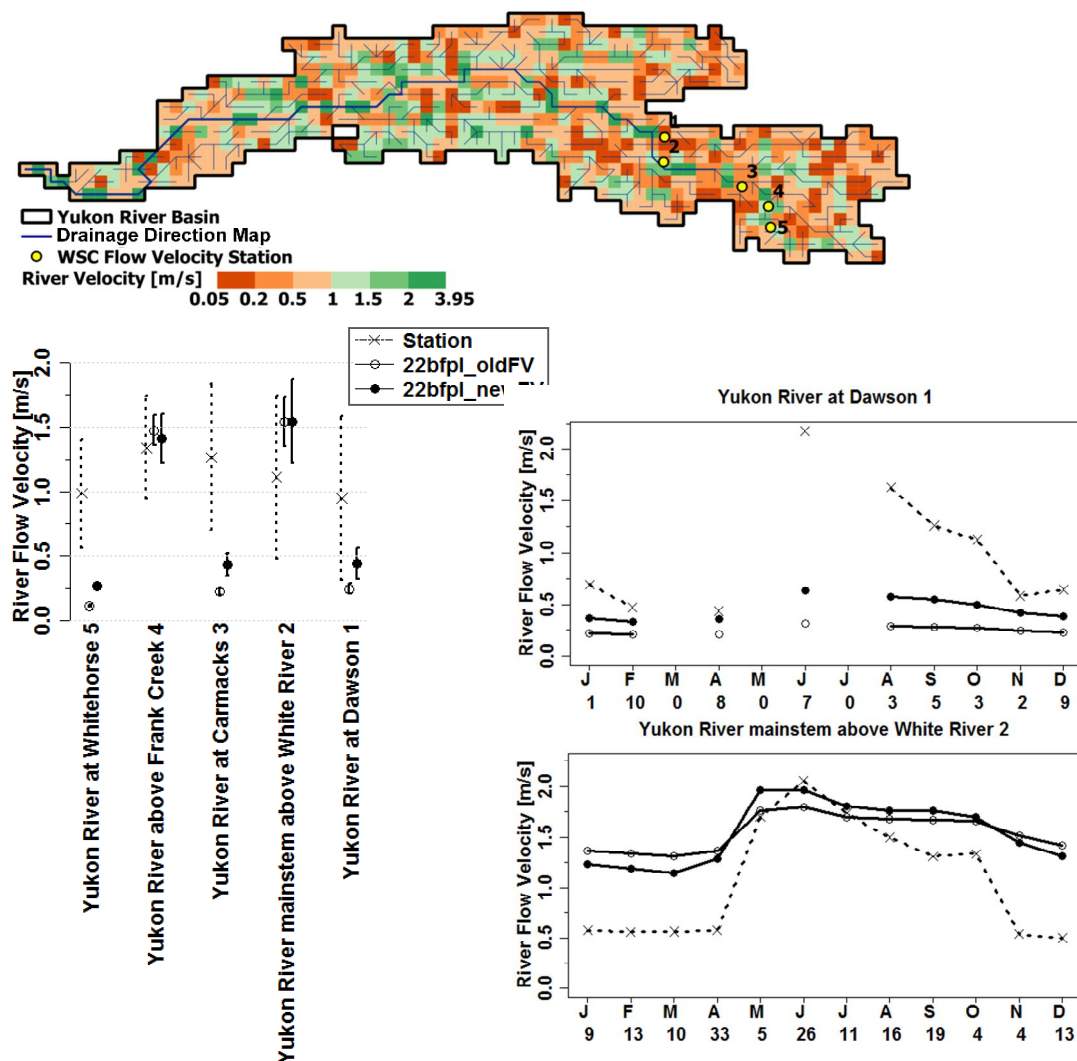


| Station | Catchment area [10³ km³] | ADCP start | ADCP end | No. of obser- vations | Mean flow velocity[m/s] obs/oldFV/newFV | R² oldFV/newFV | NSC oldFV/newFV | VE oldFV/newFV |
|---------|--------------------------|------------|----------|-----------------------|------------------------------------------|----------------|------------------|-----------------|
| 5 | 18.70 | 1944 | 1975 | 11 | 0.99/0.11/0.27 | 0.64/0.66 | -4.75/-3.14 | -0.37/-0.25 |
| 4 | 29.40 | 1952 | 1994 | 99 | 1.34/1.48/1.41 | 0.39/0.38 | 0.03/0.10 | 0.05/0.18 |
| 3 | 89.83 | 1951 | 1994 | 124 | 1.27/0.23/0.44 | 0.90/0.88 | -3.29/-1.91 | -0.26/-0.08 |
| 2 | 147.25 | 1956 | 2010 | 163 | 1.11/1.54/1.55 | 0.89/0.89 | -0.02/0.17 | 0.19/0.36 |
| 1 | 260.28 | 1956 | 1966 | 48 | 0.95/0.25/0.44 | 0.94/0.94 | -1.15/-0.34 | -0.20/0.02 |
| Mean | 109.09 | | | 89 | 1.13/0.72/0.82 | 0.75/0.75 | -1.84/-0.12 | -0.12/0.05 |

**Figure A.10** Average simulated and measured river flow velocity at 5 gauges in the Yukon River basin. Observed river flow velocity for the 5 gauges was used from 1971 to 2010 with 4 to 40 years of ADCP measures depending on gauging station (Data source: Water Survey of Canada). Modeled river flow velocity was computed by WaterGAP 2.2b with floodplain algorithm (22bfpl (kinematic)), applying variable flow velocity with river depths based on 1) river discharge (old flow velocity (oldFV)) and 2) river storage of previous time step (new flow velocity (newFV). **Top:** Mean river flow velocity [m/s] 1971-2000 computed by WaterGAP

2.2b_fpl (22bfpl_newFV) and location of gauging stations. **Centre left:** Comparison of average simulated and measured river flow velocity at 5 gauges in the Yukon River basin. The error bars indicate the standard deviations. **Centre right:** Mean monthly river flow velocity at 2 stations. The numbers on the x-axis are the number of observations per month. **Bottom:** Characteristics of flow velocity gauging stations and quality criteria.

## 2.2 Water Level and River Discharge
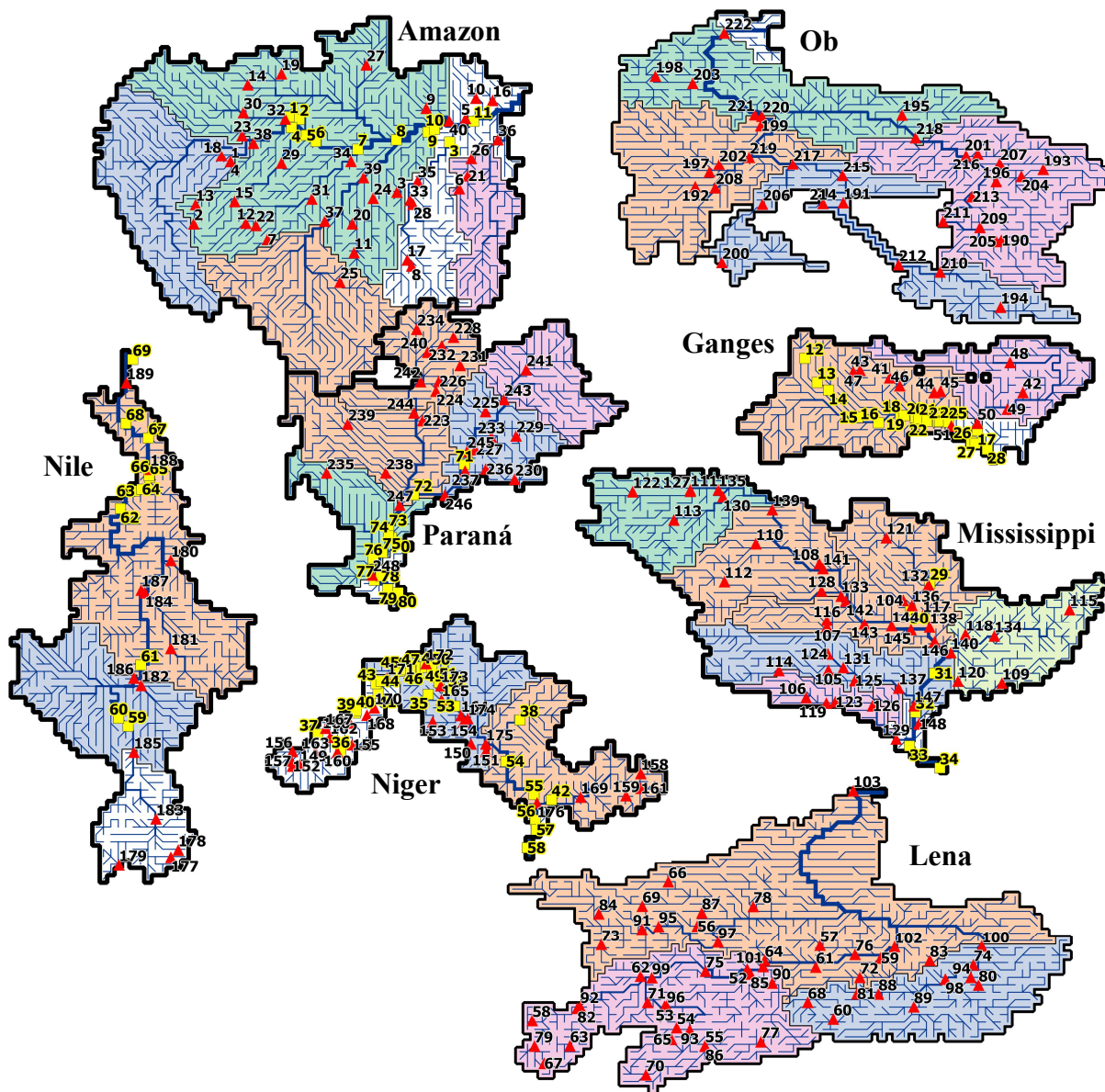


**Figure A.11** Location of river discharge gauging stations (red triangles) and altimetry gauging stations (yellow squares) used for model testing. River basins zoned into subbasins larger than 400000 km² (pastel colors). Gauging station information listed in Table A.1 and A.2 (the numbers are equal to column "No.").

**Table A.1** River discharge gauging stations used for model testing (GRDC 2013).

| No. | Basin | River | Station | Latitude | Longitude | Catchment area [10³ km³] | Time series | No. of observations 1971-2000 |
|---|---|---|---|---|---|---|---|---|
| 1 | Amazon | Rio Itacuai | Ladario | -4.73 | -70.30 | 9.19 | 1979-1994 | 192 |
| 2 | Amazon | Rio Jurua | Taumaturgo | -8.93 | -72.79 | 15.17 | 1981-2010 | 230 |

| No. | Basin | River | Station | Lati tude | Longi tude | Catch-ment area [10³ km³] | Time se-ries | No. of ob-servations 1971-2000 |
|---|---|---|---|---|---|---|---|---|
| 3 | Amazon | Rio Sucunduri | Santarem-Sucunduri | -6.80 | -59.04 | 15.24 | 1973-2010 | 313 |
| 4 | Amazon | Rio Itui | Seringal Do Itui | -4.73 | -70.30 | 18.37 | 1980-1992 | 148 |
| 5 | Amazon | Rio Maicuru | Arapari | -1.78 | -54.40 | 18.46 | 1972-2010 | 339 |
| 6 | Amazon | Rio Curua | Boca Do Inferno | -6.57 | -54.82 | 21.33 | 1973-2010 | 323 |
| 7 | Amazon | Rio Acre | Rio Branco | -9.98 | -67.80 | 24.22 | 1967-2010 | 343 |
| 8 | Amazon | Rio Do Sangue | Fazenda Tomba-dor | -11.76 | -58.04 | 27.01 | 1984-2007 | 179 |
| 9 | Amazon | Rio Mapuera | Estirao Da An-gelica | -1.10 | -57.06 | 27.69 | 1970-1999 | 311 |
| 10 | Amazon | Rio Paru De Este | Fazenda Paquira | -0.42 | -53.70 | 30.77 | 1973-1989 | 197 |
| 11 | Amazon | Rio Jiparana | Jiparana (Ron-donia) | -10.87 | -61.94 | 33.14 | 1977-2006 | 265 |
| 12 | Amazon | Rio Purus | Manoel Urbano | -8.88 | -69.27 | 33.34 | 1981-2009 | 195 |
| 13 | Amazon | Rio Jurua | Cruzeiro Do Sul | -7.63 | -72.66 | 39.54 | 1967-2010 | 354 |
| 14 | Amazon | Rio Uaupes | Uaracu | 0.48 | -69.13 | 40.00 | 1977-2010 | 276 |
| 15 | Amazon | Rio Tarauaca | Envira | -7.43 | -70.02 | 45.64 | 1978-2010 | 262 |
| 16 | Amazon | Rio Jari | Sao Francisco | -0.57 | -52.57 | 52.30 | 1968-2010 | 354 |
| 17 | Amazon | Rio Juruena | Fontanilhas | -11.36 | -58.34 | 56.97 | 1978-2007 | 276 |
| 18 | Amazon | Rio Javari | Estirao Do Re-pouso | -4.34 | -70.91 | 58.20 | 1980-2010 | 241 |
| 19 | Amazon | Rio Negro | Cucui | 1.22 | -66.85 | 61.50 | 1980-2010 | 245 |
| 20 | Amazon | Rio Jiparana | Tabajara | -8.93 | -62.06 | 63.43 | 1977-2006 | 265 |
| 21 | Amazon | Rio Iriri | Laranjeiras | -5.70 | -54.25 | 63.99 | 1976-2007 | 151 |
| 22 | Amazon | Rio Purus | Seringal Da Caridade | -9.04 | -68.58 | 69.75 | 1967-2010 | 346 |
| 23 | Amazon | Rio Ica | Ipiranga Velho | -2.94 | -69.52 | 107.65 | 1973-1993 | 236 |
| 24 | Amazon | Rio Aripuana | Prainha (Velha) | -7.21 | -60.65 | 115.24 | 1974-2010 | 319 |
| 25 | Amazon | Rio Guapore | Pedras Negras | -12.85 | -62.90 | 116.32 | 1980-2006 | 230 |
| 26 | Amazon | Rio Iriri | Pedra Do O | -4.53 | -54.01 | 122.08 | 1976-2009 | 214 |
| 27 | Amazon | Rio Branco | Caracarai | 1.82 | -61.12 | 122.88 | 1967-2010 | 341 |
| 28 | Amazon | Rio Sao Manoel | Tres Marias | -7.61 | -57.95 | 145.10 | 1975-2009 | 246 |
| 29 | Amazon | Rio Jurua | Gaviao | -4.84 | -66.85 | 167.68 | 1972-2010 | 330 |
| 30 | Amazon | Rio Japura | Vila Bittencourt | -1.39 | -69.43 | 203.07 | 1980-2010 | 250 |
| 31 | Amazon | Rio Purus | Labrea | -7.26 | -64.80 | 224.92 | 1967-2010 | 354 |
| 32 | Amazon | Rio Japura | Acanaui | -1.82 | -66.60 | 246.14 | 1973-1997 | 292 |
| 33 | Amazon | Rio Tapajos | Barra Do Sao Manuel-Jusante | -7.34 | -58.16 | 337.86 | 1975-2008 | 260 |
| 34 | Amazon | Rio Purus | Aruma-Jusante | -4.73 | -62.15 | 359.44 | 1975-2010 | 260 |
| 35 | Amazon | Rio Tapajos | Fortaleza | -6.05 | -57.64 | 365.34 | 1983-2008 | 180 |
| 36 | Amazon | Xingu | Altamira | -3.21 | -52.21 | 440.24 | 1971-2008 | 358 |
| 37 | Amazon | Rio Madeira | Porto Velho | -8.75 | -63.92 | 977.08 | 1967-2007 | 359 |
| 38 | Amazon | Amazonas (Rio Solimoes) | Sao Paulo De Olivenca | -3.45 | -68.75 | 994.61 | 1973-2010 | 326 |
| 39 | Amazon | Rio Madeira | Manicore | -5.82 | -61.30 | 1156.27 | 1967-2010 | 328 |
| 40 | Amazon | Amazonas | Obidos | -1.95 | -55.51 | 4658.80 | 1927-1998 | 329 |
| 41 | Ganges | Kali Gandaki | Kotagaon | 28.25 | 83.75 | 10.84 | 1901-2005 | 169 |

| No. | Basin | River | Station | Latitude | Longitude | Catchment area [10³ km³] | Time series | No. of observations 1971-2000 |
|-----|-------|-------|---------|----------|-----------|--------------------------|-------------|-------------------------------|
| 42 | Ganges | Jia Bhorelli | Shringe N.T. Road Crossing | 27.25 | 92.75 | 10.95 | 1901-2005 | 95 |
| 43 | Ganges | Bheri River | Jamu | 28.75 | 81.75 | 13.52 | 1901-2005 | 119 |
| 44 | Ganges | Sunkosi | Kampughat | 27.25 | 86.75 | 19.12 | 1901-2005 | 180 |
| 45 | Ganges | Arun River | Turkeghat | 27.33 | 87.19 | 27.15 | 1976-1986 | 132 |
| 46 | Ganges | Narayani River | Devghat | 27.71 | 84.43 | 32.58 | 1963-1993 | 204 |
| 47 | Ganges | Karnali River | Chisapani | 28.64 | 81.29 | 43.07 | 1962-1993 | 276 |
| 48 | Ganges | Brahmaputra | Yangcun | 29.28 | 91.88 | 158.27 | 1956-1982 | 144 |
| 49 | Ganges | Brahmaputra | Pandu | 26.13 | 91.70 | 411.22 | 1956-1979 | 85 |
| 50 | Ganges | Brahmaputra | Bahadurabad | 25.18 | 89.67 | 515.73 | 1969-1992 | 130 |
| 51 | Ganges | Ganga | Farakka | 25.00 | 87.92 | 918.37 | 1949-1973 | 36 |
| 52 | Lena | Biryuk | Biryuk | 60.30 | 119.62 | 9.07 | 1950-1994 | 288 |
| 53 | Lena | Mamakan | Mamakan | 57.80 | 114.03 | 10.15 | 1981-1990 | 120 |
| 54 | Lena | Muya | Taksimo | 56.37 | 114.85 | 10.42 | 1965-1990 | 240 |
| 55 | Lena | Kalakan | Kalakan | 55.15 | 116.77 | 10.60 | 1953-1990 | 177 |
| 56 | Lena | Ygyatta | Ygyatta | 63.24 | 116.24 | 10.96 | 1969-1994 | 182 |
| 57 | Lena | Sinyaya | Tongulakh | 61.92 | 124.55 | 11.61 | 1972-1994 | 223 |
| 58 | Lena | Kuta | Novo-Ilinka | 56.85 | 105.07 | 11.81 | 1941-1990 | 223 |
| 59 | Lena | Botoma | Brolog | 61.05 | 128.65 | 12.22 | 1936-1994 | 276 |
| 60 | Lena | Timpton | Ust-Baralas | 56.95 | 125.45 | 13.69 | 1955-1994 | 276 |
| 61 | Lena | Tuolba | Alekseievka | 60.44 | 124.26 | 14.09 | 1936-1999 | 309 |
| 62 | Lena | Peleduy | Sol'Zavod | 59.83 | 112.40 | 14.19 | 1936-1988 | 210 |
| 63 | Lena | Kirenga | Karam | 55.15 | 107.62 | 14.27 | 1966-1990 | 240 |
| 64 | Lena | Namana | Meiemkide (Myankinda) | 60.90 | 120.80 | 14.74 | 1944-1999 | 348 |
| 65 | Lena | Tsipa | Z. Uju | 55.58 | 114.50 | 16.00 | 1961-1990 | 240 |
| 66 | Lena | Markha | Shalagontsy | 66.25 | 114.28 | 16.30 | 1974-1999 | 189 |
| 67 | Lena | Lena | Kachug | 53.97 | 105.88 | 16.50 | 1936-1990 | 240 |
| 68 | Lena | Aldan | Suon-Tiit | 58.07 | 123.72 | 16.81 | 1951-1999 | 348 |
| 69 | Lena | Morkoka | Habardino | 64.60 | 112.52 | 18.04 | 1973-1994 | 189 |
| 70 | Lena | Vitim | Romanovka | 53.20 | 112.77 | 18.31 | 1944-1990 | 196 |
| 71 | Lena | Mama | Lugovsky | 58.07 | 112.88 | 18.62 | 1970-1990 | 240 |
| 72 | Lena | Amga | Buyaga | 59.75 | 127.25 | 23.67 | 1901-2005 | 168 |
| 73 | Lena | Chona | Ust-Markhaya | 61.98 | 109.75 | 24.09 | 1965-1974 | 41 |
| 74 | Lena | Allakh-Yun | Allakh | 60.60 | 134.93 | 24.14 | 1945-1999 | 348 |
| 75 | Lena | Bolshoy Patom | Patoma | 60.17 | 116.80 | 25.22 | 1934-1999 | 348 |
| 76 | Lena | Sinyaya | Peschanoye | 61.30 | 126.92 | 32.14 | 1944-1986 | 178 |
| 77 | Lena | Olekma | Srednaya Olekma | 55.42 | 120.55 | 37.50 | 1957-1999 | 317 |
| 78 | Lena | Tyung | Ugulyatsy | 64.58 | 120.03 | 37.97 | 1959-1996 | 234 |
| 79 | Lena | Lena | Gruznovka | 55.13 | 105.23 | 39.93 | 1912-1990 | 240 |
| 80 | Lena | Yudoma | Kurun-Targyukhah | 59.23 | 135.28 | 43.02 | 1944-1998 | 336 |
| 81 | Lena | Timpton | Ust-Timpton | 58.65 | 127.05 | 43.72 | 1952-1999 | 348 |

| No. | Basin | River | Station | Latitude | Longitude | Catchment area [10³ km³] | Time series | No. of observations 1971-2000 |
|---|---|---|---|---|---|---|---|---|
| 82 | Lena | Kirenga | Shorokhovo | 57.67 | 108.12 | 47.08 | 1927-1990 | 240 |
| 83 | Lena | Amga | Amga | 60.90 | 131.98 | 56.09 | 1939-1999 | 348 |
| 84 | Lena | Vilyuy | Ust-Ambardakh | 64.08 | 109.58 | 59.90 | 1965-1999 | 336 |
| 85 | Lena | Chara | Tokko | 59.98 | 119.84 | 63.70 | 1934-1994 | 276 |
| 86 | Lena | Vitim | Kalakan | 55.12 | 116.77 | 64.48 | 1953-1990 | 195 |
| 87 | Lena | Markha | Cumpuruk | 64.14 | 116.55 | 77.20 | 1954-1999 | 327 |
| 88 | Lena | Aldan | Ugino | 58.63 | 128.50 | 102.74 | 1973-1994 | 252 |
| 89 | Lena | Uchur | Chulbu | 57.77 | 130.90 | 109.54 | 1954-1999 | 348 |
| 90 | Lena | Olekma | Kudu-Kel | 59.37 | 121.32 | 116.01 | 1936-1999 | 348 |
| 91 | Lena | Vilyuy | Chernyshevskyi | 63.03 | 112.50 | 135.94 | 1959-1994 | 264 |
| 92 | Lena | Lena | Zmeinovo | 57.78 | 108.32 | 139.65 | 1936-1990 | 240 |
| 93 | Lena | Vitim | Spitsyuno | 56.22 | 115.73 | 144.13 | 1976-1990 | 180 |
| 94 | Lena | Maya | Chabda | 59.75 | 134.75 | 167.74 | 1935-1999 | 348 |
| 95 | Lena | Vilyuy | Suldukar | 63.22 | 113.63 | 169.34 | 1967-1994 | 235 |
| 96 | Lena | Vitim | Bodaibo | 57.82 | 114.17 | 186.67 | 1912-1990 | 240 |
| 97 | Lena | Vilyuy | Suntar | 62.15 | 117.65 | 208.19 | 1926-1999 | 336 |
| 98 | Lena | Aldan | Ust-Mil | 59.63 | 133.03 | 268.46 | 1934-1999 | 348 |
| 99 | Lena | Lena | Krestovski | 59.73 | 113.17 | 444.58 | 1936-1999 | 348 |
| 100 | Lena | Aldan | Ohotsky Perevoz | 61.87 | 135.50 | 517.81 | 1926-1999 | 348 |
| 101 | Lena | Lena | Solyanka | 60.48 | 120.70 | 773.12 | 1933-1999 | 348 |
| 102 | Lena | Lena | Tabaga | 61.83 | 129.60 | 895.98 | 1936-1999 | 348 |
| 103 | Lena | Lena | Stolb | 72.37 | 126.80 | 2457.20 | 1951-1994 | 288 |
| 104 | Mississippi | Des Moines River | Keosauqua, Ia | 40.73 | -91.96 | 41.19 | 1903-2004 | 360 |
| 105 | Mississippi | Cimarron River | Perkins, Ok | 35.96 | -97.03 | 44.60 | 1939-1991 | 249 |
| 106 | Mississippi | Red River | Near Burkburnett, Tx | 34.11 | -98.53 | 50.82 | 1960-2006 | 360 |
| 107 | Mississippi | Smoky Hill River | Enterprise, Ks | 38.91 | -97.12 | 52.85 | 1934-2006 | 360 |
| 108 | Mississippi | James River (Trib. Missouri) | Near Scotland, Sd | 43.19 | -97.64 | 54.31 | 1928-2006 | 360 |
| 109 | Mississippi | Tennessee River | Chattanooga, Tn | 35.09 | -85.28 | 55.18 | 1874-2004 | 360 |
| 110 | Mississippi | Cheyenne River | Near Plainview, Sd | 44.53 | -101.93 | 55.88 | 1950-2006 | 205 |
| 111 | Mississippi | Milk River | Nashua, Mt | 48.13 | -106.36 | 57.23 | 1939-2006 | 360 |
| 112 | Mississippi | Platte River (North) | Wyoming-Nebraska State Line | 41.99 | -104.05 | 57.53 | 1929-2006 | 360 |
| 113 | Mississippi | Bighorn River | Above Tullock Creek Near Bighorn, Mt | 46.12 | -107.47 | 57.89 | 1945-2006 | 360 |
| 114 | Mississippi | Canadian River | Near Canadian, Tx | 35.94 | -100.37 | 62.63 | 1938-2006 | 360 |
| 115 | Mississippi | Ohio River | Martins Ferry | 40.11 | -80.71 | 63.42 | 1978-1995 | 206 |
| 116 | Mississippi | Republican River | Clay Center, Ks | 39.36 | -97.13 | 64.03 | 1917-2006 | 360 |
| 117 | Mississippi | Illinois River (Trib. Upper Mississippi | Valley City | 39.70 | -90.65 | 67.92 | 1938-2006 | 360 |
| 118 | Mississippi | Wabash | Mount Carmel, Ill. | 38.40 | -87.75 | 73.80 | 1927-2006 | 360 |

| No. | Basin | River | Station | Latitude | Longitude | Catchment area [10³ km³] | Time series | No. of observations 1971-2000 |
|---|---|---|---|---|---|---|---|---|
| 119 | Mississippi | Red River | Near Gainesville, Tx | 33.73 | -97.16 | 79.00 | 1936-2006 | 360 |
| 120 | Mississippi | Tennessee River | Savannah, Tn | 35.22 | -88.26 | 88.15 | 1930-2004 | 360 |
| 121 | Mississippi | Mississippi | St.Paul, Mn | 44.93 | -93.11 | 91.18 | 1892-2005 | 360 |
| 122 | Mississippi | Missouri River | Virgelle, Mt | 48.01 | -110.26 | 91.43 | 1935-2006 | 360 |
| 123 | Mississippi | Red River | Denison Dam Near Denison, Tx | 33.82 | -96.56 | 106.87 | 1924-2006 | 274 |
| 124 | Mississippi | Arkansas River | Arkansas City | 37.06 | -97.06 | 119.27 | 1902-2006 | 360 |
| 125 | Mississippi | Canadian | Whitefield, Okla. | 35.26 | -95.24 | 125.18 | 1938-2006 | 360 |
| 126 | Mississippi | Red River | Index, Ar | 33.55 | -94.04 | 129.89 | 1936-2004 | 360 |
| 127 | Mississippi | Missouri River | Below Fort Peck Dam, Mt | 48.04 | -106.36 | 148.36 | 1934-2006 | 357 |
| 128 | Mississippi | Platte River | Near Duncan, Nebr. | 41.37 | -97.49 | 153.76 | 1928-2004 | 360 |
| 129 | Mississippi | Red | Alexandria, La. | 31.31 | -92.44 | 176.52 | 1928-1983 | 153 |
| 130 | Mississippi | Yellowstone | Sidney, Mont. | 47.68 | -104.16 | 179.45 | 1910-2006 | 360 |
| 131 | Mississippi | Arkansas | Tulsa, Okla. | 36.14 | -96.01 | 193.54 | 1925-2006 | 360 |
| 132 | Mississippi | Mississippi | Clinton, Iowa | 41.78 | -90.25 | 219.22 | 1873-2004 | 360 |
| 133 | Mississippi | Platte | Louisville, Nebr. | 41.02 | -96.16 | 222.99 | 1953-2004 | 360 |
| 134 | Mississippi | Ohio | Louisville, Ky. | 38.28 | -85.80 | 236.97 | 1928-2006 | 360 |
| 135 | Mississippi | Missouri | Culbertson, Mont. | 48.13 | -104.47 | 238.52 | 1941-2006 | 360 |
| 136 | Mississippi | Mississippi | Keokuk, Ia | 40.39 | -91.37 | 308.61 | 1878-2005 | 360 |
| 137 | Mississippi | Arkansas | Little Rock, Ark. | 34.75 | -92.27 | 405.76 | 1927-1984 | 168 |
| 138 | Mississippi | Mississippi | Alton, Ill. | 38.89 | -90.18 | 448.67 | 1927-1987 | 201 |
| 139 | Mississippi | Missouri River | Bismarck, Nd | 46.81 | -100.82 | 483.19 | 1927-2006 | 360 |
| 140 | Mississippi | Ohio | Metropolis, Ill. | 37.15 | -88.74 | 527.36 | 1928-2004 | 360 |
| 141 | Mississippi | Missouri | Yankton, S.D. | 42.87 | -97.39 | 722.30 | 1930-1997 | 300 |
| 142 | Mississippi | Missouri | Nebraska City, Nebr. | 40.68 | -95.85 | 1058.41 | 1929-2004 | 360 |
| 143 | Mississippi | Missouri River | Kansas City, Mo | 39.11 | -94.59 | 1246.29 | 1928-2006 | 360 |
| 144 | Mississippi | Missouri River | Boonville, Mo | 38.98 | -92.75 | 1291.46 | 1925-2006 | 360 |
| 145 | Mississippi | Missouri | Hermann, Mo. | 38.71 | -91.44 | 1347.43 | 1897-2006 | 360 |
| 146 | Mississippi | Mississippi | Chester, Il | 37.90 | -89.84 | 1844.58 | 1942-2006 | 360 |
| 147 | Mississippi | Mississippi | Near Arkansas City, Ark | 33.56 | -91.24 | 2912.84 | 1928-1980 | 117 |
| 148 | Mississippi | Mississippi | Vicksburg, Miss. | 32.32 | -90.91 | 2951.38 | 1928-1999 | 345 |
| 149 | Niger | Milo | Kankan | 10.38 | -9.30 | 9.12 | 1938-2001 | 334 |
| 150 | Niger | Mekrou | Barou | 11.80 | 2.30 | 12.09 | 1901-2005 | 81 |
| 151 | Niger | Sota | Couberi | 11.30 | 3.30 | 12.10 | 1901-2005 | 198 |
| 152 | Niger | Niandan | Baro | 10.30 | -9.80 | 12.14 | 1901-2005 | 71 |
| 153 | Niger | Faga | Liptougou | 13.30 | -0.30 | 14.96 | 1901-2005 | 133 |
| 154 | Niger | Goroubi | Diongore Amont | 13.30 | 1.80 | 15.02 | 1901-2005 | 141 |
| 155 | Niger | Banifing | Kouoro 2 | 11.75 | -5.75 | 15.07 | 1901-2005 | 71 |
| 156 | Niger | Tinkisso | Ouaran | 11.30 | -9.80 | 18.12 | 1901-2005 | 89 |
| 157 | Niger | Niger | Kouroussa | 10.65 | -9.87 | 18.18 | 1923-2002 | 300 |

| No. | Basin | River | Station | Latitude | Longitude | Catchment area [10³ km³] | Time series | No. of observations 1971-2000 |
|-----|-------|-------|---------|----------|-----------|--------------------------|-------------|-------------------------------|
| 158 | Niger | Mayo-Kebi | Cossi | 9.80 | 13.80 | 24.26 | 1901-2005 | 108 |
| 159 | Niger | Faro | Safaie | 8.30 | 12.80 | 24.40 | 1901-2005 | 6 |
| 160 | Niger | Bagoe | Pankourou | 11.25 | -6.75 | 30.27 | 1901-2005 | 251 |
| 161 | Niger | Benoue | Riao | 8.80 | 13.80 | 30.44 | 1901-2005 | 113 |
| 162 | Niger | Baoule | Dioila | 12.25 | -7.25 | 33.24 | 1901-2005 | 240 |
| 163 | Niger | Sankarani | Selingue | 11.25 | -8.25 | 33.35 | 1901-2005 | 228 |
| 164 | Niger | Sirba | Garbe-Kourou | 13.73 | 1.62 | 38.97 | 1956-2002 | 297 |
| 165 | Niger | Gorouol | Alcongui | 14.80 | 0.30 | 44.68 | 1901-2005 | 214 |
| 166 | Niger | Bani | Douna | 13.22 | -5.90 | 99.64 | 1922-2001 | 346 |
| 167 | Niger | Niger | Koulikoro | 12.87 | -7.55 | 121.08 | 1907-2002 | 360 |
| 168 | Niger | Bani | Sofara | 13.75 | -4.75 | 132.63 | 1901-2005 | 182 |
| 169 | Niger | Benue | Ibi | 8.20 | 9.73 | 258.33 | 1970-2002 | 202 |
| 170 | Niger | Niger | Mopti | 14.25 | -4.25 | 286.63 | 1901-2005 | 113 |
| 171 | Niger | Niger | Dire | 16.27 | -3.38 | 343.07 | 1924-2001 | 337 |
| 172 | Niger | Niger | Tossaye | 17.25 | -0.75 | 401.98 | 1901-2005 | 142 |
| 173 | Niger | Niger | Ansongo | 15.75 | 0.25 | 563.37 | 1901-2005 | 238 |
| 174 | Niger | Niger | Niamey | 13.52 | 2.08 | 697.60 | 1929-2001 | 360 |
| 175 | Niger | Niger | Gaya | 11.80 | 3.30 | 974.38 | 1901-2005 | 147 |
| 176 | Niger | Niger | Lokoja | 7.80 | 6.77 | 1754.31 | 1970-2002 | 319 |
| 177 | Nile | Grumet | Road Crossing | -2.30 | 34.30 | 9.23 | 1901-2005 | 99 |
| 178 | Nile | Mara | Mara Mines | -1.80 | 34.80 | 15.38 | 1901-2005 | 93 |
| 179 | Nile | Kagera | Rusumo | -2.80 | 30.80 | 30.74 | 1901-2005 | 168 |
| 180 | Nile | Atbara | Kilo 3 | 17.80 | 34.30 | 152.16 | 1901-2005 | 84 |
| 181 | Nile | Blue Nile | Roseires Dam | 11.80 | 34.30 | 202.88 | 1901-2005 | 144 |
| 182 | Nile | Sobat | Hillet Doleib | 9.30 | 32.30 | 222.93 | 1901-2005 | 113 |
| 183 | Nile | Victoria Nile | Owen Reservoir | 0.30 | 33.30 | 258.38 | 1901-2005 | 120 |
| 184 | Nile | Blue Nile | Khartoum | 15.62 | 32.55 | 322.59 | 1900-1982 | 144 |
| 185 | Nile | Bahr El Jebel | Mongalla | 4.80 | 31.80 | 470.56 | 1901-2005 | 144 |
| 186 | Nile | White Nile | Malakal | 9.80 | 31.80 | 1350.02 | 1901-2005 | 144 |
| 187 | Nile | White Nile | Mogren | 15.80 | 32.30 | 1581.65 | 1901-2005 | 120 |
| 188 | Nile | Nile | Aswan Dam | 23.96 | 32.90 | 2677.63 | 1869-1984 | 168 |
| 189 | Nile | Nile | El Ekhsase | 29.80 | 31.30 | 2878.97 | 1901-2005 | 144 |
| 190 | Ob | Biya | Biysk | 52.52 | 85.27 | 40.53 | 1895-2000 | 324 |
| 191 | Ob | Om | Kalachinsk | 55.07 | 74.58 | 45.27 | 1936-1999 | 348 |
| 192 | Ob | Iset | Mekhonskoje | 56.15 | 64.57 | 50.62 | 1936-1989 | 228 |
| 193 | Ob | Chulym | Teguldet | 57.33 | 88.10 | 55.60 | 1936-2000 | 336 |
| 194 | Ob | Chernyi Irtish | Buran | 48.00 | 85.22 | 56.16 | 1938-1987 | 204 |
| 195 | Ob | Vakh | Yobkhinskoye | 61.05 | 78.55 | 57.52 | 1953-1996 | 191 |
| 196 | Ob | Tom | Tomsk | 56.50 | 84.92 | 57.88 | 1918-2000 | 324 |
| 197 | Ob | Tura | Tiumen | 57.15 | 65.53 | 59.30 | 1896-1998 | 324 |
| 198 | Ob | Northern Sosva | Sosva | 63.67 | 61.88 | 63.89 | 1937-1999 | 348 |
| 199 | Ob | Konda | Altay | 60.33 | 69.00 | 67.99 | 1962-1999 | 339 |
| 200 | Ob | Ishim | Derjavinskoje | 51.03 | 66.37 | 75.42 | 1963-1987 | 182 |

| No. | Basin | River | Station | Latitude | Longitude | Catchment area [10³ km³] | Time series | No. of observations 1971-2000 |
|---|---|---|---|---|---|---|---|---|
| 201 | Ob | Ket (Bolshaya Ket) | Rodyonovka | 58.42 | 83.67 | 76.14 | 1955-2000 | 300 |
| 202 | Ob | Tavda | Nizhnyaya Tavda | 57.68 | 66.18 | 87.43 | 1967-1995 | 261 |
| 203 | Ob | Severnaya Sosva | Igrim | 63.18 | 64.40 | 88.07 | 1958-1999 | 345 |
| 204 | Ob | Chulym | Zyryanskoje | 56.85 | 86.62 | 95.33 | 1936-2000 | 336 |
| 205 | Ob | Ob | Phominskoje | 52.45 | 84.92 | 101.62 | 1953-2000 | 336 |
| 206 | Ob | Ishim | Petropavlovsk | 54.97 | 69.12 | 114.61 | 1959-1987 | 176 |
| 207 | Ob | Chulym | Baturino | 57.78 | 85.15 | 130.67 | 1936-2000 | 336 |
| 208 | Ob | Tobol | Karkino | 56.08 | 65.92 | 165.45 | 1976-1998 | 268 |
| 209 | Ob | Ob | Barnaul | 53.40 | 83.82 | 170.56 | 1922-2000 | 336 |
| 210 | Ob | Irtish | Shulba | 50.38 | 81.13 | 180.44 | 1937-1979 | 99 |
| 211 | Ob | Ob | Kamen'Na Obi | 53.80 | 81.33 | 214.73 | 1936-2000 | 336 |
| 212 | Ob | Irtish | Semiyarskoje | 50.88 | 78.32 | 238.81 | 1960-1987 | 204 |
| 213 | Ob | Ob | Dubrovino | 55.48 | 83.28 | 259.53 | 1962-2000 | 203 |
| 214 | Ob | Irtish | Omsk | 55.02 | 73.21 | 326.73 | 1936-1999 | 348 |
| 215 | Ob | Irtish | Ekaterininskoje | 56.92 | 74.53 | 355.91 | 1980-1999 | 240 |
| 216 | Ob | Ob | Kolpashevo | 58.30 | 82.88 | 480.48 | 1936-2000 | 336 |
| 217 | Ob | Irtish | Ust-Ishim | 57.70 | 71.17 | 554.08 | 1936-1987 | 116 |
| 218 | Ob | Ob | Prokhorkino | 59.52 | 79.47 | 744.62 | 1960-1997 | 291 |
| 219 | Ob | Irtish | Tobolsk | 58.20 | 68.23 | 1011.59 | 1891-1999 | 346 |
| 220 | Ob | Irtish | Hanti-Mansisk | 60.97 | 69.07 | 1159.35 | 1974-1999 | 236 |
| 221 | Ob | Ob | Belogorje | 61.07 | 68.60 | 2205.52 | 1936-1999 | 305 |
| 222 | Ob | Ob | Salekhard | 66.57 | 66.53 | 2449.95 | 1930-2003 | 348 |
| 223 | Paraná | Rio Apa | Sao Carlos | -22.22 | -57.30 | 11.42 | 1971-2006 | 324 |
| 224 | Paraná | Rio Miranda | Miranda | -20.24 | -56.40 | 14.36 | 1965-2006 | 329 |
| 225 | Paraná | Rio Anhandui | Delfino Costa | -21.61 | -53.05 | 14.38 | 1976-2005 | 286 |
| 226 | Paraná | Rio Negro | Fazenda Rio Negro | -19.57 | -56.20 | 14.54 | 1968-1986 | 185 |
| 227 | Paraná | Rio Piquiri | Balsa Santa Maria | -24.17 | -53.74 | 19.64 | 1969-2003 | 360 |
| 228 | Paraná | Rio Sao Lourenco | Acima Do Corrego Grande | -16.61 | -55.21 | 20.70 | 1969-2006 | 318 |
| 229 | Paraná | Rio Tibaji | Jataizinho | -23.25 | -50.98 | 22.44 | 1931-1999 | 339 |
| 230 | Paraná | Iguacu | Uniao Da Vitoria | -26.23 | -51.08 | 24.94 | 1930-2007 | 360 |
| 231 | Paraná | Rio Taquari | Coxim | -18.51 | -54.76 | 26.30 | 1966-2007 | 311 |
| 232 | Paraná | Rio Piquiri | Sao Jeronimo | -17.20 | -56.01 | 26.45 | 1967-2007 | 303 |
| 233 | Paraná | Rio Ivai | Porto Paraiso Do Norte | -23.32 | -52.66 | 28.13 | 1953-2002 | 358 |
| 234 | Paraná | Paraguai | Caceres (Dnpvn) | -16.08 | -57.70 | 32.73 | 1965-2007 | 357 |
| 235 | Paraná | Salado | El Arenal | -25.80 | -63.80 | 41.74 | 1901-2005 | 116 |
| 236 | Paraná | Iguacu | Salto Ozorio | -25.54 | -53.03 | 47.17 | 1940-1996 | 312 |
| 237 | Paraná | Iguacu | Salto Cataratas | -25.68 | -54.43 | 69.39 | 1942-2005 | 360 |
| 238 | Paraná | Bermejo | El Colorado | -25.80 | -59.80 | 76.30 | 1901-2005 | 80 |
| 239 | Paraná | Pilcomayo | La Paz | -22.45 | -62.37 | 97.96 | 1960-1980 | 116 |
| 240 | Paraná | Rio Cuiaba | Porto Alegre | -17.62 | -56.97 | 103.42 | 1967-2005 | 331 |
| 241 | Paraná | Rio Paranaiba | Fazenda Santa Fe | -18.80 | -50.30 | 170.14 | 1901-2005 | 28 |

| No. | Basin | River | Station | Latitude | Longitude | Catchment area [10³ km³] | Time series | No. of observations 1971-2000 |
|---|---|---|---|---|---|---|---|---|
| 242 | Paraná | Paraguai | Porto Esperanca (Dnos) | -19.60 | -57.44 | 367.21 | 1963-1995 | 296 |
| 243 | Paraná | Parana | Uhe Jupia-Jusante-Jju | -20.80 | -51.80 | 478.62 | 1901-2005 | 184 |
| 244 | Paraná | Paraguai | Porto Murtinho (Fb/Dnos) | -21.70 | -57.89 | 485.49 | 1939-2007 | 360 |
| 245 | Paraná | Parana | Guaira | -24.30 | -54.30 | 816.94 | 1901-2005 | 108 |
| 246 | Paraná | Parana | Posadas | -27.30 | -55.80 | 947.39 | 1901-2005 | 151 |
| 247 | Paraná | Parana | Corrientes | -27.97 | -58.85 | 2060.04 | 1904-1983 | 152 |
| 248 | Paraná | Parana | Timbues | -32.67 | -60.71 | 2486.63 | 1905-1994 | 283 |

**Table A.2** Altimetry gauging stations used for model testing (Hydroweb (Crétaux et al. 2011); Satellites: Topex/Poseidon, Jason-1).

| Basin | River | Station | Latitude | Longitude | Catchment area [10³ km³] | Time series | Water-GAP cell ID | No. of observations 1993-2010 per 0.5°cell | No. |
|---|---|---|---|---|---|---|---|---|---|
| Amazon | Amazon | 493_01 | -1.67 | -66.32 | 249.21 | 2002-2010 | 54274 | 75 | 1 |
| Amazon | Amazon | 908_01 | -1.85 | -65.64 | 255.36 | 2002-2008 | 54275 | 136 | 2 |
| Amazon | Amazon | 951_01 | -1.90 | -65.56 | 255.36 | 2002-2010 | 54275 | | |
| Amazon | Amazon | 407_02 | -3.37 | -55.48 | 490.83 | 2002-2010 | 54908 | 74 | 3 |
| Amazon | Amazon | 493_02 | -2.40 | -66.17 | 1234.22 | 2002-2010 | 54479 | 77 | 4 |
| Amazon | Amazon | 493_03 | -2.51 | -66.14 | 1234.22 | 2002-2010 | 54479 | | |
| Amazon | Amazon | 364_02 | -2.91 | -65.16 | 1697.20 | 2002-2010 | 54677 | 144 | 5 |
| Amazon | Amazon | 951_02 | -2.50 | -65.42 | 1697.20 | 2002-2010 | 54677 | | |
| Amazon | Amazon | 951_03 | -2.71 | -65.38 | 1697.20 | 2002-2010 | 54677 | | |
| Amazon | Amazon | 822_02 | -3.33 | -64.53 | 1737.10 | 2002-2010 | 54889 | 73 | 6 |
| Amazon | Amazon | 822_03 | -3.40 | -64.55 | 1737.10 | 2002-2010 | 54889 | | |
| Amazon | Amazon | T076 | -3.86 | -61.69 | 1832.23 | 1993-2002 | 55113 | 236 | 7 |
| Amazon | Amazon | T152 | -3.23 | -59.08 | 2932.85 | 1993-2002 | 54900 | 211 | 8 |
| Amazon | Amazon | T139b | -2.70 | -56.95 | 4504.96 | 1993-2002 | 54694 | 268 | 9 |
| Amazon | Amazon | T139h | -2.58 | -56.90 | 4504.96 | 1993-2002 | 54694 | | |
| Amazon | Amazon | T228 | -2.51 | -56.50 | 4523.41 | 1993-2002 | 54498 | 229 | 10 |
| Amazon | Amazon | T215 | -1.98 | -53.85 | 5266.47 | 1993-2002 | 54299 | 258 | 11 |
| Ganges | Ganges | tp116_1 | 29.56 | 78.04 | 21.31 | 1993-2002 | 40351 | 265 | 12 |
| Ganges | Ganges | j2_116 | 27.93 | 78.86 | 37.56 | 2008-2011 | 41607 | 82 | 13 |
| Ganges | Ganges | j2_181 | 27.41 | 79.63 | 72.77 | 2008-2011 | 41910 | 80 | 14 |
| Ganges | Ganges | J2_003 | 25.58 | 81.59 | 81.07 | 2008-2011 | 42802 | 82 | 15 |
| Ganges | Ganges | j2_192 | 25.21 | 83.00 | 464.12 | 2008-2011 | 43096 | 65 | 16 |
| Ganges | Bra | J2_231 | 24.68 | 89.67 | 521.32 | 2008-2011 | 43384 | 89 | 17 |
| Ganges | Ganges | j2_079 | 25.70 | 84.48 | 630.36 | 2008-2011 | 42808 | 227 | 18 |
| Ganges | Ganges | tp079_1 | 25.69 | 84.47 | 630.36 | 1993-2002 | 42808 | | |
| Ganges | Ganges | 595_02 | 25.70 | 84.74 | 714.88 | 2002-2008 | 42809 | 62 | 19 |
| Ganges | Ganges | 595_03 | 25.75 | 84.73 | 714.88 | 2002-2008 | 42809 | | |

| Basin | River | Station | Latitude | Longitude | Catchment area [10³ km³] | Time series | WaterGAP cell ID | No. of observations 1993-2010 per 0.5°cell | No. |
|---|---|---|---|---|---|---|---|---|---|
| Ganges | Ganges | 051_01 | 25.55 | 85.49 | 758.51 | 2002-2008 | 42810 | 58 | 20 |
| Ganges | Ganges | tp014_1 | 25.50 | 85.70 | 775.30 | 1993-2002 | 43101 | 240 | 21 |
| Ganges | Ganges | j2_014 | 25.51 | 85.70 | 775.30 | 2008-2011 | 43101 | | |
| Ganges | Ganges | 509_01 | 25.32 | 86.27 | 794.68 | 2002-2008 | 43102 | 62 | 22 |
| Ganges | Ganges | 509_02 | 25.35 | 86.27 | 794.68 | 2002-2008 | 43102 | | |
| Ganges | Ganges | 967_03 | 25.27 | 87.00 | 800.27 | 2002-2008 | 43103 | 31 | 23 |
| Ganges | Ganges | j2_155 | 25.29 | 87.12 | 901.76 | 2008-2011 | 43104 | 210 | 24 |
| Ganges | Kos | j2_155 | 25.42 | 87.18 | 901.76 | 2008-2011 | 43104 | | |
| Ganges | Ganges | tp155_1 | 25.26 | 87.11 | 901.76 | 1993-2002 | 43104 | | |
| Ganges | Ganges | 423_01 | 25.26 | 87.73 | 918.37 | 2002-2008 | 43105 | 55 | 25 |
| Ganges | Ganges | 423_02 | 25.30 | 87.71 | 918.37 | 2002-2008 | 43105 | | |
| Ganges | Ganges | j2_090 | 23.93 | 89.26 | 937.99 | 2008-2011 | 43947 | 507 | 26 |
| Ganges | Ganges | j2_231 | 23.92 | 89.33 | 937.99 | 2008-2011 | 43947 | | |
| Ganges | Ganges | tp090_1 | 23.92 | 89.26 | 937.99 | 1993-2002 | 43947 | | |
| Ganges | Ganges | tp231_1 | 23.92 | 89.33 | 937.99 | 1993-2002 | 43947 | | |
| Ganges | Ganges | 337_01 | 23.82 | 89.52 | 1478.93 | 2002-2008 | 43948 | 58 | 27 |
| Ganges | Ganges | 795_02 | 23.42 | 90.34 | 1487.40 | 2002-2008 | 44229 | 59 | 28 |
| Mississippi | Mississippi | tp219_2n | 41.87 | -90.17 | 230.69 | 1993-2002 | 32185 | 268 | 29 |
| Mississippi | Mississippi | tp219_2s | 41.80 | -90.22 | 230.69 | 1993-2002 | 32185 | | |
| Mississippi | Mississippi | tp219_1 | 40.11 | -91.49 | 354.51 | 1993-2002 | 33269 | 100 | 30 |
| Mississippi | Mississippi | tp026_1 | 35.75 | -89.85 | 2399.30 | 1993-2002 | 36332 | 123 | 31 |
| Mississippi | Mississippi | tp204_1 | 33.12 | -91.13 | 2912.84 | 1993-2002 | 37918 | 137 | 32 |
| Mississippi | Mississippi | tp117_1 | 30.84 | -91.54 | 3210.93 | 1993-2002 | 39494 | 252 | 33 |
| Mississippi | Mississippi | tp193_1 | 29.35 | -89.48 | 3232.18 | 1993-2002 | 40485 | 73 | 34 |
| Niger | Niger | tp122_2 | 15.16 | -0.61 | 23.84 | 1993-2002 | 48233 | 215 | 35 |
| Niger | Niger | tp085_5 | 11.31 | -6.53 | 30.27 | 1993-2002 | 49535 | 135 | 36 |
| Niger | Niger | j2_148_1 | 12.46 | -8.08 | 115.07 | 2008-2011 | 49168 | 176 | 37 |
| Niger | Niger | tp148_1 | 12.46 | -8.08 | 115.07 | 1993-2002 | 49168 | | |
| Niger | Niger | tp135_2 | 13.42 | 5.61 | 131.43 | 1993-2002 | 48824 | 214 | 38 |
| Niger | Niger | j2_085_1 | 13.90 | -5.54 | 142.06 | 2008-2011 | 48612 | 455 | 39 |
| Niger | Niger | j2_224_1 | 13.75 | -5.73 | 142.06 | 2008-2011 | 48612 | | |
| Niger | Niger | tp085_1 | 13.92 | -5.53 | 142.06 | 1993-2002 | 48612 | | |
| Niger | Niger | tp224_1 | 13.76 | -5.74 | 142.06 | 1993-2002 | 48612 | | |
| Niger | Niger | tp085_3 | 14.04 | -5.49 | 148.03 | 1993-2002 | 48419 | 209 | 40 |
| Niger | Niger | 545_02 | 15.25 | -4.00 | 307.48 | 2002-2010 | 48025 | 78 | 41 |
| Niger | Ben | j2_020_1 | 8.01 | 7.75 | 316.28 | 2008-2011 | 50968 | 80 | 42 |
| Niger | Niger | 545_01 | 15.89 | -4.14 | 316.38 | 2002-2010 | 47817 | 78 | 43 |
| Niger | Niger | j2_046_1 | 16.06 | -3.80 | 343.07 | 2008-2011 | 47605 | 212 | 44 |
| Niger | Oro | j2_046_4 | 16.23 | -3.87 | 343.07 | 2008-2011 | 47605 | | |
| Niger | Niger | tp046_4 | 16.20 | -3.86 | 343.07 | 1993-2002 | 47605 | | |
| Niger | Niger | 388_01 | 16.73 | -2.56 | 375.50 | 2002-2010 | 47392 | 120 | 45 |
| Niger | Niger | 459_01 | 16.67 | -2.89 | 375.50 | 2002-2010 | 47392 | | |

| Basin | River | Station | Lati tude | Longi tude | Catch- ment area [10³ km³] | Time series | Water- GAP cell ID | No. of ob- servations 1993-2010 per 0.5°cell | No. |
|-------|-------|---------|-----------|------------|---------------------------|-------------|--------------------|------------------------------------------------|-----|
| Niger | Niger | 917_01 | 16.83 | -2.20 | 381.39 | 2002-2010 | 47393 | 68 | 46 |
| Niger | Niger | 846_01 | 16.92 | -1.80 | 387.29 | 2002-2010 | 47394 | 64 | 47 |
| Niger | Niger | 302_01 | 17.01 | -1.06 | 399.04 | 2003-2010 | 47176 | 279 | 48 |
| Niger | Niger | 373_01 | 17.01 | -1.53 | 399.04 | 2002-2010 | 47176 | | |
| Niger | Niger | j2_122_1 | 17.01 | -1.35 | 399.04 | 2008-2011 | 47176 | | |
| Niger | Niger | j2_161_1 | 17.02 | -1.47 | 399.04 | 2008-2011 | 47176 | | |
| Niger | Niger | 831_01 | 17.00 | -0.81 | 401.98 | 2002-2010 | 47177 | 71 | 49 |
| Niger | Niger | 760_01 | 16.94 | -0.36 | 428.42 | 2002-2010 | 47397 | 63 | 50 |
| Niger | Niger | 216_01 | 15.97 | 0.13 | 563.37 | 2002-2010 | 47826 | 143 | 51 |
| Niger | Niger | 287_01 | 15.96 | 0.15 | 563.37 | 2002-2010 | 47826 | | |
| Niger | Niger | j2_237_1 | 15.44 | 0.73 | 575.25 | 2008-2011 | 48035 | 245 | 52 |
| Niger | Niger | tp237_1 | 15.43 | 0.73 | 575.25 | 1993-2002 | 48035 | | |
| Niger | Niger | 130_01 | 14.37 | 1.20 | 646.67 | 2002-2010 | 48432 | 144 | 53 |
| Niger | Niger | 745_01 | 14.31 | 1.25 | 646.67 | 2002-2010 | 48432 | | |
| Niger | Niger | 874_03 | 10.62 | 4.66 | 1252.84 | 2002-2010 | 49754 | 154 | 54 |
| Niger | Niger | 874_04 | 10.90 | 4.72 | 1252.84 | 2002-2010 | 49754 | | |
| Niger | Niger | j2_135_1 | 10.96 | 4.68 | 1252.84 | 2008-2011 | 49754 | | |
| Niger | Niger | j2_211_3 | 8.37 | 6.56 | 1416.71 | 2008-2011 | 50771 | 64 | 55 |
| Niger | Niger | 702_01 | 6.65 | 6.65 | 1766.53 | 2002-2010 | 51342 | 70 | 56 |
| Niger | Niger | 029_01 | 5.99 | 6.72 | 1781.82 | 2002-2010 | 51708 | 73 | 57 |
| Niger | Niger | j2_198_4 | 4.77 | 6.10 | 1787.96 | 2008-2011 | 52056 | 356 | 58 |
| Niger | Niger | tp198_4 | 4.76 | 6.10 | 1787.96 | 1993-2002 | 52056 | | |
| Nil | Nil | tp133_1n | 6.55 | 31.41 | 510.38 | 1993-2002 | 51391 | 269 | 59 |
| Nil | Nil | tp120_2 | 7.09 | 30.77 | 516.49 | 1993-2002 | 51203 | 283 | 60 |
| Nil | Nil | tp196_1 | 10.68 | 32.28 | 1401.52 | 1993-2002 | 49809 | 131 | 61 |
| Nil | Nil | tp018_10 | 21.30 | 30.89 | 2543.18 | 1993-2002 | 45266 | 73 | 62 |
| Nil | Nil | 414_04 | 22.50 | 31.87 | 2566.09 | 2002-2010 | 44703 | 74 | 63 |
| Nil | Nil | 771_01 | 22.61 | 32.34 | 2577.49 | 2002-2010 | 44419 | 72 | 64 |
| Nil | Nil | 227_04 | 23.40 | 32.86 | 2663.50 | 2002-2010 | 44136 | 149 | 65 |
| Nil | Nil | 227_05 | 23.26 | 32.90 | 2663.50 | 2002-2010 | 44136 | | |
| Nil | Nil | 227_06 | 23.18 | 32.92 | 2663.50 | 2002-2010 | 44136 | | |
| Nil | Nil | 872_03 | 23.12 | 32.74 | 2663.50 | 2002-2010 | 44136 | | |
| Nil | Nil | 227_03 | 23.54 | 32.83 | 2677.63 | 2002-2010 | 43854 | 149 | 66 |
| Nil | Nil | 872_01 | 23.77 | 32.90 | 2677.63 | 2002-2010 | 43854 | | |
| Nil | Nil | 872_02 | 23.62 | 32.86 | 2677.63 | 2002-2010 | 43854 | | |
| Nil | Nil | 414_02 | 26.07 | 32.77 | 2758.59 | 2002-2010 | 42424 | 59 | 67 |
| Nil | Nil | tp159_1 | 27.05 | 31.26 | 2797.31 | 1993-2002 | 41821 | 27 | 68 |
| Nil | Nil | tp170_1 | 31.38 | 31.72 | 2886.93 | 1993-2002 | 39262 | 87 | 69 |
| Parana | Parana | 134_03 | -30.16 | -59.41 | 10.70 | 2002-2010 | 64424 | 74 | 70 |
| Parana | Parana | 134_04 | -30.21 | -59.42 | 10.70 | 2002-2010 | 64424 | | |
| Parana | Parana | tp189_J | -25.22 | -54.48 | 830.95 | 1993-2002 | 62823 | 213 | 71 |
| Parana | Parana | tp178_I | -27.29 | -57.91 | 958.36 | 1993-2002 | 63479 | 290 | 72 |

| Basin | River | Station | Latitude | Longitude | Catchment area [10³ km³] | Time series | WaterGAP cell ID | No. of observations 1993-2010 per 0.5°cell | No. |
|-------|-------|---------|----------|-----------|--------------------------|-------------|------------------|----------------------------------------------|-----|
| Parana | Parana | tp102_E | -29.59 | -59.60 | 2169.51 | 1993-2002 | 64271 | 340 | 73 |
| Parana | Parana | tp113_D | -29.93 | -59.63 | 2169.51 | 1993-2002 | 64271 | | |
| Parana | Parana | 493_02 | -30.05 | -59.61 | 2182.87 | 2002-2010 | 64423 | 75 | 74 |
| Parana | Parana | 493_03 | -30.10 | -59.60 | 2182.87 | 2002-2010 | 64423 | | |
| Parana | Parana | 035_01 | -31.16 | -60.03 | 2204.15 | 2002-2010 | 64718 | 72 | 75 |
| Parana | Parana | 035_02 | -31.24 | -60.01 | 2204.15 | 2002-2010 | 64718 | | |
| Parana | Parana | 579_01 | -31.58 | -60.64 | 2406.05 | 2002-2010 | 64862 | 375 | 76 |
| Parana | Parana | tp113_C | -31.84 | -60.66 | 2406.05 | 1993-2002 | 64862 | | |
| Parana | Parana | tp026_B1 | -33.03 | -60.57 | 2486.63 | 1993-2002 | 65134 | 290 | 77 |
| Parana | Parana | tp026_B2 | -32.91 | -60.64 | 2486.63 | 1993-2002 | 65134 | | |
| Parana | Parana | 134_05 | -32.75 | -60.13 | 2491.84 | 2002-2010 | 65135 | 147 | 78 |
| Parana | Parana | 579_04 | -32.57 | -60.36 | 2491.84 | 2002-2010 | 65135 | | |
| Parana | Parana | 592_09 | -33.63 | -59.66 | 2543.93 | 2002-2010 | 65255 | 76 | 79 |
| Parana | Parana | tp189_A | -33.87 | -58.96 | 2559.30 | 1993-2002 | 65371 | 281 | 80 |
| Parana | Parana | tp189_O | -33.64 | -58.81 | 2559.30 | 1993-2002 | 65371 | | |
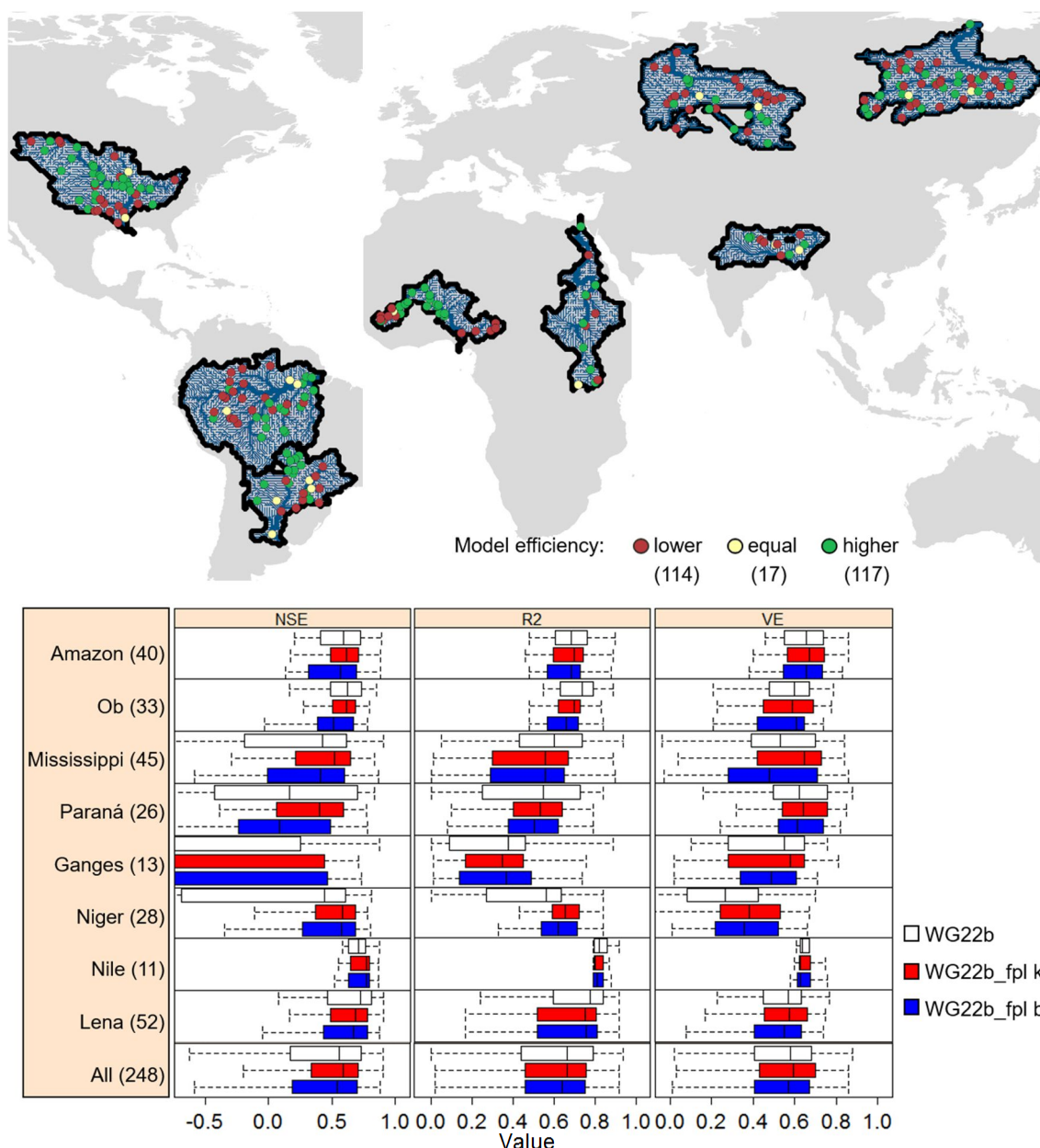
**Figure A.12** Model efficiency of WaterGAP (WG22b, WG22b_fpl k and WG22b_fpl b) simulating monthly river discharge at 248 locations within eight major river basins in the time period 1971-2000 (observed data: GRDC 2013). **Top:** change in model performance of WG22b_fpl k to the former WG22b at 248 gauging stations; at least two of the three efficiency criteria are higher (green), equal (yellow), or lower (red). **Bottom:** Box plot of model efficiency values $R^2$, NSE and VE, representing the median, 25% and 75% quartile (box) and the 1.5xIQR (whiskers). Outliers are not shown.

**Table A.3** Model efficiency ($R^2$, NSE, VE) of WaterGAP 2.2b (22b), WaterGAP 2.2b_fpl kinematic (k) and WaterGAP 2.2b_fpl backwater (b) simulating monthly river discharge at 40 locations within the Amazon River basin in the time period 1971-2000 (observed data: GRDC 2013). Note that WaterGAP 2.2b_fpl backwater is not calibrated.

| No. | mean | | | $R^2$ | | | NSE | | | VE | | |
|---|---|---|---|---|---|---|---|---|---|---|---|---|
| | observed | 22b | k | b | 22b | k | b | 22b | k | b | 22b | k | b |
| 1 | 752.71 | 726.91 | 643.75 | 655.45 | 0.28 | 0.25 | 0.25 | 0.2 | 0.17 | 0.18 | 0.63 | 0.62 | 0.62 |
| 2 | 393.11 | 426.36 | 417.15 | 425.81 | 0.6 | 0.62 | 0.6 | 0.58 | 0.59 | 0.58 | 0.51 | 0.51 | 0.51 |

| No. | mean | | | | R² | | | NSE | | | VE | | |
|---|---|---|---|---|---|---|---|---|---|---|---|---|---|
| | observed | 22b | k | b | 22b | k | b | 22b | k | b | 22b | k | b |
| 3 | 438.66 | 455.89 | 443.67 | 608.14 | 0.75 | 0.78 | 0.57 | 0.74 | 0.76 | 0.4 | 0.62 | 0.64 | 0.38 |
| 4 | 861.46 | 857.4 | 875.06 | 882.54 | 0.22 | 0.2 | 0.2 | 0.22 | 0.2 | 0.19 | 0.58 | 0.57 | 0.56 |
| 5 | 118.91 | 133.62 | 116.55 | 116.09 | 0.68 | 0.7 | 0.71 | 0.63 | 0.68 | 0.69 | 0.52 | 0.55 | 0.56 |
| 6 | 143.49 | 612.45 | 601.15 | 637.29 | 0.02 | 0.02 | 0.01 | -17.28 | -15.93 | -19.23 | -2.49 | -2.41 | -2.66 |
| 7 | 359.51 | 344.81 | 360.91 | 367.33 | 0.65 | 0.68 | 0.68 | 0.63 | 0.62 | 0.64 | 0.55 | 0.52 | 0.53 |
| 8 | 534.41 | 551.5 | 531.48 | 544.53 | 0.78 | 0.8 | 0.78 | -3.59 | -2.72 | -3.29 | 0.53 | 0.56 | 0.54 |
| 9 | 657.38 | 716.64 | 688.38 | 847.94 | 0.48 | 0.46 | 0.48 | 0.41 | 0.41 | 0.27 | 0.52 | 0.52 | 0.45 |
| 10 | 494.29 | 536.18 | 539.89 | 564.26 | 0.67 | 0.7 | 0.68 | 0.41 | 0.52 | 0.34 | 0.63 | 0.64 | 0.6 |
| 11 | 688.2 | 803.08 | 797.34 | 811.77 | 0.71 | 0.72 | 0.7 | 0.43 | 0.49 | 0.41 | 0.68 | 0.7 | 0.68 |
| 12 | 916.78 | 855.39 | 865.62 | 875.6 | 0.61 | 0.6 | 0.59 | 0.54 | 0.51 | 0.51 | 0.53 | 0.49 | 0.5 |
| 13 | 925.14 | 972.16 | 953.59 | 971.13 | 0.73 | 0.73 | 0.73 | 0.69 | 0.65 | 0.67 | 0.64 | 0.62 | 0.63 |
| 14 | 2394.29 | 2495.36 | 2436.3 | 2450.76 | 0.6 | 0.58 | 0.57 | 0.58 | 0.56 | 0.55 | 0.73 | 0.72 | 0.72 |
| 15 | 1254.78 | 1265.01 | 1344.37 | 1361.85 | 0.67 | 0.7 | 0.69 | 0.64 | 0.64 | 0.63 | 0.6 | 0.59 | 0.58 |
| 16 | 1037.54 | 1221.54 | 1195.19 | 1381.75 | 0.72 | 0.73 | 0.73 | 0.32 | 0.48 | 0.23 | 0.61 | 0.64 | 0.55 |
| 17 | 1484.9 | 1593.97 | 1520.22 | 1582.9 | 0.69 | 0.72 | 0.71 | -8.09 | -5.52 | -6.94 | 0.55 | 0.6 | 0.57 |
| 18 | 2480.45 | 2406.08 | 2399.34 | 2480.86 | 0.51 | 0.49 | 0.48 | 0.5 | 0.49 | 0.48 | 0.71 | 0.7 | 0.7 |
| 19 | 4856.03 | 5207.19 | 4446.55 | 4561.13 | 0.76 | 0.72 | 0.71 | 0.73 | 0.64 | 0.65 | 0.78 | 0.75 | 0.75 |
| 20 | 1356.27 | 1475.08 | 1431.39 | 1472.33 | 0.77 | 0.78 | 0.77 | 0.69 | 0.75 | 0.71 | 0.72 | 0.75 | 0.73 |
| 21 | 1288.25 | 1398.9 | 1420.22 | 1447.61 | 0.77 | 0.76 | 0.76 | 0.76 | 0.75 | 0.75 | 0.64 | 0.65 | 0.64 |
| 22 | 1388.9 | 1550.54 | 1561.18 | 1571.71 | 0.68 | 0.68 | 0.67 | 0.63 | 0.58 | 0.6 | 0.52 | 0.47 | 0.48 |
| 23 | 46053.24 | 5902.15 | 6515.75 | 6868.39 | 0.27 | 0.28 | 0.31 | -8.1 | -7.85 | -7.69 | 0.13 | 0.14 | 0.15 |
| 24 | 3483.42 | 3595.42 | 3456.45 | 3601.44 | 0.74 | 0.72 | 0.72 | 0.74 | 0.71 | 0.72 | 0.67 | 0.65 | 0.65 |
| 25 | 885.01 | 982.27 | 954.98 | 968.27 | 0.52 | 0.67 | 0.66 | 0.32 | 0.62 | 0.59 | 0.61 | 0.7 | 0.69 |
| 26 | 2676.62 | 2593.62 | 2601.96 | 2685.97 | 0.78 | 0.8 | 0.78 | 0.78 | 0.8 | 0.78 | 0.67 | 0.69 | 0.67 |
| 27 | 2830.46 | 2896.91 | 2709.35 | 2779.47 | 0.9 | 0.89 | 0.88 | 0.89 | 0.88 | 0.88 | 0.81 | 0.8 | 0.8 |
| 28 | 3784.67 | 4190.39 | 4026.85 | 4058.21 | 0.79 | 0.73 | 0.72 | 0.71 | 0.7 | 0.69 | 0.76 | 0.74 | 0.74 |
| 29 | 4753.63 | 4802.57 | 5006.76 | 5077.45 | 0.76 | 0.73 | 0.72 | 0.75 | 0.7 | 0.69 | 0.75 | 0.72 | 0.71 |
| 30 | 13584.13 | 14007.04 | 13662.75 | 13878.69 | 0.66 | 0.59 | 0.57 | 0.63 | 0.56 | 0.55 | 0.78 | 0.76 | 0.76 |
| 31 | 5651.07 | 5817.02 | 5823.06 | 5975.52 | 0.79 | 0.82 | 0.78 | 0.78 | 0.76 | 0.74 | 0.73 | 0.71 | 0.7 |
| 32 | 14366.35 | 16452.26 | 16115.35 | 17461.39 | 0.66 | 0.63 | 0.61 | 0.52 | 0.51 | 0.29 | 0.79 | 0.78 | 0.74 |
| 33 | 8145.93 | 9141.86 | 8725.73 | 8744.45 | 0.81 | 0.8 | 0.78 | 0.52 | 0.68 | 0.63 | 0.75 | 0.78 | 0.76 |
| 34 | 7883.92 | 6117.34 | 5618.88 | 5884.27 | 0.31 | 0.24 | 0.28 | 0.23 | 0.08 | 0.13 | 0.46 | 0.4 | 0.41 |
| 35 | 10088.15 | 10172.35 | 10049 | 9982.9 | 0.9 | 0.85 | 0.84 | 0.87 | 0.83 | 0.82 | 0.85 | 0.83 | 0.82 |
| 36 | 8250.98 | 9507.01 | 9464.77 | 9989.87 | 0.8 | 0.83 | 0.81 | 0.74 | 0.8 | 0.72 | 0.69 | 0.71 | 0.66 |
| 37 | 19538.48 | 22914.02 | 19357.72 | 19728.79 | 0.74 | 0.72 | 0.71 | 0.59 | 0.72 | 0.71 | 0.72 | 0.75 | 0.75 |
| 38 | 46001.52 | 46576.25 | 41674.99 | 44040.81 | 0.68 | 0.55 | 0.57 | 0.68 | 0.42 | 0.52 | 0.86 | 0.8 | 0.82 |
| 39 | 26582.21 | 30319.47 | 26526.83 | 26322.13 | 0.63 | 0.61 | 0.56 | 0.49 | 0.61 | 0.55 | 0.69 | 0.71 | 0.69 |
| 40 | 170356.27 | 181637.23 | 174644.22 | 170356.27 | 0.69 | 0.69 | 0.54 | 0.57 | 0.63 | 0.46 | 0.86 | 0.86 | 0.83 |

## 2.3  Water Storage

**Table A.4**   Model efficiency for major river basins and their subbasins larger than 400000 km² comparing monthly values of TWS variations simulated by three WaterGAP model variants (WG22b, WG22b_fpl k, and WG22b_fpl b) (all filtered) to GRACE observations in the time period from August 2002 to August 2009.

| Basin / Subbasin | R² | | | NSE | | | RMSE | | |
|---|---|---|---|---|---|---|---|---|---|
| | 22b | fpl k | fpl b | 22b | fpl k | fpl b | 22b | fpl k | fpl b |
| Amazon | 0.88 | 0.91 | 0.93 | 0.84 | 0.87 | 0.9 | 54.29 | 47.57 | 41.71 |
| Upstream Sao Paulo de Olivenca | 0.85 | 0.85 | 0.84 | 0.81 | 0.82 | 0.8 | 51.55 | 50.03 | 52.13 |
| Upstream Porto Velho | 0.62 | 0.62 | 0.62 | 0.6 | 0.58 | 0.56 | 47.67 | 48.54 | 49.74 |
| Upstream Obidos | 0.83 | 0.88 | 0.9 | 0.76 | 0.82 | 0.83 | 76.62 | 67.06 | 64.02 |
| Upstream Altamira | 0.87 | 0.86 | 0.86 | 0.84 | 0.82 | 0.82 | 81.45 | 85.22 | 85.08 |
| Ob | 0.68 | 0.67 | 0.65 | 0.65 | 0.62 | 0.6 | 31.59 | 32.9 | 34.15 |
| Upstream Salekhard | 0.73 | 0.72 | 0.69 | 0.69 | 0.66 | 0.64 | 37.59 | 39.39 | 40.81 |
| Upstream Hanti-Mansisk | 0.65 | 0.63 | 0.63 | 0.57 | 0.53 | 0.52 | 35.66 | 37.2 | 37.76 |
| Upstream Ust-Ishim | 0.6 | 0.59 | 0.58 | 0.53 | 0.51 | 0.48 | 28.57 | 29.09 | 30.02 |
| Upstream Prokhorkino | 0.57 | 0.54 | 0.56 | 0.56 | 0.53 | 0.52 | 40.12 | 41.45 | 41.53 |
| Mississippi | 0.58 | 0.59 | 0.6 | 0.48 | 0.5 | 0.52 | 30.76 | 30.3 | 29.73 |
| Upstream Vicksburg | 0.35 | 0.36 | 0.38 | 0.14 | 0.16 | 0.21 | 41.57 | 41.02 | 39.76 |
| Upstream Metropolis | 0.72 | 0.71 | 0.7 | 0.67 | 0.68 | 0.68 | 40.14 | 39.98 | 39.77 |
| Upstream Nebraska City | 0.56 | 0.56 | 0.5 | 0.53 | 0.53 | 0.46 | 33.41 | 33.51 | 35.74 |
| Upstream Bismarck | 0.6 | 0.6 | 0.5 | 0.58 | 0.58 | 0.5 | 35.03 | 35.13 | 38.34 |
| Paraná | 0.76 | 0.74 | 0.68 | 0.74 | 0.74 | 0.68 | 27.41 | 27.71 | 30.67 |
| Upstream Timbues | 0.59 | 0.39 | 0.33 | 0.57 | 0.36 | 0.29 | 41.42 | 50.63 | 53.28 |
| Upstream Corrientes | 0.27 | 0.22 | 0.22 | 0.25 | 0.18 | 0.19 | 41.99 | 43.93 | 43.73 |
| Upstream Porto Murtinho | 0.67 | 0.58 | 0.56 | 0.64 | 0.57 | 0.54 | 61.49 | 67.34 | 69.49 |
| Upstream Posadas | 0.69 | 0.67 | 0.58 | 0.63 | 0.64 | 0.56 | 35.05 | 34.93 | 38.39 |
| Upstream Uhe Jupia-Jusante-JJU | 0.89 | 0.87 | 0.72 | 0.78 | 0.77 | 0.62 | 59.23 | 60.95 | 78.91 |
| Ganges | 0.9 | 0.91 | 0.81 | 0.87 | 0.87 | 0.77 | 37.63 | 38.46 | 51.09 |
| Upstream Farakka | 0.82 | 0.83 | 0.66 | 0.78 | 0.78 | 0.61 | 51.93 | 52.01 | 68.11 |
| Upstream Bahadurabad | 0.89 | 0.89 | 0.88 | 0.85 | 0.82 | 0.78 | 39.04 | 42.16 | 46.59 |
| Niger | 0.82 | 0.8 | 0.76 | 0.7 | 0.68 | 0.65 | 44.24 | 45.53 | 48.22 |
| Upstream Lokoja | 0.74 | 0.74 | 0.68 | 0.65 | 0.64 | 0.59 | 62.11 | 63.05 | 67.16 |
| Upstream Gaya | 0.51 | 0.55 | 0.52 | 0.38 | 0.39 | 0.35 | 34.08 | 33.99 | 34.99 |
| Upstream Dire | 0.75 | 0.7 | 0.67 | 0.64 | 0.61 | 0.6 | 61.05 | 63.53 | 65.08 |
| Nile | 0.69 | 0.7 | 0.64 | 0.63 | 0.66 | 0.61 | 29.58 | 28.49 | 30.43 |
| Upstream El Ekhsase | 0.63 | 0.64 | 0.6 | 0.55 | 0.62 | 0.58 | 28.24 | 26.15 | 27.31 |
| Upstream Malakal | 0.75 | 0.68 | 0.66 | 0.65 | 0.61 | 0.59 | 50.7 | 53.62 | 54.74 |
| Upstream Mongalla | 0.22 | 0.2 | 0.03 | 0.11 | 0.13 | -0.19 | 51.18 | 50.65 | 59.15 |
| Lena | 0.65 | 0.58 | 0.54 | 0.58 | 0.57 | 0.54 | 30.46 | 30.84 | 31.95 |
| Upstream Stolb | 0.53 | 0.5 | 0.49 | 0.51 | 0.5 | 0.48 | 34.03 | 34.18 | 34.73 |
| Upstream Solyanka | 0.65 | 0.59 | 0.56 | 0.58 | 0.57 | 0.54 | 32.38 | 32.99 | 34.02 |
| Upstream Ohotsky Perevoz | 0.64 | 0.58 | 0.55 | 0.63 | 0.58 | 0.55 | 35.37 | 37.28 | 38.69 |
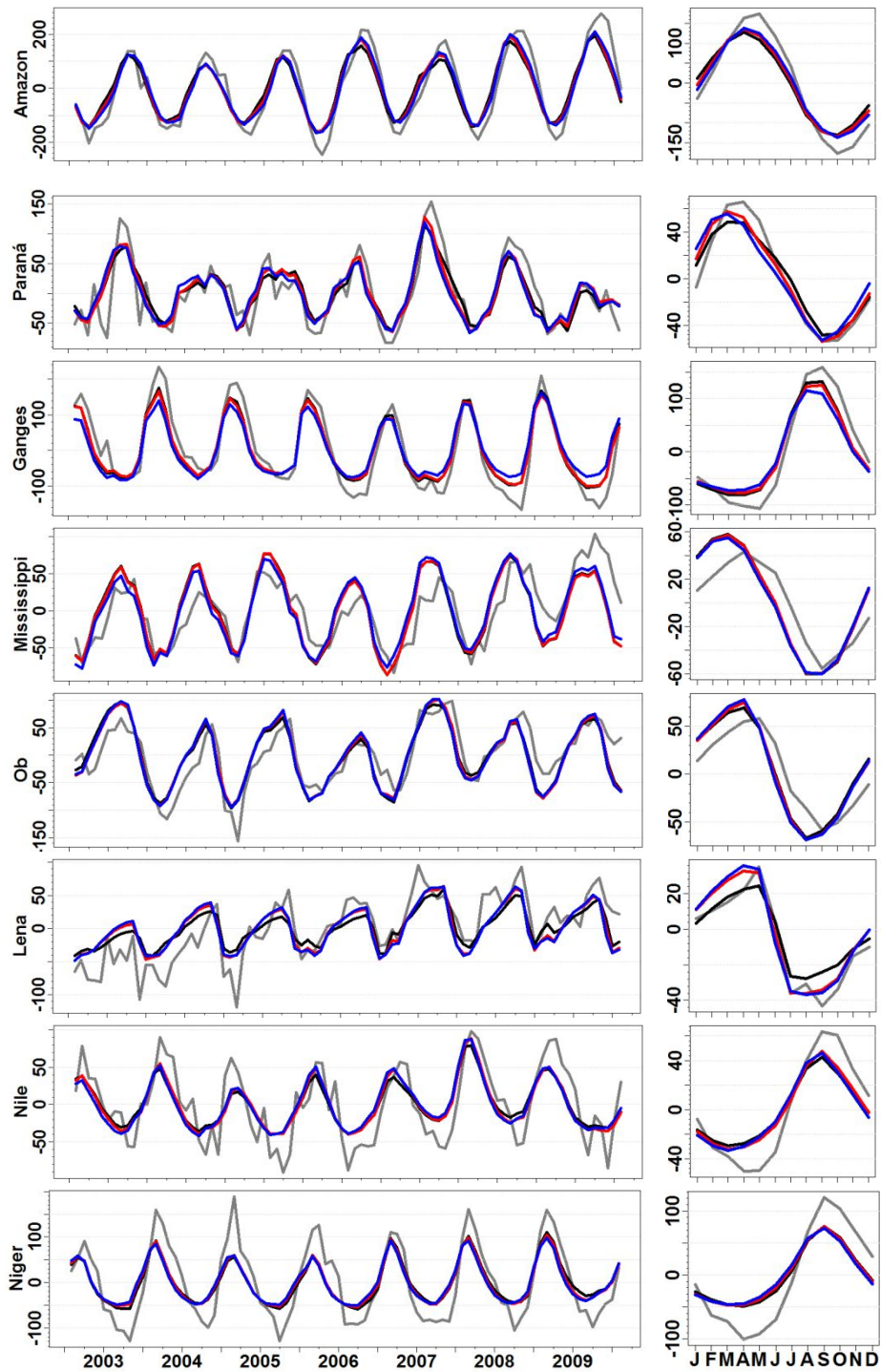
**Figure A.13** Basin-scale mean monthly (right) and monthly (left) TWS variations [mm EWH] observed by GRACE (grey) and modeled by WG22b (black), WG22b_fpl k (red), and WG22b_fpl b (blue). Model results are filtered.
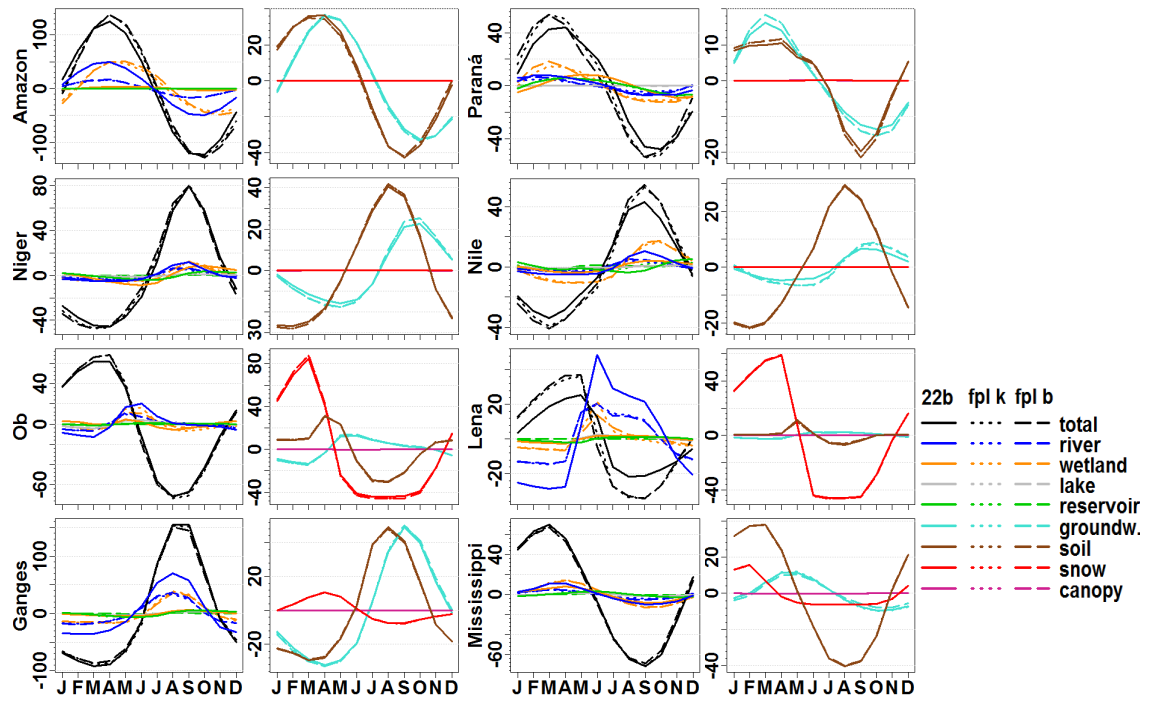
**Figure A.14** Basin-scale mean monthly (1971-2000) TWS variations and water storage variations of all single storage compartments [mm EWH] modeled by WG22b (solid), WG22b_fpl k (pointed), and WG22b_fpl b (dashed). Model results are unfiltered.

# 3  Appendix to Chapter 6

**Table A.5** Non-exhaustive overview of the various large-scale models from different communities (including WaterGAP 2.2_fpl) and their properties focused on floodplain algorithms (extended from Sood and Smakhtin (2015), and Bierkens (2015)).

| Features | WaterGAP (Water-Global Analysis and Prognosis) model | ISBA-TRIP (Interactions Between Soil, Biosphere, and Atmosphere - Total Runoff Integrating Pathways) | WBM-WTM/ WBMplus (Water Balance Model-Water Transport Model) | CaMa-Flood (Catchment-based Macro-scale Floodplain) model (runoff used from Land Surface Model MATSIRO) | PCR-GLOBWB (PCRaster GLOBal Water Balance) model | MGB- IPH (Modelo de Grandes Bacias - Instituto de Pesquisas Hidráulicas) | THMB (Terrestrial Hydrology Model with Biogeochemistry) - formerly HYDRA | JULES-G2G (Joint UK Land Environment Simulator - Grid-to-Grid) | LISFLOOD/ LISFLOOD-FP |
|---|---|---|---|---|---|---|---|---|---|
| **References** | Müller Schmied et al. (2014), floodplain algorithm developed and presented within this PhD work | Decharme et al. (2008), Decharme et al. (2012) | Beighley et al. (2009), Beighley et al. (2011) | Yamazaki et al. (2011), Yamazaki et al. (2012b) | van Beek and Bierkens (2009), Wada et al. (2014), Ringeval et al. (2014) | Paiva et al. (2011), Paiva et al. (2013) | Coe (2000), Coe et al. (2002), Coe et al. (2008) | Dadson et al. (2010) | Bates and De Roo (2000), Wilson et al. (2007), Trigg et al. (2009), Biancamaria et al. (2009), Neal et al. (2012) |
| **Type of model** | Global Hydrology Model | Global Hydrology Model | Global Hydrology Model | Large-scale coupled river routing and land surface model (runoff from MATSIRO) | Global Hydrology Model | Large-scale hydrological model | Large-scale Hydrological model | Large-scale coupled land surface and routing model | Large-scale hydrological model |
| **Spatial resolution and extent** | 0.5 degree, global extent | 1.0 degree, global extent | 0.5 degree, global extent; floodplain modeling presented only for the Amazon River basin on an irregular computational grid | 0.25 degree, global extent, river flow simulation in continental-scale rivers on unit catchment elements | 0.5 degree, global extent | Catchment units, different basins in South America | 5 minute, Amazon and Tocantis River basins | 0.5 degree, selected areas on the globe; mainly UK; floodplain modeling presented for the Niger inland delta | Raster-based discretization, resolution depends on input DEM, selected areas on the globe |
| **Validation regarding floodplain inundation** | global: floodplain area, floodplain height | global: floodplain area | Amazon river basin: floodplain width | Amazon river basin: floodplain area, floodplain height | Amazon river basin: floodplain extent and depth | Amazon river basin: floodplain area, floodplain height | Amazon river basin: floodplain area, floodplain height | Niger inland delta (study area ~13°x10°): inundated area | Ob river basin (study area 1°x5°): water heights, Amazon river basin (study area 2°x1.5°): water heights, Niger inland delta: |

| Features | WaterGAP | ISBA-TRIP | WBM-WTM/ WBMplus | CaMa-Flood | PCR-GLOBWB | MGB- IPH | THMB | JULES-G2G | LISFLOOD/ LISFLOOD-FP |
|---|---|---|---|---|---|---|---|---|---|
| | | | | | | | | | heights and extent |
| **Temporal resolution** | daily | daily (internal 20 minutes to 1 hour) | daily (internal routing time step of 15min) | daily (internal routing time step of 20-30min) | daily | daily | daily | monthly (internal 30-60min) | daily (Internal time step seconds) |
| **Drainage network** | DDM30 | Hydro1k | Derived from ground slopes using SRTM DEM | HydroSHEDS + SRTM3 | DDM30 | SRTM + GTOPO | Amazon Basin river directions (Costa et al. 2002) | Hydro1k | ACE (Ob), SRTM (Amazon) |
| **Inland water bodies** | Yes, GLWD; static but area is a function of storage (area is reduced with decreasing storage) | No | Yes, Reservoirs only (GRanD) | No (lakes and wetlands are treated as floodplains; MATSIRO includes reservoirs) | Yes, GLWD; static but lake area is a function of lake volume | No | Yes, GGHYDRO; static | Yes, global lake database GLDBv2; static | Yes; static but evaporation is a function of lake level |
| **Human water use** | Yes | No | Yes | Yes (MATSIRO) | Yes | No | Yes | Yes, irrigation only | Yes |
| **Vegetation** | Fixed, climatology of phenology, irrigated area change; 16 land cover types | 12 vegetation types (ECOCLIMAP database) | Fixed, climatology of phenology, irrigated area change; 3 vegetation types, forest, grassland, and shrubland | Simple crop growth model (MATSIRO) | Fixed, climatology of phenology, irrigated area change; 3 categories natural vegetation, rain-fed crops, and irrigated crops; further subdivided into tall and short vegetation. | Fixed, climatology of phenology, Vegetation map of South America from Eva et al. (2004) | Fixed, climatology of phenology | Dynamic + phenology + plant physiology; Optional: dynamic vegetation using TRIFFID | LAI-observed, LAI Climatology |
| **Channel geometry (river width and depth) and bankfull/flood initiation conditions** | As a function of river discharge (channel width (and channel depth at initial time step) calculated using hydraulic relationships after Allen et al. (1994)) and river water storage | As a function of river discharge and a basin-specific coefficient; bankfull height is calculated as a non-linear function of river width | As a function of drainage area (bankfull depth and width and floodplain width based on relationships presented in Gummadi (2008)) | As a function of discharge (channel width and bank height determined as a function of maximum 30 day upstream runoff) | As a function of discharge (channel depth and width calculated using hydraulic relationships after Allen et al. (1994)); bankfull discharge based on a statistical relationship | As a function of drainage area (channel width and bank height), coefficients determined using cross section profiles from 341 gauge stations located in the | As a function of drainage area (river stage height and width); coefficients determined based on visual inspection of observed hydrographs in the Amazon River basin | Not specified | Amazon: cross-sections and bankfull depth from sonar survey data; Ob: constant width and depth; Niger: as a function of discharge (using hydraulic relationships after Leo- |

| Features | WaterGAP | ISBA-TRIP | WBM-WTM/ WBMplus | CaMa-Flood | PCR-GLOBWB | MGB- IPH | THMB | JULES-G2G | LISFLOOD/ LISFLOOD-FP |
|---|---|---|---|---|---|---|---|---|---|
| | at previous time step (channel depth); bankfull discharge calculated using the partial duration series approach (Section 4.3.1) | | | | between climate indicators and observed bankfull discharge for 296 stations (Vörösmarty et al. 1998). Relationship extrapolated over the world. | Brazilian Amazon | | | pold and Maddock (1953) with coefficients from Hey and Thorne (1986)) |
| **River - floodplain interaction** | When discharge exceeds the bankfull capacity of the channel, a portion of it is routed along the floodplain; backflow to river if inflow from upstream is below actual discharge; river water level equals floodplain water level | The flood reservoir fills when the river height exceeds the critical river bankfull height, and vice versa; river-floodplain interaction as a function of river-floodplain water slope | When discharge exceeds the bankfull capacity of the channel, a portion of it is routed along the floodplain; backflow to river if discharge is below bankfull capacity; river water level equals floodplain water level | That water spilling from the river channel (flood initiation storage) is stored in the floodplain. river water level equals floodplain water level | The volume of water in excess of bankfull discharge floods the surrounding areas; no backflow to river necessary as floodplains are treated as regular river stretches; river water level equals floodplain water level | No interaction (water level (and flooded area) is calculated regarding river bottom elevation which is the lowest surface elevation of the DEM within a catchment); river water level equals floodplain water level | The volume of river water in excess of river bankfull volume (flood initiation volume) is added to the floodplain reservoir; backflow to the river if river water storage is below flood initiation storage | Overbank flows flood fractions of land cover types | When bankfull depth is exceeded, water is transferred from the channel to the overlying floodplain grid. |
| **Surface elevations** | HydroSHEDS + ACE2; 3 arc sec, global coverage | GTOPO30; 30 arc sec, global coverage | SRTM; 3 arc sec, near global coverage (±60°N) | SRTM30; 30 arc sec, near global coverage (±60°N) | Hydro1k; ~30 arc sec, global coverage | SRTM + GTOPO; 30 arc sec, global coverage; vegetation correction (17 m except for areas with low vegetation (Eva et al. 2004)) | SRTM; 3 arc sec, near global coverage (±60°N); vegetation correction (23 m for areas where forest is the predominant vegetation type (Eva et al. 2004; Hess et al. 2003)) | Hydro1k; ~30 arc sec, global coverage | ACE (Ob), SRTM (Amazon); ~30 arc sec (100 m); vegetation correction in Amazon region (data obtained doing fieldwork) |
| **Floodplain area** (CDF - cumulative distribution | CDF, floodplain storage is distributed over the | CDF, cumulative distribution of subgrid elevations | No | CDF, cumulative distribution of subgrid elevations | Optionally fixed or variable area option. | As a function of water level (sum of surface water | CDF (only the value if half of the grid cell is flooded | CDF (using only the mean and the standard deviation | The values of water depth at each cross-section |

| Features | WaterGAP | ISBA-TRIP | WBM-WTM/ WBMplus | CaMa-Flood | PCR-GLOBWB | MGB- IPH | THMB | JULES-G2G | LISFLOOD/ LISFLOOD-FP |
|---|---|---|---|---|---|---|---|---|---|
| function of sub-grid surface elevations) | subgrid cells based on the cumulative distribution of relative elevations (100 points) | | | (36 points) | For variable: CDF, floodplain storage is distributed over the subgrid cells based on the cumulative distribution of relative elevations | pixels inside a floodplain catchment that is lower than the water level) | is used); to avoid runaway flooding maximum floodable area is used as input (unpublished data from Hess et al.) | of the logarithm of elevation). A prorated fraction of the preexisting surface types is converted to have an "open water" land cover type. | are overlain onto a DEM (or the inundation extents at each cross section are linearly interpolated). |
| **Routing** | Optional: kinematic wave (kw) or kw allowing backwater flows (partial diffusive wave) for channels and floodplains | Kinematic wave | Kinematic wave for first-order tributary channels, Muskingum-Cunge for interbasin channels and floodplains | Diffusive wave | Kinematic wave | Hydrodynamic model in flat reaches of the main rivers, Muskingum-Cunge method in upstream areas | Kinematic wave, diffusive wave for floodplains | Kinematic wave | Diffusive wave for channels and floodplains |
| **Flood routing direction** | Along the river network; channel and floodplain gradients identical | No floodplain flow routing | Along the river network; channel and floodplain gradients identical | No floodplain flow routing | No floodplain flow routing; floodplains treated as regular river stretches with increased resistance | No floodplain flow routing; the floodplains act only as storage areas | According to the maximum water slope between neighboring grid cells | No floodplain flow routing | According to the maximum water slope between neighboring grid cells |
| **Flow velocity v (including specifications of the roughness coefficient n)** | Variable in time and space; Different flow velocities on river and floodplain, $n_r$ variable (global mean $n_r$=0.04), $n_f$=0.07 | Variable in time and space; $n_r$ varies arbitrary from upstream areas to the river mouth (0.04-0.06), $n_f$ according to the vegetation type (0.035 - 1.0); slope taken from STN-30p DEM (0.5° resolution) | Variable in time and space; $n_r$=0.04, $n_f$=0.07 | Variable in time and space; n=0.03 for the Amazon river basin | Variable in time and space; increased wetted perimeter and Manning's n in case of flooding --> increased hydraulic resistance (decreased vr) $n_r$=0.04, $n_f$=0.1 | Constant in time, variable in space; $n_r$= 0.035-0.04 (different values for different large river basins aiming at fitting hydrographs) | Constant in time, variable in space | Constant in time and space: $v_r$=1.0 m/s, $v_f$=0.2 m/s | Not explicitly considered by the model, $v_r$ [m/s] at high/ low water: Solimoes 1.3/ 0.77, Purus 0.86/ 0.26; nr usually 0.01 - 0.04, $n_f$ usually 0.03 - 0.15. Can be set individually for each grid cell. |
| **Soil and Groundwater dynamics** | Vertical soil, groundwater reservoir | Vertical soil, groundwater reservoir | Vertical soil, groundwater reservoir | Vertical soil, groundwater reservoir (MATSI-RO) | Vertical soil, groundwater reservoir or lateral groundwater (op- | Soil reservoir and groundwater reservoir | Vertical soil, groundwater reservoir | Vertical soil | Vertical soil, groundwater reservoir |

| Features | WaterGAP | ISBA-TRIP | WBM-WTM/ WBMplus | CaMa-Flood | PCR-GLOBWB | MGB- IPH | THMB | JULES-G2G | LISFLOOD/ LISFLOOD-FP |
|---|---|---|---|---|---|---|---|---|---|
| | | | | | tional) | | | | |
| **Floodplain-groundwater interaction** | Yes | Yes | No | No | No | No | No | No | No |
| **Institutes responsible for model development** | Kassel University (Germany), Goethe University Frankfurt (Germany) | Centre National de Recherchés Météorologiques, France | University of New Hampshire (USA), City University of New York (USA) | IIS, University of Tokyo (Japan) | Utrecht University (Netherlands), Deltares (Netherlands) | Instituto de Pesquisas Hidráulicas – IPH, Universidade Federal do Rio Grande do Sul – UFRGS (Brasil) | SAGE, University of Wisconsin-Madison (USA) | Centre for Ecology and Hydrology (UK), Met Office (UK) | University of Bristol (UK) |

166